1506
UNIVERSITÀ
DEGLI STUDI
DI URBINO
CARLO BO

Department of Pure and Applied Sciences
Dipartimento di Scienze Pure e Applicate

Philosophy Degree in Basic Sciences and Applications
Curriculum Earth Sciences
Corso di Dottorato in Scienze di Base e Applicazioni
Curriculum Scienze della Terra
XXIX Ciclo

Titolo della tesi:

Mineralogical study of the fibrous zeolites erionite and offretite and hazard assessment

Studio mineralogico delle zeoliti fibrose erionite ed offretite e valutazione della pericolosità

Settore Scientifico Disciplinare SSD: GEO/06

Dottorando
Matteo Giordani

Relatore
Prof. Michele Mattioli

Anno Accademico 2015/2016

1506
UNIVERSITÀ
DEGLI STUDI
DI URBINO
CARLO BO

Department of Pure and Applied Sciences
Dipartimento di Scienze Pure e Applicate

Philosophy Degree in Basic Sciences and Applications
Curriculum Earth Sciences
Corso di Dottorato in Scienze di Base e Applicazioni
Curriculum Scienze della Terra
XXIX Ciclo

Titolo della tesi:

Mineralogical study of the fibrous zeolites erionite and offretite and hazard assessment

Studio mineralogico delle zeoliti fibrose erionite ed offretite e valutazione della pericolosità

Settore Scientifico Disciplinare SSD: GEO/06

Dottorando
Matteo Giordani

Relatore
Prof. Michele Mattioli

Anno Accademico 2015/2016

A mio padre

List of contents

Chapter 1

GENERAL INTRODUCTION AND SUMMARY

Several fibrous minerals are known in nature, some of which have chemical and physical characteristics very useful in various industrial processes and applications. However, some of them are considered highly hazardous to human health, because of their capability to divide into inhalable size fibers, together with their biopersistence in the lungs. This is the case, for example, of the well-known asbestos. Nevertheless, there are many other fibrous minerals with physical and chemical characteristics very similar with those of asbestos, which have not been sufficiently investigated. For some of them, such as attapulgite, palygorskyte, byssolite, picrolite, sepiolite, thomsonite, scolecite, mesolite, natrolite and offretite, the dangerousness has not yet been neither confirmed nor denied. For others fibrous minerals (e.g. jamesonite, carlostauranite, wollastonite, nemalite, clinoptilolite, phillipsite, mordenite) preliminary studies seem to point out some toxic effects. Lastly, other fibrous phases have already been well studied and are currently considered carcinogenic if inhaled, such as fluoro-edenite, balangeroite, riebeckite, grunerite and erionite.

Several fibrous minerals belong to the zeolite group. Zeolites occurs worldwide and are widely used in materials for the construction industry, in paper, in agriculture and in other applications. Therefore, potential exposure to the fibres may occur during the mining, production and use of the fibrous zeolites (IARC, 1997). In particular, the exposure of erionite fibres to humans has been unambiguously linked to malignant mesothelioma (Baris et al., 1978), and in vivo studies have demonstrated that erionite is significantly more tumorigenic than asbestos (Coffin et al., 1992). For these reasons, the International Agency for Research on Cancer (IARC) has referred erionite as a Class 1 carcinogen, and at present is considered as the most carcinogenic mineral (IARC 1987; 2012). Recently, a growing concern has developed regarding the potential risks associated with environmental and occupational exposures to erionite in Turkey (Carbone et al., 2011), in the United States (Saini-Eidukat and Triplett, 2014), in Mexico (Ortega-Guerrero and Carrasco-Nùñez, 2014) and possibly in Iran (Ilgren et al., 2015). Then, it is very likely that this problem could also be extended to other countries in the future.

The main mechanisms by which inhaled fibres of erionite, as well as other fibrous particulates, induce pathological changes comprise the following factors: (a) physical features of the fibrous mineral particles such as diameter, length and aspect ratio; (b) chemical-mineralogical features (fibre type, chemical composition and surface reactivity); (c) the ability to generate reactive oxygen species (ROS); and (d) the biopersistence. Despite of the great number of researches, the relationships among mineralogical features and biological activity of erionite have not been fully understood and there are no systematic studies on the distribution of erionite or other similar fibrous zeolites in the environment. Moreover, there is another zeolite, named offretite, which is closely related both structurally and chemically to erionite. Despite commonly occurring as prisms, offretite has also been found under asbestiform habit, meaning that the morphology of its crystals has not yet been fully known and many mineralogical aspects are still to be discovered. Due to these similarities and to the possible intergrowth, the distinction between erionite and offretite can be hampered. To date, there are no studies regarding a potentially hazard of offretite fibers and it is unclear whether the mineralogical distinction between erionite and offretite has any health implications.

The gap of knowledge of the fibrous zeolites erionite and offretite has been the starting

point for the development of the present PhD project. This work is based on a detailed mineralogical study with determination of morphological and morphometric characteristics, physical properties, chemical compositions and crystalline structures of selected samples of both erionite and offretite zeolites. Successively, these samples have been used to carry out *in-vitro* experiments to assess the level of reactivity and transformation that such fibers may induce to micelles and membranes in contact with them, and therefore, indirectly the possibility of leading to asbestos-related lung diseases.

On the basis of this starting point, the Thesis has been organized in 6 Chapters.

This Chapter (Chapter 1) is dedicated to a general introduction illustrating the major aims of this project and the structure-organization of the Thesis. A brief summary with main results of each chapter is also presented.

In Chapter 2, the occurrence and characterization of the potentially carcinogenic erionite from Lessini Mounts (NE Italy) are reported. Morphological, morphometrical, mineralogical and chemical investigations performed on two representative samples of fibrous erionite, which has not been examined previously, are presented. The first sample is erionite-Ca with an extremely fibrous, hair-like and flexible appearance, growth in intimate association with levyne. The second sample is erionite-Na with prismatic to acicular crystals and rigid behavior, with significant amount of K^+ and Ca^{2+} as extra-framework cations. In both the investigated erionite samples, fibrils of inhalable size are present. Considering that the toxicity and the carcinogenic potential of erionite are associated with its size parameters, together with its *in vivo* durability and very high surface area, most of the investigated fibers may also be potentially carcinogenic.

In Chapter 3, the mineralogical characterization of erionite from Northern Italy is integrated and completed with structural data and extended to other erionite samples from Italy. A multi-methodological approach, based on field investigation, morphological characterization, SEM/EDS chemical analysis and structure refinement through X-ray powder diffraction was applied to different samples of potentially carcinogenic erionite. The chemical composition of the studied crystals ranges from erionite-Ca to erionite-Na, and they show variable morphologies, ranging from prismatic, through acicular and fibrous, to extremely fibrous asbestiform habits. The fibrous samples are characterized by an unusual preferred partition of Al at T1 instead of T2 site. Moreover, a mismatch between the a-parameter of erionite-Ca and levyne-Ca that are intergrown in the asbestiform sample has been detected. This misfit is coupled to a relevant microstrain to maintain structure coherency at the boundary. Erionite occurs in 65% of the investigated sites, with an estimated amount from 10 to 40 vol.% of the associated minerals. These amounts are not negligible for the human health, particularly if the great number of quarries and mining-related activities operating in the zeolites host rocks is considered. The discovery of fibrous and asbestiform erionite in the Northern Italy suggests the need for a detailed risk assessment in all Italian areas showing the same possible hazard, with specific studies such as a quantification of the potentially airborne fibres and targeted epidemiological surveillance.

The Chapter 4 is dedicated to the morphological, mineralogical and chemical characterization of the other fibrous zeolite offretite, which has been found with asbestiform habit in the Northern Italy and is suspected to be carcinogenic. The investigated samples show different habits, from stocky-prismatic crystals with a solid appearance (FF102), through prismatic or acicular with rigid mechanical behavior (AD13), to extremely fibrous crystals (asbestiform) with rigid to flexible behavior (MB2287). In the acicular and asbestiform offretite samples (AD13 and MB2287), fibrils of inhalable size are certainly present. The chemical composition of the investigated offretite samples is coherent with reference data and showing EF cations K^+, Mg^{2+} and Ca^{2+} in comparable proportions in all samples. Despite of the lack of epidemiological

information on populations exposed to natural asbestiform minerals other than asbestos and erionite, results acquired in the present investigation suggest that other mineral fibres of similar size, habit, and biopersistence may carry a risk for humans.

In Chapter 5, morpho-chemical characterization and surface properties determinations were performed on a selection of different asbestiform zeolite fibers: two erionite samples (GF1, MD8), one offretite sample (BV12) and, for comparison, one scolecite sample (SC1). The specific surface area determinations coupled with EPR analysis indicated a larger availability of surface sites for the adsorption onto GF1, while SC1 showed the lowest one and the presence of large pores in the poorly fibrous zeolite aggregates. Selected spin probes revealed a high adsorption capacity of GF1 compared to the other zeolites, but the polar/charged interacting sites were well distributed, intercalated by less polar sites (Si–O–Si). MD8 surface was less homogeneous and the polar/charged sites were more interacting and closer to each other compared to GF1. The interacting ability of BV12 surface was much lower than that found for GF1 and MD8 and the probes were trapped in small pores into the fibrous aggregates. In comparison with the other zeolites, the non-carcinogenic SC1 exhibited a poor interacting ability and a lower surface polarity. These results helped to clarify the chemical properties and the surface interacting ability of these zeolite fibers which may be related to their carcinogenicity.

In Chapter 6, the same selection of asbestiform zeolite fibers investigated in Chapter 5 was studied by analyzing the electron paramagnetic resonance (EPR) spectra of selected surfactant spin probes and TEM images in the presence of model membranes - cetyltrimethylammonium (CTAB) micelles, egg-lecithin liposomes, and dimyristoylphosphatidylcholine (DMPC) liposomes - to get informations on the fiber internalization in the membranes and the interactions occurring at a molecular level that mimicked the attack of the fibers at the cell membrane. For the CTAB micelles, all fibers were able to enter the micelles, but GF1 modified the micelle structure towards a bilayer-like organization, while MD8 and BV12 partially destroyed the micelles. For the liposomes, GF1 fibers partially entered inside the core solution, but DMPC liposomes showed increasing rigidity and organization of the bilayer. Conversely, for MD8 and BV12, the fibers did not cross the membrane showing a smaller membrane-structure perturbation. As comparison, scolecite fibers (SC1) showed poor interactions with the model membranes. The carcinogenicity of the zeolites, hypothesized in the series SC1<BV12<MD8<GF1, may be nicely related to the structural modifications of the model membranes when interacting with these zeolite fibers.

Introduzione generale e Sommario

In natura sono noti numerosi minerali fibrosi, alcuni dei quali possiedono caratteristiche chimiche e fisiche molto utili in vari processi industriali ed applicazioni. Tuttavia, alcuni di questi minerali fibrosi sono considerati molto pericolosi per la salute umana, per la loro capacità di dividersi in fibre di dimensioni inalabili, unitamente alla loro biopersistenza nei polmoni. Questo è il caso, ad esempio, dei ben noti minerali del gruppo degli amianti. Tuttavia, esistono molti altri minerali fibrosi con caratteristiche fisiche e chimiche molto simili a quelle dell'amianto, che non sono state sufficientemente indagate. Per alcuni di loro, come ad esempio attapulgite, palygorskyte, bissolite, picrolite, sepiolite, Thomsonite, scolecite, mesolite, Natrolite e offretite, la pericolosità non è ancora stata né confermata né smentita. Per altri minerali fibrosi (ad esempio jamesonite, carlostauranite, wollastonite, nemalite, clinoptilolite, phillipsite, mordenite) studi preliminari sembrano indicare alcuni effetti tossici. Infine, altre fibre minerali sono già state ben studiate e sono attualmente considerate cancerogene per inalazione, come fluoro-edenite, balangeroite, riebeckite, grunerite ed erionite.

Diversi minerali fibrosi appartengono al gruppo delle zeoliti. Le zeoliti si rinvengono in tutto il mondo e sono ampiamente utilizzate nei materiali per l'edilizia, nella fabbricazione della carta, in agricoltura e in altre applicazioni. Pertanto, una potenziale esposizione alle fibre può verificarsi durante l'estrazione, la produzione e l'uso di zeoliti fibrose (IARC, 1997). In particolare, l'esposizione umana a fibre di erionite è stata inequivocabilmente collegata al mesotelioma maligno (Baris et al., 1978), e studi *in vivo* hanno dimostrato che l'erionite è significativamente più cancerogena dell'amianto (Coffin et al., 1992). Per queste ragioni, l'Agenzia Internazionale per la Ricerca sul Cancro (IARC) ha classificato l'erionite come cancerogeno di classe 1, e attualmente è considerato il minerale più pericoloso (IARC 1987; 2012). Recentemente, si è sviluppata una preoccupazione crescente per quanto riguarda i potenziali rischi associati ad esposizioni ambientali ed occupazionali ad erionite in Turchia (Carbone et al., 2011), negli Stati Uniti (Saini-Eidukat e Triplett, 2014), in Messico (Ortega-Guerrero e Carrasco-Nuñez 2014) e in Iran (Ilgren et al., 2015).
Quindi, è molto probabile che in futuro questo problema venga esteso anche ad altri Paesi.
I principali meccanismi con cui le fibre di erionite, nonché altri particolati fibrosi inalabili, inducono cambiamenti patologici, comprendono i seguenti fattori: (a) le caratteristiche fisiche delle particelle fibrose come diametro, lunghezza e loro proporzione; (b) le caratteristiche chimico-mineralogiche (tipo di fibra, composizione chimica e reattività superficiale); (c) la capacità di generare reactive oxygen species (ROS); e (d) la biopersistenza. Nonostante il gran numero di ricerche, le relazioni tra caratteristiche mineralogiche ed attività biologica dell'erionite non sono state pienamente comprese e non ci sono studi sistematici sulla distribuzione di erionite o di altre zeoliti fibrose nell'ambiente. Inoltre, vi è un'altra zeolite, l'offretite, che è strettamente correlata sia strutturalmente che chimicamente con l'erionite. Nonostante sia comunemente descritta con abito prismatico, l'offretite è recentemente stata ritrovata anche con aspetto asbestiforme, a testimonianza del fatto che la sua morfologia non è stata ancora pienamente studiata, e molti aspetti mineralogici sono ancora da scoprire. A causa della somiglianza e delle possibili intercrescite, la distinzione tra erionite ed offretite può risultare molto difficile. Ad oggi, non esistono studi in merito ad una potenziale pericolosità delle fibre di offretite e non è chiaro se la distinzione tra i minerali erionite ed offretite abbia qualche implicazione per la salute.

La lacuna nelle conoscenze delle zeoliti fibrose erionite e offretite è stato il punto di partenza per lo sviluppo del presente progetto di dottorato. Questo lavoro è basato su un dettagliato studio mineralogico, con determinazione di caratteristiche morfologiche e morfometriche, proprietà fisiche, composizioni chimiche e strutture cristalline di campioni selezionati sia di erionite che di offretite. Successivamente, questi campioni sono stati utilizzati per effettuare esperimenti *in vitro* per valutare il livello di reattività e di trasformazione che tali fibre possono indurre a micelle e membrane a contatto con esse, e quindi, indirettamente la possibilità di portare a malattie polmonari asbesto correlate.

Sulla base di questo punto di partenza, la tesi è organizzata in 6 capitoli.

Questo capitolo (Capitolo 1) è dedicato ad una introduzione generale che illustra i principali obiettivi di questo progetto e la struttura-organizzazione della tesi. Inoltre, viene presentato anche un breve riassunto con i principali risultati di ogni capitolo.

Nel capitolo 2, è riportato il ritrovamento e la caratterizzazione di erionite potenzialmente cancerogena dai Monti Lessini (NE Italia). Vengono descritte le indagini morfologiche, morfometriche, mineralogiche e chimiche effettuate su due campioni rappresentativi di erionite fibrosa, che non erano mai stati esaminati prima. Il primo campione risulta erionite-Ca con aspetto estremamente fibroso, simile a capelli, e comportamento flessibile, cresciuta in stretta associazione con levyna. Il secondo campione è erionite-Na con cristalli da prismatici ad aciculari e comportamento rigido, con una significativa quantità dei cationi ex-

tra-framework K^+ e Ca^{2+}. In entrambi i campioni di erionite studiati, sono presenti fibrille di dimensioni inalabili. Considerando che la tossicità e il potenziale cancerogeno dell'erionite sono associati ai relativi parametri dimensionali, nonché alla sua durabilità *in vivo* e all'area superficiale molto elevata, la maggior parte delle fibre indagate potrebbe essere anche potenzialmente cancerogena.

Nel capitolo 3, la caratterizzazione mineralogica dell'erionite dal Nord Italia è integrata e completata con i dati strutturali ed estesa ad altri campioni di erionite italiana. L'approccio multi-metodologico, basato su indagini sul campo, caratterizzazione morfologica, analisi chimica con SEM/EDS e raffinamento strutturale attraverso diffrazione a raggi X delle polveri, è stata applicata a diversi campioni di erionite potenzialmente cancerogeni. La composizione chimica dei cristalli studiati varia da erionite-Ca a erionite-Na, e mostrano morfologie variabili, che vanno da prismatiche, passando per aciculari e fibrose, fino ad estremamente fibrose o asbestiformi. I campioni fibrosi sono caratterizzati da una partizione preferenziale insolita di Al al sito T1 anziché a T2. Inoltre, è stata rilevata una mancata corrispondenza tra i parametri-a di erionite-Ca e Levyne-Ca concresciuti nel campione asbestiforme. Questo misfit è accoppiato ad una rilevante micro-deformazione per mantenere la coerenza strutturale. Erionite si rinviene nel 65% dei siti indagati, con una quantità stimata da 10 a 40 vol.% dei minerali associati. Questi importi non sono trascurabili per la salute umana, in particolare se si considera il gran numero di cave e attività estrattive operanti nelle rocce che ospitano queste zeoliti. La scoperta di erionite fibrosa ed asbestiforme nel Nord Italia suggerisce la necessità di una valutazione dettagliata dei rischi, in tutte le zone d'Italia che mostrano lo stesso possibile pericolo, con studi specifici come ad esempio una quantificazione delle fibre potenzialmente aerodisperse e una sorveglianza epidemiologica mirata.

Il capitolo 4 è dedicato alla caratterizzazione morfologica, mineralogica e chimica dell'altra zeolite fibrosa offretite, sospettata di essere cancerogena, che nel Nord Italia è stata trovata con abito asbestiforme. I campioni esaminati mostrano diversi abiti che vanno da cristalli prismatici a barilotto, con un aspetto compatto (FF102), a prismatici o aciculari con comportamento meccanico rigido (AD13), fino a cristalli estremamente fibrosi (asbestiformi) con comportamento da rigido a flessibile (MB2287). Nei campioni di offretite aciculare ed asbestiforme (AD13 e MB2287) sono certamente presenti fibrille di dimensioni inalabili. La composizione chimica dei campioni di offretite indagati è coerente con i dati di letteratura, mostrando quantità confrontabili dei cationi EF K^+, Mg^{2+} e Ca^{2+} in tutti i campioni. Nonostante la mancanza di dati epidemiologici sulle popolazioni esposte ai minerali asbestiformi diversi da amianto ed erionite, i risultati acquisiti nel presente studio suggeriscono che altre fibre minerali di dimensioni, abito, e biopersistenza simili possono comportare un rischio per gli esseri umani.

Nel capitolo 5, sono state eseguite alcune caratterizzazioni morfo-chimiche e sono state determinate le proprietà di superficie di diverse fibre asbestiformi di zeoliti selezionate: due campioni di erionite (GF1, MD8), un campione di offretite (BV12) e, per confronto, un campione di scolecite (SC1). Le determinazioni dell'area superficiale specifica, accoppiata con l'analisi EPR, indicano una grande disponibilità di siti superficiali per l'adsorbimento per GF1, e la più bassa per SC1, e mostrano la presenza di grandi pori negli aggregati delle zeoliti poco fibrose. Gli spin probes selezionati hanno rivelato una elevata capacità di adsorbimento di GF1 rispetto alle altre zeoliti, ma i siti interagenti polari/carichi erano ben distribuiti, intercalati da siti meno polari (Si-O-Si). La superficie di MD8 è risultata meno omogenea e i siti polari/carichi erano più interagenti e vicini tra loro rispetto a GF1. La capacità di interagire delle superfici di BV12 è risultata molto più bassa rispetto a GF1 e MD8 e le sonde sono rimaste intrappolate nei piccoli pori degli aggregati fibrosi. In confronto con le altre zeoliti, la non-cancerogena SC1 ha mostrato una scarsa capacità di interazione ed una inferiore polari-

tà superficiale. Questi risultati hanno contribuito a chiarire le proprietà chimiche e la capacità di interazione superficiale di queste zeoliti fibrose, che possono essere correlate alla loro cancerogenicità.

Nel capitolo 6, è stata studiata la stessa selezione di fibre di zeoliti asbestiformi investigate nel Capitolo 5 analizzando gli spettri di risonanza paramagnetica elettronica (EPR) di spin probes surfattanti selezionati e immagini TEM in presenza di modelli di membrane - micelle cetiltrimetilammonio (CTAB), liposomi di lecitina d'uovo e liposomi dimyristoylphosphatidylcholine (DMPC) - per ottenere informazioni sulla internalizzazione delle fibre nelle membrane, e le interazioni che avvengono a livello molecolare che sono in grado di imitare l'attacco delle fibre sulla membrana cellulare. Per le micelle CTAB, tutte le fibre sono state in grado di entrare nelle micelle, ma GF1, modificandole, ha prodotto strutture con un doppio strato. MD8 e BV12 hanno invece parzialmente distrutto le micelle. Per i liposomi, le fibre di GF1 sono parzialmente entrate, mentre i liposomi DMPC hanno mostrato un aumento di rigidità e l'organizzazione del doppio strato. Viceversa, per MD8 e BV12, le fibre non hanno attraversato la membrana che mostra però una piccola perturbazione. Come confronto, le fibre di scolecite (SC1) hanno mostrato deboli interazioni con i modelli di membrane. La cancerogenicità delle zeoliti, ipotizzata nella serie SC1 <BV12 <MD8 <GF1, può essere ben correlata alle modifiche strutturali dei modelli di membrane quando interagiscono con queste fibre.

Chapter 2

POTENTIALLY CARCINOGENIC ERIONITE FROM LESSINI MOUNTAINS, NE ITALY: MORPHOLOGICAL, MINERALOGICAL AND CHEMICAL CHARACTERIZATION

2.1 Introduction

It is widely known that small particles, in particular those with fibrous appearance, may be inhaled generating biological processes that lead to toxicity and carcinogenicity within the lungs (Cook et al., 1982; Wagner et al., 1985; Pott et al., 1987; Davis et al., 1991; Coffin et al., 1992; Fubini, 2001; Crovella et al., 2016). One of the most important factors that defines the hazardousness of fibrous minerals is the size of the fibers and fibrils which may originate from the source crystals (Stanton et al., 1981; Lee, 1985; Oberdörster et al., 2005; Millette, 2006; Aust et al., 2011; Mossman et al., 2011; Boulanger et al., 2014; Oberdorster et al., 2015). The regulatory definition of "fiber" encompasses structures having a minimum length (typically 5μm) and an aspect ratio (i.e. the ratio of the length to the diameter) over 3:1 (NIOSH, 1994). "Fibril" means a single fiber that cannot be separated into smaller components without losing its fibrous properties or appearance (USBM, 1996). Fibril widths vary by mineral and geologic source, with typical values ranging from approximately 0.02 μm to 0.3 μm in diameter. Fibers may thus be single fibrils or bundles of fibrils. The World Health Organization (WHO, 1986) considers as inhalable the fibers with a diameter-length ratio ≥ 1:3, a length > 5 μm and a diameter < 3 μm. However, the majority of fibers detected in the human respiratory tract are generally < 1 μm in diameter and shorter than 5 μm in length (Dodson et al., 2003; Suzuki et al., 2005; Aust et al., 2011), and fibers ≤ 0.25 μm in diameter and > 8 μm in length seem to be the most carcinogenic (Stanton et al., 1981).

The fibers biopersistence, i.e. the length of time a particle resides within a given biological compartment, is also an important factor for fibers toxicity and carcinogenicity (Hesterberg et al., 1998; Fubini, 2001; Maxim et al., 2006). It was postulated that a inhalable fiber might be carcinogenic if it is sufficiently durable to remain chemically and physically intact in lung tissue (Muhle et al., 1991; Oberdörster et al., 2005). The fibers biopersistence is also related to the chemical composition of the mineral fibers and some elements can play a key role to determine the carcinogenic mechanisms (e.g. the presence of iron (Fe); Bonneau et al., 1986; Wiseman and Halliwell, 1996; Fubini, 2001; Gazzano et al., 2005; Crovella et al., 2016). Other fibers characteristics such as specific surface area, interacting capability, structure, net charge, zeta potential and microtopography might also act as important factors in fiber-induced toxicity and carcinogenicity (Lippmann, 1988; Hochella, 1993; Pollastri et al., 2014; Oberdörster et al., 2015; Mattioli et al., 2016b).

During the late 1970s, an epidemic of malignant pleural mesothelioma was discovered in Karain, Tuzkoy and Sarihidir, three small villages in the Cappadocia region, Central Anatolia, Turkey (Baris et al., 1978, 1979; Artvinli and Baris, 1979). Subsequently, through mineralogy and analysis of lung content, this epidemic has been linked to the occurrence of the fibrous mineral erionite of respirable size in the region's bedrock (Baris et al., 1987; Emri et al., 2002; Dogan et al., 2006; Carbone et al., 2007, 2011; Metintas et al., 2010). It was reported that 78% of the deaths that had occurred in this area were due to malignant mesothelioma, and it is estimated that 50% of the total deaths can be attributed to erionite (Metintas et al., 1999; Emri et al., 2002). Moreover, emigrants from this region were also found to have increased risk of malignant mesothelioma (Metintas et al., 1999).

Experimental studies showed that fibrous erionite of inhalable size is 300-800-fold more carcinogenic and may be 20-40-fold more active than chrysotile and crocidolite asbestos in increasing the incidence of mesothelioma (Wagner et al., 1985; Hill et al., 1990; Davis et al., 1991; Coffin et al., 1992; Bertino et al., 2007; Dogan, 2012; Croce et al., 2013; Hillegass et al., 2013; de Assis et al., 2014; Zebedeo et al., 2014). For these reasons, and according to epidemiological data (Baris et al., 1978, 1979, 1987; Temel and Gundogdu, 1996; Kokturk et al., 2005; Dogan et al., 2006; Carbone et al., 2007, 2011; Kliment et al., 2009; Metintas et al., 2010; Carbone and Yang, 2012; Demirer et al., 2015), erionite was classified as carcinogenic mineral for the human health and referred to Class 1 carcinogen by the International Agency for Research on Cancer since 1987 and, at present, is categorized as the most carcinogenic mineral (IARC, 1987; 2012).

In recent years, growing interest in this area produced new investigations on adverse health effects of erionite and its carcinogenic potential, mechanisms of carcinogenesis and potential genetic predispositions (Dogan et al., 2006; Metintas et al., 2010; Carbone and Yang, 2012; Ballirano et al., 2015; Ballirano and Cametti, 2015; Demirer et al., 2015; Pollastri et al., 2015). However, the sequence of events, following erionite fiber deposition leading to a fiber-type hazard to the human respiratory tract remains to be determined.

Despite the growing interest in this mineral, various morphological types of erionite and the different ways to form fibers and fibrils have not yet been fully understood and many mineralogical, chemical and toxicological aspects are still unknown.

The aim of this study was to present a detailed morphological, morphometrical, mineralogical and chemical characterization of two selected samples of potentially carcinogenic fibrous erionite recently discovered in the Lessini Mounts (Veneto region, Northern Italy). Data from scanning electron microscopy-energy dispersive spectroscopy (SEM-EDS), electron probe microanalysis (EPMA) and X-ray powder diffraction (XRPD) were combined and integrated, with the aim to improve knowledge of this dangerous zeolite.

2.2 Mineralogical background

Erionite is a tectosilicate belonging to the ABC-6 family of the zeolite group (Gottardi and Galli, 1985). It is hexagonal, space group symmetry $P6_3/mmc$ and unit-cell parameters a = 13.19-13.34 Å, c = 15.04-15.22 Å (Staples and Gard, 1959; Alberti et al., 1997; Gualtieri et al., 1998; Bish and Ming, 2001; Deer et al., 2004; Cametti et al., 2013). The average chemical formula is $Na_2K_2Ca_3[Al_{10}Si_{26}O_{72}]$ $30H_2O$ and the erionite framework consists of $(Si,Al)O_4$ tetrahedra linked together to form single-six rings and double six-rings, resulting in fibrous morphologies, to arrange three types of cages who characterize this zeolite: a six-membered double ring (empty), a cancrinite cage (preferred by K), and an erionite cage with dispersed Ca, Na, and Mg (Gottardi and Galli, 1985; Alberti et al., 1997; Passaglia et al., 1998; Bish and Ming, 2001; Deer et al., 2004; Cametti et al., 2013). Due to a significant chemical variability, three different species, erionite-K, erionite-Ca, and erionite-Na have been identified, depending on the most abundant extra-framework cation (Coombs et al., 1997; Deer et al., 2004; Dogan and Dogan, 2008; Dogan et al., 2008).

It should be noted that despite it is considered a rare mineral (Passaglia and Galli, 1974; Bish and Ming, 2001), erionite was detected in many localities globally such as Antarctica, Austria, Canada, the Czech Republic, France, Georgia, Germany, Iceland, Italy, Japan, Kenya, Korea, Mexico, New Zealand, Russia, Scotland, Slovakia, Tanzania, Turkey and USA (e.g. Passaglia et al., 1998; Dogan and Dogan 2008; Dogan et al., 2008; Van Gosen et al., 2013; Ortega-Guerrero and Carrasco-Nunez, 2014; Saini-Eidukat and Triplett, 2014), suggesting a more widespread distribution than supposed. The individual crystals of erionite are about 2-200 μm long and 0.1-10 μm thick. Thus, erionite is consistently elongated, but is not always fibrous. This is also evidenced by the great number of terms used in literature to describe erionite crystals in-

cluding prismatic, acicular, needles, rods, fibrous, fibers, fibrils, hair-like, wooly, bundles, radiating clusters and sprays, as well summarized by Dogan et al. (2008) and Van Gosen et al. (2013). Anyhow, it can be resumed that erionite crystal habit ranges from typically prismatic to extremely fibrous (i.e. with hair-like or wooly appearance). In the prismatic habit, erionite crystals tend not to grow with parallel alignment, but form multidirectional growth patterns instead; the crystals tend to fracture easily, fragmenting into prismatic small particles.

Differently, the erionite with extremely fibrous habit has also been described as being "asbestiform", a term applied to minerals with a macroscopic habit similar to that of asbestos (NIOSH, 2011).

The asbestiform habit can be defined as a habit where crystals grow almost exclusively in a single dimension, in a straight line until they form long, thread-like fibers with aspect ratios of 20:1 to 100:1 and higher, and exhibit narrow width (on the order of 0.1 μm; Case et al., 2011). Asbestiform fibers are also often flexible, exhibit high tensile strength and are resistant to heat and chemicals.

From an environmental health prospective, erionite with asbestiform habit has been shown to be a potent carcinogen (e.g. Dumortier et al., 2001; Hillegass et al., 2013; Zebedeo et al., 2014), whereas the prismatic morphotype is typically at least 2 μm in width and would presumably be less likely to form inhalable mineral particles. However, other potential considerations are that (1) elongated forms of erionite greater than 2 μm in width (i.e. prismatic habit) may form thinner, fibrous particles of inhalable size (e.g. Carbone et al., 2007; Ballirano and Cametti, 2015), (2) the morphology of erionite prisms that are composed of many fibers and fibrils enhances its surface-area-to-volume ratio drastically (Dogan et al., 2008; Ballirano et al., 2015), and (3) the surfaces of prismatic erionite crystals are less homogeneous and the polar/charged sites are more interacting and closed to each other compared to the asbestiform erionite (Mattioli et al., 2016b). Considering that a comprehensive study specific to erionite morphology is lacking in the literature, the carcinogenicity of all growth forms of erionite has not been established.

2.3 Materials and methods

2.3.1 Materials

Two fibrous samples of erionite (BV201 and MF2) were investigated in this study. These samples originated from the Alpone Valley, Lessini Mounts (Figure 1), where a thick sequence of lava flows of the Veneto Volcanic Province extensively crops out (De Vecchi and Sedea, 1995; Milani et al., 1999; Bonadiman et al., 2001). These lavas range from poorly- to highly-vesiculated and/or scoriaceous, and vesicles are often filled by secondary minerals, which are dominated by zeolites of hydrothermal origin (Mattioli et al., 2016a). The two samples examined were selected according to the two main morphologic types of erionite from Lessini Mounts, which also correspond to the main morphologies described for erionite worldwide: extremely fibrous with flexible, hair-like appearance (BV201) and prismatic to acicular crystals with rigid behavior (MF2).

2.3.2 Environmental Scanning Electron Microscope (ESEM)

Morphological observations were achieved with an Environmental Scanning Electron Microscope (ESEM) FEI Quanta 200 FEG at the University of Urbino Carlo Bo. Morphometric data were collected by accurate size measurements (length and diameter) of all of the erionite fibers and fibrils visible in several ESEM images. These pictures were selected according to three main criteria: to (i) be representative of the total area of each investigated sample, (ii) permit the measurements of both length and diameter of the fibers, and (iii) have a significant number of measurements (> 1000).

The micro-chemical characterization was performed using a JEOL 6400 SEM equipped with an EDX Genesis EDS system at the University of Parma. Operating conditions were 15 kV accelerating voltage, 11 mm working

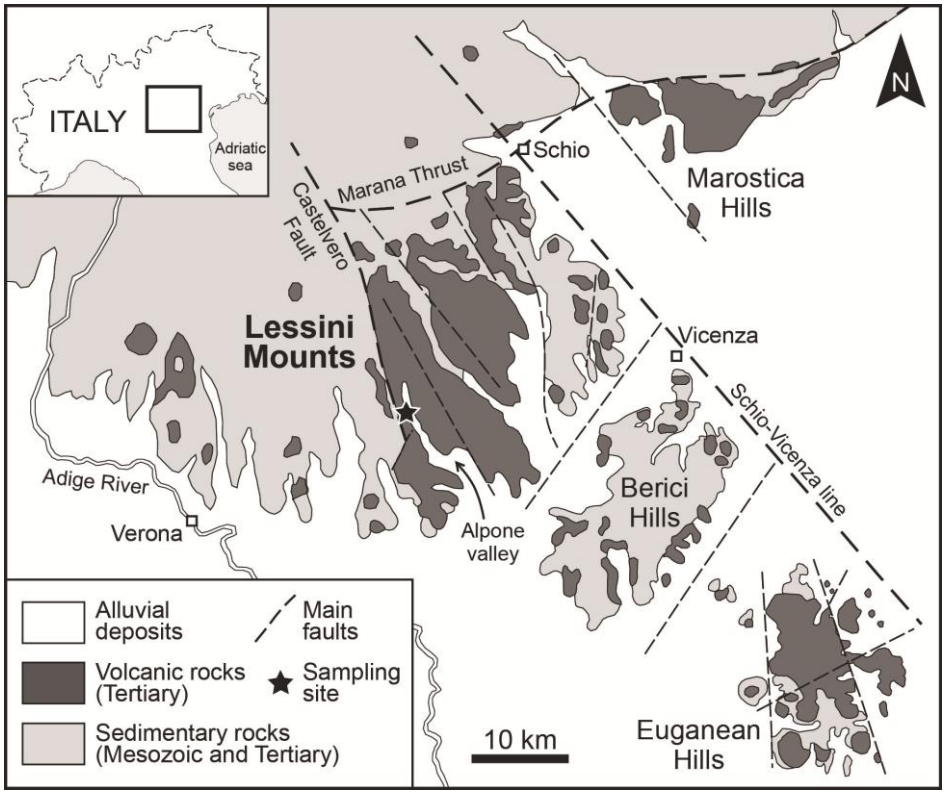

Figure 1. Geological sketch map of the volcanic rocks in the Veneto Region, NE Italy (modified from De Vecchi and Sedea, 1995), with indication of the Lessini Mounts and sampling site (star).

distance, 0° tilt angle and 1 μm beam diameter. As previously suggested (Sweatman and Long, 1969; Goldstein et al., 1992; Reed, 1993; Pacella et al., 2016), in order to minimize the alkali metal migration, chemical data was acquired using a low counting times (up to 10 sec) and a raster scan-mode to reduce the temperature increase. With these optimized experimental conditions, no significant differences between the SEM-EDS and EMPA datasets were observed, indicating the reliability of the collected data.

2.3.3 Electron Micro Probe Analysis (EMPA)

Pure crystals from the two samples of erionite were prepared for electron micro probe analysis (EMPA) by embedding a fraction of fibers in epoxy resin. Compositions were determined using a Cameca SX50 EPMA equipped with wavelength-dispersive spectrometry (WDS). According to the recommended protocol for the quantitative determination of zeolite compositions by EMPA (Campbell et al., 2016) the following conditions were used: reduced counting time (up to 10 sec), beam diameter 20 μm, accelerating voltage 15 kV, low beam current and element prioritizing with the spectrometer configuration.

Chemical data were collected from several individual point analyses for each sample, depending on the number of crystals available. In elongated crystals or crystal aggregates, several point analyses were performed along the fiber to check for chemical homogeneity. The point analyses of each sample were highly consistent, showing a variation of major elements within 2-3% of the estimated instrumental errors and indicating a high degree of chemical homogeneity within each sample. Silicates, oxides, and pure elements were used as standards; analytical errors are 1-2% rel. and 3-5% rel. for major and minor elements, respectively. The final crystal chemical formula of erionite was calculated on the basis of 36 ($Si+Al+Fe^{3+}$) apfu based on 72 oxygen atoms. The reliability of the chemical analysis used to determine the erionite species was evaluated by using a charge balance error formula (E%; Passaglia, 1970; Passaglia et

al., 1998) and the Mg-content test (Dogan and Dogan, 2008; Dogan et al., 2008). Chemical analyses for zeolites are considered to be reliable if the balance error (E%) is equal to or less than ±10%.

2.3.4 X-ray Powder Diffraction (XRDP)

After preliminary screening, a sufficient amount of pure crystals was selected from each sample under a binocular microscope on the basis of the absence of any recognizable impurity phase. They were subsequently disaggregated and pulverized in an agate mortar, and the powder was loaded in a 0.7 mm side-opened aluminum holder. XRPD data were collected using a Philips X'Change PW1830 powder diffractometer at the University of Urbino Carlo Bo. Analytical conditions were 35 kV accelerating voltage and 30 mA beam current, with CuKα radiation (λ = 1.54056 Å). Data were collected in Bragg-Brentano geometry from 2 to 65° 2Θ, with a step size of 0.01° 2Θ and 2.5 s counting time for each step. Semi-quantitative XRPD analyses were performed on both samples. The following software packages were used for the measurements and subsequent analysis: X'Pert Quantify 3.0 for data collection and instrument control, and X'Pert HighScore 3.0 for semi-quantitative phase analysis.

2.4 Results

2.4.1 Morphology

The BV201 sample is formed by alternating layers of erionite and levyne, forming a "sandwich-like" morphology (Figure 2a).

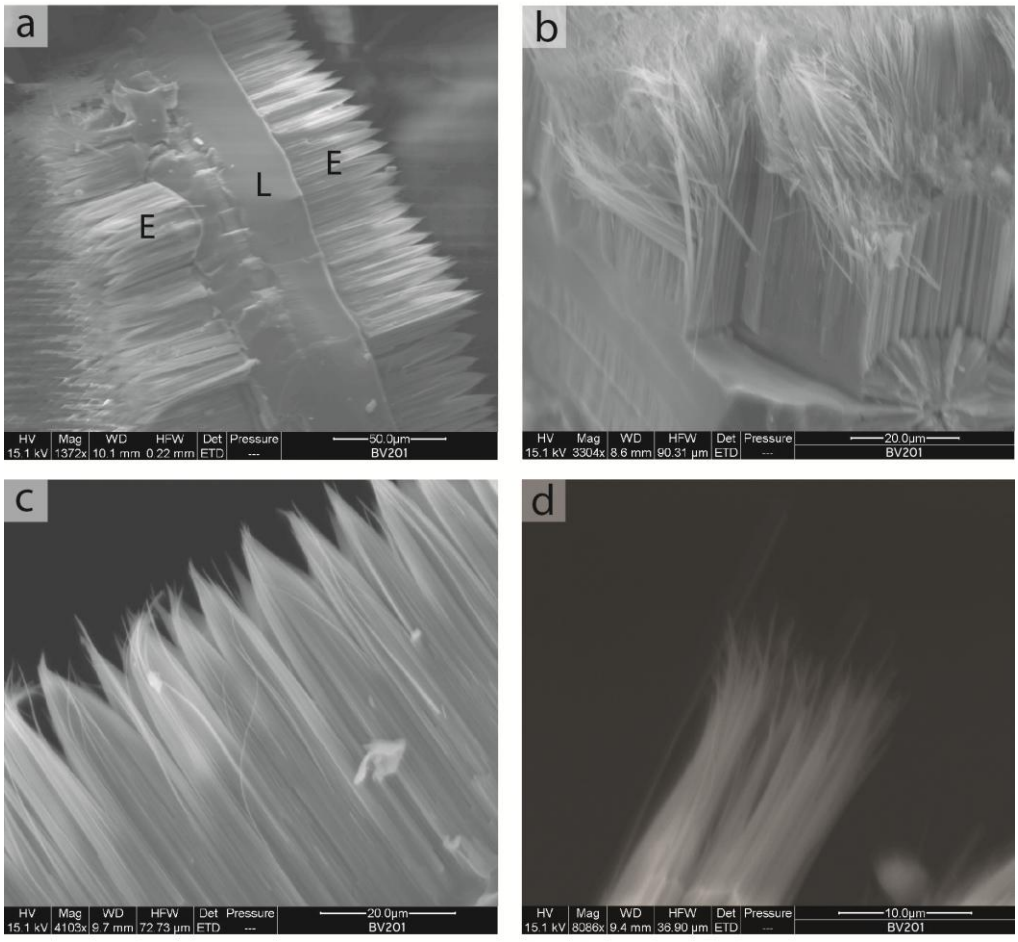

Figure 2. Electron microphotographs of erionite from BV201 sample. a) Typical erionite-levyne-erionite (ELE) sequence; b) particular of the erionite fibers with extremely fibrous habit showing flexible behavior; c) curious "like-brushes" terminations of erionite bundles; d) bundle of erionite showing high tendency to divide into very thin fibers and fibrils.

This erionite-levyne intergrowth is extremely similar to that described by Passaglia and Galli (1974) for some zeolites from Sardinia (Italy). In BV201 sample, levyne displays a highly tabular habit with hexagonal form and millimetric size, often made up of several overlapping crystals. Erionite grows up normally to the levyne surfaces, forming a typical erionite-levyne-erionite sequence (ELE, Figure 2a), which may also be repeated several times. In BV201 sample, erionite is characterized by an extremely fibrous habit which consists of flexible, hair-like fibers having a diameter on the order of 0.1 μm and extremely variable lengths. According to these characters, erionite of the BV201 sample can be described as having an asbestiform habit. In some cases, erionite fibers have a uniform length of ~50 μm over the entire surface of levyne (Figure 2b), while in other cases, the length of erionite fibers is variable, ranging from < 1 μm to ~50 μm. Curiously, these fibers tend to intimately aggregate in parallel beams with diameter of ~10 μm and pointed ends, resulting in a "brush tip" morphology (Figure 2c). However, these bundles are always characterized by a tendency to separate thin fibers and fibrils (Figure 2d). In this sample, erionite demonstrated a typical wooly aspect, which is similar in appearance to that near Durkee, Oregon (Eakle, 1898; Staples and Gard, 1959).

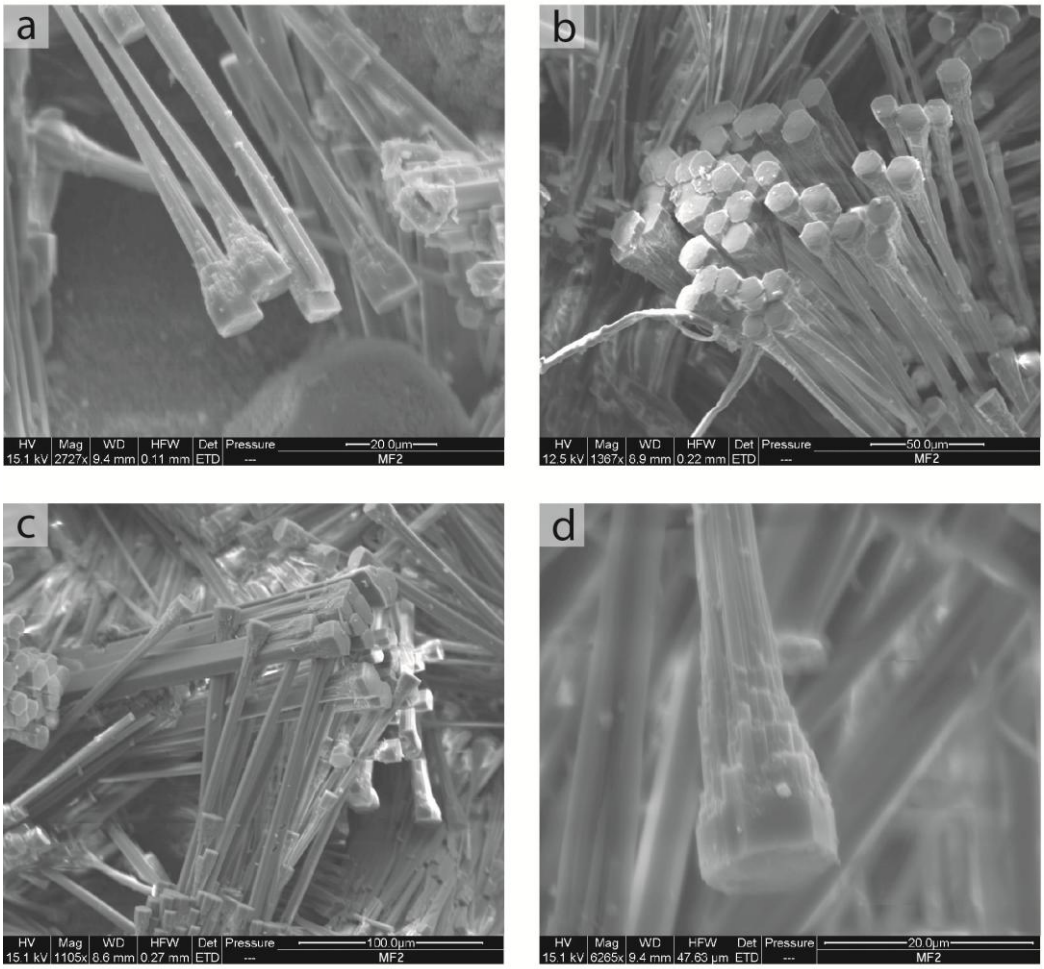

Figure 3. Electron microphotographs of erionite from MF2 sample. a) Elongated, prismatic to acicular well-shaped, single crystals; b) aggregates of many crystals radiating from a central point with well-formed hexagonal terminations; c) aggregates of crystals which mutually grow to generate irregular networks; d) particular of the crystal where hexagonal termination with solid appearance and the irregular shape of the main body can be observed.

In MF2 sample, erionite is present as prismatic to acicular crystals with diameters of ~5 μm and lengths up to 150 μm, which presents well-shaped, single crystals or discrete aggregates of several crystals (Figures 3a and 3b). In some cases, especially in discrete aggregates, crystals are joined to form packets of larger size (about 50 μm), where a clearly hexagonal shape of each crystal is recognizable (Figure 3b). In other cases, crystals grow intersecting each other in directions that may be sub-parallel (in this case the crystals seem to grow one inside the other) or crossed with various angles, generating irregular networks (Figure 3c). Based on ESEM observations, the clearly hexagonal section is present only in the terminations of crystals, where they appear as short, perfect hexagonal prisms of about 15 μm in diameter and 10 - 20 μm in length. In contrast, the main body of the crystals is thinner (diameter ~5 μm), and any geometric basal section is recognizable (Figure 3d). The short hexagonal prisms forming the ending part of the crystals show a solid appearance, whereas the main body of the crystals is of irregular shape and tend to generate a number of small-size fibers with rigid behavior, partially or totally separated from main crystal body (Figure 3d).

2.4.2 Mineralogical composition

To assess the quality of separated crystals and exclude the presence of impurities, for each sample detailed, long exposures up to 24 hr X-ray diffraction analyses were performed. Experimental XRPD data collections are shown in Figure 4.

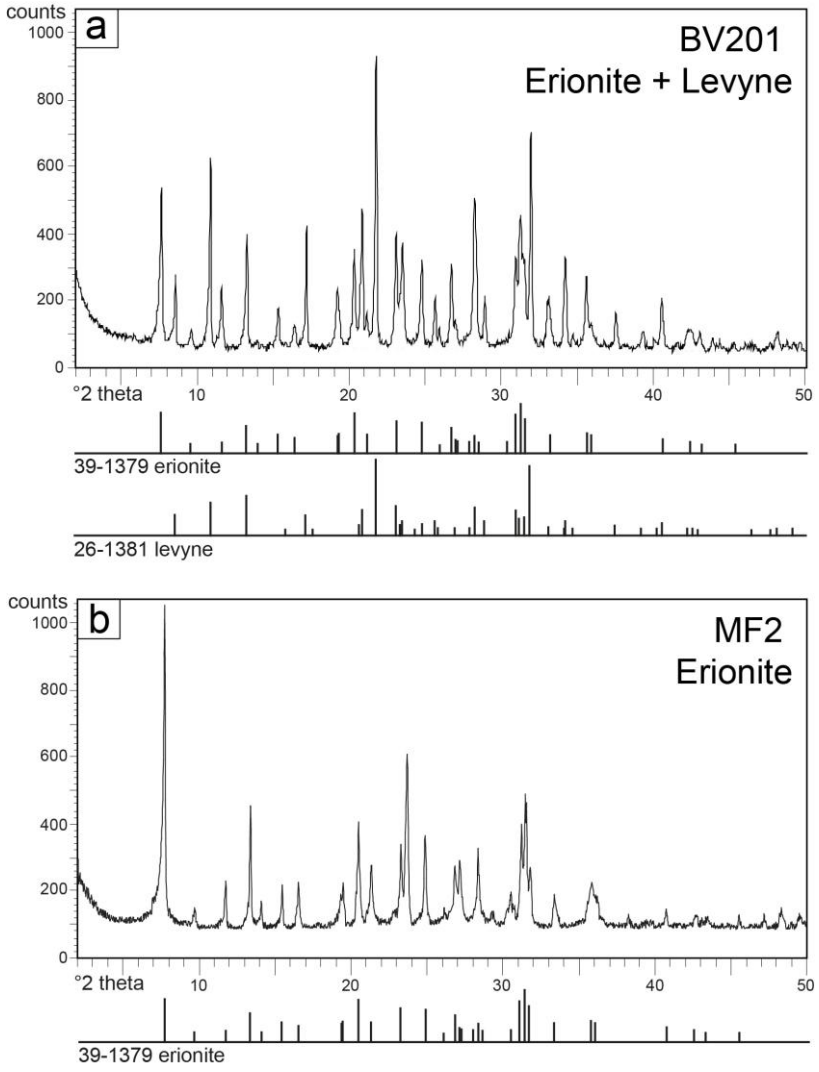

Figure 4. X-ray powder diffraction patterns produced by the BV201 (a) and FM2 (b) samples.

The BV201 sample showed a XRPD pattern consistent with the presence of two pure mineral phases corresponding to erionite and levyne. Data confirmed what has already been observed in morphological analysis, i.e. the BV201 sample consists of only these two mineral phases grown in intimate association. In contrast, XRPD analysis on the MF2 sample exhibited all typical diffraction peaks of pure erionite crystals. The erionite patterns of the two investigated samples illustrated nearly identical profiles. However, a significant variation of the relative intensities of some peaks was observed between the two samples. This is probably due to variable amounts of Ca(II), Na(I) and Mg(II) cations which are distributed on 4 distinct cation sites in the erionite cage.

2.4.3 Morphometry

Morphometric analyses were performed on selected ESEM images in order to quantify the size (length and diameter) of all the visible fibers separated and deposited on sampling plate, as well as those partially separated from the main crystals. These results are summarized in the histograms of Figure 5. The BV201 sample demonstrates flexible fibers of variable size in terms of length, but they are homogeneous (and small) as regards their diameter (Figure 5a). In term of lengths, fibers were observed in all size range from ~2 to ~85 μm with a distribution characterized by two relative modes. The main mode comprises fibers (more than 50% of the total) with a length between ~40 and ~60 μm and clearly corresponds to the average thickness of the erionite layers in the ELE sequences, which is generally ~50 μm (Figure 2a). The secondary mode matches with shorter fibers (between ~10 and ~25 μm of length) that should be linked to the fracturing of the longer fibers, with the contribution of other fibers in some

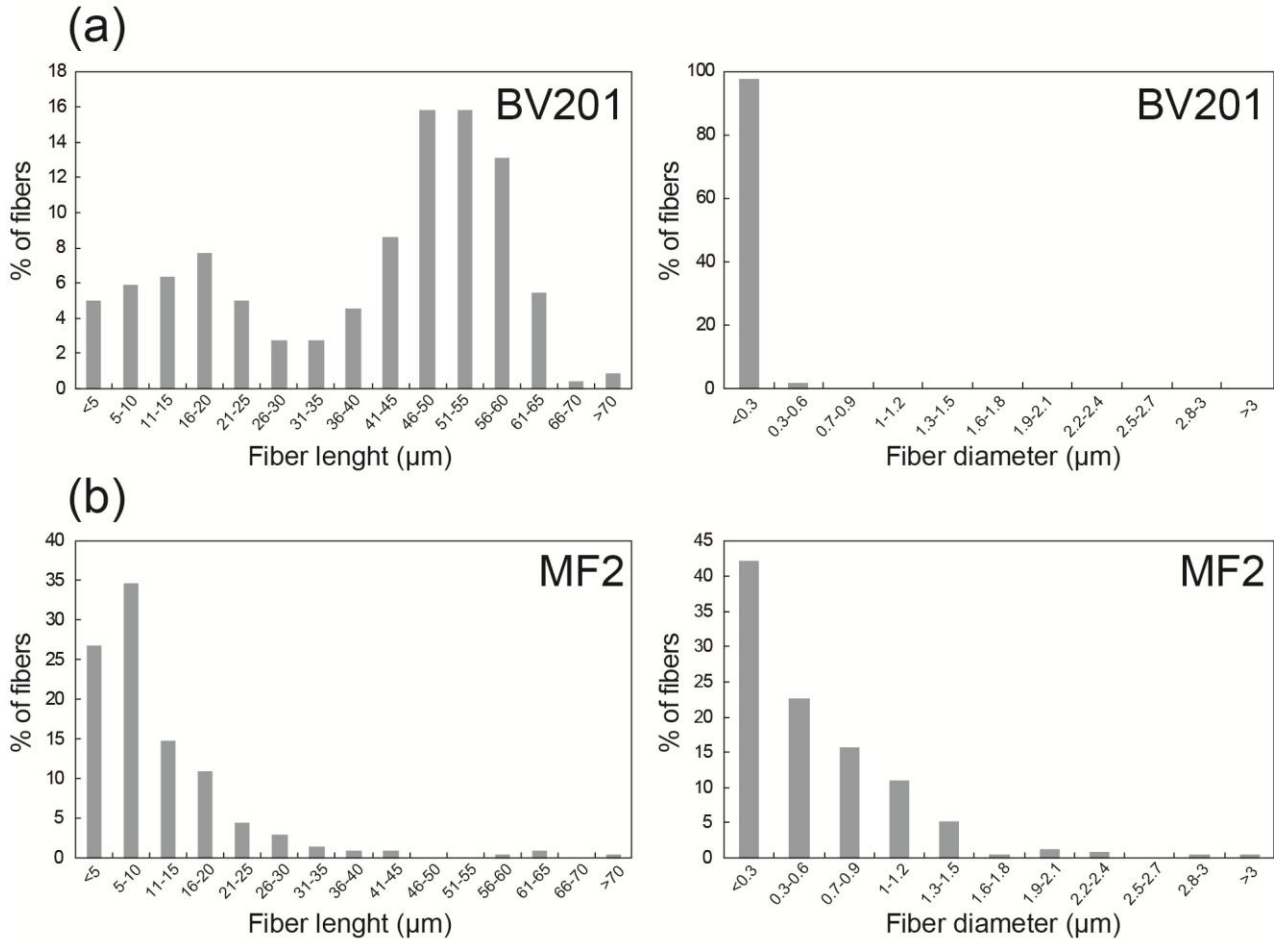

Figure 5. Size distribution of measured fibers (length and diameter) of BV201 (a) and MF2 (b) samples.

thinner ELE sequences. In contrast, regarding the diameters, the histogram is clearly unimodal and shows the presence of a huge population of fibers (~98%) which is characterized by a small diameter (< 0.3 μm), and the remaining part (~2%) which also displays a small diameter (up to 0.4 μm).
The MF2 sample shows a tendency to separate fibers with rigid behavior, which are characterized by variable length and diameter (Figure 5b). Regarding the length, the distribution of fibers is unimodal, with the mode corresponding to fibers between ~5 and ~10 μm. Whatever, the ~95% of the total measured fibers is within the range < 2 to ~30 μm, while the remaining ~5% is between ~30 and ~75 μm. In terms of diameter, more than 40% of the measured fibers possess a small diameter (0.1 to 0.3 μm, with an average of 0.2 μm). A significant population of fibers (~54%) is in the range ~0.3-1.5 μm, while the remaining ~6% shows a larger diameter (> ~1.5 μm).

2.4.4 Chemical data

All the reliable chemical data of the investigated samples are reported in Tables 1 and 2, and illustrated in the diagrams of Figure 6. The average chemical composition of extremely fibrous erionite from BV201 sample is $(Ca_{3.55}K_{2.12}Na_{0.39}Mg_{0.22})[Al_{10.37}Si_{25.69}O_{72}]\cdot 33.10H_2O$ and is classified as erionite-Ca (Figure 6a). The Si/(Si+Al) ratio is in the range 0.70-0.74, that is consistent with the interval for the erionite from volcanic rocks (Passaglia et al., 1998; Passaglia and Sheppard, 2001). Ca^{2+} is the dominant extra-framework cation in the structure (2.96-3.83 apfu), whereas K^+ and Na^+ contents are lower (1.58-2.56 and 0.14-0.87 apfu, respectively). The Mg^{2+} content is low (0.03-0.43 apfu) and the Mg/(Ca+Na) ratio, which is considered the most significant parameter for the distinction between erionite and offretite (a structurally and chemically similar zeolite), is in the range 0.01-0.11 (Figure 6b). Notwithstanding Fe^{3+} is not present in the ideal chemical formula, a small amount of Fe^{3+} is detected in the BV201 sample (0-0.15 apfu).

The average chemical composition of prismatic to acicular erionite from MF2 sample is $(Na_{2.39}K_{1.92}Ca_{1.74}Mg_{0.39})[Al_{8.82}Si_{27.18}O_{72}]\cdot 33.12H_2O$. The Si/(Si+Al) ratio varies from 0.73 to 0.77, which is numerically higher than previous sample. The prevailing dominant extra-framework cation is Na^+ (1.95-2.75 apfu) and, as a result, it is classified as erionite-Na. However, considering that the other extra-framework cations are also present in important amounts (K^+ is between 1.25-2.32 apfu and Ca^{2+} is between 1.3-2.44 apfu), the erionite composition of this sample tends to fall towards the central part of the classification diagram (Figure 6a). The Mg^{2+} content is generally low (average 0.39 apfu), although it might reach 0.7 apfu. The Mg/(Ca+Na) ratio is in the range 0.01-0.17 (Figure 6b). Similarly to the previous sample, the Fe^{3+} content is low, ranging from 0.01 to 0.3 apfu.

2.5 Discussion

The mechanisms by which an inhaled fibrous particulate induces pathological changes include (1) physical features of the inhalable fibrous mineral particles such as width, length, aspect ratio, and effective surface area available for cell contact, and (2) surface chemical composition and reactivity of the individual fiber/elongated particle.
(1) Concerning the physical features, the width and length of the fibers are the most important parameters to assess the toxicological potential. In particular, the diameter is the main factor controlling the ability of fibers to reach the lower respiratory tract, while macrophage phagocytosis is more dependent on fiber length (Fubini, 2001; Oberdörster et al., 2005). An elongated particle may be defined "inhalable" for humans when its diameter is < 3.5 μm (Lee, 1985). Stanton et al. (1981) correlated the incidence of induced lung disease with dimensional distribution of elongated particles, showing that fibers ≤ 0.25 μm in diameter and > 8 μm in length seem to be the most carcinogenic. With the aim to evaluate the severity induced by fibers the WHO (1986)

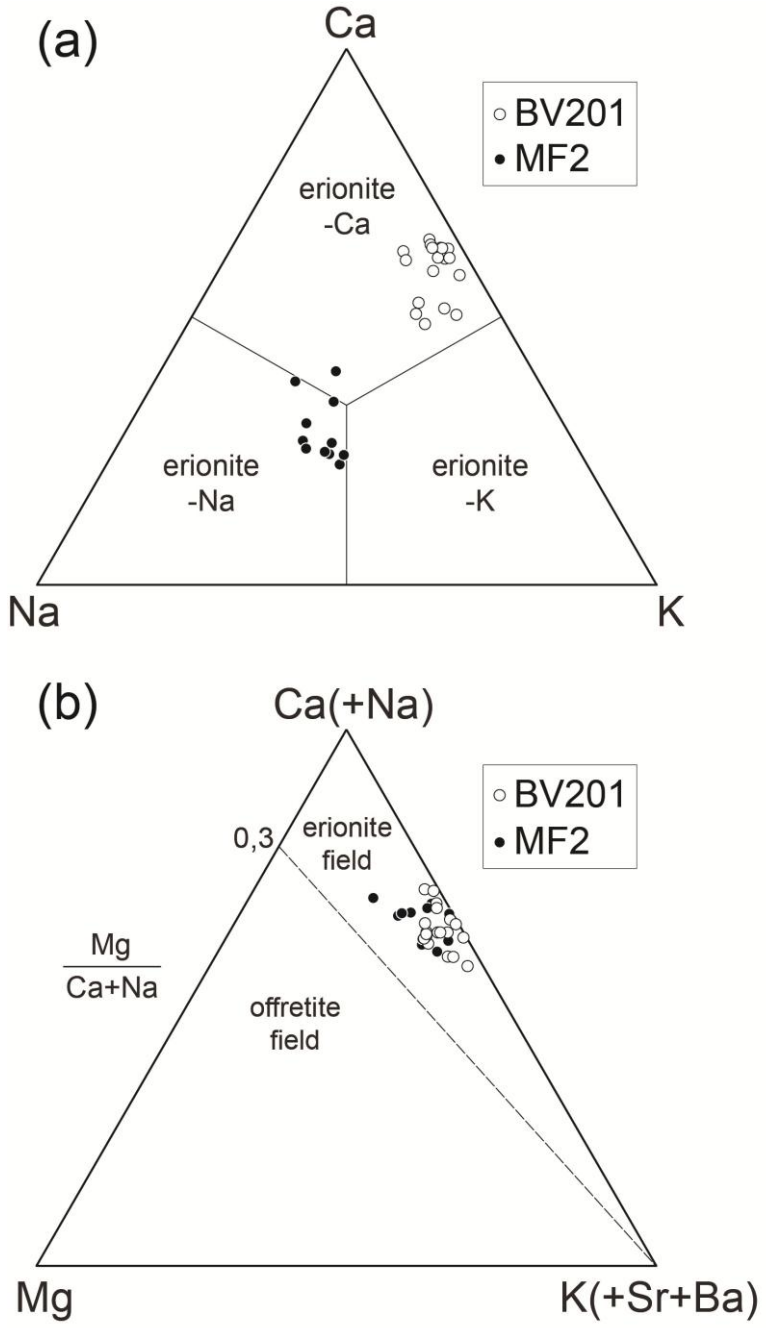

Figure 6. Ca-Na-K (a) and Ca(+Na)-Mg-K(+Sr+Ba) (b) ternary compositional plots of the studied erionite samples, showing the distribution of extra-framework cations.

considers as inhalable the fibers with a diameter-length ratio ≥ 1:3, a length > 5 μm and a diameter < 3 μm. However, the majority of fibers detected in the lung and mesothelial tissues are generally < 1 μm in diameter and shorter than 5 μm in length (Suzuki and Yuen, 2002; Dodson et al., 2003; Suzuki et al., 2005; Aust et al., 2011; Mossman et al., 2011). Therefore, small-size fibers should not be excluded from those contributing to induction of human malignant mesothelioma, especially in situations of high exposure. Moreover, as recently reported, ultra-fine fibers are particularly suitable for penetration from the proximal area to the peripheral part in the lung, and for migration from the lung to the pleura and to the other sites within the human body (Gatti and Rivasi, 2002; Roggli et al., 2002; Dodson et al., 2003; Samet et al., 2006; Straif et al., 2009; Bunderson-Schelvan et al.,

Sample	BV201	BV201	BV201	BV201	BV201	BV201	BV201	BV201	BV201	BV201	BV201	BV201	BV201	BV201	BV201	BV201	BV201	BV201	BV201	BV201
Analysis	1	2	3	4	5	6	7	8	9	10	11	12	13	14	15	16	17	18	20	average
SiO_2	51.72	52.22	50.79	52.22	50.84	51.22	51.37	50.87	52.13	52.30	51.06	51.23	51.44	52.13	52.11	50.97	51.46	51.22	53.61	*51.63*
Al_2O_3	17.85	17.88	18.32	18.61	18.22	17.46	17.81	18.22	18.54	17.98	16.98	16.55	17.32	17.46	18.01	18.03	17.55	16.84	16.31	*17.68*
Fe_2O_3	-	-	0.02	0.01	-	0.03	-	0.04	0.01	-	0.02	0.10	0.02	-	-	0.40	0.03	0.04	0.10	*0.07*
MgO	0.55	0.54	0.13	0.51	0.34	0.57	0.16	0.22	0.53	0.46	0.08	0.04	0.17	0.44	0.04	0.34	0.35	0.08	0.20	*0.30*
CaO	6.46	6.88	7.06	7.11	6.88	6.49	6.79	7.13	7.06	7.11	6.88	5.94	6.47	7.11	5.84	6.44	6.15	7.08	5.59	*6.66*
BaO	0.02	0.04	-	-	0.02	0.04	-	0.02	-	-	-	-	0.03	0.02	0.04	0.02	-	-	0.05	*0.03*
Na_2O	0.22	0.23	0.27	0.21	0.14	0.28	0.28	0.19	0.20	0.30	0.44	0.88	0.56	0.20	0.87	0.82	0.56	0.66	0.44	*0.41*
K_2O	3.17	3.19	2.88	3.22	3.24	3.07	2.87	3.56	3.22	3.09	3.44	3.56	2.46	4.08	3.88	3.64	4.02	2.89	3.98	*3.34*
H_2O	20.01	19.02	20.53	18.11	20.32	20.84	20.72	19.75	18.31	18.76	21.10	21.70	21.53	18.56	19.21	19.34	19.88	21.19	19.72	*19.93*
Total*	79.99	80.98	79.47	81.89	79.68	79.16	79.28	80.25	81.69	81.24	78.90	78.30	78.47	81.44	80.79	80.66	80.12	78.81	80.28	*80.07*
apfu on the basis of 72 oxygen atoms																				
Si	25.69	25.66	25.42	25.41	25.42	25.72	25.71	25.36	25.42	25.62	25.84	26.09	25.93	25.67	25.75	25.34	25.69	25.89	26.54	*25.69*
Al	10.45	10.36	10.81	10.67	10.74	10.33	10.51	10.71	10.66	10.38	10.13	9.93	10.29	10.13	10.49	10.57	10.33	10.03	9.52	*10.37*
Fe^{2+}	-	-	0.01	-	-	0.01	-	0.02	-	-	0.01	0.04	0.01	-	-	0.15	0.01	0.02	0.04	*0.02*
ΣT	36.13	36.02	36.24	36.08	36.16	36.06	36.22	36.08	36.08	36.01	35.98	36.06	36.23	35.81	36.24	36.06	36.03	35.94	36.09	*36.08*
Mg	0.41	0.40	0.10	0.37	0.25	0.43	0.12	0.16	0.39	0.34	0.06	0.03	0.13	0.32	0.03	0.25	0.26	0.06	0.15	*0.22*
Ca	3.44	3.62	3.79	3.71	3.69	3.49	3.64	3.81	3.69	3.73	3.73	3.24	3.49	3.75	3.09	3.43	3.29	3.83	2.96	*3.55*
Ba	-	0.01	-	-	-	0.01	-	-	-	-	-	-	0.01	-	0.01	-	-	-	0.01	-
Na	0.21	0.22	0.26	0.20	0.14	0.27	0.27	0.18	0.19	0.28	0.43	0.87	0.55	0.19	0.83	0.79	0.54	0.65	0.42	*0.39*
K	2.01	2.00	1.84	2.00	2.07	1.97	1.83	2.26	2.00	1.93	2.22	2.31	1.58	2.56	2.45	2.31	2.56	1.86	2.51	*2.12*
Σef	6.07	6.25	5.98	6.27	6.15	6.17	5.87	6.42	6.27	6.28	6.44	6.45	5.76	6.83	6.41	6.79	6.65	6.40	6.06	*6.29*
H_2O	33.14	31.18	34.27	29.39	33.89	34.90	34.59	32.84	29.78	30.66	35.61	36.86	36.20	30.48	31.66	32.07	33.11	35.72	32.56	*33.10*
E%	5.35	0.83	9.60	3.15	6.43	2.50	9.15	3.09	3.08	0.28	-0.97	2.54	9.72	-7.12	9.97	2.32	1.32	-2.45	4.06	*3.31*
R	0.71	0.71	0.70	0.70	0.70	0.71	0.71	0.70	0.70	0.71	0.72	0.72	0.72	0.72	0.71	0.71	0.71	0.72	0.74	*0.71*
Mg/(Ca+Na)	0.11	0.10	0.02	0.09	0.07	0.11	0.03	0.04	0.10	0.08	0.01	0.01	0.03	0.08	0.01	0.06	0.07	0.01	0.04	*0.06*

Table 1. Chemical composition of the investigated erionite fibers in the BV201 sample. Total* excludes water content; *ΣT,* sum of cations in tetrahedral sites; *Σef,* sum of cations in extra- framework sites; E%, measure of charge balance: E% = 100*[(Al+Fe^{3+})–Alk_{th}]/Alk_{th} where Alk_{th} = Na+K+2*(Ca+Mg); R, Si/(Si+Al) ratio.

Sample	MF2	MF2	MF2	MF2	MF2	MF2	MF2	MF2	MF2	MF2	MF2	MF2
Analysis	1	3	4	5	8	9	10	13	14	15	20	average
SiO_2	55.26	56.02	56.01	55.42	55.66	54.79	55.98	52.35	56.01	53.14	55.46	*55.10*
Al_2O_3	14.60	14.61	14.33	15.31	14.55	14.81	14.88	16.65	15.02	16.98	15.05	*15.16*
Fe_2O_3	0.80	0.40	0.10	0.20	0.24	0.10	0.31	0.05	0.02	0.11	0.04	*0.22*
MgO	0.70	0.51	0.05	0.60	0.61	0.28	0.22	0.81	0.97	0.32	0.77	*0.53*
CaO	2.77	2.46	2.88	3.14	2.88	2.81	3.03	4.55	4.01	4.11	3.64	*3.30*
BaO	0.04	0.04	-	-	-	-	0.03	-	-	0.03	0.02	*0.03*
Na_2O	2.55	2.42	2.64	2.82	2.36	2.46	2.89	2.01	2.30	2.33	2.77	*2.50*
K_2O	3.33	3.46	3.31	2.89	3.14	3.64	3.07	2.71	2.01	3.11	2.88	*3.05*
H_2O	19.95	20.08	20.68	19.62	20.56	21.11	19.59	20.87	19.66	19.87	19.37	*20.12*
Total*	80.05	79.92	79.32	80.38	79.44	78.89	80.41	79.13	80.34	80.13	80.63	*79.88*
apfu on the basis of 72 oxygen atoms												
Si	27.28	27.57	27.75	27.15	27.52	27.39	27.43	26.18	27.28	26.29	27.14	*27.18*
Al	8.49	8.48	8.37	8.84	8.48	8.73	8.59	9.81	8.62	9.90	8.68	*8.82*
Fe^{2+}	0.30	0.15	0.04	0.07	0.09	0.04	0.11	0.02	0.01	0.04	0.01	*0.08*
ΣT	36.07	36.20	36.16	36.06	36.09	36.16	36.13	36.02	35.90	36.23	35.83	*36.08*
Mg	0.52	0.37	0.04	0.44	0.45	0.21	0.16	0.60	0.70	0.24	0.56	*0.39*
Ca	1.47	1.30	1.53	1.65	1.53	1.51	1.59	2.44	2.09	2.18	1.91	*1.74*
Ba	0.01	0.01	0.00	0.00	0.00	0.00	0.01	0.00	0.00	0.01	0.00	*0.00*
Na	2.44	2.31	2.54	2.68	2.26	2.38	2.75	1.95	2.17	2.23	2.63	*2.39*
K	2.10	2.17	2.09	1.81	1.98	2.32	1.92	1.73	1.25	1.96	1.80	*1.92*
Σef	6.53	6.16	6.19	6.57	6.22	6.42	6.42	6.72	6.22	6.62	6.90	*6.45*
H_2O	32.85	32.96	34.18	32.06	33.91	35.20	32.01	34.81	31.93	32.78	31.61	*33.12*
E%	3.26	9.99	8.32	2.96	4.57	7.75	6.46	0.73	-4.27	9.99	-7.25	*3.86*
R	0.76	0.76	0.77	0.75	0.76	0.76	0.76	0.73	0.76	0.73	0.76	*0.76*
Mg/(Ca+Na)	0.13	0.10	0.01	0.10	0.12	0.05	0.04	0.14	0.17	0.05	0.12	*0.09*

Table 2. Chemical composition of the investigated erionite fibers in the MF2 sample. Total* excludes water content; *ΣT*, sum of cations in tetrahedral sites; *Σef*, sum of cations in extra-framework sites; E%, measure of charge balance: E% = 100*[(Al+Fe^{3+})–Alk_{th}]/Alk_{th} where Alk_{th} = Na+K+2*(Ca+Mg); R, Si/(Si+Al) ratio.

2011; Boulanger et al., 2014). Thus, it is difficult to exclude fibers of a particular dimension from those causing disease within the lung or extra-pulmonary sites.

The erionite-Ca of BV201 sample is represented by extremely thin fibers showing asbestiform habit, with ~98% of the total measured fibers having a diameter ≤ 0.3 μm. According to WHO (1986) indications, all of these fibers may be considered as inhalable. Further, these fibers are well within the range of "more carcinogenic fibers" in terms of diameter (Stanton et al., 1981). The two main modes observed in the erionite fibers of BV201 sample (40-60 μm and 10-25 μm) are > 5 μm and thus considered as carcinogenic in term of lengths (Stanton et al., 1981; WHO, 1986).

Similarly, almost all fibers and fibrils from the prismatic Na-erionite of MF2 sample are thin (~94% of the measured fibers has a diameter <1.5 μm) and ~75% of fibers has a

length > 5 μm. Therefore, the majority of the MF2 fibers are inhalable (WHO, 1986), while only a part of these fibers are also within the range of "more carcinogenic fibers" (~42% has a diameter < 0.3 μm and ~50% has a length > 8 μm; Stanton et al., 1981).

In summary, in both the investigated samples, erionite is present as fibers of inhalable size, and most of these are potentially dangerous. However, erionite in the BV201 sample seems to be able to generate fibers dimensionally more homogeneous and more carcinogenic than erionite from MF2 sample.

Concerning the mechanical properties, the two studied samples displayed different behavior having an extremely fibrous with flexible, hair-like appearance (BV201) or forming prismatic to acicular, brittle crystals (MF2). Flexibility in minerals is defined as the ability of a particle to bend without breaking and without resuming its original shape (Bates and Jackson, 1987). In the mineral fibers, this flexibility might significantly transform the shape of the particles, leading to variations of both aerodynamic properties and physical particle deposition mechanisms (Lippmann et al., 1980; Donaldson et al., 2010; Hofmann, 2011). In addition, Matassa et al. (2015) found that the flexibility of erionite fibers is related to the nanostructural features of the fibrils aggregating to form different morphologies. The different dimensions of the fibrils, coupled with the extended defectivity, are responsible for the different mechanical behavior of the erionite samples (flexibility vs. brittleness). Therefore, particular attention needs to be paid to reliably evaluate the toxicological effects related not only to the dimension of erionite fibers, but also to their tendency to split, as the latter feature may significantly modify their surface area and, consequently, their reactivity (Matassa et al., 2015; Mattioli et al., 2016b). Bearing this in mind, to assess the potential human health effects of exposures to erionite in the Lessini area, different mechanical behavior of these two fiber varieties (flexibility instead of brittleness) needs to be considered.

(2) The chemical composition of the mineral fibers is also of critical importance to evaluate the pathological changes, being related to the biopersistence and biodurability of fibers in contact with cells and tissues (e.g. in the lungs). If one considers that the main biological interactions or exchange processes develop at the surface of the fibers, the surface chemical composition and specific surface area are the most important elements that need to be considered. It is well known that some chemical elements in contact with cells and tissues are more effective in induction of pathological changes. In particular, the presence and structural coordination of Fe are considered key factors for explaining fiber-mediated toxicity (Bonneau et al., 1986). Further, only Fe exposed at the fiber surface, especially Fe(II), seems to be relevant in the reactive oxygen species (ROS) production (Fubini and Mollo, 1995; Gazzano et al., 2005).

Although erionite is a nominally Fe-free phase (Eberly, 1964; Passaglia et al., 1998; Dogan et al., 2006), Fe(II) might be present as extra-framework cation through an ion-exchange process, mainly involving Na^+ (Ballirano et al., 2015). However, Fe(II) might also be found on the zeolite surface as Fe oxide nanoparticles, as a thin coating of Fe-bearing silicates, or as Fe-bearing clay minerals (Ballirano et al., 2009; Cametti et al., 2013; Croce et al., 2015; Matassa et al., 2015). In the investigated erionite samples, Fe was detected in low amounts, ranging from 0 to 0.15 apfu in BV201 sample, and from 0.01 to 0.3 apfu in MF2 sample. However, available data do not allow to discriminate if the origin of this Fe is internal (Fe(II) as extra-framework cation) or external (Fe(II) on the fibers surface).

2.5.1 Environmental occurrence of erionite and risk assessment in Italy

Although zeolites represent one of most widespread mineral groups in the Earth's crust, in Europe there are no systematic studies on the distribution of erionite or other similar fibrous zeolites in the environment. This is mostly due to the fact that previous approaches to the hazard posed by fibrous zeolites were con-

ducted only in the areas with an anomalous incidence of mesothelioma, such as in Turkey, USA and Mexico (Dogan et al., 2006; Carbone et al., 2007, 2011; Ortega-Guerrero and Carrasco-Nunez, 2014; Saini-Eidukat and Triplet, 2014).

In Italy, epidemiological and toxicological knowledge of mesothelioma linked to erionite exposure is extremely scarce, and the phenomenon is still little investigated, although it is known that about 20% of national cases of mesothelioma is not linked to asbestos (INAIL, 2012). In particular, if we exclude the three regions (Piemonte, Lombardia and Liguria) where the high amount of mesothelioma is clearly linked to the presence of asbestos minerals, Veneto is the region that is characterized by one of the highest percentages of mesothelioma in Italy (8% of the total cases) in the time interval 1993-2008. This is a significant percentage in which the contribution of exposure to erionite cannot be excluded. However, it is worth noting that epidemiological and public health data are available according to the administrative borders (e.g. provincial or regional areas) which do not correspond to the real limits of geological deposits, i.e. erionite-containing rocks. For this reason, it is extremely difficult extrapolate the data regarding the incidence of mesotheliomas unrelated to asbestos in the Lessinia region, which could be a very useful element for the comprehension of the erionite contribution.

While mesothelioma cases attributed to asbestos exposure are well known and recorded (Crovella et al., 2016), little or nothing is known about domestic cases from exposure to airborne erionite fibers. Until a few years ago, findings of erionite specimens in Italy were limited to few localities in Sardinia (Passaglia and Galli, 1974) and Colli Euganei (Passaglia and Tagliavini, 1995). However, recently, Mattioli et al. (2016a) reported erionite and other associated zeolites within vugs and vesicles in the Tertiary basalts of the Lessini Mounts. These basalts are extensively quarried and largely employed for a variety of uses, most commonly as an aggregate. Crushed basalt is added to many construction jobs including asphalt paving, mixed with concrete, and as a rock filtering agent in many drain fields. Basalt is also used as bedrock for railroad tracks providing drainage and support. So, beyond of the potential environmental exposure produced by natural weathering processes affecting these basaltic rocks, it should also be taken into account the occupational exposure during the phases of extraction and processing of the erionite-containing rock, and a further environmental exposure due to the uses of such material.

The results acquired in the present investigation provide the basis for a health and safety protection program in Italy and for a better scientific understanding of erionite and its potential carcinogenicity. Another outcome is to stimulate future systematic studies on the possible presence and amount of such hazardous minerals in rocks and soils, suggesting at the same time a methodology to be applied to hazard identification processes in areas characterized by the possible natural presence of hazardous mineral phases.

2.6 Conclusions

In this study morphology, morphometry, mineralogical and chemical composition of two erionite samples from Lessini Mounts (NE Italy) was examined, where this carcinogenic zeolite had not apparently been found until now. On the basis of morphological and chemical data, the BV201 sample is erionite-Ca with an extremely fibrous, hair-like structure, with flexible appearance, growth in intimate association with levyne. Conversely, the MF2 sample is erionite-Na characterized by prismatic to acicular crystals with rigid behavior, which is also enriched in K^+ and Ca^{2+} extra-framework cations. Although erionite is a nominally Fe-free phase, Fe was detected in low amounts in both the investigated samples. Considering the size parameters, in both the investigated samples erionite was present as fibers of inhalable size, and most of these are also potentially carcinogenic. However, erionite in the BV201 sample seems to be able to generate fibers dimensionally more homogeneous and greater potential for car-

cinogenicity than erionite from MF2 sample. Further, the mechanical behavior of the erionite fibers is different (flexible or brittle) and this fact might exert some effect on the carcinogenic potential. Taking into account that the studied samples originated from basalts which are extensively quarried and largely employed, it is of great importance to evaluate (1) potential environmental exposure mediated by natural weathering processes of these rocks, (2) occupational exposure during the phases of extraction and processing of the erionite-containing rocks, and (3) a further environmental exposure due to the uses of such material. Finally, the results acquired in this investigation contribute to the knowledge of the erionite and provide the basis for a health and safety protection program in Italy.

Chapter 3

GEOLOGICAL OCCURRENCE, MINERALOGICAL CHARACTERIZATION AND RISK ASSESSMENT OF POTENTIALLY CARCINOGENIC ERIONITE IN ITALY

3.1 Introduction

A few decades ago, an epidemic of malignant mesothelioma (MM) was recognized in some villages of Cappadocia, Central Anatolia, Turkey (Baris et al., 1978; 1979; Artvinli and Baris, 1979). According to mineralogical studies and analysis of lung content, this epidemic was unequivocally linked to the occurrence of fibers of erionite of inhalable size in the region's bedrock (Baris et al., 1987; Metintas et al., 1999; Emri et al., 2002; Dogan et al., 2006; Carbone et al., 2007; 2011). Further, experimental studies demonstrated that fibrous erionite of inhalable size is more carcinogenic and more active than chrysotile and crocidolite asbestos in increasing the incidence of mesothelioma (Wagner et al., 1985; Hill et al., 1990; Davis et al., 1991; Coffin et al., 1992; Bertino et al., 2007; Dogan, 2012; Croce et al., 2013; Hillegass et al., 2013; de Assis et al., 2014; Pollastri et al., 2014; Zebedeo et al., 2014; Andujar et al., 2016; Crovella et al., 2016). For these reasons, and according to epidemiological data (Baris et al., 1978; 1979; 1987; Temel and Gundogdu, 1996; Kokturk et al., 2005; Carbone et al., 2007; Kliment et al., 2009; Carbone and Yang, 2012; Demirer et al., 2015; Baumann and Carbone, 2016), erionite has been classified as carcinogenic mineral for human health and referred to as a Class 1 carcinogen by the International Agency for Research on Cancer since 1987, and at present is categorized as the most carcinogenic mineral (IARC, 1987; 2012).

Despite the fact that erionite has been considered for a long time as a relatively uncommon mineral (Passaglia and Galli, 1974; Bish and Ming, 2001), this fiber was recently found in many localities worldwide (Supplementary Material, Table S1).

In Italy, the occurrence of erionite was reported in some areas of Sardinia and Veneto regions (Passaglia and Galli, 1974; Pongiluppi et al., 1974; Giovagnoli and Boscardin, 1979; Passaglia and Tagliavini, 1995). However, despite the knowledge that this fiber is highly dangerous, a systematic investigation and mapping of its distribution is still missing for the Italian area, and little attention has been given to the potential adverse health risks attributed to environmental exposures. Recently, new occurrences of erionite were detected in volcanic rocks of NE Italy (Giordani et al., 2016; Mattioli et al., 2016a), suggesting that this hazardous mineral may be more widespread than currently presumed, especially in other areas with suitable geological characteristics.

The aim of the present investigation was to provide a field description and detailed mineralogical characterization of selected samples of potentially carcinogenic fibrous erionite recently discovered in the Lessini Mountains (Veneto region, NE Italy).

Scanning electron microscopy with energy dispersive spectroscopy (SEM-EDS) and X-ray powder diffraction (XRPD) data were combined and integrated, in order to characterize from a crystal chemical and structural point of view this health-threatening mineral.

Another aim of this study was to review the locations in which erionite fibers were detected and described in Italy, trying to recognize the other geological settings where it may potentially occur. This information represents a useful basis for future studies by geological, mining, and medical investigators in particular aimed at examining potential correlations between geological occurrences and epidemiological data of the distribution of pulmonary diseases typically related to erionite exposure.

3.2 Background

3.2.1 Mineralogy

Erionite was first identified near Durkee, Oregon, (USA) by Eakle (1898) who described the "wooly" variety (the erionite name derives from the Greek word for wool) that occurs at the type locality consisting of white, woolly-like fibers. Erionite is a zeolite belonging to the ABC-6 family (Gottardi and Galli, 1985). It is hexagonal, space group $P6_3/mmc$, unit-cell parameters a = 13.19-13.34 Å, c = 15.04-15.22 Å (Staples and Gard, 1959; Alberti et al., 1997; Gualtieri et al., 1998; Bish and Ming, 2001; Deer et al., 2004; Cametti et al., 2013), and average chemical formula $Na_2K_2Ca_3[Al_{10}Si_{26}O_{72}]$ $30H_2O$. Its framework consists of $(Si,Al)O_4$ tetrahedra linked together to form single- or double-layers of 6-membered rings, whose stacking along the z-axis, following the AABAAC sequence, produces three types of cages: a double 6-membered [D6R] ring (empty), a cancrinite [CAN] cage (preferred by K), and an erionite [ERI] cavity hosting Ca, Na, Mg and additional K (Gottardi and Galli, 1985; Alberti et al., 1997; Passaglia et al., 1998; Bish and Ming, 2001; Deer et al., 2004; Ballirano et al., 2009; Cametti et al., 2013).

Previously, erionite was described as a single mineral species (Sheppard and Gude, 1969; Gude and Sheppard, 1981; Passaglia and Sheppard, 2001), while at the present it is classified as a series, owing to a significant chemical variability, consisting of three different species, erionite-K, erionite-Ca, and erionite-Na, depending upon the most abundant extra-framework (EF) cation (Coombs et al., 1997; Dogan and Dogan, 2008; Dogan et al., 2008; Ballirano et al., 2009).

Erionite is often misidentified with offretite, a closely related zeolite (AAB stacking sequence). The distinction between these species may be difficult because of their physical, chemical and structural similarities, and because of the possibility of their intergrowth within a single crystal (Gualtieri et al., 1998; Passaglia et al., 1998). The most significant discrimination between erionite and offretite is based upon the Mg/(Ca + Na) cation ratio. Under such aspect, offretite shows values close to 1 whereas those of erionite do not exceed 0.3 (Passaglia et al., 1998). Among the minerals that might be found in intimate association with erionite, levyne, another ABC-6 zeolite (AABCCABBC stacking sequence), is the most relevant as it generally forms an epitaxial intergrowth, giving rise to an alteration of levyne-erionite layers (Passaglia and Galli, 1974; Rinaldi, 1976; Wise and Tschernich, 1976; Giordani et al., 2016).

3.2.2 Erionite geology

Erionite, as well as many other zeolites, often has hydrothermal origin and is related to the presence of fluids arising and/or heated from below (Wylie and Candela, 2015). Under favourable conditions, these hydrothermal solutions can be able to induce crystallizations in the empty spaces of traprocks, especially in the case of high-vesiculated tuff and lavas (Gottardi and Galli, 1985; Passaglia et al., 1998; Bish and Ming, 2001). However, Bish and Ming (2001) recognized that huge quantities of zeolites also occur as low-temperature, low-pressure alteration products of pyroclastic material, and that many of the zeolites filling vugs and cavities of basalts are diagenetic in origin, being precipitated directly from ground water percolating through the rock mass.

In recent years, erionite has been recognized as important mineral in low-grade metamorphic and in a variety of sedimentary rocks of different lithology, age, and depositional environments. Erionite of sedimentary origin might originate from a variety of precursor materials including volcanic glass and aluminosilicate minerals that react to form zeolites by a dissolution-precipitation processes (Gottardi and Galli, 1985; Passaglia et al., 1998; Bish and Ming, 2001; Deer et al., 2004). Erionite from Cappadocia, Turkey, appears to have formed in this manner where huge deposits of volcanic tuffs have undergone, after deposition, a series of geochemical changes including a dissolution of volcanic glass and re-precipitation of smectite, followed by widespread crystallization of erionite in the

pore spaces. Most erionites in sedimentary rocks occur as microscopic or submicroscopic crystals being therefore hardly recognizable in the hand-specimen. However, deposits of this type are voluminous and display significant geological relevance and economic/toxicologic potential.

Erionite is just one among several natural zeolites commonly occurring with fibrous habit and is by far the most studied from the toxicological point of view. However, attention is in the scientific community to determine if fibers of zeolites such as mordenite, clinoptilolite, phillipsite, offretite, thomsonite, mesolite, scolecite, natrolite, paranatrolite, gonnardite, mazzite, roggianite and perlialite, may also be hazardous to human health. As reported in the IARC Monograph (1997), there is inadequate evidence in humans for carcinogenicity of zeolites other than erionite, and there is inadequate evidence in experimental animals for carcinogenicity attributed to clinoptilolite, phillipsite and mordenite. Nevertheless, recent investigations on the surface properties of selected fibers of zeolites revealed that the availability of surface sites for adsorption and interacting ability are significant not only for erionite, but also for fibrous offretite and scolecite (Mattioli et al., 2016b). Considering that these properties may be related to carcinogenic potential, a great necessity emerges to increase the available information on these minerals, given the abundant occurrence of zeolite deposits worldwide.

3.2.3 Erionite health risks

It is well known that small particles, especially those with fibrous morphology, generate biological processes leading to toxicity and carcinogenicity inside the lungs (Stanton et al., 1981; Cook et al., 1982; Wagner et al., 1985; Pott et al., 1987; Davis et al., 1991; Coffin et al., 1992; Fubini, 2001; Millette, 2006; Aust et al., 2011; Crovella et al., 2016; Andujar et al., 2016; Lemen, 2016; Larson et al., 2016). One of the most important factors that define the adverse health severity of a mineral fiber is its breathability, which depends on the size including length, diameter and relative ratio and the aerodynamic equivalent diameter (Stanton et al., 1981; Lee, 1985; Pott et al., 1987; Dodson et al., 2003; Oberdörster et al., 2005; 2015; Millette, 2006; Aust et al., 2011; Boulanger et al., 2014; Wylie and Candela, 2015). The fibers biopersistence is also an important factor for their toxicity and carcinogenicity (Hesterberg et al., 1998; Fubini, 2001; Maxim et al., 2006). It was postulated that a fiber with critical dimensions may be carcinogenic if sufficiently durable to remain chemically and physically intact in lung tissue (Muhle et al., 1991; Oberdörster et al., 2005). The fibers biopersistence is also related to their chemical composition, with some elements potentially playing a key role to determine carcinogenicity such as the presence of iron; Bonneau et al., 1986; Wiseman and Halliwell, 1996; Fubini, 2001; Gazzano et al., 2005; Ballirano et al., 2015; Crovella et al., 2016). Further, trace elements content, including As, Be or Pb, and some rare earth elements, may also play a role in fiber toxicity (Bloise et al., 2016).

Other features such as specific surface area, interacting capability, durability, structure, net charge and microtopography might also act as important factors in particle-induced toxicity and carcinogenicity (Lippmann, 1988; Hochella, 1993; Oberdörster et al., 2005; Mattioli et al., 2016b). It is relevant to note that these features are the same for a given mineral species regardless of the morphological habit. For this reason, non-fibrous particles released from erionite with prismatic habit could also be considered potentially able to elicit reactions in the respiratory system. Moreover, the potential for reactivity is further enhanced for some dusts like erionite because of inherent pores/voids which create notable surface areas for reactions to occur in a biosystem. In addition, fibrils originating by splitting of fibers may display different mechanical behaviors such as brittle or flexible, and this feature represents a critical factor in the assessment of the hazard.

Much of the scientific knowledge regarding toxicity and carcinogenicity of fibrous particles arise from studies carried out on asbestos, certainly the most studied mineral fibers. However, in recent years the number of stud-

ies devoted to erionite fibers has significantly increased, shedding new light on the toxicology of fibrous particles. Most of the investigations focused to the Cappadocian emergency following the observation of a high mortality rate from MM in the local population (Dogan, 2003; Carbone et al., 2007). Recently, targeted epidemiological studies were performed in other sites of the world, with the aim of clarifying whether high incidences of typical asbestos-related lung diseases are linked to the natural presence of erionite fibers. Evidence that is emerging is really troublesome. Within a few years, deaths attributed to inhalation of erionite fibers were confirmed in Turkey (Dogan et al., 2006; Carbone et al., 2011), in the USA (Carbone et al., 2011; Saini-Eidukat and Triplett, 2014) as well as in Mexico (Ortega-Guerrero et al., 2015) and possibly in Iran (Ilgren et al., 2015). Notwithstanding the growing interest in this particular zeolite and important findings noted regarding the mechanisms underlying carcinogenesis and the potential genetic predispositions (Metintas et al., 2010; Carbone and Yang, 2012; Hillegass et al., 2013; Ballirano et al., 2015; Ballirano and Cametti, 2015; Pollastri et al., 2015; Lemen, 2016), the precise sequence of events ranging from deposition of fibers in the human respiratory tract to production of related diseases has not been fully clarified.

3.3 Field description and materials

The studied samples are from the Tertiary basalts of Northern Italy (Figure 1), where a thick sequence of lava flows of Veneto Province extensively crops out (De Vecchi and Sedea, 1995; Milani et al., 1999; Bonadiman et al., 2001; Beccaluva et al., 2007). Whereas the dominant magmatism in the western side of the Northern Apennines during the Tertiary is of subduction-related type (Mattioli et al., 2012), an extensional-related volcanic activity developed in the eastern side of the South Alpine foreland, with the greatest part of the eruptions taking place in submarine environments. Several magmatic pulses occurred between the Late Paleocene and Miocene periods, all of which were of a short duration and separated by periods of magmatic inactivity during which shallow-water carbonate sedimentation occurred (De Vecchi and Sedea, 1995). The Tertiary basalts of the Veneto Province are well known to be suitable host rocks for development of secondary mineral associations (Cenni, 2009; Mattioli et al., 2016a). These secondary mineral assemblages that develop within vesicles and veins are mainly concentrated at the bottom and at the top of each basaltic lava flow. The lower level consists of a thin (up to 30 cm thick), discontinuous, vesicular interval with vesicles of less than 10 vol%, ranging from 1 to 5 cm in diameter. The upper level is characterized by altered facies with a huge quantity of vesicles and important concentrations of secondary minerals. At the top of this level, which is 5 to 10 m thick, the vesicularity is approximately 40 vol%, with vesicle diameters from 0.1-1 cm, whereas at the base of the upper zone the diameters of the vesicles increase to up to 20 cm and the associated porosity is in the range 5-10 vol% (Mattioli et al., 2016a). Secondary minerals from veins and vesicles were investigated during several field trips. More than one thousand vesicles were studied in the field, approximately 300 of which were sampled and analyzed for identification of secondary minerals. Locations, geographic coordinates, assemblages of secondary minerals and estimated amounts of erionite are summarized in Table 1. The secondary phases are mainly zeolites and clay minerals, which represent approximately 90 vol% of total secondary minerals; other silicates (apophyllite, gyrolite, prehnite, pectolite) are rare, as are oxides (quartz) and carbonates (calcite, aragonite). Clay minerals, which form botryoidal aggregates, are generally the first minerals that precipitated along the walls, whereas the core of the vesicles commonly contains well-shaped zeolites. The thickness of the coating is generally less than 0.5 mm, while the zeolite crystals range in size from <1 mm to 1 cm. Among zeolites, that are normally the last phases to crystallize, typical vesicle infillings consist of, in order of abundance, chabazite,

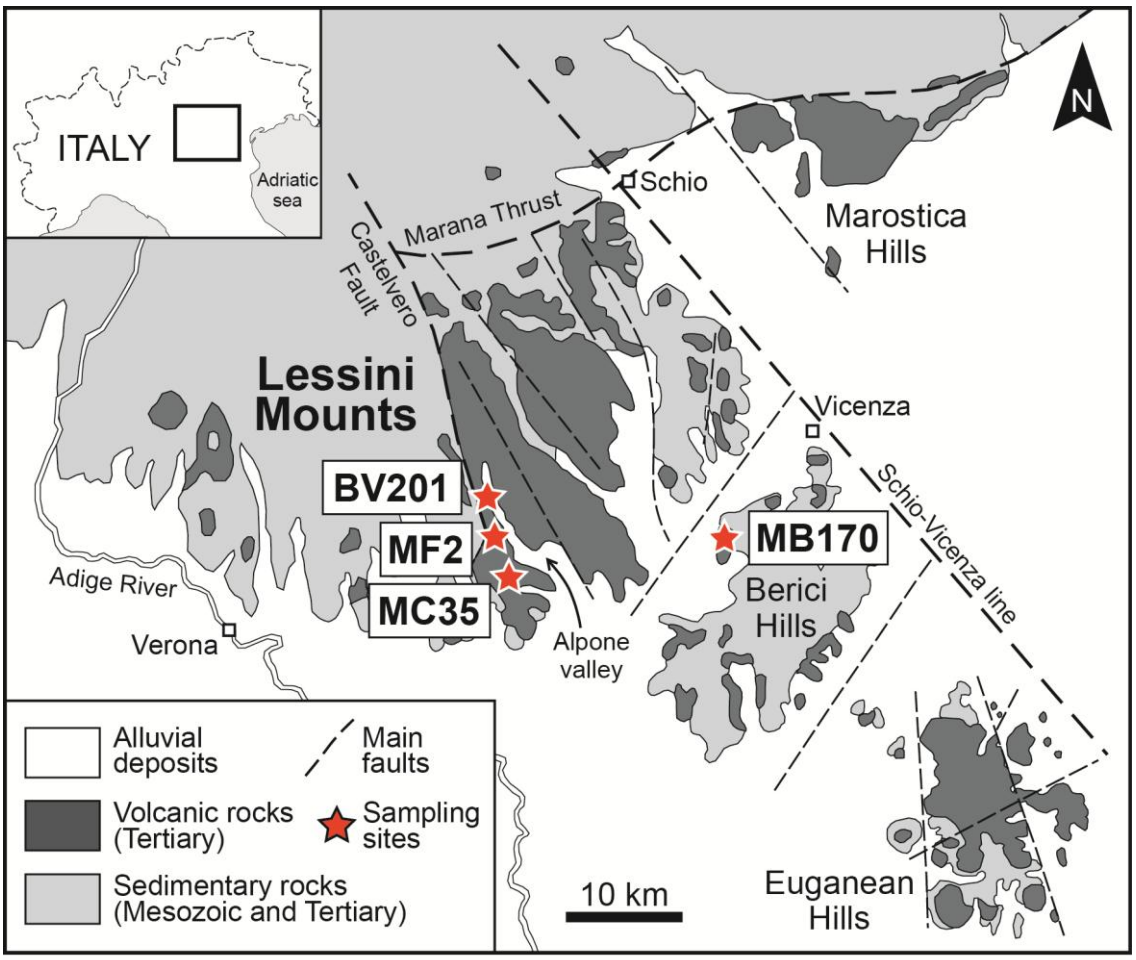

Figure 1. Geological sketch map of the Veneto Volcanic Province (NE Italy), with indication of the sampling sites (modified from De Vecchi and Sedea, 1995).

phillipsite-harmotome, analcime, natrolite, gmelinite, and offretite. Heulandite, stilbite and erionite are less common, whereas willhendersonite and yugawaralite are rare.

Frequently, several species are present within the same vesicle, even if only one or two of these minerals are detected. The occurrence of different zeolite species and their frequency in the studied rocks is non-homogeneous, and their associations may be significantly different on both the outcrop- and sample-scale, showing a variability that might be in the order of a few cm. By comparing all of the detailed systematic observations of the assemblages of the main secondary minerals (zeolites and clay minerals), it is apparent that erionite is present in 65% of the investigated outcrops, with an estimated amount varying from 10 to 40 vol% of total secondary minerals (Table 1).

From the entire suite, 4 representative samples of erionite were investigated in this study. The 4 samples were selected on the basis of the main morphological types observed for all erionite occurrences in this area: (1) prismatic crystals with a solid appearance (MC35); (2) acicular crystals with rigid behavior (MF2); (3) acicular to fibrous crystals with rigid to flexible mechanical behavior (MB170); and (4) extremely fibrous with flexible, hair-like appearance (BV201). Morphometric and preliminary chemical data of MF2 and BV201 samples were reported in Giordani et al. (2016). In this investigation the mineralogical characterization was completed and data integrated with those of the new samples MC35 and MB170, in order to present a picture as comprehensive as possible of the distribution and types of erionite in Italy.

Locality	*Latitude*	*Longitude*	*Altitude (m a.s.l.)*	*Mineral association*	*Erionite (vol. %)*
Cercene Mt.	45.430677	11.257841	159	CHA + OFF + CM	-
Foscarino Mt.	45.439427	11.258779	296	PHI/HAR + **ERI** + OFF + CM	35
Colombara	45.426723	11.277245	140	PHI/HAR + CHA + OFF + **ERI** + CM	10
Fittà	45.453548	11.253994	281	GME + PHI/HAR + **ERI** + OFF + CM	15
Gambaretti	45.501002	11.232667	213	CHA + GME + CM	-
Calvarina Mt.	45.490955	11.269361	280	NAT + ANA + **ERI** + OFF + CM	20
Chiereghini Valley	45.549751	11.219361	285	PHI/HAR + NAT + OFF + CM	-
S.Giovanni Ilarione	45.521057	11.236276	194	ANA + **ERI** + OFF + PHI/HAR + CM	35
Beltrami	45.525522	11.229305	253	PHI/HAR + CHA + OFF + CM	-
Bagattei	45.551624	11.218733	329	PHI/HAR + **ERI** + OFF + YUG + CM	40
Contrada Moretti	45.553182	11.218772	312	CHA + WHI + CM	-
Soave	45.419776	11.247955	50	OFF + **ERI** + GYR + PRE + CM	35
Roncà	45.480646	11.288877	80	ANA + OFF + PHI/HAR + CM	-
Prun	45.577982	10.951481	541	CHA + OFF + **ERI** + CM	20
S. Cristina	45.581039	10.940663	683	PHI/HAR + CHA + **ERI** + OFF + CM	15
Mont. Maggiore	45.493091	11.469650	150	PHI/HAR + CHA + **ERI** + CM	30

Table 1. Synoptic table showing locations, geographic coordinates, mineral assemblages and erionite amounts of the investigated outcrops of the Tertiary basalts from the Lessini Mountains (NE Italy).

3.4 Analytical methods

3.4.1 Scanning Electron Microscopy (SEM)

The morphological investigation was carried out at the University of Urbino Carlo Bo using a SEM FEI Quanta 200 FEG Environmental Scanning Electron Microscope (ESEM) equipped with an energy dispersive X-ray spectrometer (EDAX) for semi-quantitative chemical analyses. The micro-chemical composition was determined at the Dipartimento di Scienze della Terra, Sapienza Università di Roma using a SEM FEI Quanta 400 equipped with an EDS system. Operating conditions were 15 kV accelerating voltage, 11 mm working distance, 0° tilt angle and 1 μm beam diameter. Chemical data were collected at 30 analytical points. The final crystal chemical formula was calculated, after renormalization of chemical analyses hypothesizing a water content of 18.5 wt.% (corresponding to approximately 30 atoms per formula unit, *apfu*), on the basis of 36 (Si+Al) *apfu*. As previously suggested (Sweatman and Long, 1969; Goldstein et al., 1992; Reed, 1993; Pacella et al., 2016), in order to minimize the alkali metal migration, chemical data were acquired using a low counting time (up to 10 sec) and a raster scan-mode to reduce the temperature increase. The reliability of the chemical analysis used to classify the erionite samples was evaluated by using the charge balance error formula (E%: Passaglia, 1970; Passaglia et al., 1998), the Mg-content (Dogan and Dogan, 2008; Dogan et al., 2008) and K-content tests (Cametti et al., 2013). Chemical analyses of zeolites are considered to be reliable if the balance error (E%) is within ±10%.

To evaluate the quality of the SEM-EDS micro-chemical data, two samples (BV201 and MF2) were also investigated by Electron MicroProbe Analysis (EMPA). Pure crystals from these samples were prepared embedding a fraction of fibers in epoxy resin. Compositions were determined at the Istituto di Geoscienze e Georisorse, CNR, Padua, using a Cameca SX50 EMPA equipped with Wave-

length-Dispersive Spectrometry (WDS). According to the recommended protocol for the quantitative determination of zeolite compositions by EMPA (Campbell et al., 2016), the following conditions were used: reduced counting time (up to 10 sec), beam diameter 20 μm, accelerating voltage 15 kV, low beam current and element prioritizing with the spectrometer configuration. Silicates, oxides, and pure elements were used as standards; analytical errors are 1-2% rel. and 3-5% rel. for major and minor elements, respectively. Comparing the compositions of the duplicate samples, no relevant differences between the two datasets were observed, indicating the full reliability of the chemical data obtained by the SEM-EDS technique.

3.4.2 X-Ray Powder Diffraction (XRPD)

X-Ray powder diffraction(XRPD) data were collected only for samples BV201 and MB170 owing to their fibrous habit and corresponding potential toxicity for humans. Bundles of fibers were selected under a binocular microscope and reduced to powder using an agate mortar and pestle that were loaded into 0.7 mm diameter SiO_2-glass capillaries. Data from XRPD were collected in transmission mode using a D8 Advance diffractometer (Bruker AXS, Karlsruhe, Germany) operating in θ/θ geometry. The instrument is fitted with focusing Göbel mirrors on the incident beam, Soller slits on both incident and (radial) diffracted beams, and a PSD VÅNTEC-1 detector. Preliminary diffraction patterns indicated the occurrence of relevant amounts of levyne-Ca (BV201) and minor calcite and barite (MB170). Structure refinements were carried out by the Rietveld method using TOPAS v.4.2 (Bruker AXS, 2009) and modelling the peak shape by FPA (Fundamental Parameters Approach). Owing to the relatively similar chemical composition, the selected starting structural model of erionite was taken from Alberti et al. (1997). Structural data of levyne-Ca were taken from Sacerdoti (1996), whereas those of barite and calcite from Jacobsen et al. (1998) and Ballirano (2011), respectively. The same Rietveld refinement procedure used by the present research group was adopted in several structure refinements of erionite fibers (Ballirano et al., 2009; Ballirano and Cametti 2012). Absorption correction was performed following the procedure of Sabine et al. (1998) and the occurrence of preferred orientation was modelled by spherical harmonics selecting the number of terms to be employed according to the procedure devised by Ballirano (2003). In the case of sample MB170, the refinement was performed using the ellipsoid-model of Katerinopoulou et al. (2012) describing the diffraction-vector dependent broadening of diffraction maxima. Miscellaneous data of the refinements are listed in Table 2. Rietveld plots of both samples are shown in Figure 2.

3.5 Results and discussion

3.5.1 Morphology

The main morphological features of the investigated erionites are illustrated in Figure 3.
In the MC35 sample, erionite commonly occurs as elongated, prismatic crystals having a length of about 100-500 μm and a diameter ranging from 10 to 50 μm (Figure 3a). SEM images show that some crystals possess well-formed hexagonal cross-sections, while other crystals exhibit irregular morphologies. Much of erionite occurs in radial aggregates or spherulites up to a mm in size. More rarely, erionite occurs in stubby bundles of 5-80 μm in length, each of them consisting of tens to hundreds of individual crystals. In this sample, all crystals display a solid appearance and a rigid behavior and no fibrous elements detected. In the MF2 sample, erionite is present as single, acicular crystals with diameter of approximately 5 μm and length up to 150 μm demonstrating hexagonal section, or as discrete aggregates of several crystals generally radiating from a central point, joined to form packets of larger size (about 50 μm), where the hexagonal symmetry of each crystal is still recognizable (Figure 3b). Based on SEM observations, the well-developed hexagonal section is present only in the terminations of crystals, consisting of perfect hexagonal prisms of about 15 μm in diameter and 10-20 μm in length.

Instrument	Bruker AXS D8 Advance	
Radiation	CuKα	
Primary and secondary radius (mm)	250	
Detector	PSD VÅNTEC-1	
Sample mount	Rotating capillary (60 r/min)	
Incident beam optics	60 mm multilayer (Göbel) focussing X-ray mirror	
Detector window (°)	6	
Divergence slits (°)	0.3	
Soller slits	Primary beam (2.3°); diffracted beam (radial)	
	BV201	MB170
2θ range (°)	6-145	
Step size (°2θ)	0.022	
Counting time (s)	10	
a (Å)	13.34082(18)	13.31490(13)
c (Å)	15.1229(3)	15.09267(19)
Volume (Å^3)	2330.94(8)	2317.25(5)
c/*a*	1.1342	1.1335
R_{Bragg} (%)	0.356	0.966
R_p (%)	1.445	1.729
R_{wp} (%)	1.877	2.329
GoF	1.714	3.645
Weighted DWd	0.758	0.237
Microstrain ε_0	0.0736(17)	0.0445(17)
L_{vol} (nm)	72.3(9)	-
r_a (nm)	-	576(9)
r_c (nm)	-	567(11)

Table 2. Experimental details and miscellaneous data of the Rietveld refinements. Statistical parameters as defined in Young (1993). Microstructural parameters micro-strain ε_0, volume-weighted mean column height L_{vol} and the principal radii perpendicular and parallel to the rotation axis r_a and r_c are also reported (see text for explanation).

In contrast, the main body of the crystals is thinner (diameter approximately 5 µm) and loss of any reference to the hexagonal basal section. The short hexagonal prisms forming the termination of the crystals show a solid appearance, whereas the main body tends to split up into a great number of fibrils with rigid behavior, partially or totally separated from the main crystal body (Giordani et al., 2016). The MF2 sample display a marked tendency to subdivide into fibers and fibrils with rigid behavior, which are characterized by variable length and diameter. Regarding the length, the majority of the fibers shows a size generally up to approximately 30 µm, rarely longer, while in terms of diameter, these fibrils are commonly thinner than approximately 1.5 µm.

In the MB170 sample, erionite occurs as acicular to fibrous crystals always grouped in radial aggregates forming spherules up to one mm in size (Figure 3c). The acicular crystals possess dimensions up to some hundreds of mm in terms of length, and up to approximately 10 µm in diameter. At higher magnification the spherules and prisms that compose them, appear as constituted by bundles of rigid fibers of small diameter, generally less than a few mm (Figure 3d).

Moreover, whenever fractures and discontinuities occur in these bundles, the presence of a large number of small fibrils was noted with

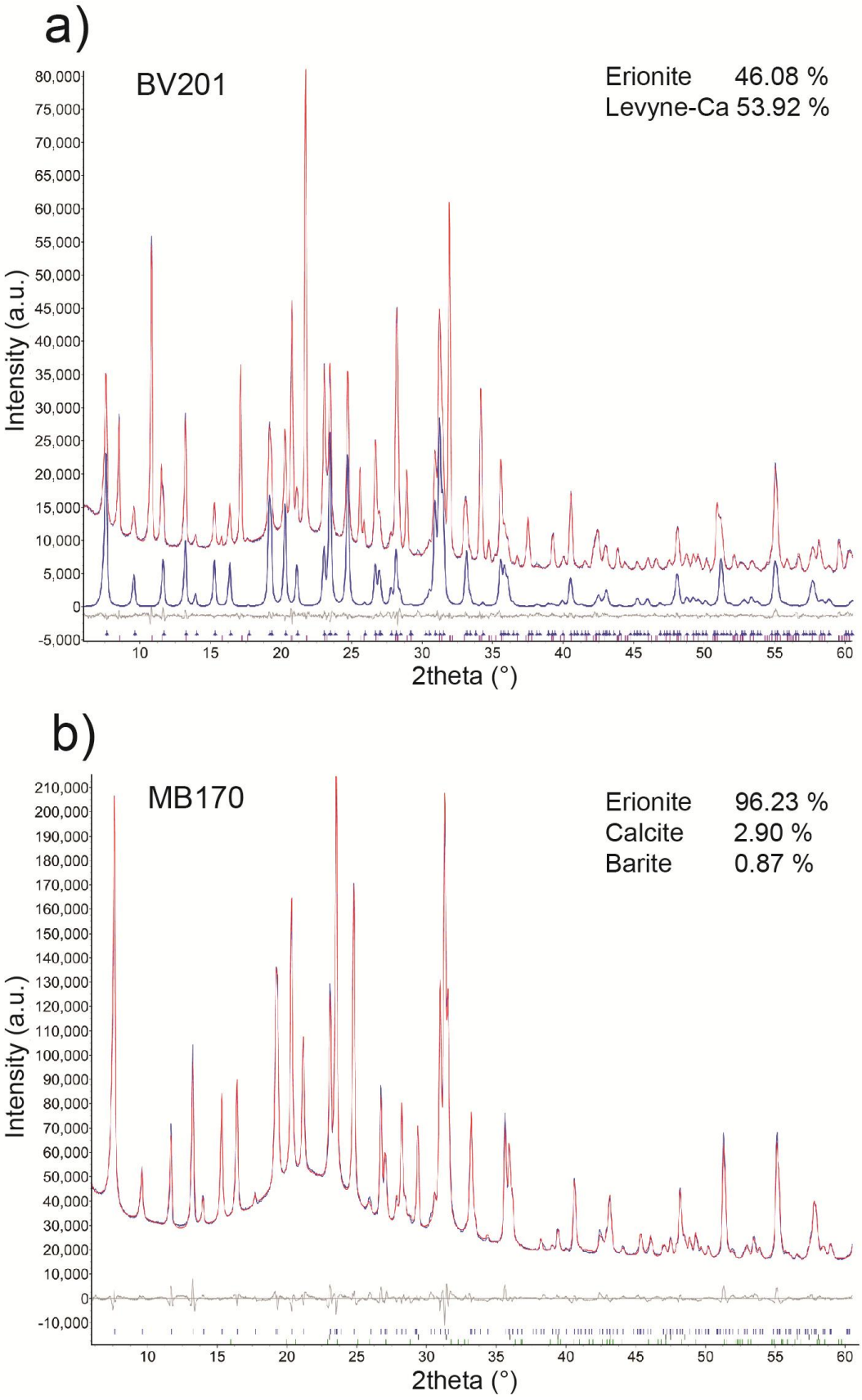

Figure 2. Rietveld plots of samples **a)** BV201 **b)** MB170. Blue dotted line: experimental pattern; red continuous line: calculated; grey continuous line: difference plot; blue continuous line (BV201) calculated erionite contribution; vertical bars: position of the calculated Bragg reflections of the various mineral phases.

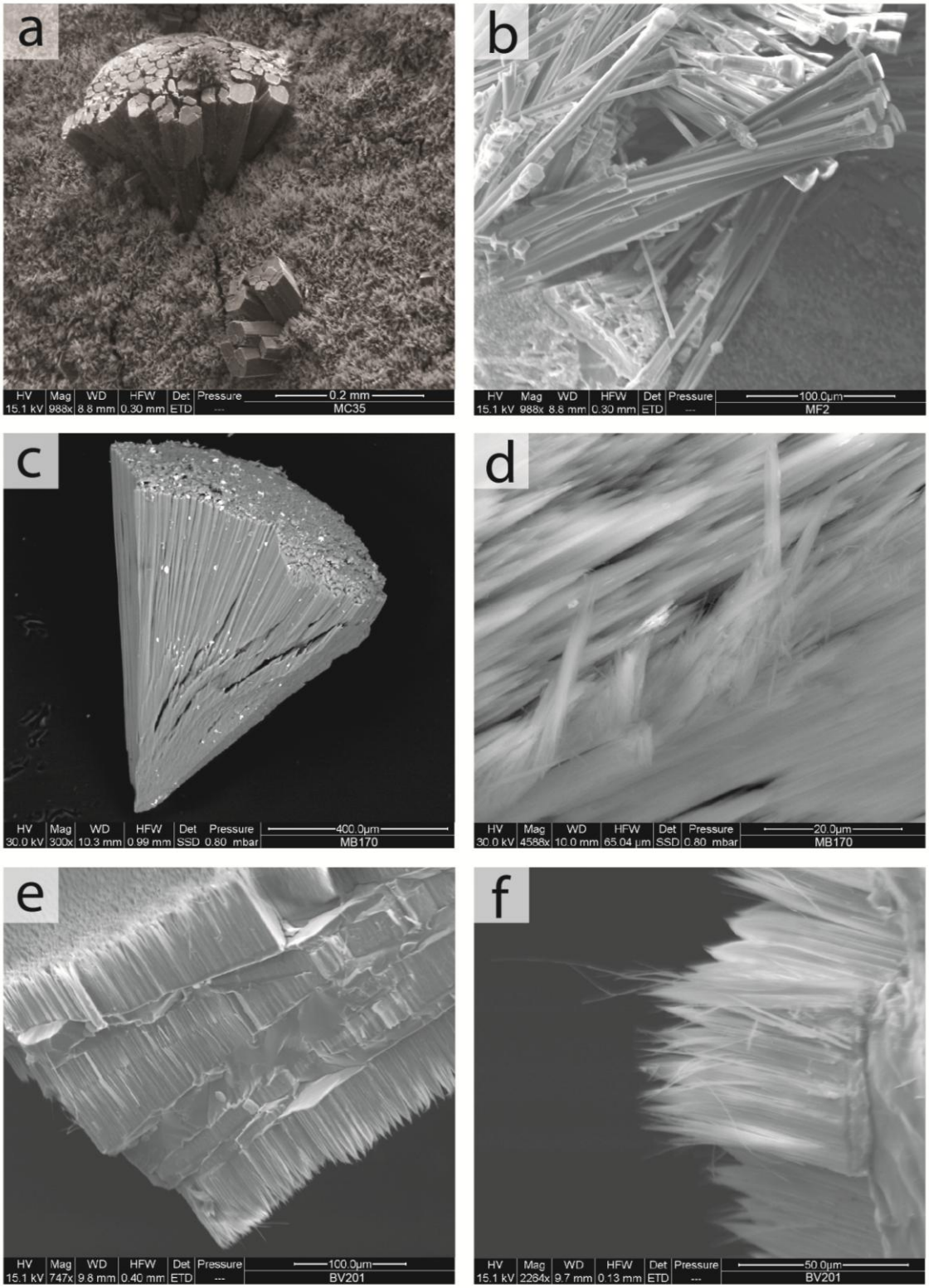

Figure 3. Representative SEM images of the studied samples. **a)** Prismatic crystals of erionite grouped in radial aggregate of millimetric size (MC35). **b)** Acicular erionite crystals with hexagonal section often grouped in packets of larger size (MF2). **c**) Acicular to very fibrous crystals of erionite grouped in radial aggregates (MB170). **d)** Particular of the previous sample showing a large number of small fibrils with rigid to flexible behavior (MB170). **e)** Typical erionite-levyne-erionite sequence forming a "sandwich-like" morphology (BV201). **f)** Details of the extremely fibrous habit consisting of flexible fibres with a typical woolly aspect (BV201).

rigid to flexible behavior, with length ranging up to approximately 30 µm and small diameter, consistently smaller than 1 µm. The BV201 sample consists of two mineralogical species, erionite and levyne, which are grown in intimate association (Figure 3e). This particular intergrowth was previously reported in the Italian area, particularly in Sardinia (Passaglia and Galli, 1974) and in the Lessini Mounts (Giordani et al., 2016). In BV201 sample, levyne displays a highly tabular habit with hexagonal section and mm size, while erionite grows up normally to the levyne surfaces, forming a typical erionite-levyne-erionite sequence (ELE), which may also be repeated several times forming a "sandwich-like" morphology. In this sample, erionite is characterized by an extremely fibrous habit which consists of flexible fibers grouped in bundles of a few tens of mm in diameter, and variable length, up to approximately 100 µm (Figure 3f). These bundles are consistently prone to separate in a myriad of thin fibres and fibrils of variable size in terms of length (from approximately 5 to 85 µm, main mode 40-60 µm), but homogeneous in terms of diameter, which is <0.3 µm. In this sample, erionite demonstrated the typical woolly aspect of the holotype from Durkee, Oregon (Eakle, 1898; Staples and Gard, 1959).

3.5.2 Chemistry

The point analyses of the samples are highly consistent, showing a variation of major elements within 2-3%, indicating a high degree of chemical homogeneity of each sample. The chemical data of the investigated samples (i.e. analyses passing the quality checks described in Analytical Methods) are presented in Table 3 and depicted diagrammatically in Figure 4. The prismatic erionite from MC35 has an average chemical formula $(Ca_{2.80}K_{2.29}Na_{1.35}Mg_{0.26})[Al_{10.09}Si_{25.91}O_{72}]\cdot 30.23H_2O$ and classified as erionite-Ca (Figure 4). Ca^{2+} is generally the prevailing EF cation with a content ranging from 2.12 to 3.51 *apfu*, but the amount of K^+ and Na^+ is also high: 2.04-2.51 *apfu* and 0.29-2.62 *apfu*, respectively. In contrast, the Mg^{2+} content is low, 0.11-0.48 *apfu*, leading to a Mg/(Ca+Na) ratio, which is considered the most significant parameter for the distinction between erionite and offretite, of 0.06 (range 0.03-0.11). However, if one examines the data in more detail, it may be noted that the chemical compositions of the analyzed crystals define two distinct fields in the Figure 4 diagram. The first group of crystals are typically erionite-Ca having Ca^{2+} as the dominant EF cation, while K^+ is slightly subordinate and Na^+ is present in low amounts. The second group of crystals display a composition that fall in the central part of the triangular plot, corresponding to comparable amounts of the EF cations Ca^{2+}, K^+ and Na^+. Unfortunately, these two chemical populations of crystals do not correspond to any difference in morphology and/or physical properties, making their distinction not possible utilizing only macro- and/or microscopic investigations. For this reason, in this sample there is reference to an intermediate composition between those of the two populations.

The prismatic to acicular erionite from MF2 has an average chemical formula $(Na_{2.43}K_{2.08}Ca_{1.59}Mg_{0.28})[Al_{8.72}Si_{27.28}O_{72}]\cdot 29.90H_2O$. According to the prevailing EF cation (Na^+: 2.23-2.75 *apfu*), it is classified as erionite-Na. However, because significant amounts of other EF cations are also present, (K^+: 1.92-2.32 *apfu*; Ca^{2+}: 1.30-2.18 *apfu*) the composition of this sample falls towards the central part of the classification diagram of erionite (Figure 4). The Mg^{2+} content ranges from 0.04 to 0.52 *apfu* corresponding to a Mg/(Ca+Na) ratio of 0.07 (range 0.01-0.13).

The acicular to fibrous erionite from MB170 is classified as erionite-Ca (Figure 4) according to its average chemical formula $(Ca_{2.77}K_{2.44}Na_{0.46}Mg_{0.33})[Al_{9.09}Si_{26.91}O_{72.01}]\cdot 30.02H_2O$. Ca^{2+} is the prevailing EF cation (2.44-3.09 *apfu*) but K^+ is only slightly less abundant (2.05-2.81 *apfu*). In contrast, Na^+ content is lower (0.28-0.65 *apfu*) and comparable to that of Mg^{2+} (0.22-0.45 *apfu*: Mg/(Ca+Na) = 0.10, range 0.08-0.16).

The extremely fibrous erionite from BV201 displays an average chemical formula $(Ca_{3.51}K_{2.21}Na_{0.39}Mg_{0.26})[Al_{10.35}Si_{25.65}O_{72}]\cdot 30.23H_2O$ and classified as erionite-Ca (Figure 4). Ca^{2+}

content ranges from 2.96 to 3.81 *apfu* whereas that of K^+ is consistently lower (1.93-2.56 *apfu*). Similarly to MB170, the Na^+ content (0.14-0.87 *apfu*) is comparable to that of Mg^{2+} (0.03-0.43 *apfu*: Mg/(Ca+Na) = 0.07, range 0.01-0.11).

3.5.3 Structure of the fibrous samples

A full structure refinement was carried out for erionite and levyne (sample BV201) and erionite (sample MB170). However, due to the presence of a mixture of two phases occurring almost exactly at 50 wt % (sample BV201) it is postulated that the structural results are less accurate than those retrieved for sample MB170, in particular as far as the EF cation and water molecules position and population is referred to. Therefore, in this section mainly the structural features of MB170 are described. Fractional coordinates, isotropic displacement parameters, site multiplicity and occupancy, and site scattering of MB170 are reported in Table 4. Relevant bond distances and contacts are presented in Table 5. Fractional coordinates, isotropic displacement parameters, site multiplicity and occupancy, and site scattering of BV201 are provided in Supplementary Material, Table S2.

The cell parameters and volume of samples BV201 and MB170 are a = 13.34082(19) Å, c = 15.1229(3) Å, V = 2330.94(8) Å^3 and a = 13.31490(13) Å, c = 15.09267(19) Å, V = 2317.25(5) Å^3, respectively (Table 2). Owing to the fact that in recent years several samples of fibrous erionite were characterized in detail from the crystal chemical and structural point

Sample	**BV201**		**MF2**		**MB170**		**MC35**	
	average	σ	average	σ	average	σ	average	σ
	N = 15		*N = 7*		*N = 10*		*N = 10*	
SiO_2	52.52	0.71	56.71	1.18	55.43	0.38	53.15	0.66
Al_2O_3	17.97	0.56	15.35	0.88	15.87	0.23	17.54	0.69
MgO	0.35	0.19	0.39	0.24	0.46	0.10	0.36	0.21
CaO	6.70	0.49	3.07	0.52	5.15	0.35	5.35	1.11
Na_2O	0.40	0.27	2.59	0.19	0.49	0.11	1.42	0.89
K_2O	3.54	0.37	3.38	0.23	4.10	0.27	3.68	0.26
H_2O	18.50*	-	18.50*	-	18.50*	-	18.50*	-
Total	81.50	-	81.50	-	81.50	-	81.50	-
Si	25.65	0.33	27.28	0.52	26.91	0.12	25.91	0.38
Al	10.35	0.33	8.72	0.52	9.09	0.12	10.09	0.38
ΣT	*36.00*	-	*36.00*	-	*36.00*	-	*36.00*	-
Mg	0.26	0.14	0.28	0.17	0.33	0.07	0.26	0.15
Ca	3.51	0.26	1.59	0.28	2.77	0.23	2.80	0.58
Na	0.39	0.26	2.43	0.18	0.46	0.10	1.35	0.85
K	2.21	0.23	2.08	0.14	2.44	0.19	2.29	0.17
H_2O	30.23	0.08	29.90	0.14	30.02	0.17	30.23	0.12
R	0.713	-	0.758	-	0.748	-	0.720	-
E%	2.20	3.53	5.56	3.07	0.64	4.62	3.30	5.06

Table 3. Chemical composition of the investigated erionite samples, showing the average values (*N* is the number of point analysis) and standard deviation (σ). *ΣT,* is the sum of cations in tetrahedral sites; E%, measure of charge balance: E% = 100*[Al–Alk_{th}]/Alk_{th} where Alk_{th} = Na+K+2*(Ca+Mg); R, Si/(Si+Al) ratio. Crystal chemical formula calculated on the basis of 36 (Si+Al) *apfu*. *Hypothesized water content of 18.5 wt.% (corresponding to ca. 30 H_2O *pfu*).

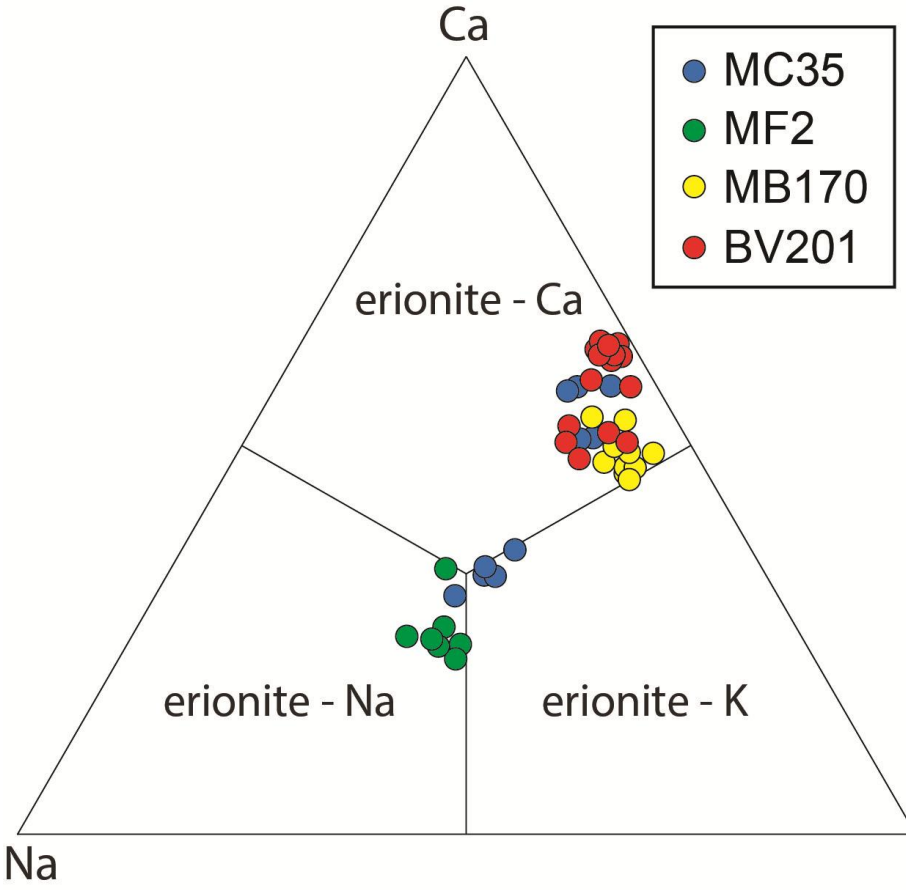

Figure 4. Ca-Na-K ternary compositional plots of the studied samples, showing the distribution of EF cations.

of view, a new graph, reporting the dependence of the cell volume on $R = \frac{Si}{Si+Al}$ derived from chemical data (Figure 5) is proposed. This relationship was first reported by Passaglia et al. (1998) using a set of 23 samples that were implemented in the present investigation with 9 further samples. The new equation $R = \frac{Si}{Si+Al}$ = -0.021+5.593 has a correlation factor R (unfortunately it takes the same symbol of the Si fraction) of 0.98 (R^2 = 0.96), which represents an improvement with respect to the value of 0.96 reported by Passaglia et al. (1998). It is worth noting that erionite-K is consistently characterized by a smaller volume (and a higher $R = \frac{Si}{Si+Al}$) than that of erionite-Ca. In contrast, a few fibrous samples of erionite-Na are characterized by a volume comparable to that of erionite-K. The cell parameters of levyne-Ca associated to erionite in sample BV201 are a = 13.32924(12) Å, c = 22.9296(3) Å, V = 3528.08(8) $Å^3$. Owing to the small dimensions of the crystals and the "sandwich like" morphology it was not possible to retrieve a reliable chemical composition. Microstructural parameters were obtained by the analysis of the integral breadths β_i of the individual reflections (Ballirano and Sadun, 2009). In particular, in the case of BV201 a volume-weighted mean column height L_{vol} of 72.3(9) nm and ε_0 micro-strain (lattice strain) of 0.0736(17) were obtained. In the case of MB170 an attempt to apply an ellipsoid modelling of the average shape of the crystallites using the approach of Katerinopoulou et al. (2012) was undertaken. In the hexagonal system, the shape ellipsoid parameters b_{ij} are constrained as $b_{11} = b_{22} = 2b_{12}$; $b_{13} = b_{23} = 0$. The orientation of the ellipsoid is such that the principal radii $r_a \perp c$ and $r_c \parallel c$. Nevertheless, the refined r_a and r_c radii were of 576(9) and 567(11) nm indicating an isotropic coherency domain that

Site	*x*	y	z	B_{iso}(Å^2)	Site occ.	s.s.(e$^-$)	Proposed site partition	s.s.(e$^-$) from site partition
			Framework					
T1	0.23230(16)	-0.0028(2)	0.10423(9)	0.94(2)	1		$Si_{17.08}Al_{6.92}$	
T2	0.0943(2)	0.4263(2)	1/4	0.94(2)	1		$Si_{10.09}Al_{1.91}$	
O1	0.3505(3)	0.0263(3)	0.6626(3)	1.74(7)	1			
O2	0.09763(20)	2*x*	0.1261(4)	1.74(7)	1			
O3	0.1265(2)	2*x*	0.6310(4)	2.74(11)	1			
O4	0.2719(3)	0	0	1.74(7)	1			
O5	0.2318(3)	2*x*	1/4	2.74(11)	1			
O6	0.4531(3)	2*x*	1/4	2.74(11)	1			
			EF cations					
Ca1	1/3	2/3	0.9368(13)	12.43(19)	0.71(2)	57.0(20)	$Mg_{0.33}Ca_{2.27}$	49.4
Ca2	1/3	2/3	0.1066(12)	12.43(19)	0.312(6)	24.9(5)	$Na_{0.46}$	5.1
Ca3	1/3	2/3	0.626(8)	12.43(19)	0.13(2)	10.1(19)	$Ca_{0.50}$	10.0
K1	0	0	1/4	1.57(11)	1	38	$K_{2.00}$	38.0
K2	1/2	0	0	1.57(11)	0.065(10)	7.4(11)	$K_{0.41}$	7.8
					$\Sigma_{cat.}$	137(5)		110.2
			Water molecules					
OW7	0.245(4)	2*x*	3/4	6.22(9)	0.23(5)	11(2)		
OW8	0.2510(4)	2*x*	0.0160(9)	12.43(19)	0.802(6)	77.0(6)		
OW9	0.4317(6)	2*x*	0.8943(10)	12.43(19)	0.781(11)	75.0(10)		
OW10	0.4126(17)	2*x*	0.705(3)	12.43(19)	0.57(3)	55(3)		
OW11	0.2446(13)	2*x*	0.692(2)	12.43(19)	0.219(13)	21.0(12)		
OW12	0.4707(11)	2*x*	0.0330(18)	12.43(19)	0.463(15)	44.4(14)		
					Σ_{water}	284(9)		

Table 4. Fractional coordinates, isotropic displacement parameters, site multiplicity and occupancy, and site scattering (*s.s.*) of samples MB170. Si, Al site partition from Jones' (1968) determinative curves. The scattering power of Ca has been used to model the Ca1, Ca2 and Ca3 extra-framework sites.

is of one order of magnitude greater than that of BV201. This is in agreement with the results of the morphological analysis by ESEM (see above). Micro-strain was significantly smaller than that of BV201 as indicated by ε_0 value of 0.0445(17).

The moderate strain of BV201 is related to curling of the fibrils (Cametti et al., 2013) and possibly to the requirement to maintain some coherency at the boundary with levyne that has a slightly smaller *a*-parameter as compared to erionite.

The mean bond distances <T1-O> = 1.649 Å and <T2-O> = 1.629 Å of MB170 are consistent with a disordered Si/Al distribution (<T1-O> - <T2-O> = 0.020 Å) leading to a preferential partition of Al at the tetrahedral T1 site (Table 6). This behavior represents a novelty as our previous structure refinements of fibrous erionite-K and -Na samples (Ballirano et al., 2009; 2015; Cametti et al., 2013; Ballirano and Pacella, 2016; Pacella et al., 2016) consistently indicated a preferential partition of Al at tetrahedral T2 site, whereas the sample of prismatic erionite-Ca from Nizhnyaya Tunguska, Siberia analyzed by Alberti et al. (1997) was characterized by an almost identical distribution between T1 and T2. Two R ratios were calculated by using both the Jones' determinative curves

T1	-O2	1.629(2)	T2	-O6	1.609(4)
	-O3	1.652(4)		-O1 x2	1.632(4)
	-O4	1.654(2)		-O5	1.640(4)
	-O1	1.660(5)			
			K2	-OW12	*0.84(2)*
K1	-O2 x6	2.972(5)		-OW9 x2	*2.243(14)*
	-O3 x6	3.427(5)		-O4 x2	3.037(4)
				-O1 x4	3.287(5)
Ca1	-OW8 x3	2.244(15)		-OW8 x4	3.338(12)
	-OW9 x3	2.356(15)			
	-OW10 x3	2.82(5)	Ca2	-OW8 x3	2.341(15)
	-OW11 x3	2.83(3)		-O5 x3	3.188(13)
				-OW12	*3.36(2)*
Ca3	-OW10 x3	2.19(8)	Ca1	-Ca3	*0.94(13)*
	-OW11 x3	2.28(6)	OW7	-OW11	*0.87(4)*
	-OW9 x3	2.29(2)		-OW10	*2.05(5)*
	-OW7 x3	2.76(11)	OW9	-OW10	*1.56(5)*
	-OW8 x3	2.86(10)		-OW12	*2.28(3)*
	-OW10 x3	3.14(11)	OW10	-OW10	*1.36(10)*
				-OW11	*1.96(2)*
			OW11	-OW11	*1.74(7)*

Table 5. Relevant bond distances and contacts (in Å) of MB170. Never occurring contacts reported in italics.

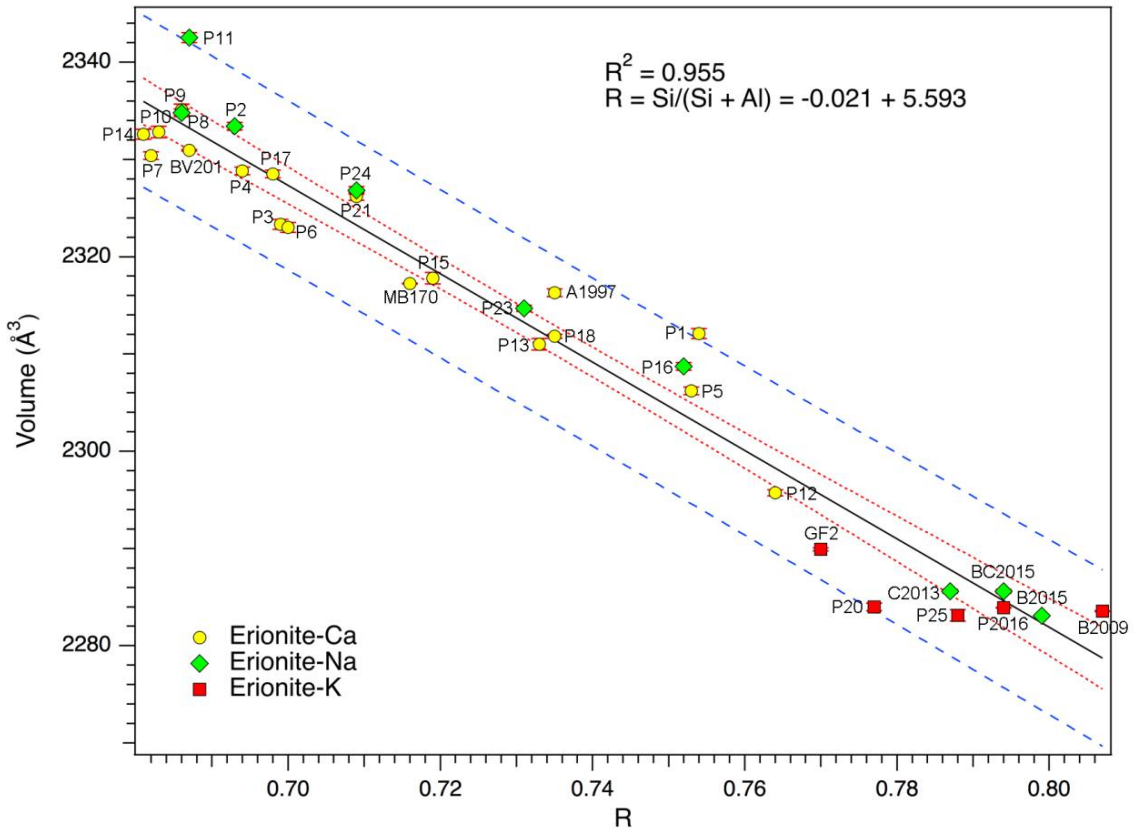

Figure 5. Dependence of the cell volume of erionite on $R = \frac{Si}{Si+Al}$. Red dotted and blue dashed lines represent the 95% confidence and 95% prediction bands, respectively. Sample labels refers to: A1997: Alberti et al. (1997); B2009: Ballirano et al. (2009); B2015: Ballirano et al. (2015); BC2015: Ballirano and Cametti (2015); C2013: Cametti et al. (2013); GF2: woolly sample from Nevada (unpublished results); P1-P25: Passaglia et al. (1998); P2016: Pacella et al. (2016).

(Jones, 1968) based upon <T-O> (R_{Jones}) and the regression equation based upon cell volume, modified from Passaglia et al. (1998), derived in the present investigation (R_{Vol}). An R_{Jones} value of 0.755, resulting from the population of the T1 ($Al_{6.92}Si_{17.08}$) and T2 ($Al_{1.91}Si_{10.09}$) sites, was determined, as well as an R_{Vol} value of 0.727 (Table 6). Those values are reasonably close with that of 0.748 obtained from chemical data (R_{Che}). Similarly, the R_{Jones} and R_{Vol} values of 0.714 and 0.698, respectively, were obtained for erionite BV201, both comparing favorably with R_{Che} of 0.713 (Table 6). Simultaneously, an R_{Jones} value of 0.729 was calculated for levyne occurring in association with erionite in sample BV201. This value exceeds that commonly observed in levyne-samples ($0.62 < R < 0.70$; Passaglia and Sheppard 2001). However, as indicated by Ballirano and Cametti (2013) a relatively high underestimation of the Al content from <T-O> was found as compared to chemical data for levyne samples.

SEM-EDS analysis of MB170 indicates a total site scattering (*s.s.*) of the EF cations of 110(10) e^-. This value is in agreement with the *s.s.* of 137(5) e^- obtained from the Rietveld refinement (Table 4). The relatively low *s.s.* resulting from SEM-EDS may be reasonably attributed to EF cations mobilization. Further, a total of 35.5(11) water molecules *pfu* were allocated by the refinement, in agreement with reference data (Coombs et al 1997; Passaglia et al 1998), albeit numerically higher. The structure is similar to that of erionite-Ca from Nizhnyaya Tunguska, Siberia (Alberti et al. 1997), except for minor differences in EF cation and water molecule sites population. Electron density was detected at the K2 site and, consistently with the chemical analysis, attributed to K cations in excess of 2 *apfu*. It was found that the refined *s.s.* of K1 + K2 agrees with the K content quantified by SEM-EDS. Therefore, one might expect that the relatively large difference between the total EF *s.s.* retrieved from the Rietveld refinement and that from the chemical data may be predominantly assigned to Na volatilization occurring during the micro-chemical analysis. EF cation sites coordination is illustrated in Figure 6. A reasonable 6-fold coordination for Ca may be observed at Ca1 considering 3 x OW8 at 2.244(15) Å and 3 x OW10 at 2.82(5) Å. Similarly, to the sample of erionite-Ca investigated by Alberti et al. (1997), an anomalous coordination of Ca2 was found. In fact, the present refinement indicates a 9-fold coordination to 3 x OW8 at 2.341(15) Å, 3 x O5 at 3.188(13) Å and 3 x OW12 at a long 3.36(2) Å distance, which is potentially compatible with the occurrence of Na. However, the refined *s.s.* of 24.9(5) e^- largely exceeds that potentially provided by all available Na (ca. 5 e^-). Two hypotheses may be proposed to justify this result, a significant volatilization of Na during SEM-EDS analysis and/or the occurrence of static disorder impossible to model under the present experimental conditions. A reasonable 6-fold coordination for Ca may be noted at Ca3 considering 3 x OW9 at 2.29(2) Å and 3 x OW7 at 2.76(11) Å.

3.5.4 Erionite occurrences and risk assessment in Italy

The initial findings of erionite in Italy date back to the '70s, when Passaglia and Galli (1974) and Pongiluppi et al. (1974) reported the presence of erionite within basic volcanic rocks in Montresta (OR) and Nurri (CA) areas, Sardinia region. Data indicated that the erionite crystals occur as a sub-mm coating of slight thin fibres in epitaxial growth with levyne crystals, forming a typical sandwich-like intergrowth. Those crystals were found in vugs and cavities of weathered andesites and basalts. In the same period, Giovagnoli and Boscardin (1979) detected the presence of erionite as fibrous spherulitic aggregates within amygdaloidal basalts at Montecchio Maggiore (VI), Veneto region. Successively, erionite was also found in the Tertiary volcanites (latitic and trachytic lavas) in the Euganean Hills, Veneto region (Passaglia and Tagliavini 1995). In this case, erionite occurs as clear-white radiating bundles of needles 2-3 mm long, with a chemical composition

dominated by Ca as EF cation. Examination of secondary mineral assemblages in the Tertiary volcanic rocks of the Lessini Mountains indicated a significant occurrence of erionite (Cenni, 2009; Mattioli et al., 2016a), which is present in 65% of the investigated outcrops, with an estimated amount varying from 10 to 40 vol% of the total secondary minerals. In these volcanic rocks, erionite also displayed different morphological types, ranging from prismatic crystals with "rigid" behavior to extremely fibrous with flexible "hair-like" appearance (Giordani et al., 2016).

These features, combined with the noteworthy amounts reported above, are not negligible for effects on human health, especially if one considers that these basalts often host active mining or quarrying activities and that these rocks are extensively used as aggregate in asphalt and concrete pavements, as a road base, railroad ballast and cobblestone pavement. Nonetheless, a detailed description and quantification of erionite presence in all of these areas is still lacking.

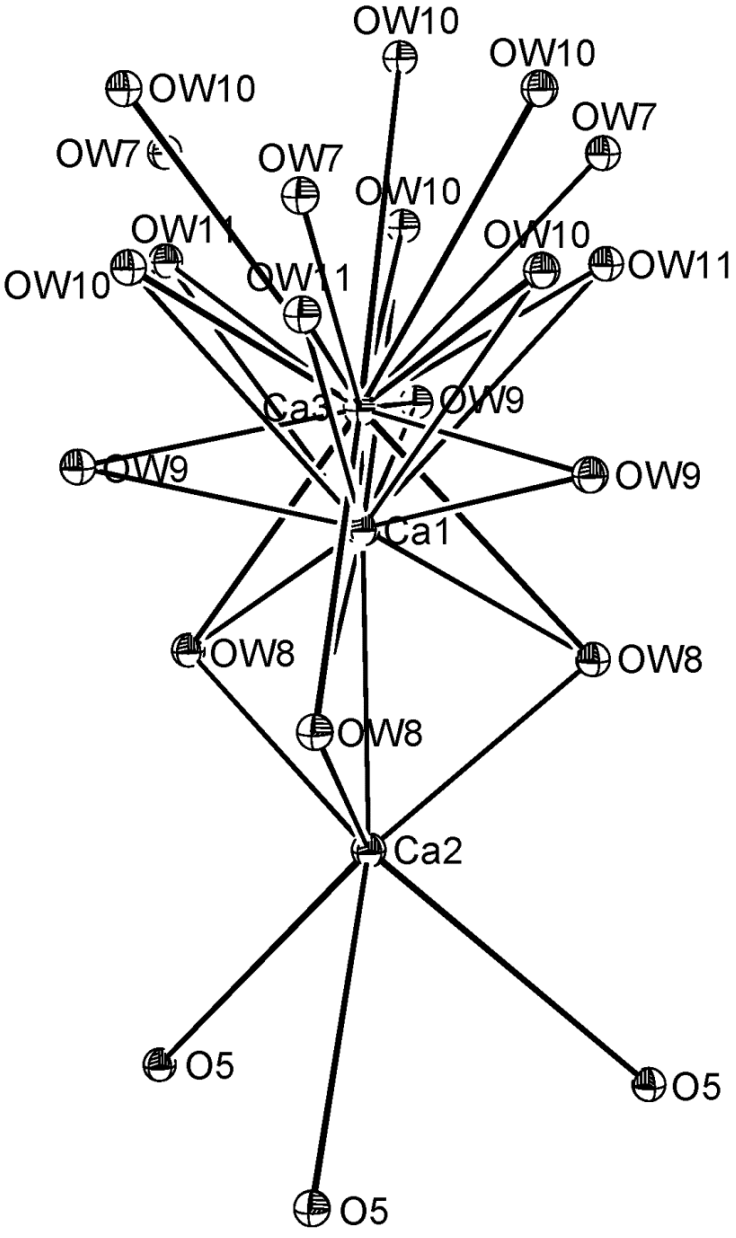

Figure 6. ORTEP-3 plot (Farrugia, 1999) showing the coordination of the Ca1, Ca2 and Ca3 cation sites.

In addition to these erionite occurrences, it is of importance to consider that there are many other volcanic rocks, such as ignimbrites, lavas and tuffaceous sediments, which extensively crop out in further regions of Italy, especially Lazio and Campania (Figure 7). It is relevant to note that most of these volcanites possess a huge thickness and are affected by a variety of secondary mineralization processes similar to those described in other areas where erionite has been widely found (Van Gosen et al., 2013; Ortega-Guerrero and Carrasco-Núñez, 2014; Saini-Eidukat and Triplett, 2014). Therefore, it cannot be excluded *a priori* that erionite, or some other fibrous zeolites, might also be extensively present in these volcanic rocks. Nevertheless, most of these rocks have not apparently been investigated with this aim in mind and specific studies on the occurrence of fibrous minerals are currently lacking. Given the huge extension of these volcanic rocks, the possibility of an environmental exposure to this hazardous fibrous zeolite needs to be taken into serious consideration.

The discovery of fibrous erionite in the Lessini Mountains, coupled with its occurrence as fibers of inhalable size (Giordani et al., 2016), suggests the need for a detailed risk assessment in Italy. A risk assessment will require coordinated actions from government agencies, local health authorities, Universities and research centers, in order to record the presence of erionite or other fibrous zeolites, recognizing mineral species and quantifying their abundance in rock deposits. In sites where the presence of fibrous zeolites has been confirmed by lab results, an accurate field surveys and sampling campaigns need to be planned, in order to determine detailed geological-, stratigraphic- and structural features, measuring the thickness, area extent and volume of lithostratigraphic units containing these minerals (Vignaroli et al., 2014). These data may be entered into a GIS to produce a result that might be used immediately and in the long period by research institutes, local authorities and regional agencies for environmental protection. In sites where the presence of hazardous fibrous minerals has been confirmed, several airborne fibers sampling campaigns need to be conducted, with the aim to assess the extent of airborne dispersion produced by natural agents and human activity. This is of paramount importance in the case that these sites host active mining or quarrying activities, where a quantification of the airborne fibres contamination at workplaces is the first fundamental step to propose measures for environmental risk mitigation. In addition to the environmental risk related with the presence of natural erionite, this dangerous fibrous zeolite may also be present in association with other zeolites widely used for various purposes such as petrochemical and nuclear industry, agriculture, medical and domestic uses.

Further, the knowledge of the epidemiology of mesothelioma linked to erionite in Italy is extremely scarce, and the phenomenon is still little investigated. While mesothelioma cases attributed to asbestos exposure are well known and recorded (INAIL, 2012), virtually little is known regarding domestic cases from exposure to airborne erionite fibres. In Italy it is known that approximately 20% of mesothelioma cases are not linked to asbestos (INAIL, 2012). In particular, one of the highest percentages of mesothelioma in Italy in the time interval 1993-2008 characterizes the Veneto Region. The contribution of exposure to erionite cannot be excluded in this significant percentage. Unfortunately, epidemiological and public health data are available according to the administrative borders (e.g. provincial or regional areas) that do not correspond to the real limits of geological deposits, in this case the erionite-containing rocks. Consequently, it is extremely problematic extrapolate data regarding incidence of mesotheliomas unrelated to asbestos in the Lessini Mountains area, that instead would be a very useful information for the understanding of erionite contribution.

For this reason, targeted epidemiological surveillance is necessary for a more comprehensive risk assessment and because these findings may be crucial to understand the effect of the choices made in the field of risk management.

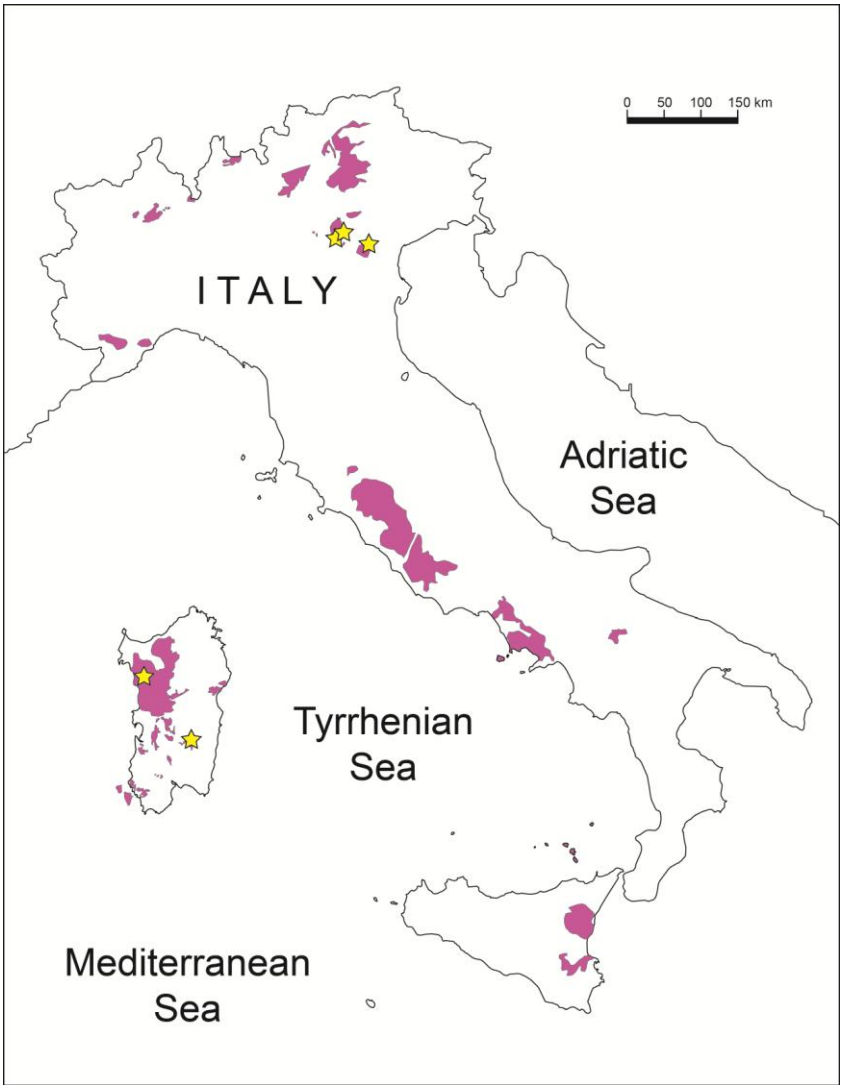

Figure 7. Sketch map of Italy showing the sites where erionite crystals have been described in literature (stars) and the geological distribution of the other potentially erionite-bearing volcanic rocks (purple red).

3.6 Concluding remarks

In this study new mineralogical, structural and chemical data of 4 representative erionite samples (MC35, MF2, MB170, BV201) from Northern Italy were reported, where this carcinogenic zeolite occurs as fibers of inhalable size. The following conclusions may be inferred from the present contribution:

- MC35 is an erionite-Ca characterized by prismatic habit with solid appearance and rigid behavior, and no apparent fibrous elements were detected. MF2 is an erionite-Na formed by acicular crystals with a great tendency to separate fibers and fibrils with rigid behavior. MB170 is an erionite-Ca showing acicular to fibrous crystals, often separating in a great number of small fibrils with rigid to flexible behavior. BV201 is an erionite-Ca with an extremely fibrous, hair-like habit, with flexible appearance and a marked tendency to split up into thin fibres and fibrils. From the structural point of view, MB170 is characterized by an unusual preferred partition of Al at the T1 site instead of T2 as observed in all refinements of erionite samples. A discrepancy between the total EF *s.s.* determined from SEM-EDS and Rietveld refinement was noted that has been attributed to EF cation volatilization/migration (mainly Na) during micro-chemical analysis. A mismatch was detected between the *a*-

parameter of erionite-Ca and levyne-Ca that are intergrown in sample BV201. As the single-layer of 6-membered rings of $(Si,Al)O_4$ tetrahedra, whose stacking along the *z*-axis build both structures, is common, the mismatch produced some strain that possibly favors the curling of fibrils.

- As a whole, erionite is present in 65% of the investigated outcrops, with an estimated amount varying from 10 to 40 vol% of the total secondary minerals, which are crystallized within vugs and cavities of basaltic rocks. These amounts are not negligible for effects on human health, especially if one considers that these basalts often host active mining or quarrying activities and that these rocks are extensively used as construction material.
- The discovery of fibrous erionite in the Lessini Mountains suggests the need for a detailed risk assessment in Italy, with specific studies such as a quantification of the potentially airborne fibers and targeted epidemiological surveillance. This need is even more evident if one considers that erionite, or some other fibrous zeolites, might be potentially present in many other volcanic rocks, which extensively crop out in many regions of Italy. Given the huge extension of these volcanic rocks, the possibility of an environmental exposure to hazardous fibrous zeolites needs to be given serious consideration. These results provide the basis for health and safety protection programs and for a better scientific understanding of this carcinogenic fibrous zeolite.

Chapter 4

PRISMATIC TO ASBESTIFORM OFFRETITE FROM NORTHERN ITALY: NEW MORPHOLOGICAL AND CHEMICAL DATA OF A POTENTIALLY HAZARDOUS ZEOLITE

4.1 Introduction

In the recent years, a subject of great interest has been that of inhalable fibrous minerals and their potential health effects. One of the most important factors for defining the hazardousness of mineral fibres is their size or that of fibrils that may originate from the source crystals (Stanton et al., 1981; Lee, 1985; Oberdorster et al., 2005; Aust et al., 2011; Mossman et al., 2011; Boulanger et al., 2014).

The biopersistence of fibres, which is the amount of time a particle resides within a given biological compartment, is also an important factor for inducing toxicity and carcinogenicity (Hesterberg et al., 1998; Fubini, 2001; Maxim et al., 2006). It has been shown that an inhalable fibre might be carcinogenic if it is sufficiently durable to remain chemically and physically intact within the lung tissue (Muhle et al., 1991; Oberdörster et al., 2005). The biopersistence of mineral fibres is also related to their chemical composition and some elements can play a key role to determine the carcinogenic mechanisms, such as the presence of iron (Bonneau et al., 1986; Fubini, 2001; Gazzano et al., 2005; Crovella et al., 2016).

Other properties of fibres, including specific surface area, interacting capability, structure, net charge, zeta potential, and microtopography, might also act as important factors in fibre-induced toxicity and carcinogenicity (Lippmann, 1988; Hochella, 1993; Oberdörster et al., 2005; Pollastri et al., 2014; Mattioli et al., 2016b).

The inhalable mineral fibres of primary concern are those with an extremely fibrous habit which has also been described as "asbestiform," a term applied to minerals with a macroscopic habit similar to that of asbestos (NIOSH, 2011). The asbestiform habit may be defined as one in which crystals grow almost exclusively in a single dimension, in a straight line, until they form long, thread-like fibres with aspect ratios of 20:1 to 100:1 and higher, and exhibit narrow width (on the order of 0.1 μm; Case et al., 2011).

There are six minerals currently regulated by the normative as asbestos (e.g. Ross et al., 1984; World Health Organization-WHO, 1986; NIOSH 2011): chrysotile, amosite, crocidolite, tremolite, actinolite and anthophyllite. In addition, there is a growing interest in other unregulated asbestiform minerals to which humans might be exposed that are (1) not commercially used but would have been mineralogically identified as asbestos minerals (e.g., asbestiform winchite, richterite and magnesioriebeckite; Metcalf and Buck, 2015); (2) other asbestiform amphiboles (e.g., fluoroedenite; Paoletti et al., 2000; Manna and Comba, 2001;Gianfagna et al., 2003; Burragato et al., 2005; Gianfagna et al., 2007); (3) mineral species that might resemble asbestos (e.g., fibrous antigorite, balangeroite; Groppo et al., 2005; Groppo and Compagnoni, 2007; Cardile et al., 2007); (4) other elongated mineral particles (e.g., zeolites as erionite and mordenite, fibrous talc, and clay minerals as sepiolite and palygorskite; IARC, 1997; Santaren and Alvarez, 1994; Galan, 1996).

One of such minerals is erionite, which has been responsible for an epidemic of mesothelioma deaths in the Cappadocia region of Turkey, where villagers had built their homes out of erionite-bearing rock (e.g. Baris et al., 1987; Carbone et al., 2011). In some villages, 20 to 50% of the yearly deaths were due to mesothelioma, the highest rates of cancer related to an environmental exposure to toxic fibrous minerals ever reported (Dogan et al., 2006; Carbone et al., 2007).

Experimental studies have shown that fibrous erionite of inhalable size is more carcinogenic and more active than chrysotile and crocidolite asbestos in increasing the incidence of malignant mesothelioma (MM) (Coffin et al., 1992; Bertino et al., 2007; Dogan, 2012; Croce et al., 2013; Hillegass et al., 2013; de Assis et al., 2014; Pollastri et al., 2014; Zebedeo et al., 2014 and references therein).

For these reasons, and according to epidemiological data (e.g. Baris et al., 1987; Temel and Gundogdu, 1996; Dogan et al., 2006; Carbone et al., 2011; Kliment et al., 2009; Metintas et al., 2010; Carbone and Yang, 2012; Demirer et al., 2015), erionite has been classified as a carcinogenic mineral for the human health and listed as a Class 1 carcinogen by the International Agency for Research on Cancer since 1987.

At present, it is categorized as the most carcinogenic mineral (IARC, 1987; 2012). In the last years many concerns have developed regarding the potential risks for environmental and occupational exposures to fibrous zeolites in Turkey (e.g. Dogan et al., 2006; Carbone et al., 2007, 2011), in Western USA (Stephenson et al., 1999; Carbone et al., 2011; Van Gosen et al., 2013; Saini-Eidukat and Triplett, 2014), in Mexico (Ortega-Guerrero and Carrasco-Nùñez, 2014; Ortega-Guerrero et al., 2015) and very recently in Iran (Ilgren et al., 2015). Accordingly, it is of paramount importance to improve the knowledge of erionite and all other zeolites with fibrous or asbestiform habit.

In this work we focus our attention on offretite, a zeolite closely related, both structurally and chemically, to erionite that, despite commonly occurring as prisms, it has also been found under asbestiform habit. Offretite is hexagonal, space group *P*6*m*2, cell parameters a = 13.27-13.32 Å, c = 7.56-7.61 Å, average chemical formula $KCaMg[Al_5Si_{13}O_{36}]\cdot 16H_2O$. As above mentioned, offretite generally forms simple hexagonal prisms and needles associated in both parallel and radiating aggregates (Gottardi and Galli, 1985; Passaglia et al., 1998; Bish and Ming, 2001; Deer et al., 2004), but it is also known to crystallize with fibrous habit (Passaglia and Tagliavini, 1994). Offretite typically occurs as fine microscopic crystals of hydrothermal origin clustered in vugs and veins of basic volcanic rocks, but it has also been found in cavities of arenaceous metasiltites or cornubianites (Bish and Ming, 2001). Frequently, it is associated with many other zeolites such as mazzite, chabazite, levyne, erionite, phillipsite, faujasite, and epitaxial overgrowths on levyne and chabazite have been described (Passaglia and Tagliavini, 1994; Bish and Ming, 2001). Moreover, given the strong correlation between their respective structures and chemistry, the structural epitaxy of offretite and erionite is common (Bennet and Gard, 1967; Gard and Tait, 1972). Consequently, the distinction between these two species is often very difficult.

The first occurrence of offretite in Italy was reported in a cornubianite rock from Passo Forcel Rosso, Adamello, as milky-white fibres in epitaxy with chabazite (Passaglia and Tagliavini, 1994). From another locality of this area and in the same host-rock, it has been found offretite with a barrel-like habit (Guastoni et al., 2002). Other occurrences of offretite in Italy have been reported in the vugs of basaltic rocks outcropping in several localities in the Vicenza and Verona provinces (Fittà, Cerealto, Alvese, Montorso Vicentino and Passo Roccolo).

The corresponding offretite crystals generally show habits ranging from barrel- to needle-like prisms, frequently associated in parallel aggregates or grouped in sub-spherical forms (Passaglia et al., 1996; Passaglia et al., 1998; Boscardin et al., 1998; Daleffe and Boscardin, 2005; Mattioli et al., 2016a). Despite these researches, the various morphological types of offretite and the different ways to form fibres and fibrils have not yet been fully understood and many morphological, mineralogical, chemical, and toxicological aspects remain unknown.

A recent investigation on the surface properties of fibrous zeolites (Mattioli et al., 2016b) showed that interacting ability of offretite surface, despite being lower than that found for erionite, is significant and this can be able to cause some toxic effect on health. Those re-

sults suggest that, similarly to erionite, a very detailed characterization is strongly required to predict the potential toxicity of this fibrous mineral and to prevent other occurrences of unexpected pathologies.
In this study we present a detailed morphological, mineralogical, and chemical characterization of different samples of offretite recently discovered in Northern Italy, some of which showing asbestiform habit. Scanning Electron Microscopy with Energy Dispersive Spectroscopy (SEM-EDS) and X-ray Powder Diffraction (XRPD) data were combined and integrated, in order to characterize from the morphological, crystal chemical and structural point of view this mineral, with particular attention to small fibres of inhalable size, that could be generate from these samples.

4.2 Materials and methods

4.2.1 Materials

Three different samples of offretite (named FF102, AD13 and MB2287) were investigated in this study. They were selected according to the main morphologic types recognised in Northern Italy: stocky-prismatic with a solid appearance (FF102), prismatic to acicular with rigid mechanical behavior (AD13), and extremely fibrous crystals (asbestiform) with rigid to flexible behavior (MB2287).
The sample FF102 originated from Valdagno (VI), whereas AD1 from Fittà (VR), in the Lessini Mountains (northern Italy), where a thick sequence of lava flows of the Veneto Volcanic Province extensively crops out (De Vecchi and Sedea, 1995; Milani et al., 1999; Bonadiman et al., 2001; Beccaluva et al., 2007). These lavas range from poorly to highly vesiculated and/or scoriaceous basalts and basanites. Their vesicles are often filled by secondary minerals, which are dominated by zeolites of hydrothermal origin (mainly analcime, chabasite, phillipsite-harmotome, gmelinite, erionite and offretite; Cenni, 2009). Based on the different secondary mineral assemblages, multi-stage alteration processes have been described in the Lessini basalts (Mattioli et al., 2016a).The sample MB2287 originated from Saviore dell'Adamello (BS) and has been found in cavities of an arenaceous metasiltite, metasomatised by the Adamello intrusion. This rock, which is a fine-grained, black cornubianite belonging to the Servino Formation, is reported as having large druses filled by secondary minerals such as zeolites (chabazite, gismondine, offretite, mesolite, phillipsite) and other phases (calcite, pyrite, actinolite and muscovite; Kueng, 1983). The association offretite-chabazite is already known in this area, (Passaglia and Tagliavini, 1994; Guastoni et al., 2002), but the morphology of offretite crystals in our sample is notably different with respect to that described in literature.

4.2.2 Scanning Electron Microscopy (SEM)

Morphological observations were performed at the University of Urbino Carlo Bo using an Environmental Scanning Electron Microscope (ESEM) FEI Quanta 200 FEG, equipped with an energy-dispersive X-ray spectrometer (EDS) for microchemical analyses.
Operating conditions were 15 kV accelerating voltage, 11 mm working distance, 0° tilt angle, and 1 µm beam diameter. For the sample MB2287, given the very small size fibres and asbestiform habit, morphometric data were collected by accurate size measurements (length and diameter) of the offretite fibres and fibrils visible in several ESEM images.
SEM-EDS analyses were renormalized using a theoretical water content of 19.34 wt%, corresponding to the grand mean values of offretite samples previously analised; the final crystal-chemical formula was calculated on the basis of 36 (Si+Al) atoms per formula unit (apfu). As previously suggested (Goldstein et al., 1992; Pacella et al., 2016), in order to minimize the alkali metal migration, chemical data were acquired using a low counting time (up to 10 s) and a raster scan mode to reduce the temperature increase. The reliability of the chemical analysis used to classify the offretite samples was evaluated by using the charge balance error formula (E% within ±10%; Passaglia, 1970; Passaglia et al., 1998), the Mg-content (Dogan and Dogan, 2008; Dogan et al., 2008) and the K-content tests, similarly to erionite (Cametti et al., 2013).

4.2.3 X-ray Powder Diffraction (XRPD)

Under a binocular microscope, some crystals was selected from the FF102 sample. The resulting material amount has allowed to performed semi-quantitative XRPD analysis.
After pulverization in agate mortar, the powder was loaded in a 0.7-mm side-opened aluminum holder. XRPD data were collected using a Philips X'Change PW1830 powder diffractometer at the University of Urbino Carlo Bo. Analytical conditions were 35 kV accelerating voltage and 30 mA beam current, with CuKα radiation (λ = 1.54056 Å).
Data were collected in Bragg-Brentano geometry from 2 to 65° 2Θ, step size of 0.01° 2Θ and 2.5 s counting time for each step. The following software packages were used for the measurements and subsequent analysis: X'Pert Quantify 3.0 for data collection and instrument control, and X'Pert HighScore 3.0 for semi-quantitative phase analysis. Due to very scarce amounts of material, the other samples will be analyzed with SiO2-glass capillary tubes in future.

4.3 Results

4.3.1 Morphology

The FF102 sample contains stocky-prismatic crystals of offretite showing well-shaped hexagonal or pseudo-hexagonal habits with diameters of ~50 μm and lengths up to 200 μm. Generally, they occurs as irregular aggregates of several individual crystals, but isolated single prisms are also observed. In some cases, the crystals termination shows smaller size and irregular morphology due to the presence of a network of fractures.
The crystals of this sample generally have a compact aspect and a rigid behavior, and do not originate any fibrous element (Figure 1a, b). In the AD13 sample, offretite generally occurs as very elongated, hexagonal (or pseudo-hexagonal) prismatic crystals of solid appearance, with a size ~50 μm in terms of diameter, and up to 500 μm in terms of length. Furthermore, in the same sample, acicular to fibrous offretite crystals with diameters < 1 μm and lengths up to 500 μm are also present, sometimes grouped in radiating bundles of larger size. These fibrous crystals generally show a rigid behavior, even if some fibres are curved and seem to display a flexible mechanical performance. At any case, both single prismatic and acicular crystals present a well-shaped morphology, and no fractures are recognizable (Figure 1c, d).
In the MB2287 sample, offretite is found under the form of very thin fibres densely associated in parallel aggregates, which grow as coating on the main surfaces of platy, rhombohedral chabazite crystals, creating a sandwich-like morphology. In this sample offretite is characterized by an extremely fibrous habit, consisting of fibres and fibrils with a diameter ranging from << 1 μm to about 4 μm, and variable lengths (generally about 20 μm). Accordingly, it might be described as having an asbestiform habit. The coatings are always characterized by a great tendency to separate in fibres and fibrils of thinner section, with rigid to flexible behavior (Figure 1e, f).
Considered the asbestiform nature of this sample, morphometric analyses were performed on selected ESEM images in order to quantify the size (length and diameter) of all the visible fibres separated and deposited on sampling plate, as well as those partially separated from the main crystals.
The results are summarised in Figure 2. As regards the length, about 99% of the total of the measured fibres lies in the range from ~2 to ~30 μm (with an average of 17.7 μm), while the remaining ~1% is longer than 30 μm. With over 65% of the measured fibres, the main mode corresponds to a fibre length between ~15 and ~25 μm. In terms of diameter, the histogram shows the presence of a large population of fibres (~95%) characterized by a small diameter (<1.5 μm; average of 0.6 μm), and the remainder (~5%) shows a small diameter (up to 2 μm). In particular, more than 30% of the measured fibres have a very small diameter, up to 0.3 μm, with a mean value of 0.25 μm.

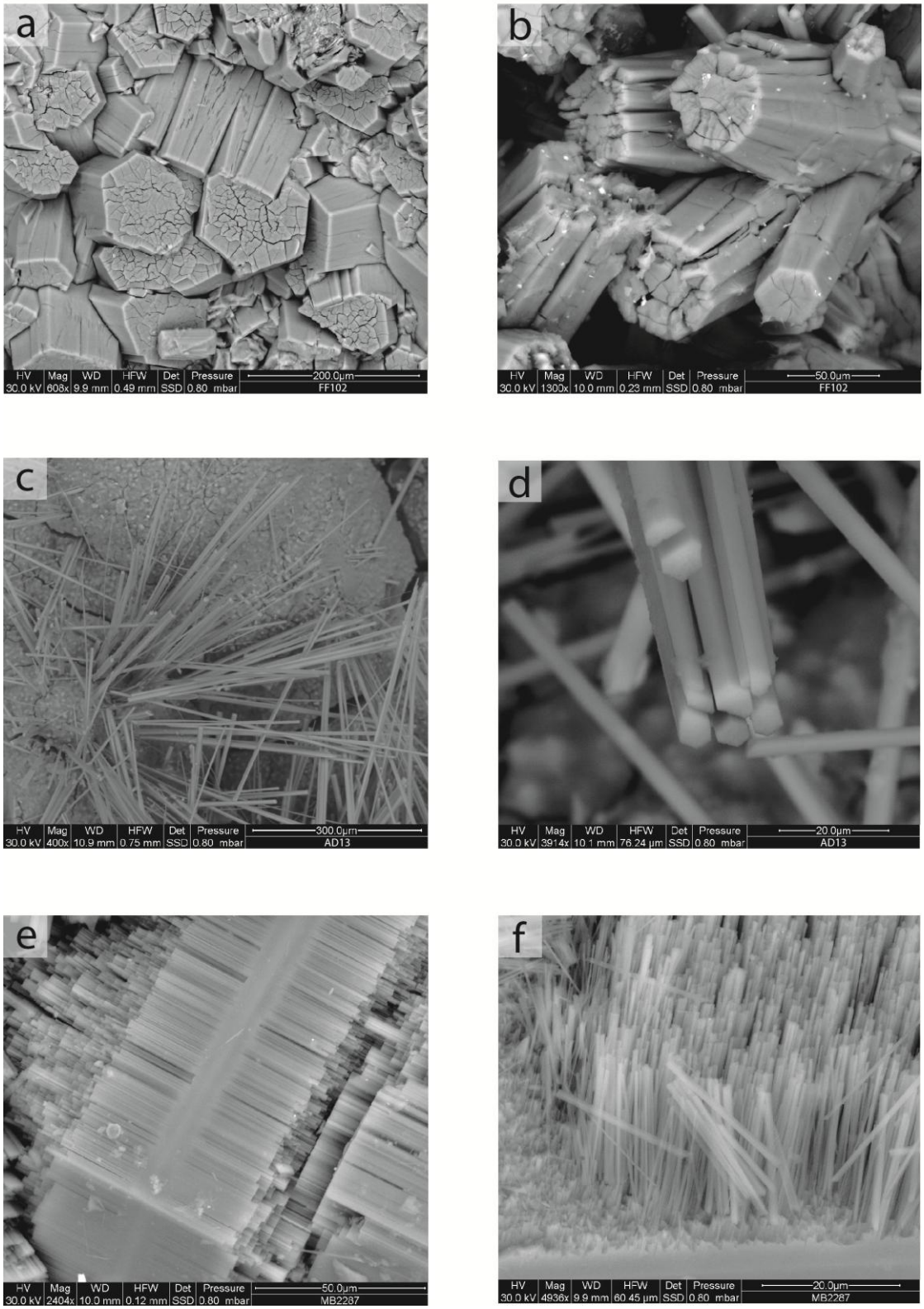

Figure 1. Representative SEM images of the studied samples. **a**) Stocky-prismatic crystals of offretite with hexagonal section (FF102). **b**) Radial aggregates of offretite prisms, characterized by evident fractures (FF102). **c**) Very elongated, acicular to fibrous offretite crystals grouped in radial aggregates with rigid to flexible behavior (AD13). **d**) Particular of the previous sample showing the thin diameter of hexagonal offretite fibrils (AD13). **e**) Offretite-chabasite-offretite sequence forming a sandwich-like morphology (MB2287). **f**) Details of the parallel growth of the extremely fibrous (asbestiform) offretite consisting of rigid to flexible thin fibres and fibrils (MB2287).

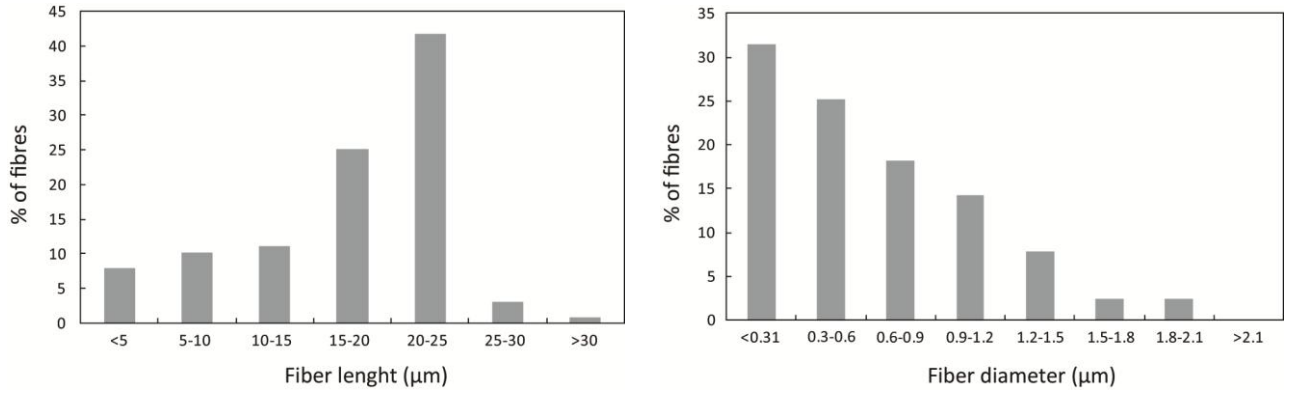

Figure 2. Size distribution of measured fibres (length and diameter) of the asbestiform MB2287 sample.

4.3.2 Mineralogical composition

To assess the mineralogical composition of FF102 sample, long exposures up to 24-h x-ray diffraction analysis was performed. The obtained XRPD pattern is illustrated in Figure 3. The collecting data clearly shows the presence of offretite and low amount of other phases as clay minerals (e.g. smectite) and pyroxene.

Due to their similar structures and unit-cell parameters, offretite and erionite have similar X-ray diffraction patterns (Gualtieri et al., 1998; Passaglia et al., 1998) and most of the Bragg peaks of the two zeolites exactly coincide. However, a few relatively strong diffraction lines due to the unit-cell doubling in erionite (namely the 101, 201, 211, 213, 311 reflections) confirm the distinction of the two species.

FF102 sample exhibits a XRPD pattern consistent with pure offretite, being absent any extra lines, in particular those at 9.1 Å, 5.3 Å and 4.2 Å ascribable to possible erionite intergrowths.

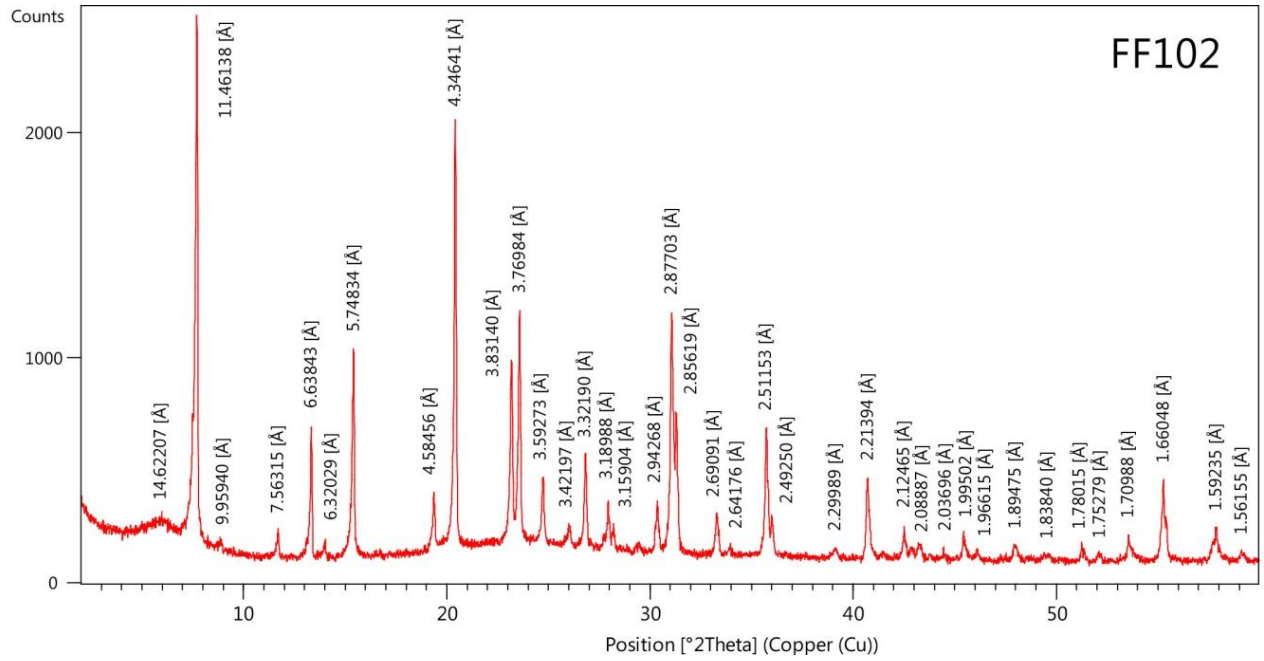

Figure 3. X-ray powder diffraction patterns produced by the FF102 sample.

4.3.3 Chemical data

The point analyses acquired on the investigated samples are highly consistent, showing a variation of major elements within 2-3%, indicating a high degree of chemical homogeneity of each sample.
The average chemical composition and relative standard deviations (σ) are reported in Table 1, whereas all the collected data are shown in Figure 4.
The average chemical composition of stocky-prismatic offretite of sample FF102 is $(K_{2.43}Mg_{1.49}Ca_{2.25})[Al_{9.92}Si_{26.08}O_{72}]$ $31.59H_2O$. The Si/(Si+Al) ratio (R) is in the range 0.71-0.74 (average 0.72), which is consistent with the interval 0.69-0.74 identified by Passaglia et al. (1998) for offretite.
The K^+ and Ca^{2+} extra-framework (EF) cations are present in comparable amount, being in the range 2.23-2.59 *apfu* and 1.73-2.56 *apfu*, respectively. The Mg^{2+} content ranges from 1.39-1.58 *apfu* and the Mg/(Ca+Na) ratio, which is considered the most significant chemical parameter for the distinction between erionite and offretite, is in the range 0.54-0.88 (average 0.68).
The prismatic to acicular offretite AD13 has an average chemical formula $(K_{2.31}Mg_{1.94}Ca_{2.19})[Al_{9.92}Si_{26.09}O_{72}]$ $31.40H_2O$. The R ratio lies in the range 0.72-0.73, in agreement with literature data.
The K^+ content (1.82-2.73 *apfu*) is similar to that of Ca^{2+} (1.82-2.41 *apfu*), but with an average value slightly higher for K^+.
Moreover, the Mg^{2+} content is also high, ranging from 1.75 to 2.22 *apfu*, while the Mg/(Ca+Na) ratio range from 0.73 to 1.22 (average 0.89).

Sample	**FF102**		**AD13**		**MB2287**	
	average *N = 7*	σ	average *N = 8*	σ	average *N = 7*	σ
SiO_2	53.27	1.42	53.06	0.30	52.29	0.42
Al_2O_3	17.18	0.91	17.07	0.33	18.59	0.38
MgO	2.04	0.11	2.65	0.25	2.98	0.20
CaO	4.28	0.57	4.17	0.36	3.68	0.22
Na_2O	-	-	-	-	-	-
K_2O	3.89	0.21	3.70	0.41	3.12	0.20
H_2O	19.34*	-	19.34*	-	19.34*	-
Total	80.66	-	80.66	-	80.66	-
Si	26.08	0.58	26.09	0.18	25.36	0.20
Al	9.92	0.58	9.92	0.18	10.64	0.20
ΣT	*36.00*	-	*36.00*	-	*36.00*	-
Mg	1.49	0.08	1.94	0.17	2.16	0.14
Ca	2.25	0.31	2.19	0.27	1.92	0.12
Na	-	-	-	-	-	-
K	2.43	0.14	2.31	0.27	1.94	0.13
H_2O	31.59	0.18	31.40	0.08	31.56	0.05
R	0.72	0.02	0.72	0.01	0.70	0.01
E%	-0.22	3.12	-6.05	3.75	5.38	3.52

Table 1. Chemical composition of the investigated offretite samples, showing the average values (*N* is the number of point analysis) and standard deviation (σ). *ΣT,* is the sum of cations in tetrahedral sites; E%, measure of charge balance: $E\% = 100*[Al–Alk_{th}]/Alk_{th}$ where $Alk_{th} = Na+K+2*(Ca+Mg)$; R, Si/(Si+Al) ratio. Crystal chemical formula calculated on the basis of 36 (Si+Al) *apfu*. *Hypothesized water content of 19.34 wt.%.

The extremely fibrous, asbestiform offretite MB2287 has an average chemical formula $(K_{1.94}Mg_{2.16}Ca_{1.92})[Al_{10.64}Si_{25.36}O_{72}]$ $31.56H_2O$. The R ratio varies from 0.70 to 0.71, an interval well within the range defined for offretite (Passaglia et al., 1998). In this sample, all EF cations K^+, Ca^{2+} and Mg^{2+} are present in comparable amounts. The K^+ content ranges from 1.82-2.12 *apfu*, while Ca^{2+} ranges from 1.78 to 2.09 *apfu*. The Mg^{2+} content is slightly higher than that of the previous samples, ranging from 1.91 to 2.40 *apfu*, and the Mg/(Ca+Na) ratio is in the range 0.91-1.27 (average 1.13).
It is interesting to notice that the analysed samples show an inverse correlation between both K and Mg and Ca and Mg content. All chemical data plot within the offretite field in the Ca(+Na)-Mg-K(+Sr+Ba) ternary compositional plot (Figure 4).

4.4 Discussion and conclusions

The main mechanisms by which an inhaled fibrous particulate induces pathological changes comprise the following factors: (a) physical features of the fibrous mineral particles such as diameter, length and aspect ratio; (b) chemical-mineralogical features (fibre type, chemical composition and surface reactivity); (c) the ability to generate reactive oxygen species (ROS); and (d) the biopersistence. These factors are also deeply interconnected: the fibre dimensions influence its surface reactivity, fibre composition controls its biopersistence and biopersistence is associated to the fibre habit.
Physical features, which influence the deposition of mineral fibres in the lung, lung clearance mechanisms, and retention time in the lung, are very important determinants of toxicity. In particular, the diameter seems to be the main factor controlling the ability of fibres to reach the lower respiratory tract, while macrophage phagocytosis is more dependent on fibre length (Fubini, 2001; Oberdörster et al., 2005). According to Lee (1985) an elongated particle is defined as "respirable" for humans when its diameter is <3.5 μm, while WHO (1986) considers as respirable the fibres with a diameter-length ratio ≥1:3, a length >5 μm, and a diameter <3 μm. Stanton

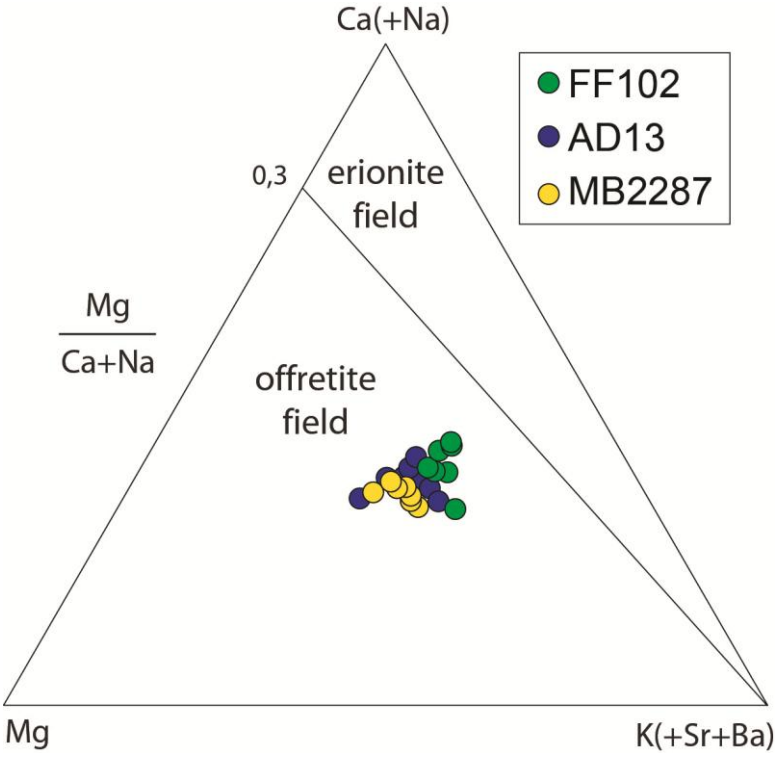

Figure 4. Ca(+Na)-Mg-K(+Sr+Ba) ternary compositional plot of the studied offretite samples, showing the distribution of extra-framework cations and the fields of erionite and offretite (from Passaglia et al., 1998).

et al. (1981) have shown that fibres ≤0.25 μm in diameter and >8 μm in length seem to be the most carcinogenic, but the majority of fibres detected in the lung and mesothelial tissues are generally <1 μm in diameter and shorter than 5 μm in length (Dodson et al., 2003; Suzuki et al., 2005; Aust et al., 2011; Mossman et al., 2011).

Consequently, small-size fibres should not be excluded from those contributing to the induction of human MM, especially in high exposure environments. This is further supported by the fact that ultrafine fibres are particularly suitable for penetration from the proximal area to the peripheral part in the lung, and for migration from the lung to the pleura and to the other sites within the human (Gatti and Rivasi, 2002; Dodson et al., 2003; Samet et al., 2006; Straif et al., 2009; Bunderson-Schelvan et al., 2011; Boulanger et al., 2014). Therefore, it is difficult to exclude fibres of a particular dimension from those producing disease within the lung or extrapulmonary sites.

In the investigated samples, the habit of offretite varies, from stocky-prismatic crystals with a solid appearance of FF102, through prismatic or acicular with rigid mechanical behavior of AD13, to extremely fibrous crystals (asbestiform) with rigid to flexible behavior of MB2287. The prismatic and acicular crystal habits occur more commonly, while asbestiform habit is relatively rare. The stocky-prismatic and prismatic crystals have diameters of ~50 μm and lengths up to 500 μm, while the acicular variety is characterized by the same lengths but very small diameters (< 1 μm).

The extremely fibrous crystals with asbestiform habit consist of fibres and fibrils with a diameter ranging from << 1 μm to about 4 μm, and a length which is in the range from ~2 to ~30 μm (average ~18 μm). In particular, ~95% of fibres are characterized by a small diameter (<1.5 μm, average 0.6 μm), and more than 30% of the measured fibres has a very small diameter (<0.3 μm, average 0.25 μm). According to WHO (1986) indications, all of these fibres may be considered as "inhalable" and they are well within the range of the "more carcinogenic fibres" in terms of diameter (Stanton et al., 1981).

The main mode observed in the erionite fibres of MB2287 is 20-25 μm and ~93% of the measured fibres are >5 μm, and therefore they may be significantly associated with carcinogenesis when breathed also in term of lengths (Stanton et al., 1981; WHO, 1986; Bernstein et al., 2005). In relation to the physical features, particular attention needs also to be paid to reliably evaluating the toxicological effects related not only to the dimension of offretite fibres, but also to their flexibility and their tendency to split, features that may significantly modify their surface area and, consequently, their reactivity (Matassa et al., 2015; Mattioli et al., 2016b).

The various offretite samples show different mechanical behavior, having an extremely fibrous with flexible to rigid appearance or forming prismatic to acicular, brittle crystals. In the mineral fibres, the flexibility might significantly transform the shape of the particles, leading to variations of both aerodynamic properties and physical particle deposition mechanisms (Lippmann et al., 1980; Donaldson et al., 2010; Hofmann, 2011).

The chemical features of the mineral fibres are also of critical importance to evaluate the pathological changes, being related to the biopersistence and biodurability of fibres in contact with cells and tissues such as the lungs. Bearing in mind that the main biological interactions or exchange processes develop at the surface of the fibres, the surface chemical composition and specific surface area are the most important elements that need to be considered.

The chemical composition of the investigated offretite samples is coherent with reference data: R ranges from 0.71 to 0.74, the EF cations K^+, Mg^{2+} and Ca^{2+} are present in all samples in comparable proportions, and Na^+, Sr^{2+}, Ba^{2+} and Fe are absent. All compositions plot within the offretite field in the ternary diagram of Figure 4. However, observing the chemical data in greater detail, it can be observed that the prismatic to acicular crystals have similar compositions, with Mg^{2+} content slightly lower than K^+ and Ca^{2+}; differently,

the asbestiform offretite crystals are characterized by a Mg^{2+} content which is slightly higher than that of the other EF cations. However, in addition to the major mineral elements, mineral fibres could contain trace elements and their content may play a role in fibre toxicity (Bloise et al., 2016).

There are both epidemiological and experimental indications that trace elements such as trace metals may provoke lung cancer (Nemery, 1990; IARC, 1993), and some researchers have claimed that asbestos fibres may play a passive role in producing diseases as carriers of trace elements (Harington et al., 1967; Dixon et al., 1970).

The present study indicates that, in some lithotypes of the Northern Italy, the zeolite offretite may crystallize with asbestiform habit, becoming potentially harmful. For the above reason, the related host-rocks should be carefully checked before their use as building or construction materials and, to this aim, the role of geoscientists is crucial in guiding safe rock extraction.

The present results suggest the needing of a detailed Italian mapping of natural sites characterized by the potential occurrence of fibrous minerals, with particular regard, a part of asbestos, to the zeolites erionite and offretite. Furthermore, these data can be used in order to assess the health risks related to the exposure to mineral fibres during human activities, such as road constructions, quarry excavations and farming that may induce disturbance in the mineral fibres-bearing rocks and trigger unplanned fibres release process.

It is relevant to note that, among the fibrous zeolites, erionite is the only one that was classified as a human carcinogen (IARC 1987), although other species should not be considered intrinsically safe (IARC 1997; Stephenson et al., 1999).

Despite of the lack of epidemiological information on populations exposed to natural asbestiform minerals other than asbestos and erionite, results acquired in the present investigation suggest that other mineral fibres of similar size, habit, and biopersistence may carry a risk for humans.

Finally, we believe the results obtained in this research could be used: (i) to identify potentially health hazardous areas in view of the presence of zeolite minerals fibres; (ii) to provide data for the compulsory Italian mapping of natural sites that are characterized by the presence of the fibrous zeolites; and (iii) to map fibrous minerals (e.g., offretite and erionite) that are classified as non-asbestos and, therefore, not regulated by law but that could be just as hazardous to human health.

Chapter 5

MORPHO-CHEMICAL CHARACTERIZATION AND SURFACE PROPERTIES OF CARCINOGENIC ZEOLITE FIBERS

5.1 Introduction

Still uncertain molecular mechanisms underlie pulmonary toxicity of solid particulates. Several steps of these mechanisms need to be understood and clarified (Guthrie and Mossman, 1993; Davis et al., 1994; Aust et al., 2011; de Assis et al., 2014). The chemical reactions implied in pathogenesis take place mainly at the solid-liquid interface. For this reason, it is of great importance to know the role of the solid surface based on the chemical nature of the surface sites responsible for the pathogenic response.

This is of paramount importance mainly in the cases of the most infamous hazardous minerals such as asbestos or crystalline silicas (Fubini, 1993; Fubini et al., 1995; Fubini, 1996; Ottaviani and Venturi, 1996; Ottaviani et al., 2001c; Oberdorster et al., 2005; Carbone and Bedrossian, 2006; Carbone et al., 2012; Baumann et al., 2013). Molecular interactions between the cells and the solid surface regulate inflammation, immune cell recruitment, and release of cytokines and oxidants, which play crucial roles in the pathogenic response (Fubini et al., 1995; Castranova et al., 1996; Kane et al., 1996; Carbone and Bedrossian, 2006; Gaudino et al., 2014).

It is generally agreed that toxicity stems from various aspects of the solid particle, namely its form (fibers are more dangerous than isometric particles), its chemical composition (iron associated with asbestos is implicated in carcinogenicity), and its biopersistence, i.e., the length of time a particle resides within a given biological compartment. Moreover, various particle-tissue interactions take place in subsequent steps, involving different surface functionalities. Therefore, overall pathogenicity may be ascribed to several physicochemical properties (Fubini et al., 1995; Fubini, 1996; Carbone and Bedrossian, 2006).

We focused our attention to fibrous zeolite minerals, specifically erionite and offretite. Erionite was discovered to be carcinogenic for the human health (Hill et al., 1990; Coffin et al., 1992; Carbone et al., 2007; Dogan, 2012; Pollastri et al., 2014; Zebedeo et al., 2014), while offretite is only suspected carcinogenic on the basis of its fibrous structure and strong mineralogical similarities.

Erionite and offretite are two natural zeolites of the ABC-6 family (Gottardi and Galli, 1985). Erionite is hexagonal with space group symmetry $P6_3/mmc$ and unit-cell parameters a = 13.19-13.34 Å, c = 15.04-15.22 Å,and has a chemical formula $Na_2K_2Ca_3[Al_{10}Si_{26}O_{72}]$ $30H_2O$ (Staples and Gard, 1959; Gualtieri et al., 1998; Passaglia et al., 1998; Cametti et al., 2013).

Three types of cages characterize this mineral: a six-membered double ring (empty), a cancrinite cage (preferred by K), and an erionite cage with dispersed Ca, Na, and Mg (Gualtieri et al., 1998). Due to its large chemical variability, erionite was elevated to group status and its member species were re-defined as erionite-Ca, erionite-Na, and erionite-K, according to the most abundant extra framework cation (Coombs et al., 1997; Dogan et al., 2008).

Offretite is hexagonal with space group symmetry $P6m2$ and unit-cell parameters a = 13.27-13.32 Å, c = 7.56-7.61 Å, and has a chemical formula of $KCaMg[Al_5Si_{13}O_{36}]\cdot 16H_2O$ (Gualtieri et al., 1998; Passaglia et al., 1998).

Four types of cages characterize this mineral: six-membered double rings (empty or at very low occupancy), cancrinite cage (preferred by K), a gmelinite cage filled with Mg surrounded by disorderd H_2O, and the wide channels whose centers are occupied by Ca-H_2O complexes (Gualtieri et al., 1998).

The framework of both minerals is composed of columns of $(Si,Al)O_4$ tetrahedra linked together to form single six-rings and double six-rings, resulting in fibrous morphologies (Gottardi and Galli, 1985; Gualtieri et al., 1998; Cametti et al., 2013). The distinction between erionite and offretite can be difficult because of their structural and chemical similarities (Gualtieri et al., 1998; Passaglia et al., 1998), and because of the possibility of intergrowth of the two species within each crystal (Tschernich, 1992; Coombs et al., 1997).

The most significant discrimination between erionite and offretite is based on the Mg/(Ca+Na) cation ratio, with offretites showing values close to 1.0 and erionites showing values less than 0.3 (Passaglia et al., 1998).

According to epidemiological data (Dogan et al., 2006; Carbone et al., 2007; Kliment et al., 2009; Metintas et al., 2010; Carbone et al., 2011; Demirer et al., 2015), erionite has been classified as carcinogenic mineral for the human health and has been referred to Class 1 by the International Agency for Research on Cancer (IARC).

Experimental studies show that erionite is 800 times more carcinogenic and may be 20-40 times more active than chrysotile and crocidolite asbestos (Hill et al., 1990; Coffin et al., 1992; Kokturk et al., 2005; Bertino et al., 2007; Zebedeo et al., 2014). Supporting studies on animals (rats) have shown that inhaled erionite fibers resulted in increased incidence of mesothelioma (Wagner et al., 1985; Davis et al., 1991; Zebedeo et al., 2014).

Growing interest in this subject produced new investigations on the health effects of erionite and its carcinogenic potential, mechanisms of carcinogenesis, and potential genetic predispositions (Dogan et al., 2006; Carbone and Yang, 2012; Hillegass et al., 2013; Ballirano et al., 2015; Pollastri et al., 2015). However, notwithstanding this, the morphology of erionite fibers have not yet been fully understood and many mineralogical and toxicological aspects are still unknown. Similarly, there is no data on the toxicity of offretite and it is unclear whether the mineralogical similarity (and/or differences) between erionite and offretite has any health implications.

In this work, we present a detailed morphological, mineralogical and physico-chemical characterization of (i) two selected samples of carcinogenic fibrous erionite, (ii) one sample of a suspected carcinogenic fibrous offretite, and (iii) one sample of non-carcinogenic fibrous scolecite.

Data from scanning electron microscopy-energy dispersive spectroscopy (SEM-EDS), X-ray powder diffraction (XRPD), electron paramagnetic resonance (EPR), and specific surface area of Brunauer-Emmett-Teller (BET; Brunauer et al., 1938) analysis were combined and integrated.

Our aim is to investigate the relationships between morphology, mineralogy, crystal chemistry, BET specific surface area, and interacting ability of these zeolites surfaces, providing a background for future experiments on the biological activity of erionite and offretite.

The analysis of the EPR spectra of selected spin probes has already demonstrated to be very useful to provide information about surface and interfacial properties of zeolites and other solids (Ottaviani et al., 2001b; Moscatelli et al., 2008; Angelov et al., 2014). In the present case, these information are precious because they may be related to the eventual carcinogenicity of the fibrous zeolites. Therefore, the scope of this study is to investigate the morphology and the chemical and surface properties of these zeolites, mainly providing information on the interacting ability of the surface at the liquid/solid interface using selected spin probes

- 4-trimethylammonium, 2,2,6,6 tetramethyl-piperidine-1oxyl Bromide (CAT1) and 4-octyl dimethylammonium, 2,2,6,6 tetramethyl -piperidine-1oxyl Bromide (CAT8) -

which well mimic specific moieties of biocompounds and have been successfully employed for investigations in surfaces and interfaces characterization studies (Ottaviani and Venturi, 1996; Ottaviani et al., 2001c; Angelov et al., 2014).

These information may help understanding the carcinogenicity of these zeolite fibers.

5.2 Experimental

The details of the investigated materials and experimental methods are reported in Supplementary material SD1, so only a brief summary is provided here. The chemical formulas of the spin probes, the variation of the pore diameter as a function of the pore area obtained from BET analysis, and computations of the EPR spectra and spectral components are reported in the Supplementary data SD2.

5.2.1 Materials

Four fibrous samples have been investigated in this study. Two samples represent erionite: GF1 is from Nevada, USA (Gude and Sheppard, 1981) and MD8 is from Karain, Turkey (Temel and Gündogdu, 1996; Dogan et al., 2008). The sample BV12 is offretite from Lessini Mountains, Italy (De Vecchi and Sedea, 1995; Mattioli et al., 2016a). The fourth sample (SC1) is scolecite from Poone, India (Gottardi and Galli, 1985). This latter is considered a non-carcinogenic fibrous mineral and has been used for comparison.
For the EPR study we used the stable piperidine- N -oxyl derivatives (nitroxides) termed CAT1 (purchased from Sigma-Aldrich and used as received) and CAT8 (donated by Dr. Xuegong Lei, Columbia University, NY, USA).

5.2.2 Methods

5.2.2.1 SEM-EDS and EPMA

Morphological observations were achieved with a Quanta FEI 200 ESEM and the microchemical characterization was performed using a JEOL 6400 SEM. The experimental conditions follow the indications reported in refs. Sweatman and Long, 1969; Goldstein et al., 1992; Reed, 1993; Pacella et al., 2015. To test the reliability of SEM-EDS results, two duplicate samples of erionite were analyzed by electron probe micro analysis (EPMA) using a Cameca SX50 equipped with a wavelength-dispersive spectrometer (WDS). The reliability of the chemical analysis was evaluated by using a charge balance error formula (E%; Passaglia, 1970; Coombs et al., 1997; Passaglia et al., 1998) and the Mg-content test (Dogan et al., 2008).

5.2.2.2 XRPD

Pure crystals was selected from each sample under a binocular microscope and were subsequently disaggregated and carefully pulverized in an agate mortar. XRPD data were collected using a Philips X'Change PW1830 powder diffractometer. Semi-quantitative XRPD analyses were performed on all samples.

5.2.2.3 Surface area-BET

To evaluate the specific surface area, the pore volume and the porosity of the various zeolite samples, Brunauer-Emmett-Teller (BET) method based on nitrogen-adsorption measurements was used (Brunauer et al., 1938). Pore size distribution was calculated using Barrett-Joyner-Halenda (BJH) method applied to the nitrogen desorption curve. Nitrogen adsorption isotherms at 77 K were recorded by means of a COULTER SA 3100 surface analyzer.

5.2.2.4 EPR

Selected pure zeolite crystals were dried and then left equilibrating with the probe solution. After filtration of the supernatant solution, the solid fibers were gently dried onto a filter paper and tested by EPR. We also analyzed the EPR spectra of both the stock solutions of CAT1 and CAT8 and the supernatant solutions after adsorption. EPR spectra were recorded by means of an EMX-Bruker spectrometer operating at X band (9.5 GHz) and interfaced with a PC (software from Bruker). The temperature was controlled with a Bruker ST3000 variable-temperature assembly cooled with liquid nitrogen.

5.2.2.5 Simulation of the EPR spectra

Simulation of the EPR line shape was performed by using Budil and Freed program (Budil et al., 1996), and the main parameters extracted from computation were: (a) A_{zz}

which measures the environmental polarity of the nitroxide group; (b) the correlation time for the rotational diffusion mobility of the probe (τ), which measures the probe-surface strength of interaction; (c) the line width which increases due to paramagnetic species close to each other; (d) the relative percentages of different spectral components due to fractions of probes distributed in the different environments.

5.3 Results and discussion

5.3.1 Morphological data

The mineral's morphology is an important factor in its potential for health impacts. From a morphological point of view, erionite and offretite have been described in terms of a variety of elongated shapes. Erionite crystals may occur individually as 'fibers', 'fibrils' and 'bundles' (Bertino et al., 2007; Dogan and Dogan, 2008; Croce et al., 2013), 'radiating clusters' and 'sprays' (Lowers et al., 2010; Cattaneo et al., 2011; Van Gosen et al., 2013). Terms that have been used in the literature to describe erionite crystal habits include 'prismatic', 'acicular' (needle like), 'needles', 'fibrous', 'rod-like', 'hair-like', and 'woolly'. The individual crystals are about 2-200 μm long and 0.1-10 μm thick. Thus, erionite is consistently elongated and fibrous, but this zeolite is not always extremely fibrous or hair-like. The two samples studied in this work were selected according to the two main morphologies described for erionite: extremely fibrous (hair-like) and acicular to fibrous. Figure 1 shows the SEM images of the investigated zeolite fibers.

In GF1 sample, erionite is characterized by an extremely fibrous habit which consists of hair-like fibers having a diameter ranging from 0.5 to 3 μm and extremely variable lengths, up to 200-300 μm (Figure 1). In this sample, erionite shows a typical 'woolly' aspect, which is identical in appearance to that at the type locality, near Durkee, Oregon (Eakle, 1898; Staples and Gard; 1959). Both of these erionites differ in appearance from all other erionites reported worldwide which are described as prismatic or acicular in habit. The longer fibers are tensile, elastic and flexible, and each fiber is composed of very thin and curled fibrils which may be as small as 10-15 nm. Fibers and fibrils are often grouped in sub-parallel or bent bundles that ravel and fray into aggregate bundles from 10 to 20 μm in diameter. This sample is representative of the extreme fibrous (hair-like) morphology for erionite crystals.

In MD8 sample, erionite is present as acicular to fibrous crystals with diameter of 2-5 μm and length up to 30 μm, generally associated in irregular to parallel growing forming bundles and shifts up to 100 μm in length and variable diameter (Figure 1). These associations show a pronounced tendency to separate individual fibrils with a diameter of the order of 0.5 μm or less. This sample represents the prismatic-type morphology for erionite, but with a great tendency to generate fibers and fibrils.

In BV12 sample, offretite is present as elongated, acicular to fibrous crystals of 10 to 20 μm in length and less than 1 μm in diameter, often grouped to constitute irregular to roughly prismatic forms of 40 to 60 μm in length (Figure 1). Locally, these prismatic forms tend to separate very small fibres and fibrils, less than 0.5 μm in diameter, with a 'rigid' behavior. This sample is representative of elongated, acicular to fibrous offretite crystal with a low tendency to generate fibers.

The SC1 sample is a scolecite constituted by prismatic, elongated crystals with diameter ranging from 0.5 mm to 30 μm, and a very variable length (Figure 1), often associated in irregular to radiating aggregates; in this case, the tendency to generate thin fibers is very low to absent.

5.3.2 Mineralogical data

To evaluate the quality of separated crystals and to exclude the presence of impurities, for each sample we performed detailed, long exposures (up to 24 hours) X-ray diffraction analyses. Experimental XRPD data collections are shown in Figure 2.

A careful scrutiny of the diffraction patterns confirmed the absence of any detectable crys-

talline impurity, within the limits of the diffractometer sensitivity (ca. 0.1 wt%). GF1 and MD8 samples show nearly identical patterns corresponding to pure erionite. However, a significant variation of the relative intensities of some peaks is evident between the two samples (Figure 2).

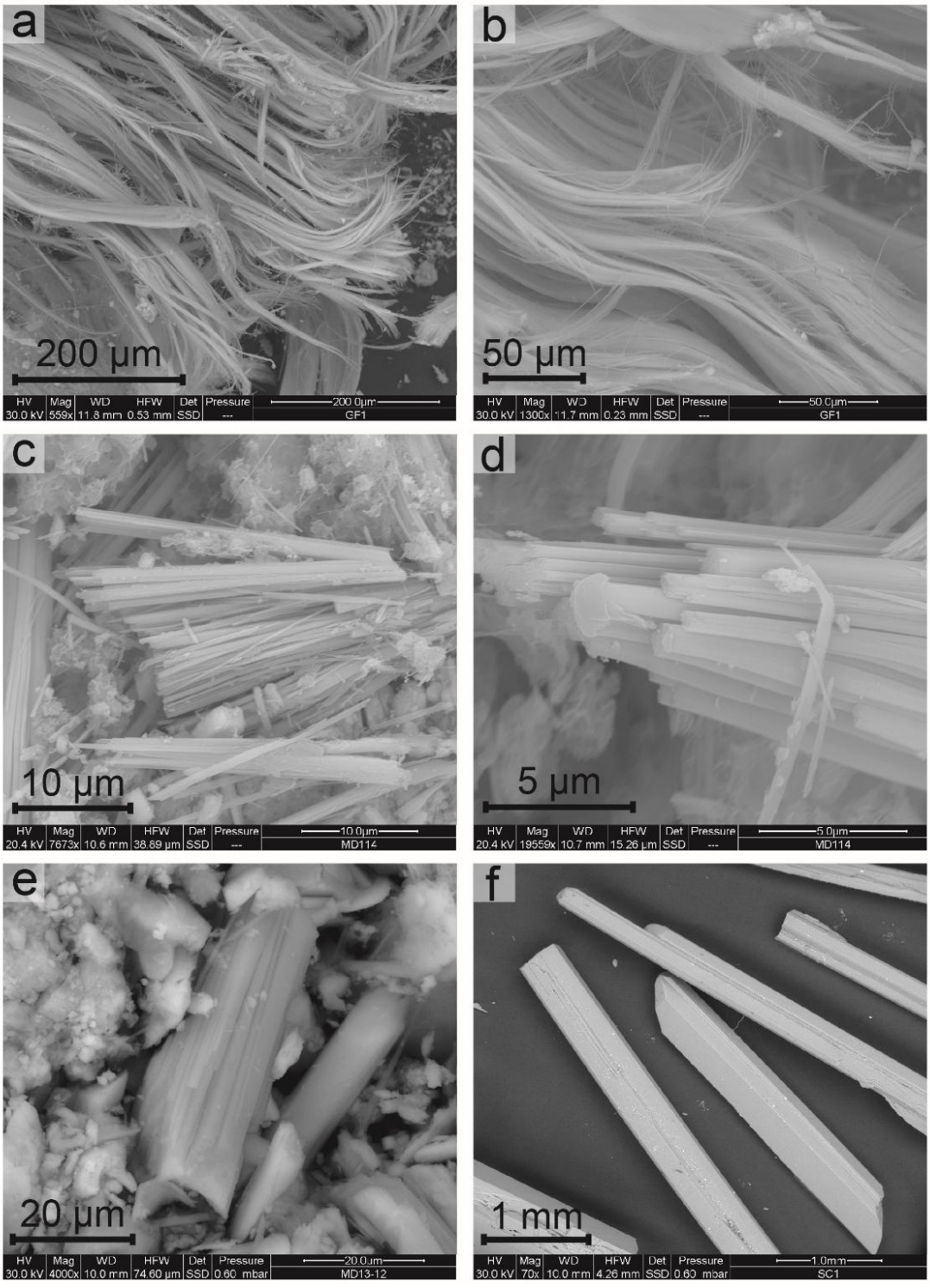

Figure 1. SEM images of the investigated zeolite fibers; (a) and (b) erionite with an extremely fibrous, hair-like habit (GF1); (c) and (d) acicular to fibrous erionite crystals (MD8); (e) acicular to fibrous offretite crystals, often grouped in roughly prismatic forms (BV12); (f) prismatic, elongated crystals of scolecite (SC1).

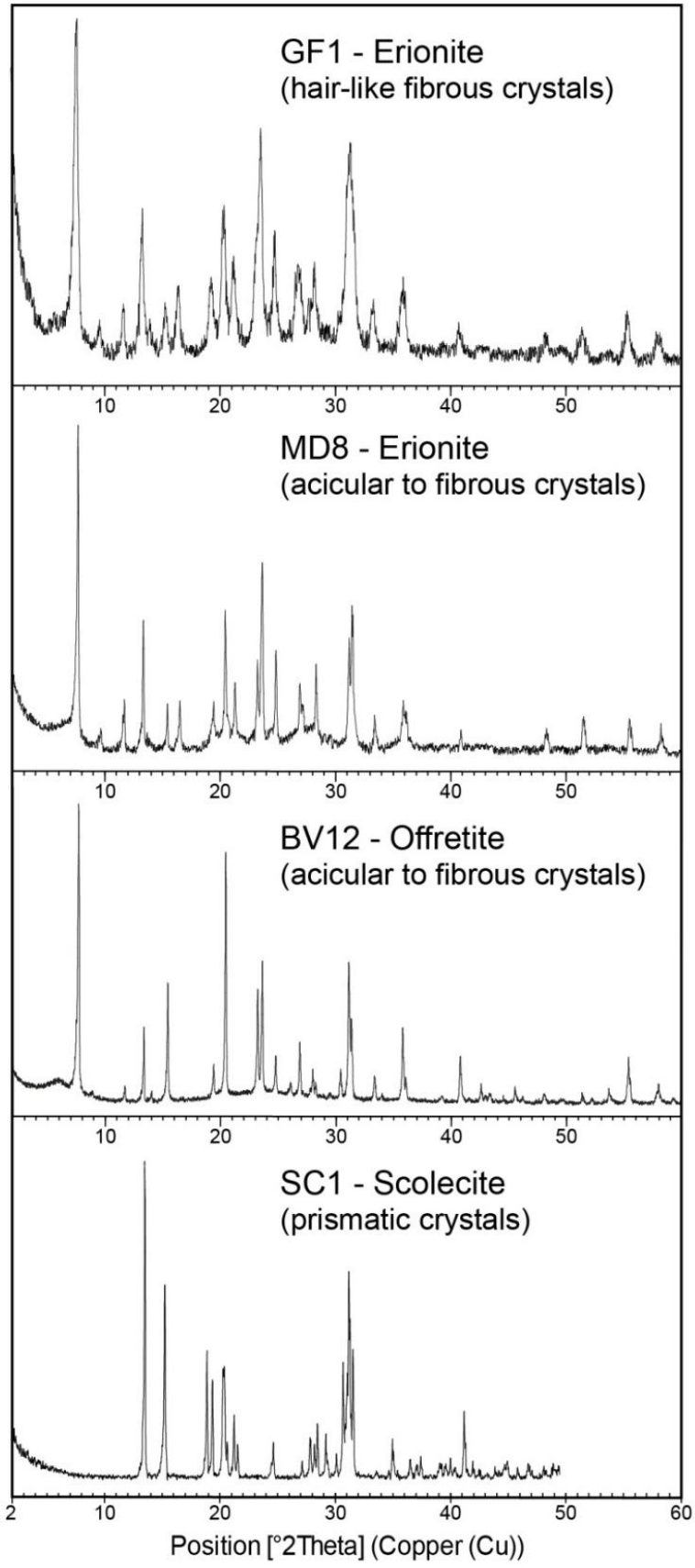

Figure 2. XRPD patterns of the investigated zeolite fibers.

This is probably due to variable amounts of Ca(II), Na(I) and Mg(II) cations which are distributed on four distinct cation sites in the erionite cage (Gualtieri et al., 1998; Passaglia et al., 1998; Ballirano et al., 2009; Cametti et al., 2013). Notably, it has been demonstrated that the ion exchange properties of erionite may play a primary role in its toxicity (Cametti et al., 2013).

Erionite and offretite have similar X-ray diffraction patterns, due to their similar structures and unit-cell parameters (Gualtieri et al., 1998; Passaglia et al., 1998). Most of the Bragg peaks of the two zeolites exactly coincide in their diffraction patterns. However, a few relatively strong diffraction lines due to the unit-cell doubling in erionite (namely the 101, 201, 211, 213, 311 reflections) confirm the distinction of the two species.

BV12 sample exhibits a XRPD pattern consistent with pure offretite, being absent any extra lines, in particular those at 9.1 Å, 5.3 Å and 4.2 Å ascribable to possible erionite intergrowths. The very low-baseline suggests high crystallinity for BV12 sample. XRPD analysis on the SC1 sample shows all typical diffraction peaks of pure, highly crystalline scolecite, all of which were indexed to a monoclinic cell.

5.3.3 Chemical data

The obtained average chemical compositions from the investigated zeolites are reported in Table 1, whereas all the collected data are shown in Figure 3.

Sample	**GF1**		**MD8**		**BV12**		**SC1**	
	average	σ	average	σ	average	σ	average	σ
	N = 12		*N = 13*		*N = 12*		*N = 4*	
SiO_2	58.47	0.35	56.66	0.32	58.49	1.00	48.15	0.06
Al_2O_3	14.30	0.21	13.63	0.27	13.43	0.37	26.28	0.03
Fe_2O_3	0.13	0.05	0.07	0.04	0.78	0.21	-	-
MgO	0.48	0.12	0.22	0.35	2.33	0.37	-	-
CaO	3.35	0.23	1.85	0.10	2.27	0.40	11.80	0.09
Na_2O	0.80	0.10	2.48	0.16	-	-	-	-
K_2O	4.17	0.29	5.49	0.45	3.35	0.30	-	-
H_2O	18.46	0.45	19.60	0.42	19.34	0.00	13.67	0.00
Total*	81.54	0.45	80.40	0.42	80.66	0.00	86.23	0.00
apfu on the basis of 72 oxygen atoms								
Si	28.05	0.10	28.00	0.15	28.14	0.35	22.31	0.02
Al	8.08	0.12	7.94	0.15	7.61	0.20	14.35	0.01
Fe^{2+}	0.05	0.02	0.03	0.01	0.28	0.08	-	-
ΣT	*36.18*	*0.09*	*35.96*	*0.18*	*36.04*	*0.20*	*36.66*	*0.03*
Mg	0.35	0.09	0.16	0.26	1.67	0.27	-	-
Ca	1.72	0.12	0.98	0.05	1.17	0.22	5.86	0.05
Na	0.74	0.10	2.38	0.15	-	-	-	-
K	2.55	0.18	3.46	0.30	2.06	0.19	-	-
Σef	*5.36*	*0.23*	*6.98*	*0.43*	*4.90*	*0.67*	*5.86*	*0.06*
H_2O	29.54	0.77	32.31	0.81	31.03	0.18	21.12	0.01
E%	7.04	4.19	2.48	3.86	7.49	1.39		

Table 1. Chemical composition of the investigated zeolite fibers. Crystal chemical formula calculated on the basis of 36 ($Si+Al+Fe^{3+}$) apfu; Total* excludes water content. N, number of points; σ, standard deviation; *ΣT,* sum of cations in tetrahedral sites; *Σef,* sum of cations in extra-framework sites; E%, measure of charge balance: $E\% = 100*[(Al+Fe^{3+})–Alk_{th}]/Alk_{th}$ where $Alk_{th} = Na+K+2*(Ca+Mg)$.

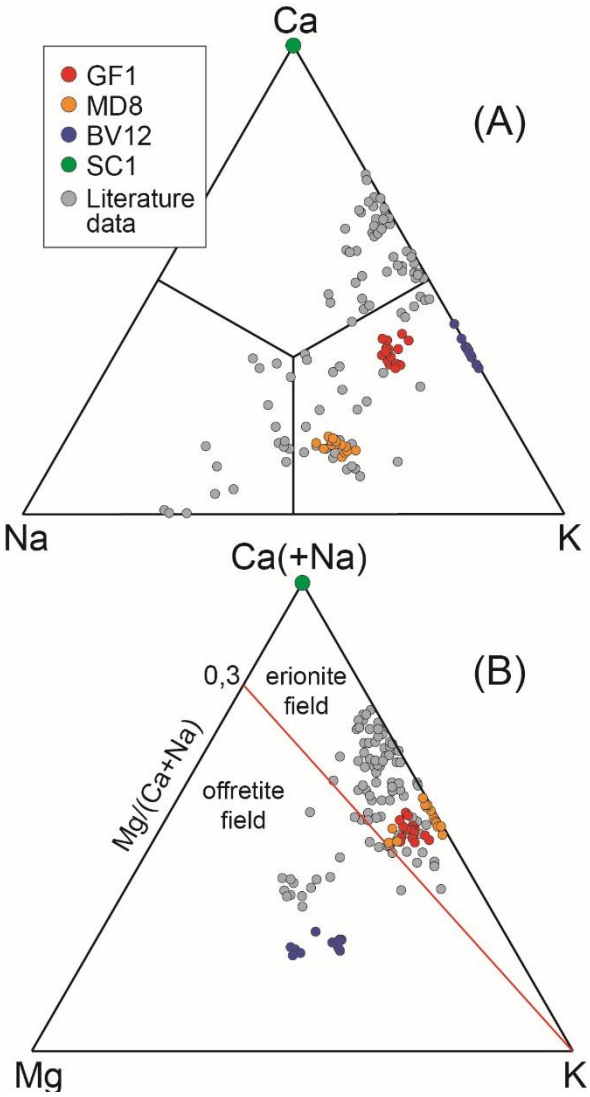

Figure 3. Ca-Na-K and Ca(+Na)-Mg-K ternary compositional plots of the studied zeolite fibers, showing the distribution of extra-framework cations.

The average chemical composition of extremely fibrous, hair-like erionite from GF1 sample is $(K_{2.56}Ca_{1.72}Na_{0.74}Mg_{0.35})[Al_{8.08}Si_{28.05}O_{72}]\cdot 29.54H_2O$ which is classified as erionite-K.
The Si/(Si+Al) ratio is in the range 0.77-0.78, which is slightly higher with respect to the literature interval for the erionite from volcanic rocks (Passaglia et al., 1998; Ballirano et al., 2009) but is identical to that found in the erionite from Durkee, Oregon, USA (Passaglia et al., 1998).
K^+ is the dominant extra-framework cation in the structure (2.3-2.87 apfu), whereas Ca^{2+} and Na^+ contents are generally low (1.6-2.01 and 0.54-0.87 apfu, respectively). The Mg^{2+} content is very low (0.21-0.53 apfu) and the Mg/(Ca+Na) ratio, which is considered to be the most significant parameter for the distinction between offretite and erionite, is in the range 0.09-0.2. Notwithstanding Fe^{3+} is not present in the ideal chemical formula, a small amount of Fe^{3+} is detected in the GF1 sample (0.03-0.08 apfu).
The average composition of acicular to fibrous erionite from MD8 sample is $(K_{3.46}Na_{2.38}Ca_{0.98}Mg_{0.16})[Al_{7.94}Si_{28}O_{72}]\cdot 32.31H_2O$, with a Si/(Si+Al) ratio in the range 0.77-0.79. Even in this type of erionite the dominant extra-framework cation is K^+ (3.06-4.11 apfu), and, as a result, it can be classified as erionite-K, with Na^+ (2.16-2.75 apfu) and Ca^{2+} (0.88-1.07 apfu) as minor cations. The Mg^{2+} content is generally low (average 0.16

apfu), although in some cases it reaches 0.74 apfu. The Mg/(Ca+Na) ratio is in the range 0.01-0.22. The Fe^{3+} content is very low, ranging from 0.01 to 0.05 apfu. Acicular to fibrous offretite from BV12 sample has an average composition $(K_{2.06}Mg_{1.67}Ca_{1.17})[Al_{7.61}Si_{28.14}O_{72}]\cdot 31.03H_2O$, with a Si/(Si+Al) ratio ranging from 0.78 to 0.79. All of the extra-framework sites are occupied by K^+ (1.78-2.21 apfu) and Ca^{2+} (1.01-1.49 apfu), whereas Na^+ is always absent. The Mg^{2+} content is high (1.41-1.93 apfu) and the Mg/(Ca+Na) ratio varies from 1.29 to 1.86, falling within the offretite field (Figure 3). Differently from erionite, offretite sample shows a high Fe content which varies from 0.22 to 0.4 apfu.

Prismatic scolecite from SC1 sample has the average formula $Ca_{5.86}[Al_{14.35}Si_{22.31}O_{80}]\cdot 21.12H_2O$. The only extra-framework cation is Ca^{2+} and scolecite data occur at the Ca-rich corner of the cation distribution ternary diagram. The Si/(Si+Al) ratio for the studied scolecite is ~0.61, which is in the range of literature data (Passaglia and Sheppard, 2001).

5.3.4 Specific surface area analysis

The BET analysis on the basis of the nitrogen-adsorption/desorption isotherms allowed us to evaluate the specific surface area, the total pore volume, and the preferential porosity for each zeolite used in this work. These data (accuracy 2-3%) are reported in Table 2.

We reported the values which were reproducible at least in three different measurements on the same sample in the same experimental conditions. From these data we observed that the specific surface area and the total pore volume decrease in the series GF1 > MD8 > BV12 > SC1 but the surface areas were indeed much smaller than expected for zeolite samples and reported in some studies (Aguilar-Armenta and Patiño-Iglesias, 2002; Mertens et al., 2009; Ballirano et al., 2015). However, other studies report surface area values for similar zeolite samples in line with the data obtained in the present study (Aguilar-Armenta and Patiño-Iglesias, 2002; Pollastri et al., 2014).

Sample	Area* (m^2/g)	Total pore volume (mL/g)	Pore diameter (nm)	Pore volume (%)
GF1	22.3	0.140	<6 6-20 20-80 >80	0.7 30 58.3 11
MD8	15.4	0.064	<6 6-20 20-80 >80	9 29 41 21
BV12	9.92	0.022	<6 6-20 20-80 >80	19 22 38 21
SC1	1.5	0.007	<6 6-20 20-80 >80	5 16 36 43

Table 2. Surface area, total pore volume, and preferential porosity (pore volume for different pore diameter ranges) of the investigated zeolite fibers. *Due to data variability caused by possible fiber aggregation and experimental variables, we reported the values which were reproducible at least in three different measurements on the same sample in the same experimental conditions used for the EPR analysis.

On the basis of the EPR results (see below), these differences may arise from fiber aggregation. But other experimental variables could influence the final results. The fact that there are only few scattered data on different erionite samples does not permit to clarify the reasons of the surface area variability.
The differences in surface area in Table 2 indicate a larger availability of surface sites for the adsorption for GF1, while SC1 shows the lowest one. However, the distributions of the pore volume and pore diameter show interesting variations: small porosities (pore diameter < 6 nm) are increasingly present from GF1 to MD8 and BV12, but for SC1 the amount of such small pores is relatively low, while macropores with pore diameter > 80 nm are prevailing. From the variation of the pore diameter as a function of the pore area (Figure S2 in SD2), GF1 mostly shows mesoporous porosities and the average pore size diminishes for MD8 and more for BV12, while SC1 is poorly porous and shows a spreading out of pore sizes. Here we have to underline that the pore diameter above 1-2 nm (which is the maximum diameter size of natural zeolites) indicates the size of the channels which are formed in the aggregates and nanostructures mainly promoted by the fibrous nature of these zeolites. The probes in solution may enter in these interconnected channels of the fibers aggregates to give interactions with the solid surface. In this respect the different distributions of pore volume and diameter may modulate the adsorption behavior at the liquid/solid interface.

5.3.5 EPR analysis

CAT1 and CAT8 (Figure S1 in SD2) are good spin probes to characterize the interacting ability of the zeolite fibers towards differently polar species since they possess an EPR spectrum extremely sensitive to the surrounding medium (Ottaviani and Venturi, 1996; Ottaviani et al., 2001c; Angelov et al., 2014). Indeed, the positively charged CAT group may interact with both the charged (Si-O^- and Al-O^- sites) and the polar (Si-OH) surface groups. However, CAT8 also bears a C8 hydrophobic chain, and therefore, it is able to monitor the presence of low polar sites (mainly Si-O-Si sites). Variations of pH may modify the adsorption capacity. Since we wanted to analyze the probe-surface interactions, we remained at the natural pH (about 5) of the systems.
After the external drying of the filtered fibers on a filter paper, micropools of probe solutions were trapped into the porosities, mainly those formed by fiber aggregation. The EPR spectra of these probes provided information about the interactions at the liquid/solid interfaces.
Figure 4 shows the EPR spectra recorded for CAT1 (A) and CAT8 (B) adsorbed onto the different zeolites. As a reference, the spectra of the radicals in water are also reported which are constituted by three narrow lines as expected for free moving radicals in solution. This signal, henceforth termed "free", is also present in the spectra in Figure 4, due to micro-pools of solution trapped into the pores formed by fiber aggregates. A second spectral component, less resolved, is due to probes interacting with the surface and henceforth termed "interacting" component. The computations of the different components, extracted from a subtraction procedure among the experimental spectra, are shown in Figure S3 (SD2). These computations provided the Azz, τ, and line widths parameters, and the percentages of free and interacting components reported in Table 3.
The parameters of the "free" signal in Table 3 are consistent with fast moving radicals in a polar medium, while the parameters of the interacting component (mainly the high τ values) indicate a slowing down of mobility as expected for the radicals interacting with the polar-charged surface groups.
The parameters of both the free and the interacting component changed from one to another sample. It is interesting to discuss these variations of parameters for each zeolite together with the amount of adsorbed species, reported in Table 4, which was calculated (in percentage) by evaluating the intensity decrease of the EPR spectra from the unadsorbed solution (no solid) to the supernatant solution after equilibration of the radical

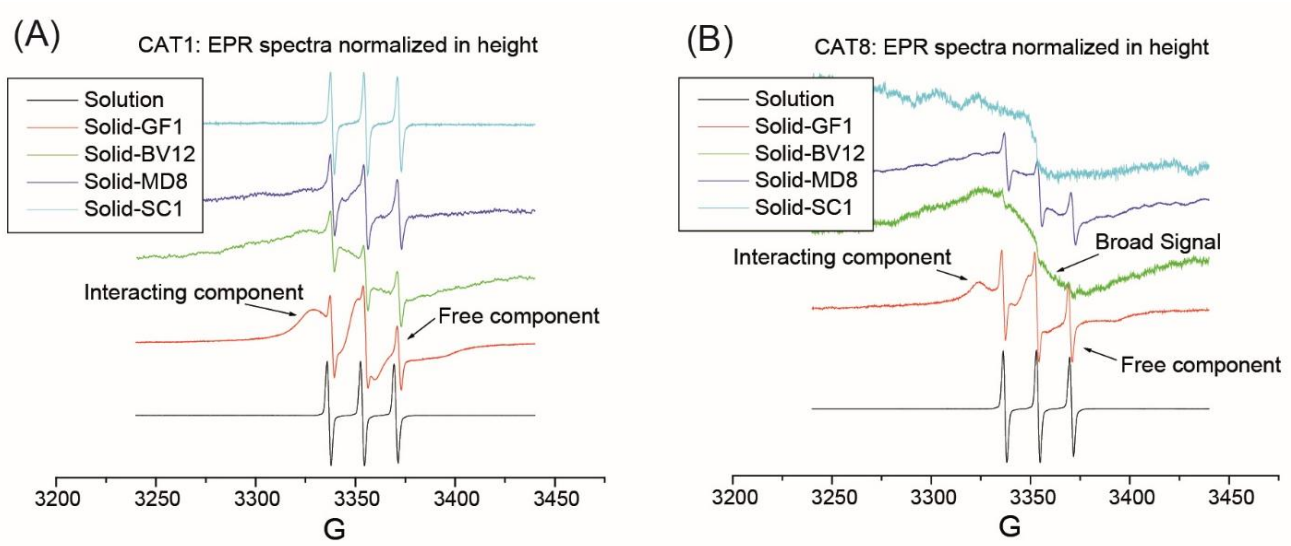

Figure 4. EPR spectra recorded for CAT1 (A) and CAT8 (B) adsorbed onto the different zeolite fibers. The spectra of the radicals in water are also reported.

(A)

Sample CAT1	% Free	A_{zz} (G)	τ (ns)	Line width (G)	% Inter-acting	A_{zz} (G)	τ (ns)	Line width (G)
Solution	100	37.85	0.017	1.35	0	(-)	(-)	(-)
GF1	18	37.83	0.035	1.45	82	37.8	5.5	5.4
MD8	25	37.83	0.035	1.45	45	37.8	50	25
					30	37.8	3.3	7
BV12	15	37.83	0.035	1.45	85	37.8	0.7	28
SC1	100	37.80	0.028	1.36	0	(-)	(-)	(-)

(-) Values cannot be measured because the component is absent or too weak

(B)

Sample CAT8	% Free	A_{zz} (G)	τ (ns)	Line width (G)	% Interac-ting	A_{zz} (G)	τ (ns)	Line width (G)
Solution	100	37.8	0.035	1.3	0	(-)	(-)	(-)
GF1	30	37.83	0.1	1.5	70	37.9	10	6
MD8	15	37.85	0.037	1.3	85	37.9	10	21
BV12	5	(-)	(-)	(-)	95	37.9	10	21
SC1	0	(-)	(-)	(-)	100	37.8	23	13

(-) Values cannot be measured because the component is absent or too weak

Table 3. Main parameters extracted from the computation of the EPR spectra of CAT1 (A) and CAT8 (B) adsorbed onto the zeolites.

Zeolite	Adsorbed % - CAT1	Adsorbed % - CAT8
GF1	54	99.5
MD8	49.5	84.5
BV12	43.5	96
SC1	1.5	0.5

Table 4. Adsorbed % (accuracy ± 0.5 %) evaluated from the intensity decrease from the unadsorbed probe solution to the supernatant solution after adsorption.

solution with the solid (Ottaviani et al., 2010). To correctly assess the adsorbed percentages, we repeated the EPR measurements on the unadsorbed and supernatant solutions 5 times for each sample in the same experimental conditions (using a flat cell fixed in the EPR cavity). It was found that these parameters were reproducible with a high accuracy (± 0.5 %, see Table 4).

In summary, the results from Tables 3 and 4 are discussed as follows:

- In the unadsorbed solutions, CAT8 is less mobile (higher τ) than CAT1, due to the effect of the chain attached to the CAT group in CAT8. However, the mobility of the free radicals decreases from the unadsorbed to the adsorbed solutions (the micro-pools into the inter-fibers porosities). This happens because the rheological properties of the solution at the solid interface are affected by the surface potential and bulk conditions cannot be attained.

- For CAT1 onto SC1, the adsorbed percentage is very low, in agreement with a low available surface area, and correspondingly, no interacting component is recognizable for the adsorbed solution. Furthermore, this free component is somewhat less "free" and less polar than the unadsorbed solution showing that the small amount of adsorbed solution remains trapped into particle clusters, but poorly interacting with the solid surface, mainly affected by medium-polar interacting sites. In line with this finding, CAT8 onto SC1 also shows an almost negligible adsorbed percentage, but, in this case, only the "interacting" component was found, showing a decreased mobility and a broadened line width, which usually occur when the radicals are interacting in close sites. The difference between CAT1 and CAT8 adsorptions into SC1 indicates that the radical chain plays a significant role, favouring the interaction with the surface, which contains less polar sites. Therefore, these chains tend to self-aggregate at the surface itself.

- A significantly different behavior if compared to SC1 was revealed by GF1: as it is evident from Table 4, the adsorbed percentages of both CAT1 and CAT8 (mainly CAT8) onto GF1 were higher than measured for the other zeolites. However, less CAT1 than CAT8 radicals were adsorbed onto GF1, but CAT1 was mainly interacting with the surface at quite distributed sites (relatively small line broadening) and with a medium-strength bonding (τ=5.5 ns), which suggests ion-dipole bonds. On the other side, the free CAT8 probes into the GF1 inter-particle porosities show a more significant decrease in mobility if compared to CAT1. It is interesting that a large fraction (70 %) of the adsorbed CAT8 radicals are strongly bonded at the GF1 surface, where the interacting sites are well distributed (not at close distances), while the other fraction (30 %) of radicals remains in micro-drops of solution trapped into the pores of GF1-fiber aggregates.

- The percentages of CAT1 and CAT8 radicals adsorbed onto MD8 (Table 4) are smaller than those onto GF1, which is in agreement with a smaller available surface for MD8. 75 % of CAT1 probes are interacting with the MD8 surface; among them, 45% show a strong motion hindering due to interactions at close positions in a restricted space, while the remaining 30% were distributed at weakly interacting sites. For CAT8 adsorbed at MD8 surface, the relative percentage of free component is smaller than for GF1 (Table 3). The interacting component has the same mobility and polarity conditions as the interacting component onto GF1, but the line width is much higher for MD8 than for GF1. This indicates that the interacting sites for CAT8 at the MD8 surface are close to each other, as already revealed by CAT1 adsorbed onto MD8.

- In respect to CAT1 adsorption, BV12 shows a decreased adsorbed percentage (Table 4) if compared to MD8 as expected for a smaller available surface area (Table 2). Also the percentage of free probes (Table 3) is smaller but almost comparable with their percentage in GF1. The most interesting information is that the interacting ability of BV12 surface sites is much lower than that found for MD8 and GF1. This is evidenced by the small τ value of the interacting component for BV12 (τ = 0.7 ns). The corresponding in-

crease in line width may be related to trapping in small pores created by fibers aggregation. The adsorption of CAT8 onto BV12 is comparable to that described for MD8, but the adsorbed percentage and the relative amount of interacting component are higher for BV12. BV12 has a lower surface area available for the adsorption, but the radical solution is easily trapped into the interstices among the fibers. This effect mainly holds for CAT8 due to self-aggregation of the radicals into these small porosities.
These results demonstrate that the adsorption behavior of the offretite sample BV12 differ from that of the erionite samples, but BV12 and MD8 show interesting similarities, while GF1 shows a significantly different adsorption mode suggesting that the hair-like structure favours a more homogeneous site distribution intercalating more and less hydrophilic sites. The non-fibrous and non-carcinogenic SC1 shows a reduced interacting ability if compared to the fibrous-carcinogenic or suspected carcinogenic zeolites.

5.4 Conclusions

The combined approach consisting of morphological, mineralogical, chemical, and surface characterization of the four zeolites termed GF1, MD8, BV12, and SC1, coupled with reactivity studies by means of spin probes proved to be very helpful to shed new light on the surface properties and interacting ability of these materials which are very likely related to their eventual carcinogenicity.
First, we obtained a detailed view of the morphology, chemical compositions and surface characterization (BET) of representative samples of erionite and offretite fibers. In summary, the chemical, morphological and BET characterization indicated an extremely fibrous, hair-like structure for the carcinogenic erionite-K GF1, which is rich in K^+ and Ca^{2+}, and characterized by a relatively high surface area. The MD8 sample, compared to GF1, is less rich in Ca^{2+}, and less homogeneous in structure since it is characterized by well-developed, acicular to fibrous erionite-K crystals. It also has a lower surface area than GF1. The offretite BV12 sample shows a further decrease in surface area if compared to the erionite samples, but the number of its small pores (interstices among fibers aggregates) increases at the expense of the large ones. However, BV12 and MD8 are quite similar in structure, being the former constituted by elongated fibers often grouped in roughly prismatic forms. Chemically speaking, the offretite is characterized by a relatively high amount of Mg^{2+}, but also MD8 shows some Mg-rich zones which are absent in GF1. The zeolite sample SC1 is almost non fibrous and its surface area is the smallest. It is characterized by large pores, that is, open windows in the zeolite-fibers aggregates, and Ca^{2+}. Therefore, it shows significantly different chemical and morphological properties with respect to the erionite and offretite fibrous zeolites.
Useful information about the interacting ability of the different zeolites were obtained by means of the EPR study using CAT1 and CAT8 as spin probes. These information were related to the morphology and BET characterization of the zeolites. We graphically summarize in Figure 5 the EPR results about the adsorption mechanism of the spin probes onto the four different zeolites.
In detail, GF1 surface binds the positively charged CAT group at polar/charged interacting sites which are well distributed, intercalated by less polar sites (Si-O-Si) which are interacting with the hydrophobic part of the probes. MD8 surface is less homogeneous and the polar/charged sites are closer to each other than in case of GF1. This provokes a stronger binding, but also some spin-spin interactions between the nitroxide groups in close positions. The interacting ability of offretite BV12 surface is much lower than that found for the erionite samples, mainly GF1: the probes interacting with BV12 are mainly trapped in small pores created in the fibers aggregates and spin-spin interactions are favoured. However, the interacting ability of BV12 is much higher than that of SC1. For this non-fibrous and non-carcinogenic zeolite, the adsorption is poor and the few adsorbed CAT1 radicals are free while CAT8 radicals self-aggregate and poorly interact.

These results help to clarify the surface interacting properties of the erionite and offretite fibrous zeolites which may be related to the eventual carcinogenicity of these zeolite fibers.

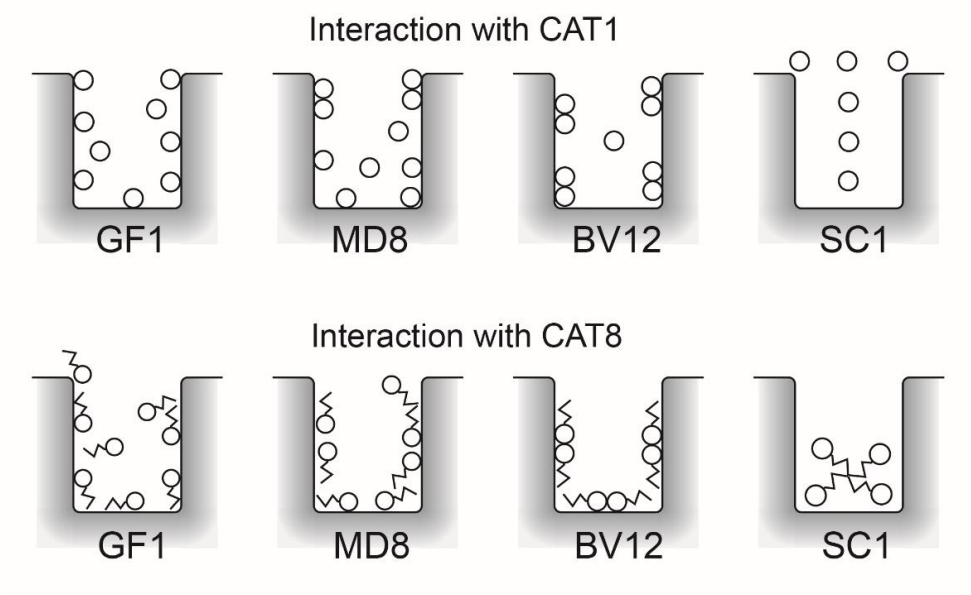

Figure 5. Graphical summary of the interaction modes of CAT1 and CAT8 onto the zeolite surface, as obtained from the EPR analysis.

Chapter 6

EPR AND TEM STUDY OF THE INTERACTIONS BETWEEN ASBESTIFORM ZEOLITE FIBERS AND MODEL MEMBRANES

6.1 Introduction

Solid particles are well known to be toxic to humans and animals in function of their morphologic and physico-chemical properties, as such as their fibrous structure which favors the cell membrane penetration, and the presence of functionalities which are able to capture pollutants and interact with the bioenvironment thus increasing biopersistence (Aust et al., 2011; Carbone et al., 2012; Davis and Jaurand, 1994; Fubini, 1993; 1996; Fubini et al., 1995; Guthrie et al., 1993; Hochella, 1993).

One of the most important factors that define the dangerousness of a fibrous particulate is its breathability, which depends on the size (i.e. lengths, diameters and relative ratio) and the aerodynamic equivalent diameter (e.g. Stanton et al., 1981; Dodson et al., 2003; Oberdörster et al., 2005; Aust et al., 2011; Boulanger et al., 2014). The fibres biopersistence is another important factor for their toxicity and carcinogenicity (Hesterberg et al., 1998; Fubini, 1996; Maxim et al., 2006) and it is also related to their chemical composition, with some elements potentially playing a key role to determine the carcinogenicity such as iron (Fubini, 1993; Gazzano et al., 2005; Ballirano et al., 2015) or specific trace elements (As, Be, Pb, REEs; Bloise et al., 2016). Other features such as structure, net charge, microtopography and porosity increase the specific surface area and the interacting capability, therefore acting as important factors in fibre-induced toxicity and carcinogenicity (e.g. Hochella, 1993; Oberdörster et al., 2005; Mattioli et al., 2016b). Nevertheless, several aspects of the molecular mechanisms which underlie pulmonary toxicity of solid particulates are still uncertain and need to be understood and clarified (Baumann et al., 2013; Davis and Jaurand, 1994; Guthrie et al., 1993; Metintas et al., 2010). The pathogenesis is constituted by several chemical steps which take place mainly at the solid-liquid interface and depend on the chemical nature of the surface sites responsible for the pathogenic response. This mainly holds for the most disreputable hazardous minerals such as crystalline silicas or asbestos (Davis and Jaurand, 1994; Fubini, 1993; 1996; Fubini et al., 1995; Guthrie et al., 1993; Hochella, 1993; Ottaviani et al., 1996; 1997; 2001). A crucial step of the pathogenic mechanism involves the molecular interactions between the cells and the solid surface which regulate inflammation, release of cytokines and oxidants, and immune cell recruitment (Barrett et al., 1999; Becher et al., 2001; Bertino et al., 2007; de Assis et al., 2014; Gaudino et al., 2014; Hillegass et al., 2013; Johnston et al., 2000; Kane et al., 1996; Liu et al., 2000; Olbruck et al., 1998; Ovrevik et al., 2004; 2006; Scapoli et al., 2004; Schins et al., 2002; Zanella et al., 1996; 1999). Therefore, it is of great importance to clarify the interactions occurring between the cell membrane and the toxic fibers.

Actually, the interaction between asbestiform fibers and biological membrane is thought to be carried out by at least two different mechanisms which cannot be excluded one from the other. Firstly a receptor mediated interaction, followed by the fiber ingestion through an endocytic process (Nagai et al., 2012). Secondly by a passive interaction through which the fiber pierces the membrane and accesses the cell cytoplasm and the nuclear compartment, independently of the cell participation (Andolfi et al., 2013). Distinguish these two possibilities (or demonstrating that both of them are working) is a very important goal which could allow to find new therapeutic approaches for preventing diseases in exposed patients. Very recently (Mattioli et al., 2016b), we have described the morphologic and surface properties of natural fibrous zeo-

lites of the ABC-6 family (Cametti et al., 2013; Gottardi and Galli, 1985) termed erionite and offretite, which were demonstrated or suspected to be carcinogenic, respectively (Dogan, 2012; Pollastri et al., 2014; Zebedeo et al., 2014). Mainly, epidemiological data demonstrated the carcinogenicity of erionite (Carbone et al., 2007; 2011; Kliment et al., 2009; Metintas et al., 2010), which has been referred to Class-I by the International Agency for Research on Cancer (IARC). Severe problems of mesothelioma arising from the carcinogenicity of erionite were found in Turkish villages, like in Cappadocia, but also in North America, as such as in North Dakota (ND) and in Nevada, where recent findings have reported human exposure to erionite and possibly an increase of mesotheliomas in young individuals (Carbone et al., 2007; 2011; Kliment et al., 2009; Metintas et al., 2010). Concentrations of erionite in school buses in ND were as high as in the Turkish villages. Erionite was found to be 800 times more carcinogenic and about 20-40 times more toxic than chrysotile and crocidolite asbestos (Coffin et al., 1992; Hill et al., 1990). More recently, further details about the carcinogenicity of erionite were discovered (Ballirano and Cametti, 2015; Ballirano and Pacella, 2015; Ballirano et al., 2015; Bloise et al., 2016; Carbone and Yang, 2012; Croce et al., 2015; Demirer et al., 2015; Giordani et al., 2016; Pollastri et al., 2015), but several aspects about the pathological mechanism involving the interactions at a molecular level are still unknown. Furthermore, offretite has close structural and chemical similarities with erionite, but its pulmonary toxicity still needs to be demonstrated and clarified.

In the previous study from our group, two erionite fibers, named GF1 and MD8, and a third type of fiber belonging to the offretite mineral species, named BV12, were used (Mattioli et al., 2016b). For comparison, we also analysed a different zeolite mineral scolecite, termed SC1; it is also fibrous, but the crystal size is large enough to expect that cell internalization is avoided. For the present study, as in the previous one, we used well purified samples of these four zeolite fibers. After preliminary screening, pure crystals were selected from each sample under a binocular microscope on the basis of the absence of any recognizable impurity phase. Moreover, presence of impurities was excluded on the basis of X-ray diffraction analyses (Mattioli et al., 2016b). Figure 1 shows the environmental scanning electron microscope (ESEM) images of the investigated zeolite fibers, while Table 1 reports the average chemical compositions and the surface areas, obtained by electron probe micro-analysis (EMPA) and Brunauer-Emmett-Teller (BET) method. For a better understanding of the ability of these fibrous zeolites to enter the cell membrane and damage the cells, we analysed the zeolite fibers in the presence of model membranes. First, the simplest model membrane, the micelle, was chosen; due to the negative potential of the zeolite surface, we used the positively charged cetyltrimethylammonium bromide (CTAB) micelles. Then, more reliable model membranes were selected, constituted by egg-lecithin and dimyristoylphosphatidylcholine (DMPC) liposomes.

To investigate the first step in cell-particle interactions, we used the spin probe method. We selected 4-cetyl dimethylammonium, 2,2,6,6 tetramethyl-piperidine-1oxyl Bromide (termed CAT16) and 5-doxyl stearic acid (termed 5DSA) (Figure 2) which, being surfactant probes, insert into surfactant aggregates, like the model membranes, and report about eventual structural variations occurring when the fibers interact with the membrane. CAT16, having the positively charged radical group as the polar head of the surfactant probe, provide information on the interactions at the membrane/solution interface, while 5DSA has the radical group embedded in the lipid region of the membrane and indicates if the lipid structure is affected by membrane-interacting fibers. These probes were previously used for similar studies (Angelov et al., 2014; Galarneau et al., 2006; 2010; Ottaviani et al., 2011; Ruthstein et al., 2004; 2006). The EPR spectra of probes in the membranes ideally monitor: a) adsorption of endogenous matter; b) adhesion of cell membrane to the solid; and c) internalization of the particle, the most likely event taking place when particles or fibers are in direct contact with the membrane,

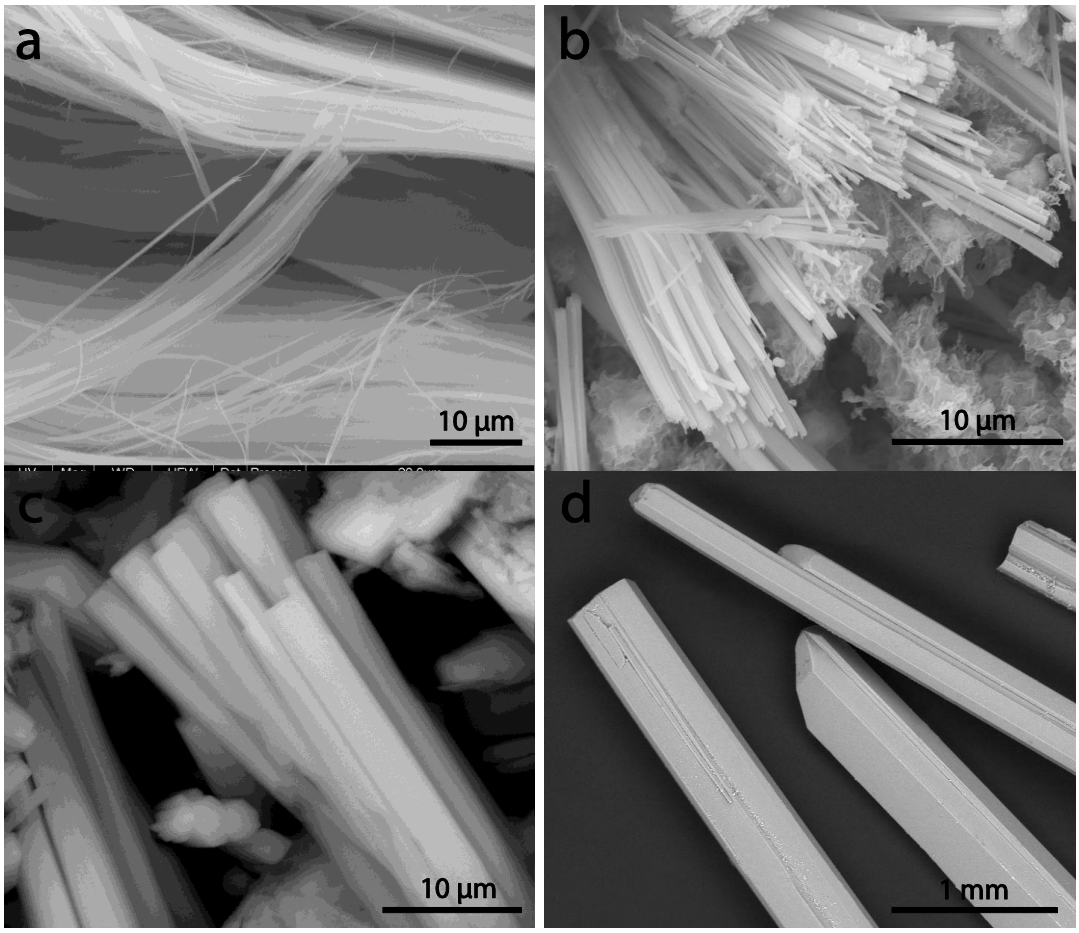

Figure 1. ESEM images of the investigated zeolite fibers. (a) Erionite with extremely fibrous, asbestiform habit (GF1); (b) acicular to fibrous erionite crystals (MD8); (c) acicular to fibrous offretite crystals, often grouped in prismatic forms (BV12); (d) prismatic, elongated crystals of scolecite (SC1).

Sample	Zeolite family	Average chemical composition	Area (m^2/g)
GF1	Erionite	$K_{2.56}Ca_{1.72}Na_{0.74}Mg_{0.35}[Al_{8.08}Si_{28.05}O_{72}]\cdot 29.54H_2O$	22.3
MD8	Erionite	$K_{3.46}Na_{2.38}\ Ca_{0.98}Mg_{0.16}[Al_{7.94}Si_{28}O_{72}]\cdot 32.31H_2O$	15.4
BV12	Offretite	$K_{2.06}Mg_{1.67}Ca_{1.17}[Al_{7.61}Si_{28.14}O_{72}]\cdot 31.03H_2O$	9.92
SC1	Scolecite	$Ca_{5.86}[Al_{14.35}\ Si_{22.31}O_{80}]\cdot 21.12H_2O$	1.5

Table 1. Average chemical compositions and surface areas, obtained by the EPMA and BET methods, respectively, of the zeolite fibers investigated in this study.

monitoring the ability to penetrate the membrane structure. However, these spin probes work both as spectator and reporter of the membrane-fiber interactions, but also as protagonists, due to their chemical similarities with several endogenous and exogenous materials, like drugs and pollutants.

It is important to underline that we analysed only the short term effect of these fibers on the model membrane, but, mineral fiber carcinogenesis appears -at least in part- related to biopersistence. For example Qi and coworkers (Qi et al., 2013) reported that crocidolite and chrysotile induced the same genetic

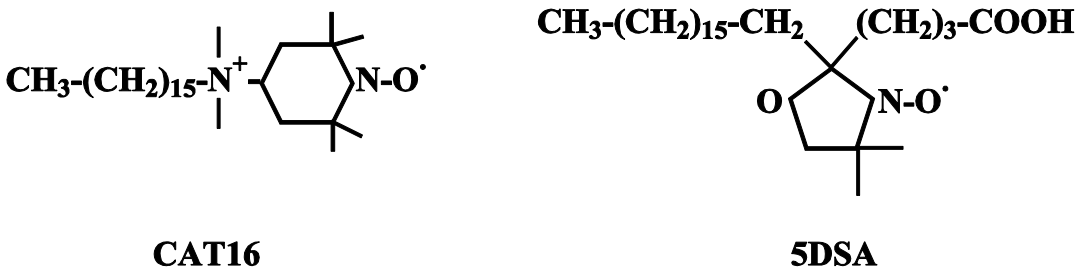

CAT16 **5DSA**

Figure 2. Chemical formulas of the selected probes.

changes and both induced HMGB1 release, except that crocidolite effects were long lasting and chrysotile not, an effect largely related to biopersistence. This suggests that erionite is characterized by a very long biopersistence in human body thus increasing its toxicity. Indeed, it is also necessary to emphasize the role of chronic inflammation in regulating mineral fiber carcinogenesis -a process that takes years- as described in the literature (see, for instance, Qi et al., 2013, and Hillegass et al., 2010).

Since we simply used model membranes, we did not discuss the very important concept about genetics influencing mineral fiber carcinogenesis, but relevant literature well explains this significant point (see for example Napolitano et al., 2016, and Carbone et al., 2016). Finally, mineral fibers are known to induce by themselves specific genetic alterations (see for example Guo et al., 2015, Nasu et al., 2015, and Altomare et al., 2009). On this basis, we are also interested to verify in the next future (manuscript in preparation) if the EPR technique may provide information on gene modifications when the erionite fibers are investigated in-vitro also in the presence of cells.

6.2 Experimental

6.2.1 Materials

The two samples GF1 and MD8 are from Nevada, USA (Gude and Sheppard, 1981) and Karain, Turkey (Carbone et al., 2007; 2011; Dogan et al., 2008), respectively, and they belong to the erionite family, known to be carcinogenic. The sample BV12 is offretite from Lessini Mountains, Italy (Mattioli et al., 2016a), which is suspected to be carcinogenic. The sample SC1 is scolecite from Poone, India (Gottardi and Galli, 1985). This latter is considered a non-carcinogenic fibrous mineral and has been used for comparison. See SD for further details on starting samples.

The tested erionite from GF1 consists of fibers and fibrils with a diameter in the range 10-100 nm and an extremely variable length, up to 20-30 μm. The tested erionite from MD8 are fibers and fibrils with diameter of 10-50 nm and a length up to 20 μm, with a great tendency to separate individual fibrils < 0.5 μm in diameter. The tested offretite material consists of fibers and fibrils 10-100 nm in diameter and up to 20 μm in length. The tested scolecite is made up by fibers and fibrils with diameter ranging from 20 nm to 80 nm, and a length up to 5 μm. The average chemical composition of the tested mineral fibers are reported in Table 1. In the erionites GF1 and MD8 the dominant extraframework cation is K, with Ca (in GF1) and Na (in MD8) as subordinate cations, while Mg is present in minor amount. Offretite material contains K, Mg and Ca as extraframework cations, whereas SC1 material is pure Ca-zeolite. The investigated materials also show different values of surface areas (Table 1), ranging from 22.3 m^2/g for GF1 to 1.5 m^2/g for SC1. The physico-chemical and morphological properties of the fibers are maintained in the tested samples in the absence and presence of the model membranes.

Doubly distilled and purified water (Millipore System) was used in all EPR measurements. CTAB, DMPC and 5DSA were purchased from Sigma Aldrich. CAT16 spin probe is a gift from Dr. X. Lei, Columbia University,

New York. Lecithin from egg yolk (L-R Lecithin) was purchased from Fluka.

6.2.2 Methods

6.2.2.1 Electron Paramagnetic Resonance (EPR)

Sample preparation: Liposomes and micelle solutions (0.1 M in surfactants) containing the spin probes (0.5 mM) were obtained as described in the SD. Selected pure zeolite crystals (300 mg) were dried in the oven at 110 °C overnight and then left equilibrating with 0.5 mL of the probe+model membrane solutions. After filtration of the supernatant suspension, the solid fibers were gently dried on a filter paper and tested by EPR. The supernatant suspensions and unadsorbed solutions were alto tested by EPR to investigate the interactions between the fibers and the model membranes in suspension and to evaluate the adsorbed-probe percentage.
Instrumentation: EPR spectra were recorded by means of an EMX-Bruker Spectrometer operating at X band (9.5 GHz) and interfaced with a PC (software from Bruker). The temperature was controlled with a Bruker ST3000 variable-temperature assembly cooled with liquid nitrogen.
Simulation of the EPR spectra: Simulation of the EPR line shape was performed by using Budil and Freed program (Budil et al., 1996), and the SD reports a description of the main parameters extracted from the spectral analysis, that is $<A> = (A_{xx}+A_{yy}+A_{zz})/3$, measuring the micropolarity; τ, measuring the microviscosity; the % of the spectral components, measuring the distribution of the probes in the different environments, and the S parameter, measuring the order of the surfactant aggregates

6.2.2.2 Transmission Electron Microscopy (TEM)

Sample preparation: The samples containing the model membranes and the zeolite fibers were prepared as described for the EPR samples (see SD for details), from the supernatant suspensions after filtration of the solid fraction. Model membranes with particles were adsorbed to formvar-carbon coated 200 mesh grids (Agar Scientific Ltd.) for 2 min and negatively stained with 2% (wt/vol) Na-phosphotungstate for 1 min.
Instrumentation: The TEM observations were carried out by means of a Philips CM10 transmission electron microscope at 80 kV.

6.3 Results and discussion

6.3.1 EPR analysis

The main information stem from the comparison between the model membranes in the absence and presence of the fibers. In the presence of the zeolite fibers we analysed both the supernatant liquids after adsorption and the filtered solids, after drying onto a filter paper. The EPR analysis of the supernatant suspensions served: (a) to verify if the aggregates in suspension retained a fraction of dispersed solid material, and (b) to evaluate the percentage of model membranes adsorbed (mainly trapped) onto the solid fibers that separated as a precipitate from the solution. Indeed, the probes distribute between the model membrane trapped into the solid fibers, which precipitated at the bottom of the solution, and the model membranes which remain in the supernatant suspension. Therefore the percentage of adsorbed membrane onto the precipitated solid is measured by the decrease of the spectral intensity from the unadsorbed model membrane solution to the supernatant suspensions. It is necessary to clarify the advantages of analysing by EPR the precipitate of fibers+model membranes where these two components are forced to come into contact with each other. Therefore the EPR analysis of the filtered solids provides direct information on the interactions occurring between the fiber and the model membrane, which may be at the basis of the carcinogenicity of the fibers.

6.3.1.1 CTAB micelles

First, we calculated the percentage of probes adsorbed onto the filtered solids, obtained from the intensity decrease in the EPR spectra from the unadsorbed to the supernatant suspension after adsorption. This “adsorbed percentage” is reported in Figure 3 in form of histogram for the different zeolites and for the

two probes. All zeolites are able to interact with the positively charged micelles, but the adsorbed percentage follows the series GF1>MD8>BV12>SC1 in line with the decrease in surface area evaluated using BET method (Table 1). Of course, the adsorption does not occur in the internal porosities of the fibers, since the pore size is too small, but at the external surface, which also changes in function of the total area. We also noted that the adsorbed percentage of micelles is higher for CAT16 with respect to 5DSA because CAT16 solubility in the micellar water solution is high and increases in the presence of the fibers. Further interesting information were obtained by analysing the EPR spectral line shape. Figure 4 shows as examples the EPR experimental spectra (298 K) obtained for CAT16 and 5DSA inserted into CTAB micelles in the absence (black lines) and presence (red lines) of GF1.

The spectra of CAT16 in the micelles are constituted by two components. A fraction of probes shows slow motion conditions, that is, $\tau > 0.9$ ns. The other fraction characterized by $\tau < 0.9$ ns is henceforth indicated as "fast" component.

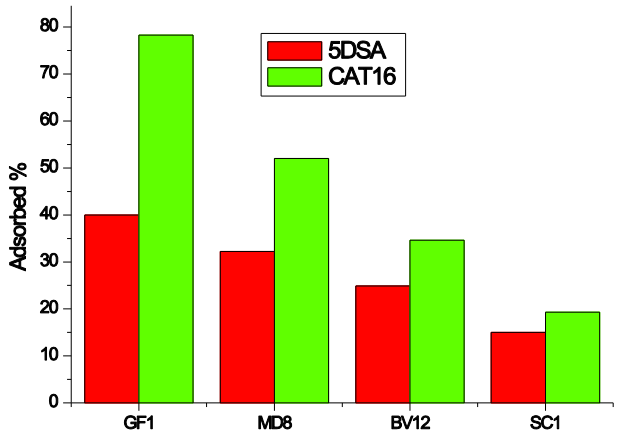

Figure 3. Adsorbed percentage of 5DSA and CAT16 probes onto the different zeolites evaluated from the decrease in the intensity of the EPR spectra from unadsorbed solutions to the supernatants after adsorption.

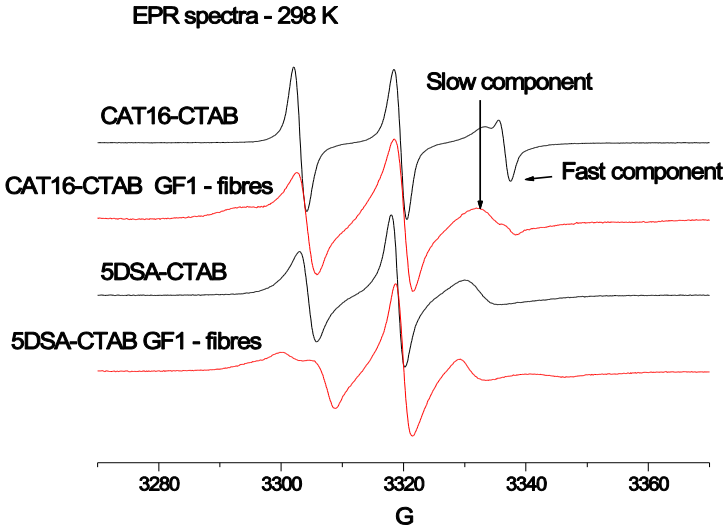

Figure 4. EPR experimental spectra (298 K) obtained for CAT16 and 5DSA inserted into CTAB micelles in the absence (black lines) and presence (red lines) of GF1 fibers. The spectra are normalized in height and, therefore, the intensity is not reported in the Y axis. G stands for Gauss, indicating the variation of the Magnetic Field in the X axis.

This is because the CAT group, being positively charged, is repulsed by the CTAB heads, and localizes both externally and internally the CTAB surface. However, an accurate computer aided analysis of the spectra (examples of computations of the various components are shown in Figure S1, SD, for CAT16 (A) and 5DSA (B)) revealed the appearance of other slow-motion components for the micelle-GF1 system. The same holds for the other fibers.

The main parameters obtained from the computations of the EPR spectra (see SD for the details about the parameters) are listed in Table 2 for CAT16 (A) and 5DSA (B).

For CAT16, by comparing the spectra of the supernatant suspensions after filtration with those in the absence of fibers, we note the following variations: (i) for GF1, the fast component increases in polarity and in microviscosity: this indicates that GF1 particles modify the structure of CTAB micelles in solution; (ii) for all the zeolites, the relative percentages of the fast component increases: this indicates the extraction of the probes from the micelle to the external solution. The probe extraction is the highest for BV12 and the lowest for GF1. Therefore, the micelle - GF1 fiber interaction in suspension modifies the st ructure of the micelles but poorly extracts the surfactants from the micelles, while BV12 offretite particles partially destroy the micelle structure when entering the micelles in suspension. MD8 and SC1 show similar percentages of adsorption, but the mechanisms are probably different as suggested by the other parameters in Table 2: MD8 behaviour is intermediate between GF1 and BV12, while SC1 is poorly interacting with the micelles and therefore the surfactant extraction is mainly driven by the charge effects played by this zeolite in the micellar solution.

The 5DSA point of view in the supernatant suspensions is different, since the doxyl group of 5DSA localizes internally to the micelles and reports about the structural variations upon interactions and eventual internalization of the fibers into the micelles.

(A) CAT16	%	<A> (G)	τ (ns)
No fibers	30	16.87	0.05
	70	16.07	0.95
GF1	40	16.93	0.1
	60	16.07	0.95
MD8	46	16.87	0.05
	54	16.07	0.95
BV12	57	16.87	0.05
	43	16.07	0.95
SC1	45	16.87	0.05
	55	16.07	0.95

(B) 5DSA	<A> (G)	τ (ns)	S
No fibers	15.37	1.7	0.14
GF1	15.37	1.5	0.334
MD8	15.37	1.5	0.267
BV12	15.37	1.5	0.267
SC1	15.37	1.5	0.252

Table 2. Main parameters of computation of the EPR spectra of CAT16 (A) and 5DSA (B) in CTAB-micelle water solutions in the absence and presence of the various fibers: $<A> = (A_{xx}+A_{yy}+A_{zz})/3$, measuring the micropolarity; τ, measuring the microviscosity; % of the spectral components, measuring the distribution of the probes in different environments; order parameter S.

The EPR spectrum of the probe in the micelles is characterized by slow motion and a small order parameter. In the presence of the zeolite particles entering the micelles in the supernatant suspension, the main effect is an increase of the order parameter which reports on the formation of a bilayer-like structure. This effect is the stronger for GF1 which therefore significantly modifies the micelle structure in the supernatant suspension, and it is the smaller for SC1 which is less perturbing the micellar structure if compared to the other zeolites. BV12 and MD8 give equivalent parameters in the supernatant which indicate a much smaller variation of the micelle structure if compared to GF1. In the presence of all zeolites the microviscosity slightly decreases, also reporting about the micelle structural perturbation due to fiber insertion. The analysis of the solid particles after filtration and a mild drying procedure also shows interesting results as described in the following.

For CAT16 in the solid+micelles, the spectra were constituted by three components termed for simplicity fast, medium and slow on the basis of the microviscosity parameter, τ. As indicated above, the fast component ($\tau < 0.9$ ns) arises from CAT16 free moving at the external interface of the micelles due to repulsion with the CTAB heads. The medium and the slow components (0.9 ns < τ < 2-3 ns, and $\tau > 3$ ns, respectively) are mainly ascribed to micelles or surfactant aggregates interacting with the fibers or fiber aggregates. The freedom of motion significantly decreases giving rise to slow motion when the micelles strongly interact with the fibers, also squeezing among them and/or forming bilayer-like structures. The relative percentages of these components, together with the correspondent microviscosity parameters (τ) obtained by computation, are compared in the histogram in Figure 5.

We note that SC1 particles poorly affects the micellar structure even in the filtered-solid sample, and the micellar suspension was mostly trapped into the interstices among the particles providing a small increase in microviscosity for the medium component.

For BV12, the mobility of the fast and medium components is a little bit lower and about 20 % of probes generate the slow-motion component at the expenses of the medium one.

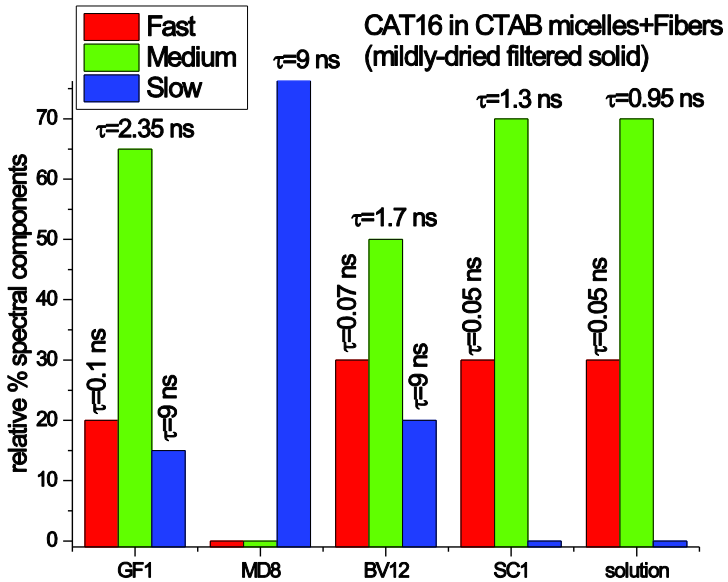

Figure 5. Relative percentages of the "fast", "medium" and "slow" components constituting the spectra of the fibers+micelle filtered solid; the correspondent microviscosity parameters (τ) are shown at the top of the bars.

Therefore, in line with the results from the supernatant suspensions, in the filtered BV12 solid, the micelles partially destructured and partially host the BV12 fibers. For MD8, the slow component was the only one present. This indicated squeezed and destructurated micelles in the fiber-aggregates porosities. For GF1, a significant increase in microviscosity occurs for both the fast and medium components, and the slow component is formed at the expenses of the fast one. So, the GF1 zeolite particles significantly affect the micelle structure. These results indicate that GF1 is better interacting with the membrane model constituted by the micelles if compared to the other zeolites. This effect is not related to the surface area, but to the chemical characteristics of the zeolite surface which is able to generate quite strong bonds (probably ion-ion binding) with the CTAB surfactants modifying the head-head distances which induces the formation of a bilayer-like CTAB structure at the fiber surface.

The parameters of the EPR spectra of 5DSA in the solid samples reported in Table 3 provide the following information: (i) GF1 shows two components, where the first one (70 %) comes from micelles with a significant increase in the order parameter, which is characteristic of a double-layer organization of the surfactants. The other component (30 %) is in very slow motion conditions, probably arising from destructurated micelles which are squeezed in the fiber-aggregates porosities; (ii) the other zeolites only show a slow motion spectrum with the microviscosity increasing in the series MD8<BV12<SC1. This trend goes in the opposite direction in respect to the surface area availability and the adsorbed percentage, that is, the lower the surface area and the adsorbed percentage, the higher the microviscosity. This result indicates that, for SC1, the low amount of adsorbed micelles squeezed in the interstices of the solid particle aggregates, while, for MD8, the adsorbed micelles are interacting with the solid surface, but they destructurate without forming the ordered layer found for GF1 due to a different interacting ability of the solid surface which binds the surfactants by separating them from each other after entering the micelles. For BV12, the behavior is in between MD8 and SC1.

6.3.1.2 Lecithin liposomes

Figure 6 shows the adsorbed percentages obtained for the lecithin liposomes after equilibration with the various zeolites.

This adsorbed percentage follows the same trend as found for CTAB micelles, but, contrary to CTAB, lecithin liposomes adsorb more 5DSA than CAT16. This is probably due to a better insertion of 5DSA into the liposomes if compared to the micelles. Conversely, CAT16 is poorly solubilized into the lecithin liposomes and its spectrum is almost not recordable for SC1 and BV12. Therefore, we do not discuss henceforth the results obtained using CAT16.

Figure 7 shows representative experimental and computed spectra of 5DSA in lecithin liposomes in the absence and presence of the various zeolites. The main parameters obtained from computation are listed in Table 4. In the absence of the zeolites, the parameters indicate the insertion of 5DSA into the liposomes. For GF1 in the supernatant suspension, we found that the fibers enter into the liposomes without changing the structural order of the membrane but generating

Sample	%	<A> (G)	τ(ns)	S
GF1	70	15.5	1.7	0.43
	30	15.37	50	0
MD8	100	15.37	13	0
BV12	100	15.37	24	0
SC1	100	15.37	28	0

Table 3: Main parameters of computation of the EPR spectra of 5DSA in the filtered solids constituted by CTAB-micelles and the various fibers.

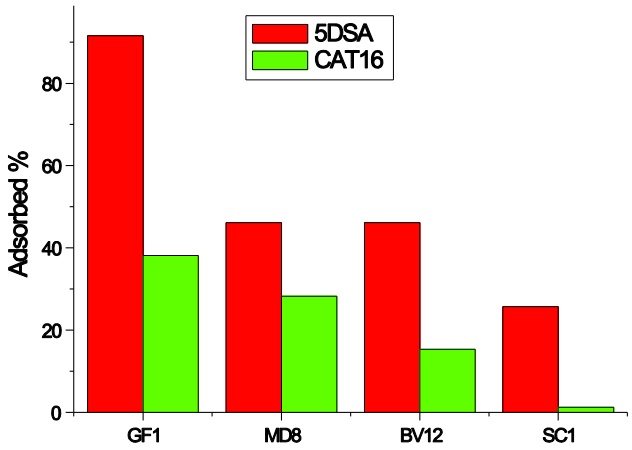

Figure 6. Adsorbed percentages obtained from the decrease in intensity from the unadsorbed solution (lecithin liposomes + 5DSA or CAT16) to the supernatant suspensions obtained after adsorption of the mother solution onto the different zeolite fibers.

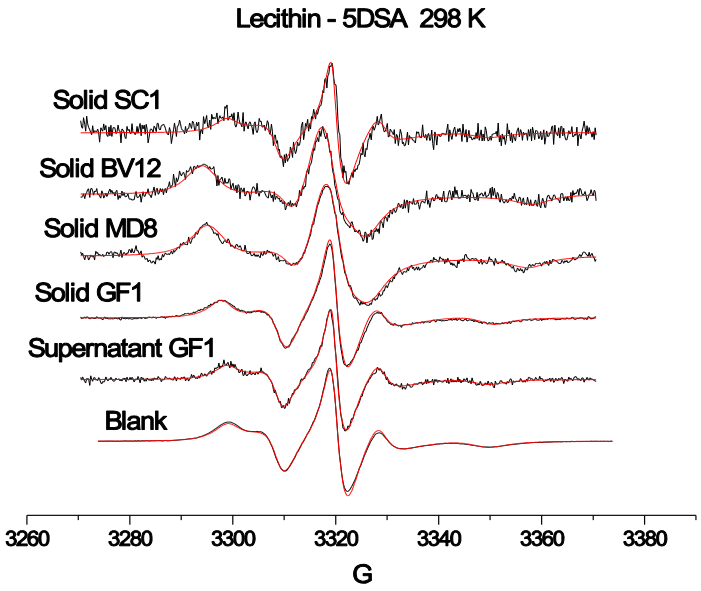

Figure 7. Representative experimental (black lines) and computed (red lines) spectra obtained using 5DSA as a probe for the analysis of the lecithin liposomes in the absence and presence of the various zeolites. The spectra are normalized in height and, therefore, the intensity is not reported in the Y axis. G stands for Gauss, indicating the variation of the Magnetic Field in the X axis.

Sample	<A> (G)	τ (ns)	S
No fibers	14	6.35	0.38
Supernatant GF1	14.5	7.2	0.38
Supernatants MD8-BV12	14.6	6.5	0.35
Supernatant SC1	14	6.4	0.38
Solid GF1	14.8	8.35	0.38
Solid MD8	14.87	25	0
Solid BV12	14.93	20	0
Solid SC1	14.5	7	0.38

Table 4: Main parameters of computation of the EPR spectra of 5DSA in lecithin liposomes in the absence and presence of the various fibers.

interactions (mainly ionic) between the fibers and the surfactants at the probe level. From the supernatant to the GF1 solid, the polarity and microviscosity further increase, but the bilayer order remains constant. This should mean that GF1 fibers do not destructurate the membrane, but are probably able to cross the liposome and enter inside the core solution. The spectra of the supernatants of MD8 and BV12 (not shown) were computed with the parameters in Table 4 which indicate that these fibers were more perturbative on the lecithin liposome structure in suspension then GF1. Probably, in these cases the fibers are associated to or included into the liposome membrane and do not cross the membrane to go inside, since the distribution of the differently polar or charged sites at the zeolite surface provokes interactions and repulsions which destroy the membrane structure. Indeed, the filtered solids for MD8 and BV12 show a significant increase in microviscosity. The order parameter in these conditions is no more measurable. The polarity also increases. This means that the structure of the liposomes in the filtered solids strongly changes due to the insertion of these fibers into the liposome bilayer and its consequent destructuration when squeezed in the fiber aggregates. SC1 is poorly changing the liposome structure in the supernatant suspension, while the filtered solid gives a very low intensity spectrum whose parameters suggest weak interactions between the fibers and the lecithin liposomes.

6.3.1.3 DMPC Liposomes

The probes show a low solubility into DMPC liposomes at 300 K (just above the sol-gel transition). This is shown in Figure 8(a), which reports the intensities of the EPR spectra of supernatant liposome solutions in the absence and presence of the fibers. The probe solubility, measured by the intensity, increased by adding the fibers with the exception of SC1 which provoked a further decrease in intensity. This increase was particularly high for GF1 while it was the lowest for MD8. This means that GF1 fibers are selectively internalized into DMPC liposomes also changing their structure which becomes more permeable to the surfactant probe. Representative experimental and computed spectra of 5DSA in DMPC liposome in the absence and presence of the different fibers are shown in Figure 8(b) and the main parameters from computation of all samples are reported in Table 5. GF1 supernatant displays an increased order, polarity and microviscosity with respect to the unadsorbed solution.

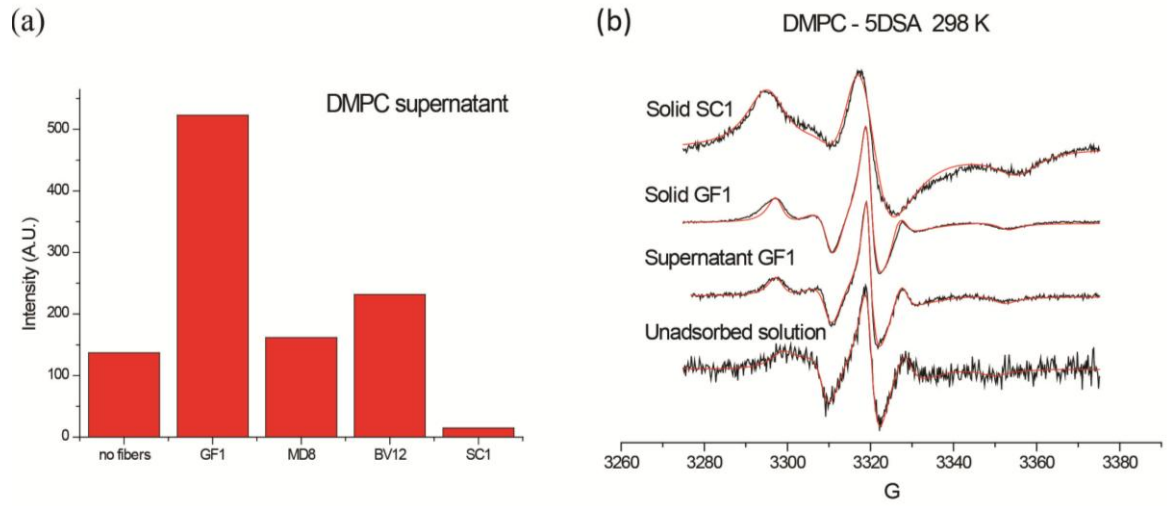

Figure 8. (a) Intensities of the EPR spectra of DMPC-liposomes in the absence and presence of the fibers; (b) representative experimental (black lines) and computed (red lines) spectra obtained using 5DSA as a probe for the analysis of the DMPC liposomes in the absence and presence of the various zeolites. The spectra are normalized in height and, therefore, the intensity is not reported in the Y axis. G stands for Gauss, indicating the variation of the Magnetic Field in the X axis.

Sample	<A> (G)	□ (ns)	S
No fibers	14	6.34	0.38
Supernatant GF1	14.97	8.35	0.44
Supernatant MD8	15	8.3	0.43
Supernatant BV12	14.5	7.7	0.41
Solid GF1	14.97	9.37	0.51
Solid MD8	14.7	18	0
Solid BV12	14.6	23	0
Solid SC1	14.4	31.6	0

Table 5: Main parameters of computation of the EPR spectra of 5DSA in DMPC-liposomes in the absence and presence of the various fibers.

So, the structural variations of the DMPC liposomes when including the GF1 fibers in suspension go towards an increasing rigidity and organization of the bilayer, similar to the behavior of the CTAB micelles. In this case too, ionic interactions between the liposome heads and the zeolite surface sites are probably responsible for these structural modifications. The site distribution in this case plays an important role too. The low intensity spectrum of the supernatant of MD8 shows parameters quite similar to those of GF1. The supernatant of BV12 shows mobility and order conditions in between the unadsorbed solution and MD8-supernatant suspensions. This indicates that offretite fibers induce less structural modifications of the liposomes with respect to erionite fibers. The spectrum for SC1 supernatant is poorly visible because the highly polar zeolite, staying outside the liposomes, impedes to the apolar probes to enter the liposome structure.

The order and microviscosity further increased from the supernatant to the solid GF1 sample. But, for the other zeolites, the order parameter is no more needed in the computation, while the microviscosity significantly increases in the series GF1<MD8<BV12<SC1 and the polarity measured by <A> goes in the opposite direction. This means that the carcinogenicity of the zeolites, hypothesized in the series SC1<BV12<MD8<GF1, may be correlated to the formation of a less rigid, more polar, and more ordered DMPC-membrane structure in the filtered solid. This is related to the squeezing of the liposomes in the fiber aggregates in the solids and the interactions occurring between the surface sites of both the fibers and the liposome, which are less pronounced for GF1 if compared to the other fibers because a large amount of GF1 fibers is internalized in the liposomes.

6.3.1.4 TEM Results

TEM images are only presented here for the different zeolites and CTAB micelles, because the liposomes showed a much lower fiber internalization if compared to the micelles. Furthermore, equivalent differences among images using the different fibers were found for micelles and liposomes. Finally, the EPR results are more complete for the micelles using both CAT16 and 5DSA, if compared to liposomes only using 5DSA.

TEM images were obtained from the supernatant suspensions, and, therefore, they will be compared in the following with the EPR results from the same samples.

Figure 9 shows some selected TEM images of SC1 (A), GF1 (B-D), BV12 (E, F) and MD8 (G, H) zeolites included into CTAB micelles. Mostly, zeolite fibers can be observed inside the micelles, where they appear elongated and, only occasionally, ring shaped. In particular, fibers were observed nearby or appeared totally incorporated by the micelles, as demonstrated by micrographs in which fibers are on the same focus plane of the micelles. Some images clearly show that several micelles are condensing and it is easy to find fibers inside enlarged micelles. The size of the CTAB aggregates ranges from 20 nm to 400 nm in the samples containing the fibers. The morphometric analysis revealed that 60% of

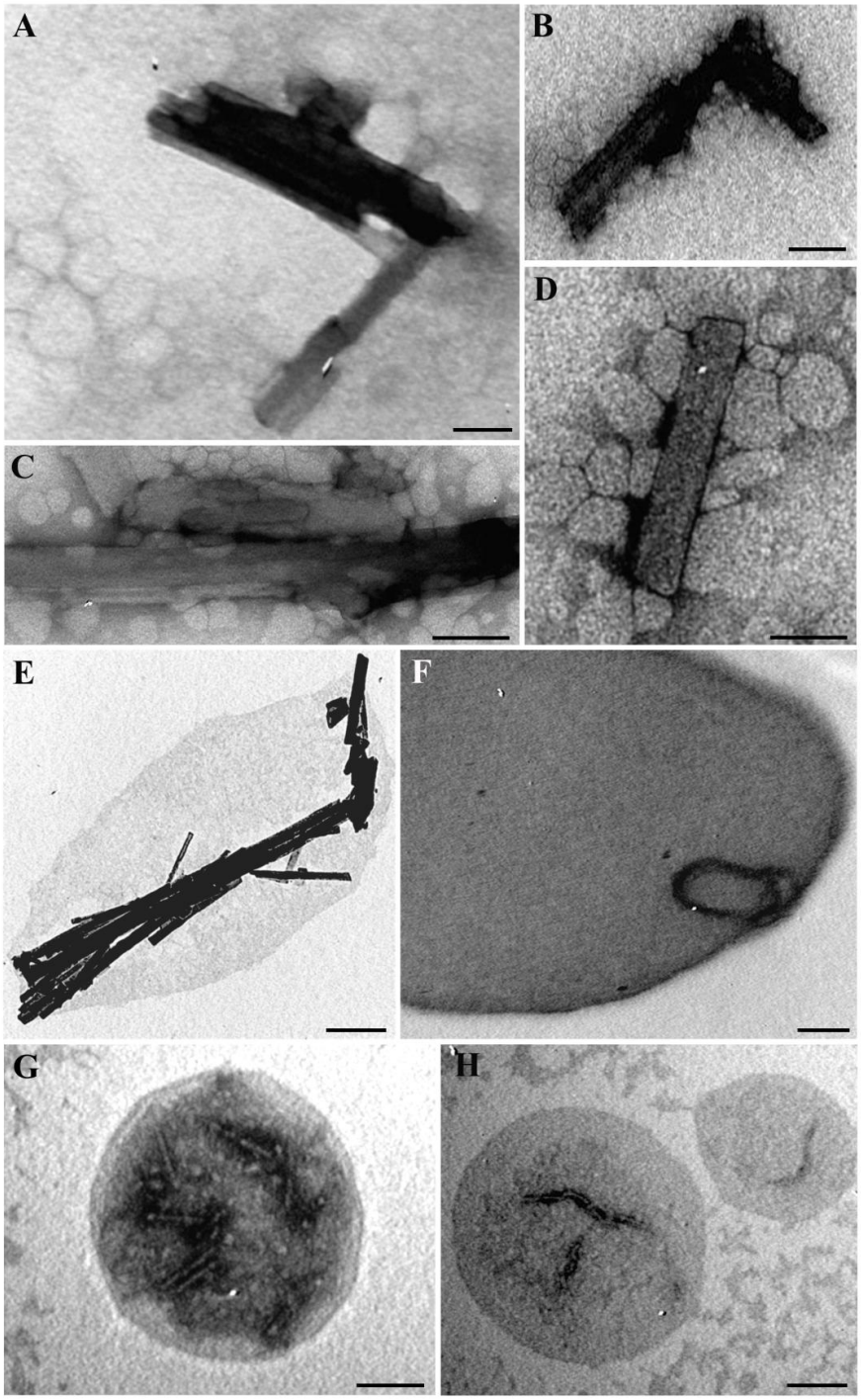

Figure 9. TEM images of SC1 (A), GF1 (B-D), MD13 (E, F) MD8 (G, H) zeolites internalized by the micelles. Bars: 50 nm (magnification 92000x) for A, B, D; 100 nm for C (magnification 130000x), G, H (magnification 62000x); 200 nm for E (magnification 32000x) and F (magnification 62000x).

aggregates have a size of 20- 100 nm which is the usual range of CTAB micelle size (Das et al., 2012), while 40% show a size of 200-400 nm, which is strongly in favor of a possible micelle fusion. In particular, Figure 9A shows a 300 nm micelle, surrounded by others of smaller size, which has incorporated SC1 zeolite. So, interestingly, also SC1 shows to be internalized into the model membranes when forming membrane-membrane aggregates, even if at a smaller extent with respect to the other zeolite fibers. Negative staining evi-

dences GF1 electrondense fiber presence, surrounded by several 10-40 nm circular structures (Fig. 9B-D) presumably merging together, to form a larger micelle containing the entire fiber. This is in line with the EPR results which indicate, for GF1, a variation of micellar structure toward a bilayer-like organization, without destroying the micelles (similar behavior as for the DMPC liposomes which show an increased order of the structure when including the fibers). Moreover, a crystalline large BV12 fiber as well as a circular one are observed inside a single micelle (Fig. 9E, F) but, in agreement with the EPR analysis, images showing fiber inclusion are more difficult to find, since a fraction of micelles are destructurated by the BV12 fibers. Finally, MD8 zeolite, which presents a smaller size if compared to the other fibers, appears perfectly internalized by single micelles (Fig. 9G, H). As found from the EPR analysis, the micellar structure changes much less for BV12 and MD8 then for GF1, even if a much lower internalization occurs, in agreement with the presence of isolated spherical micelles containing the fibers, as evidenced by the TEM images. Therefore the TEM results confirm that micelles adapt to the GF1 fiber surface forming a bilayer like structure, while the other fibers are included into the micelles without structurally modifying them, even if BV12 partially destroys the micelles.

6.4 Conclusions

The spin-probe EPR and TEM study of CTAB micelles, and egg-lecithin and DMPC liposomes in the presence of two erionite fibrous zeolite, named GF1 and MD8, and one offretite fibrous zeolite, named BV12, demonstrated the internalization of the fibers into the aggregates and clarified both the structure organization of the fiber-containing aggregates and the interactions occurring at a molecular level. For comparison, we also analysed a different fibrous zeolite of the scolecite family, termed SC1 with a relatively higher crystal size.

For the CTAB micelles both the spin probes, CAT16 and 5DSA, provided information on structure and interactions by means of a computer aided EPR analysis. The adsorbed percentage for the various zeolites follows the series GF1>MD8>BV12>SC1 in line with the decrease in surface area evaluated using BET method. In this case, it is the external surface area which makes the difference.

EPR parameters indicate that GF1 particles enter the CTAB micelles in the supernatant suspension and modify their structure towards a bilayer like organization, as also shown by TEM analysis, but GF1 fibers do not destroy the micelles. In the filtered solid, the micelles seem to well integrate with the zeolite particles being affected in their structure. 70 % of the micelles form a double-layer organization of the surfactants, while 30 % of the micelles are squeezed in restricted space in the fiber-aggregates porosities Definitely, GF1 is better entering the membrane structure if compared to the other zeolites. Conversely, BV12 offretite particles partially destroy the micelle structure when entering the micelles in suspension but a fraction of micelles is hosting the fibers with a relatively smaller structural variation with respect to GF1, as also shown by TEM images. Also in the filtered BV12 solid, the micelles partially destructurate and partially host the BV12 fibers. MD8 behaviour in suspension is intermediate between GF1 and BV12, but quite similar to BV12 for the structural variations, as indicated by TEM analysis; in the filtered BV12 solid, the micelles are squeezed and destructurate without forming the ordered layer found for GF1 and the surfactant heads go to interact with the zeolite surface. SC1 is poorly interacting with the micelles, even if a small internalization occurrs as also demonstrated by TEM. SC1 particles poorly affects the micellar structure even in the filtered-solid sample, and a low amount of adsorbed micelles is squeezed in the interstices of SC1 solid-particle aggregates.

For the lecithin liposomes, only 5DSA could be used as a probe, while CAT16 is poorly entering the liposomes and not considered. The modifications induced by GF1 fibers on the liposome structure are mainly due to interactions at the liposome interfaces, without

perturbing the order. The fibers do not destroy the membrane, but are probably able to cross the liposome and enter inside the core solution. For MD8 and BV12, the probe environment strongly changes due to the insertion of these fibers into the liposome bilayer. Therefore, we suppose that the fibers remain into the lecithin liposomes and do not cross the membrane to go inside. Indeed, the structure of the liposomes in the filtered solids strongly changes due to liposome squeezing in the fiber aggregates. The liposomes only slightly interact with SC1 which is poorly changing the liposome structure in suspension with respect to the liposomes in the absence of the fibers.

GF1 fibers are selectively internalized into DMPC liposomes also changing their structure which becomes more rigid and ordered, and also more permeable to the surfactant probe. In this case the fibers do not cross the membrane, but remain inside it changing the structure. A smaller structural variation was found for MD8 and BV12 if compared to GF1, as found for the micelles. The SC1 fibers are poorly included in DMPC liposomes and work as a barrier which impedes to the apolar probes to enter the liposome structure.

The carcinogenicity of the zeolites, hypothesized in the series SC1<BV12<MD8<GF1, may be correlated to an increased destructuration of the membrane. The results from the filtered solids are in line with this expectations indicating, for the series above, the formation of a membrane structure which is progressively less squeezed in the fiber-aggregate porosities, more polar and more ordered in the filtered solid.

This study is therefore helpful in clarifying the structural modifications and the interactions occurring when model membranes are in contact with asbestiform zeolite fibers which are known or suspected to be carcinogenic. Of course the model membranes constitute a simplified system to investigate the action of the carcinogenic fibers on lung and mesothelial cell membranes to cause mesothelioma cancer disease. We may try to extrapolate the information of these simplified systems onto the true ones really involved in the pathology, but, in light of the obtained results, we are investigating by EPR and TEM the systems constituted by the erionite and offretite fibers in cell dispersions (manuscript in preparation). Furthermore, we plan to study asbestos and other asbestiform fibers with both model membranes and cell lines. For example, crocidolite and amosite, asbestos fibers containing iron (not present in erionite), which are demonstrated to induce lung tumors, could give interesting results.

REFERENCES

Aguilar-Armenta, G., and Patiño-Iglesias, M. E. 2002. Adsorption equilibria and kinetics of propylene and propane on natural erionite and on erionite exchanged with K+ and Ag+. *Langmuir* 18: 7456-7461.

Alberti, A., Martucci, A., Galli, E., and Vezzalini, G. 1997. A re-examination of the crystal structure of erionite. *Zeolites* 19: 349-352.

Altomare, D. A., Menges, C. W., Pei, J., Zhang, L., Skele-Stump, K. L., Carbone, M., Kane, A. B., and Testa, J. R. 2009. Activated TNF-α/NF-κB signaling via down-regulation of Fas-associated factor 1 in asbestos-induced mesotheliomas from *Arf* knockout mice. *Proc. Natl. Acad. Sci.* 106: 3420-3425.

Andolfi, L., Trevisan, E., Zweyer, M., Prato, S., Troian, B., Vita, F., Borelli, V., Soranzo, M. R., Melato, M., and Zabucchi, G. 2013. The crocidolite fibres interaction with human mesothelial cells as investigated by combining electron microscopy, atomic force and scanning near-field optical microscopy. *J. Microsc*. 249(3): 173-83.

Andujar, P., Lacourt, A., Brochard, P., Pairon, J-C., Jaurand, M-C., and Jean, D. 2016. Five years update on relationships between malignant pleural mesothelioma and exposure to asbestos and other elongated mineral particles. *J. Toxicol. Environ. Health B* 19: 151-172.

Angelov, V., Velichkova, H., Ivanov, E., Kotsilkova, R., Delville, M. E., Cangiotti, M., Fattori, A., and Ottaviani, M. F. 2014. EPR and Rheological Study of Hybrid Interfaces in Gold-Clay-Epoxy Nanocomposites. *Langmuir* 30: 13411-13421.

Artvinli, M., and Baris, Y. I. 1979. Malignant mesotheliomas in a small village in the Anatolian region of Turkey: An epidemiologic study. *J. Natl. Cancer Inst.* 63: 17-22.

Aust, A. E., Cook, P. M., and Dodson, R. D. 2011. Morphological and chemical mechanisms of elongated mineral particle toxicities. *J. Toxicol. Environ. Health B* 14: 40-75.

Ballirano, P. 2003. Effects of the choice of different ionisation level for scattering curves and correction for small preferred orientation in Rietveld refinement: the $MgAl_2O_4$ test case. *Journal of Applied Crystallography* 36: 1056-1061.

Ballirano, P. 2011. Laboratory parallel beam transmission X-ray powder diffraction investigation of the thermal behavior of calcite: comparison with X-ray single-crystal and synchrotron powder diffraction data. *Periodico di Mineralogia* 80: 123-134.

Ballirano, P. and Sadun, C. 2009. Thermal behavior of trehalose dihydrate (T_h) and β-anhydrous trehalose (T_β) by in-situ laboratory parallel-beam X-ray powder diffraction. *Structural Chemistry* 20: 815-823.

Ballirano, P., and Cametti, G. 2012. Dehydration dynamics and thermal stability of erionite-K: Experimental evidence of the "internal ionic exchange" mechanism. *Microporous and Mesoporous Materials* 163: 160-168.

Ballirano, P., and Cametti, G. 2013. Crystal chemical and structural investigation of levyne-Na. *Mineralogical Mag*azine 77: 2887-2899.

Ballirano, P., and Cametti, G. 2015. Crystal chemical and structural modifications of erionite fibers leached with simulated lung fluids. *Am. Mineral*. 100: 1003-1012.

Ballirano, P., and Pacella, A. 2016. Erionite-Na upon heating: dehydration dynamics and exchangeable cations mobility. *Scientific Reports* 6: 22786.

Ballirano, P., Andreozzi, G. B., Dogan, M., and Dogan, A. U. 2009. Crystal structure and iron topochemistry of erionite-K from Rome, Oregon, U.S.A. *Am. Mineral.* 94: 1262-1270.

Ballirano, P., Pacella, A., Cremisini, C., Nardi, E., Fantauzzi, M., Atzei, D., Rossi,

A., and Cametti G. 2015. Fe (II) segregation at a specific crystallographic site of fibrous erionite: A first step toward the understanding of the mechanisms inducing its carcinogenicity. *Microporous Mesoporous Mater.* 211: 49-63.

Baris, I., Artvinli, M., Saracci, R., Simonato, L., Pooley, F., Skidmore, J., and Wagner, C. 1987. Epidemiological and environmental evidence of the health effects of exposure to erionite fibres: A four-year study in the Cappadocian region of Turkey. *Int. J. Cancer* 39: 10-17.

Baris, Y. I., Artvinli, M., and Sahin, A. A. 1979. Environmental mesothelioma in Turkey. *Ann. N. Y. Acad. Sci* 330: 423-432.

Baris, Y. I., Sahin, A. A., Ozesmi, M., Kerse, I., Ozen, E., Kolacan, B., Altinörs, M., and Göktepeli, A. 1978. An outbreak of pleural mesothelioma and chronic fibrosing pleurisy in the village of Karain/Urgüp in Anatolia. *Thorax* 33: 181-192.

Barrett, E. G., Johnston, C., Oberdorster, G., and Finkelstein, J. N. 1999. Silica-induced chemokine expression in alveolar type II cells is mediated by TNF-alpha-induced oxidant stress. *Am. J. Physiol.-Lung Cell. Mol. Physiol*. 276: 979-988.

Bates, R. L., and Jackson, J. A. 1987. *Glossary of Geology (3nd ed.)*. Alexandria, Va., USA: American Geological Institute.

Baumann, F., Ambrosi, J. P., and Carbone, M. 2013. Asbestos is not just asbestos: an unrecognised health hazard. *Lancet Oncol.* 14 (7): 576-578.

Baumann, F., and Carbone, M. 2016. Environmental risk of mesothelioma in the United States: An emerging concern-epidemiological issues. *J. Toxicol. Environ. Health B* 19: 231-249.

Beccaluva, L., Bianchini, G., Bonadiman C., Coltorti M., Milani L., Salvini L., Siena F., and Tassinari R. 2007. Intraplate litospheric and sublitospheric components in the Adriatic domain: nephelinite to tholeiite magma generation in the Paleogene Veneto volcanic province, southern Alps. *Mineral. Soc. Am. Spec. Paper* 418: 131-152.

Becher, R. Hetland, R. B., Refsnes, M., Dahl, J. E., Dahlman, H. J., and Schwarze, P. E. 2001. Rat lung inflammatory responses after in vivo and in vitro exposure to various stone particles. *Inhal. Toxicol*. 13: 789-805.

Bennett, J. M., and Gard, J. A. 1967. Non-identity of the zeolites erionite and offretite. *Nature*, 214: 1005-1006.

Bernstein, D. M., Rogers, R., and Smith, P. 2005. The biopersistence of Canadian chrysotile asbestos following inhalation: Final Results Through 1 Year After Cessation of Exposure. *Inhal. Toxicol*. 17(1): 1-14.

Bertino, P., Marconi, A., Palumbo, L., Bruni, B. M., Barbone, D., Germano, S., Dogan, A. U., Tassi, G. F., Porta, C., Mutti, L., and Gaudino, G. 2007. Erionite and asbestos differently cause transformation of human mesothelial cells. *Int. J. Cancer* 121: 2766-2774.

Bish, D. L., and Ming, D. W. 2001. *Natural Zeolites: Occurrence, Properties, Applications*, ed. D. L. Bish and D. W. Ming, 45. Reviews in Mineralogy and Geochemistry.

Bloise, A., Barca, D., Gualtieri, A. F., Pollastri, S., and Belluso, E. 2016. Trace elements in hazardous mineral fibres. *Environ. Pollut.* 216: 314-323.

Bonadiman, C., Coltorti, M., Milani, L., Salvini, L., Siena, F., and Tassinari, R. 2001. Metasomatism in the lithospheric mantle and its relationships to magmatism in the Veneto Volcanic Province, Italy. *Period. Mineral.* 70: 333-357.

Bonneau, L., Malard, M., and Pezerat, H. 1986. Studies on surface properties of asbestos II. Role of dimensional characteristics and surface properties of mineral fibers in the induction of pleural tumors. *Environ. Res.* 41: 268-275.

Boscardin, M., Checchi, A., Filippi, F., Guglielmino, S., Pegoraro, S., Pretto, G.,

and Zattra, A. 1998. Offretite del Veneto. *Riv. Min. Ital*. Milano, 22: 25-29.

Boulanger, G., Andujar, P., Pairon, J. C., Billon-Galland, M. A., Dion, C., Dumortier, P., Brochard, P. Sobaszek, A. Bartsch, P., Paris, C., and Jaurand, M. C. 2014. Quantification of short and long asbestos fibers to assess asbestos exposure: A review of fiber size toxicity. *Environ. Health* 13: 59.

Bruker, AXS. 2009. Topas V.4.2: General profile and structure analysis software for powder diffraction data. Bruker AXS, Karlsruhe, Germany.

Brunauer, S., Emmett, P. H., and Teller, E. 1938. Adsorption of gases in multimolecular layers. *J. Am. Chem. Soc.* 60: 309-319.

Budil, D. E., Lee, S., Saxena, S., and Freed, J. H. 1996. Nonlinear-least-squares analysis of slow-motion EPR spectra in one and two dimensions using a modified Levenberg-Marquardt algorithm. *J. Magn. Reson. Ser. A.* 120: 155-189.

Bunderson-Schelvan, M., Pfau, J. C., Crouch, R., and Holian, A. 2011. Non-pulmonary outcomes of asbestos exposure. *J. Toxicol. Environ. Health B* 14: 122-152.

Burragato, F., Comba, P., Baiocchi, V., Palladino, D. M., Simei, S., Gianfagna, A., et al. 2005. Geovolcanological, mineralogical and environmental aspects of quarry materials related to pleural neoplasm in the area of Biancavilla, Mount Etna (eastern Sicily, Italy). *Environ. Geol*. 47: 855-68.

Cametti, G., Pacella, A., Mura, F., Rossi, M., and Ballirano, P. 2013. New morphological, chemical, and structural data of woolly erionite-Na from Durkee, Oregon, U.S.A. *Am. Mineral*. 98: 2155-2163.

Campbell, L. S., Charnock, J., Dyer, A., Hillier, S., Chenery, S., Stoppa, F., Henderson, C. M. B., Walcott, R., and Rumsey, M. 2016. Determination of zeolite-group mineral composition by electron probe microanalysis (EPMA). *Mineral. Mag*. 80(5): 781-807.

Carbone, M., and Bedrossian, C. W. M. 2006. The pathogenesis of mesothelioma. *Semin. Diagn. Pathol.* 23: 56-60.

Carbone, M., and Yang, H. 2012. Molecular pathways: Targeting mechanisms of asbestos and erionite carcinogenesis in mesothelioma. *Clin. Cancer Res.* 18: 598-604.

Carbone, M., Baris, Y. I., Bertino, P., Brass, B., Comertpay, S., Dogan, A. U., Gaudino, G., Jube, S., Kanodia, S., Petridge, C. R., Pass, H. I., Rivera, Z. S., Steele, I., Tuncer, M., Way, S., Yang, H., and Miller, A. 2011. Erionite exposure in North Dakota and Turkish villages with mesothelioma. *Proc. Natl. Acad. Sci. U.S.A.* 108: 13623-13628.

Carbone, M., Bevan, H. L., Dodson, R. F., Pagano, I., Morris, P. T., Dogan, U. A., Gazdar, A. F., Pass, H. I., and Yang, H. 2012. Malignant mesothelioma: facts, myths, and hypotheses. *J. Cell. Physiol.* 227: 44-58.

Carbone, M., Emri, S., Dogan, A. U., Steele, I., Tuncer, M., Pass, H. I., and Baris, Y. I. 2007. A mesothelioma epidemic in Cappadocia: Scientific developments and unexpected social outcomes. *Nat. Rev. Cancer*. 7: 147-154.

Carbone, M., Kanodia, S., Chao, A., Miller, A., Wali, A., Weissman, D., Adjei, A., Baumann, F., et al. 2016. Consensus Report of the 2015 Weinman International Conference on Mesothelioma. *J. Thorac. Oncol.* 11: 1246-1262.

Cardile, V., Chillemi, R., Lombardo, L., Sciuto, S., Spatafora, C., and Tringali, C. 2007. Antiproliferative activity of methylated analogues of E- and Z-resveratrol. *Z. Naturforsch. C* 62: 189-195.

Case, B. W., Abraham, J. L., Meeker, G., Pooley, F. D. and Pinkerton, K. E. 2011. Applying definitions of "asbestos" to environmental and "low-dose" exposure levels and health effects, particularly malignant mesothelioma. *J. Toxicol. Environ. Health B* 14: 3-39.

Castranova, V., Vallyathan, V., and Wallace, W. E. 1996. Silica and Silica-induced Lung Diseases, Boca Raton, FL:CRC Press.

Cattaneo, A., Rossotti, A., Pasquarè, G., Somigliana, A., and Cavallo, D. M. 2011. Analysis of fibrous zeolites in the volcanic deposits of the Viterbo Province, Italy. *Environ. Earth Sci*. 63: 861-871.

Cenni, M. 2009. Le mineralizzazioni secondarie nelle rocce basaltiche: esempi dai Monti Lessini (Italia). *PhD thesis*, University of Urbino, Italy, 193 pp.

Coffin, D. L., Cook, P. M., and Creason, J. P. 1992. Relative mesothelioma induction in rats by mineral fibers: comparison with residual pulmonary mineral fiber number and epidemiology. *Inhal. Toxicol*. 4: 273-300.

Cook, P. M., Palekar, L. D., and Coffin, D. L. 1982. Interpretation of the carcinogenicity of amosite asbestos and ferroactinolite on the basis of retained fiber dose and characteristics in vivo. *Toxicol. Lett*. 13: 151-158.

Coombs, D. S., Alberti, A., Armbruster, T., Artioli, G., Colella, C., Galli, E., Grice, J. D., Liebau, F., Mandarino, J. A., Minato, H., Nickel, E. H., Passaglia, E., Peacor, D. R., Quartieri, S., Rinaldi, R., Ross, M., Sheppard, R. A., Tillmanns, E., and Vezzalini, G. 1997. Recommended nomenclature for zeolite minerals: Report of the subcommittee on zeolites of the International Mineralogical Association, Commission on New Minerals and Mineral Names. *Can. Mineral*. 35: 1571-1606.

Croce, A., Allegrina, M., Rinaudo, C., Gaudino, G., Yang, H., and Carbone, M. 2015. Numerous iron-rich particles lie on the surface of erionite fibers from Rome (Oregon, USA) and Karlik (Cappadocia, Turkey). *Microsc. Microanal*. 21: 1341-1347.

Croce, A., Musa, M., Allegrina, M., Rinaudo, C., Baris, Y. I., Dogan, A. U., Powers, A., Rivera, Z., Bertino, P., Yang, H. Gaudino, G., and Carbone, M. 2013. Micro-Raman spectroscopy identifies crocidolite and erionite fibers in tissue section. *J. Raman Spectrosc.* 44: 1440-1445.

Crovella, S., Bianco, A. M., Vuch, J., Zupin, L., Moura, R. R., Trevisan, E., Schneider, M., Brollo, A., Nicastro, E. M., Cosenzi, A., Zabucchi, G., and Borelli, V. 2016. Iron signature in asbestos-induced malignant pleural mesothelioma: A population-based autopsy study. *J. Toxicol. Environ. Health A* 79*:* 129-141.

Daleffe, A., and Boscardin, M. 2005. Offretite di Passo Roccolo tra Chiampo e S. Giovanni Ilarione (Lessini Orientali). *Studi e Ricerche*, Associazione Amici del Museo Civico "G. Zannato" Montecchio Maggiore. 12: 57-59.

Das, N. C., Cao, H., Kaiser, H., Warren, G. T., Gladden, J. R., and Sokol, P. E. 2012. Shape and Size of Highly Concentrated Micelles in CTAB/NaSal Solutions by Small Angle Neutron Scattering (SANS). *Langmuir* 28(33): 11962-11968.

Davis, J. M. G., and Jaurand, M. C. 1994. Cellular and Molecular Effects of Mineral and Synthetic Dusts and Fibres, North Atlantic Treaty Organization Advanced Study Institute Series, Springer-Verlag, Berlin/Heidelberg, 85.

Davis, J. M. G., Bolton, R. E., Miller, B. G., and Niven, K. 1991. Mesothelioma dose response following intraperitoneal injection of mineral fibres. *Int. J. Exp. Pathol.* 72: 263-274.

de Assis, L. V. M., Locatelli, J., and Isoldi, M. C. 2014. The role of key genes and pathways involved in the tumorigenesis of malignant mesothelioma. *Biochim. Biophys. Acta* 1845: 232-247.

De Vecchi, G. P., and Sedea, R. 1995. The Paleogene basalt of the Veneto region (NE Italy). *Mem. Ist. Geol. Miner.Univ. Padova* 47: 253-274.

Deer, W. A., Howie, R., Wis, W. S., and Zussman, J. 2004. *Rock Forming Minerals. Framework Silicates: Silica Minerals, Feldspathoids and the Zeolites*. London, UK: 4B, The Geological Society.

Demirer, E., Ghattas, C. F., Radwan, M. O., and Elamin, E. M. 2015. Clinical and prognostic features of erionite-induced malignant mesothelioma. *Yonsei Med. J.* 56: 311-323.

Dixon, J. R., Lowe, D. B., Richards, D. E., Cralley, L. J., and Stokinger, H. E. 1970. The role of trace metals in chemical carcinogenesis: asbestos cancers. *Cancer res*. 30(4): 1068-1074.

Dodson, R. F., Atkinson, M. A. L., and Levin, J. L. 2003. Asbestos fiber length as related to potential pathogenicity: A critical review. *Am. J. Ind. Med.* 44: 291-297.

Dogan, A. U. 2003. Zeolite Mineralogy and Cappadocian Erionite. *Indoor and Built Environment* 12: 337-342

Dogan, A. U., and Dogan, M. 2008. Re-evaluation and re-classification of erionite series minerals. *Environ. Geochem. Health* 30: 355-366.

Dogan, A. U., Baris, Y. I., Dogan, M., Emri, S., Steele, I., Elmishad, A. G., and Carbone M. 2006. Genetic predisposition to fiber carcinogenesis causes a mesothelioma epidemic in Turkey. *Cancer Res*. 66: 5063-5068.

Dogan, A. U., Dogan, M., and Hoskins, J. A. 2008. Erionite series minerals: mineralogical and carcinogenic properties. *Environ. Geochem. Health* 30: 367-381.

Dogan, M. 2012. Quantitative characterization of the mesothelioma-inducing erionite series minerals by transmission electron microscopy and energy dispersive spectroscopy. *Scanning* 34: 37-42.

Donaldson, K., Murphy, F. A., Duffin, R., and Poland, C. A. 2010. Asbestos, carbon nanotubes and the pleural mesothelium: A review of the hypothesis regarding the role of long fibre retention in the parietal pleura, inflammation and mesothelioma. *Part. Fibre Toxicol.* 7: 5.

Dumortier, P., Coplü, L., Broucke, I., Emri, S., Selcuk, T., de Maertelaer, V., De Vuyst, P., and Baris, I. 2001. Erionite bodies and fibres in bronchoalveolar lavage fluid (BALF) of residents from Tuzköy, Cappadocia, Turkey. *Occup. Environ. Med.* 58: 261-266.

Eakle, A. S. 1898. Erionite, a new zeolite. *Am. J. Sci.* 6: 66-68.

Eberly, P. E. J. 1964. Adsorption properties of naturally occurring erionite and its cationic-exchanged forms. Am. Mineral.49: 30-40.

Emri, S., Demir, A., Dogan, M., Akay, H., Bozkurt, B., Carbone, M., and Baris, I. 2002. Lung diseases due to environmental exposures to erionite and asbestos in Turkey. *Toxicology Letters*, 127: 251-257.

Farrugia, L.J. 1999. ORTEP-3 for Windows. University of Glasgow, Scotland.

Fubini, B. 1996. Use of physico-chemical and cell free assays to evaluate the potential carcinogenicity of fibres, in: A.B. Kane, P. Boffetta, R. Saracci, J.D. Wilbourn (Eds.), Mechanisms of Fibre Carcinogenesis, IARC Sci. Publ., Lyon: International Agency for Research on Cancer, 140: 35-54.

Fubini, B. 2001. *The physical and chemical properties of asbestos fibers which contribute to biological activity*. Asbestos Health Effect Conference, May 24-25, Oakland, CA, US Environmental Protection Agency.

Fubini, B. and Mollo, L. 1995. Role of iron in the reactivity of mineral fibers. *Toxicol. Lett.* 82/83: 951-960.

Fubini, B., 1993. The possible role of surface chemistry in the toxicity of inhaled fibres, in: D.B. Warheit (Ed.), Fibre Toxicology, Academic Press, San Diego CA, 11: 229-257.

Fubini, B., Bolis, V., Cavenago, A., and Volante M. 1995. Physico-chemical properties of crystalline silica dusts and their possible implication in various biological responses. *Scand. J. Work. Environ. Health* 21(2): 9-14.

Galan, E. 1996. Properties and applications of paligorskite-sepiolite clays. *Clay Miner*. 31: 443-453.

Galarneau, A., Cangiotti, M., di Renzo, F., Sartori, F., and Ottaviani, M. F. 2006.

Synthesis of Large-Pore Micelle-Templated Silico-Aluminas at Different Alumina Contents. *J. Phys. Chem. B* 110: 20202-20210.

Galarneau, A., Sartori, F., Cangiotti, M., Mineva, T., Di Renzo, F., and Ottaviani, M. F. Sponge Mesoporous Silica Formation Using Disordered Phospholipid Bilayers as Template. *J. Phys. Chem. B* 114: 2140-2152.

Gard, J. A., and Tait, J. M. 1972. The crystal structure of the zeolite offretite, K1. 1Ca1. 1Mg0. 7 [Si12. 8Al5. 2O36]. 15.2 H2O. *Acta Cryst. B* 28(3): 825-834.

Gatti, A. M. and Rivasi, F. 2002. Biocompatibility of micro- and nanoparticles. Part I: In liver and kidney. *Biomaterials* 23: 2381-2387.

Gaudino, G., Yang, H., and Carbone, M. 2014. HGF/Met signaling is a key player in malignant mesothelioma carcinogenesis. *Biomedicine* 2: 327-344.

Gazzano, E., Riganti, C., Tomatis, M., Turci, F., Bosia, A., Fubini, B., and Ghigo, D. 2005. Potential toxicity of nonregulated asbestiform minerals: Balangeroite from the Western Alps. Part 3: Depletion of antioxidant defenses. *J. Toxicol. Environ. Health* 68: 41-49.

Gianfagna, A., Andreozzi, G. B., Ballirano, P., Mazziotti-Tagliani, S., and Bruni, B. M. 2007. Structural and chemical contrasts between prismatic and fibrous fluoro-edenite from Biancavilla, Sicily, Italy. *Can. Mineral*. 45(2): 249-262.

Gianfagna, A., Ballirano, P., Bellatreccia, F., Bruni, B., Paoletti, L., and Oberti, R. 2003. Characterisation of amphibole fibres linked to mesothelioma in the area of Biancavilla, eastern Sicily, Italy. *Mineral. Mag.* 67(6): 1221-1229.

Giordani, M., Mattioli, M., Dogan, M., and Dogan, A. U. 2016. Potential carcinogenic erionite from Lessini Mounts, NE Italy: morphological, mineralogical and chemical characterization. *J. Toxicol. Environ. Health A* 79(18): 808-824.

Giovagnoli, L. and Boscardin, M. 1979. Ritrovamento di levyna ed erionite a Montecchio Maggiore (Vicenza). *Rivista Mineralogica Italiana* 1(2):44-45.

Goldstein, J. I., Newbury, D. E., Echlin, P., Joy, D. C., Roming, A. D., Lyman, C. E., Fiori, C., and Lifshin, E. 1992. *Scanning Electron Microscopy and X-Ray Microanalysis.* 2nd ed. New York, USA: Plenum Press.

Gottardi, G., and Galli, E. 1985. *Natural Zeolites*. Heidelberg, Germany: Springer-Verlag.

Groppo, C., and Compagnoni, R. 2007. Ubiquitous fibrous antigorite veins from the Lanzo Ultramafic Massif, Internal Western Alps (Italy): characterisation and genetic conditions. *Per. Mineral*. 76: 169-181.

Groppo, C., Tomatis, M., Turci, F., Gazzano, E., Ghigo, D., Compagnoni, R., and Fubini, B. 2005. Potential toxicity of nonregulated asbestiform minerals: Balangeroite from the western Alps. Part 1: Identification and characterization. *J. Toxicol. Environ. Health A* 68: 1-19.

Gualtieri, A., Artioli, G., Passaglia, E., Bigi, S., Viani, A., and Hanson, J. C. 1998. Crystal structure-crystal chemistry relationships in the zeolites erionite and offretite. *Am. Mineral.* 83: 590-606.

Guastoni, A., Dugnani, M., Pezzotta, F., and Bardelli, G. 2002. Offretite del lago d'Arno in alta Val Saviore, Parco dell'Adamello (Bs). *Atti Soc. Ital. Sci. Nat*. 143: 195-207.

Gude, A. J., and Sheppard, R. A. 1981. Woolly erionite from the Reese River zeolite deposit, Lander County, Nevada, and its relationship to other erionites. *Clays Clay Miner*. 29: 378-384.

Guo, G., Chmielecki, J., Goparaju, C., Heguy, A., Dolgalev, I., Carbone, M., Seepo, S., Meyerson, M., and Pass, H. I. 2015. Whole-Exome Sequencing Reveals Frequent Genetic Alterations in *BAP1*, *NF2*, *CDKN2A*, and *CUL1* in Malignant Pleural Mesothelioma. *Cancer Res*. 75: 264-269.

Guthrie, G. D. J., and Mossman, B. T. 1993. Health Effects of Mineral Dusts, Reviews

in Mineralogy, Mineralogical Society of America, Washington, 28.

Harington, J. S., Roe, F. J., and Walters, M. 1967. Studies of the mode of action of asbestos as a carcinogen. *S. Afr. Med. J.* 41(32): 800-804.

Hesterberg, T. W., Chase, G., Axten, C., , Miller, W. C., Musselman, R. P., Kamstrup, O., Hadley, J., Morscheidt, C., Bernstein, D. M., and Thevenaz, P. 1998. Biopersistence of synthetic vitreous fibers and amosite asbestos in the rat lung following inhalation. *Toxicol. Appl. Pharmacol.* 151: 262-275.

Hetland, R. B., Schwarze, P. E., Johansen, B. V., Myran, T., Uthus, N., and Refsnes, M. 2001. Silica-induced cytokine release from A549 cells: importance of surface area versus size. *Hum. Exp. Toxicol.* 20: 46-55.

Hill, R. J., Edwards, R. E., and Carthew, P. 1990. Early changes in the pleural mesothelium following intrapleural inoculation of the mineral fibre erionite and the subsequent development of mesotheliomas. *Br. J. Exp. Pathol*. 71: 105-118.

Hillegass, J. M., Miller, J. M., MacPherson, M. B., Westbom, C. M., Sayan, M., Thompson, J. K., Macura, S. L., Perkins, T. N., Beuschel, S. L., Alexeeva, V., Pass, H. I., Steele, C., Mossman, B. T., and Shukla, A. 2013. Asbestos and erionite prime and activate the NLRP3 inflammasome that stimulates autocrine cytokine release in human mesothelial cells. *Part. Fibre Toxicol*. 10: 39.

Hochella, M. F. 1993. Surface chemistry, structure, and reactivity of hazardous mineral dust. In *Health Effects of Mineral Dusts*, ed. G. D. Guthrie and B. T. Mossman, 28: 275-308. Chelsea, MI: Bookcrafters. Reviews in Mineralogy.

Hofmann, W. 2011. Modelling inhaled particle deposition in the human lung – A review. *J. Aerosol Sci.* 42: 693-724.

Hubbard, A. K., Timblin, C. R., Shukla, A., Rincon, M., and Mossman, B. T. 2002. Activation of NF-kappa B-dependent gene expression by silica in lungs of luciferase reporter mice. *Am. J. Physiol.-Lung Cell. Mol. Physiol.* 282: 968-975.

IARC, 1987. Overall evaluations of carcinogenicity: an updating of IARC monographs volumes 1 to 42. *IARC Monogr. Eval. Carcinog. Risks Hum.* Suppl. 7: Lyon, 440 p.

IARC, 1993. Some naturally occurring substances: food items and constituents, heterocyclic aromatic amines and mycotoxins. *IARC Monogr. Eval. Carcinog. Risks Hum.* 56: Lyon, 609 p.

IARC, 1997. Zeolites other than erionite. In Silica, some silicates, coal dust and para-aramid fibrils. *IARC Monogr. Eval. Carcinog. Risks Hum.* 68: Lyon, 521 p.

IARC, 2012. Arsenic, metals, fibres, and dusts. *IARC Monogr. Eval. Carcinog. Risks Hum.* 100C: Lyon, 501 p.

Ilgren, E. B., Kazemian, H., and Hoskins, J. A. 2015. Kandovan the next Capadoccia? A potential public health issue for erionite related mesothelioma risk. *Epidemiology, Biostatistics and Public Health* 12: 1-12.

INAIL, 2012. Il Registro Nazionale dei Mesoteliomi (ReNaM): quarto rapporto. *INAIL, Settore Ricerca, Dipartimento Medicina del Lavoro*: Roma, 220 p.

Jacobsen, S.D., Smyth, J.R., Swope, R.F., and Downs, R.T. 1998. Rigid body character of the SO_4 group in celestine, anglesite and barite. *Canadian Mineralogist* 36: 1053-1060.

Johnston, C. J., Driscoll, K. E., Finkelstein, J. N., Baggs, R., O'Reilly, M. A., Carter, J., Gelein, R., and Oberdorster, G. 2000. Pulmonary chemokine and mutagenic responses in rats after subchronic inhalation of amorphous and crystalline silica. *Toxicol. Sci*. 56: 405-413.

Jones, J.B. 1968. Al-O and Si-O tetrahedral distances in aluminosilicate framework structures. *Acta Crystallographica* B24: 355-358.

Kane, A. B., Boffetta, P., Saracci, R., and Wilbourn, J. D. 1996. Mechanisms of Fibre Carcinogenesis. IARC Sci. Publ., Lyon: International Agency for Research on Cancer, 140.

Katerinopoulou, A., Balic-Zunic, T., and Lundegaard, L.F. 2012. Application of the ellipsoid modeling of the average shape of nanosized crystallites in powder diffraction. *Journal of Applied Crystallography* 45: 22-27.

Kliment, C. R., Clemens, K., and Oury, T. D. 2009. North american erionite-associated mesothelioma with pleural plaques and pulmonary fibrosis: A case report. *Int. J. Clin. Exp. Pathol.* 2: 407-410.

Kokturk, N., Firat, P., Akay, H., Kadilar, C., Ozturk, C., Zorlu, F., Gungen, Y., and Emri, S. 2005. Prognostic significance of Bax and Fas Ligand in erionite and asbestos induced Turkish malignant pleural mesothelioma. *Lung Cancer* 50: 189-198.

Kueng, A. 1983. Geologie und petrographie am Westrand des Adamello. Diplomarbeit Eidgenoessischen Technischen Hochschule Zuerich.

Larson, D., Powers, A., Ambrosi, J-P., Tanjia, M., Napolitano, A., Flores, E. G., Baumann, F., Pellegrini, L., Jennings, C. J., Buck, B. J., McLaurin, B. T., Merkler, D., Robinson, C., Morris, P., Dogan, M., Dogan, A. U., Pass, H. I., Pastorino, S., Carbone, M., and Yanga, H. 2016. Investigating palygorskite's role in the development of mesothelioma in southern Nevada: Insights into fiber-induced carcinogenicity. *J. Toxicol. Environ. Health B* 19(5-6): 213-230.

Lee, K. P. 1985. Lung response to particlates with emphasis on asbestos and other fibrous dusts. *Crit. Rev. Toxicol*. 14: 33-86.

Lemen, R.A. 2016. Mesothelioma from asbestos exposures: Epidemiologic patterns and impact in the United States. *J. Toxicol. Environ. Health B* 19: 250-265.

Lippmann, M. 1988. Asbestos exposure indices. *Environ. Res.* 46: 86-106.

Lippmann, M., Yeates, D. B., and Albert, R. E. 1980. Deposition, retention, and clearance of inhaled particles. *Br. J. Ind. Med.* 37: 337-362.

Liu, W., Ernst, J. D., and Broaddus, V. C. 2000. Phagocytosis of crocidolite asbestos induces oxidative stress, DNA damage, and apoptosis in mesothelial cells. *Am. J. Respir. Cell Mol. Biol.* 23: 371-378.

Lowers, H. A., Adams, D. T., Meeker, G. P., and Nutt, C. J. 2010. Chemical and morphological comparison of erionite from Oregon, North Dakota, and Turkey, U.S. Geological Survey Open-file Report 1286: 1-13.

Manna, P., and Comba, P. 2001. Comunicazione con le autorità sanitarie e con il pubblico sui rischi da amianto a Biancavilla (CT). *Epidemiol. Prev*. 25: 28-30.

Matassa, R., Familiari, G., Relucenti, M., Battaglione, E., Downing, C., Pacella, A., Cametti, G., and Ballirano, P. 2015. A deep look into erionite fibres: An electron microscopy investigation of their self-assembly. *Sci. Rep*. 5: 16757.

Mattioli, M., Cenni, M., and Passaglia, E. 2016a. Secondary mineral assemblages as indicators of multi stage alteration processes in basaltic lava flows: Evidence from the Lessini Mountains, Veneto Volcanic Province, Northern Italy. *Per. Mineral*. 85: 1-24.

Mattioli, M., Giordani, M., Dogan, M., Cangiotti, M., Avella, G., Giorgi, R., Dogan, A. U., and Ottaviani, M. F. 2016b. Morpho-chemical characterization and surface properties of carcinogenic zeolite fibers. *J. Hazard. Mater*. 305: 140-148.

Mattioli, M., Lustrino, M., Ronca, S., and Bianchini, G. 2012. Alpine subduction imprint in Apennine volcaniclastic rocks. Geochemical–petrographic constraints and geodynamic implications from Early Oligocene Aveto-Petrignacola Formation (N Italy). *Lithos* 134: 201-220.

Maxim, D. L., Hadley, J. G., Potter, R. M., and Niebo, R. 2006. The role of fiber durability/biopersistence of silica-based synthetic vitreous fibers and their influence on toxicology. *Reg. Toxicol. Pharmacol*. 46: 42-62.

Mertens, G., Snellings, R., Van Balen, K., Bicer-Simsir, B., Verlooy, P., and Elsen, J. 2009. Pozzolanic reactions of common natural zeolites with lime and parameters affecting their reactivity. *Cem. Conc. Res*. 39: 233-240.

Metcalf, R. V., and Buck, B. J. 2015. Genesis and health risk implications of an unusual occurrence of fibrous NaFe3+-amphibole. *Geology* 43(1): 63-66.

Metintas, M., Hillerdal, G., and Metintas, S. 1999. Malignant mesothelioma due to environmental exposure to erionite: follow-up of a Turkish emigrant cohort. *European Respiratory Journal*, 13: 523-526.

Metintas, M., Hillerdal, G., Metintas, S. and Dumortier, P. 2010. Endemic malignant mesothelioma: Exposure to erionite is more important than genetic factors. *Arch. Environ. Health* 65: 86-93.

Milani, L., Beccaluva, L., and Coltorti, M. 1999. Petrogenesis and evolution of the Euganean magmatic complex, Veneto Region, North-East Italy. *Eur. J. Mineral.* 11: 379-399.

Millette, J. R. 2006. Asbestos analysis methods. In *Asbestos-Risk Assessment, Epidemiology, and Health Effects,* ed. R. F. Dodson and S. P. Hammar, pp. 9-37. Boca Raton, FL: Taylor and Francis.

Moscatelli, A., Liu, Z., Lei, X., Dyer, J., Abrams, L., Ottaviani, M. F., and Turro, N. J. 2008. Photolysis of dibenzyl ketones sorbed on MFI zeolites in the presence of spectator molecules: Cage effects, kinetics, and external surface sites characterization. *J. Am. Chem. Soc.* 130 (34): 11344-11354.

Mossman, B. T., Lippmann, M., Hesterberg, T. W., Kelsey, K. T., Barchowsky, A., and Bonner, J. C. 2011. Pulmonary endpoints (lung carcinomas and asbestosis) following inhalation exposure to asbestos. *J. Toxicol. Environ. Health. B* 14: 76-121.

Muhle, H., Bellmann, B., and Pott, F. 1991. *Durability of various mineral fibres in rat lungs, mechanisms in fibre carcinogenesis,* ed., R. C. Brown, J. A. Hoskins and N. F. Johnson, pp. 181-187. New York, NATO ASI series A: Life Sciences, Vol. 223. Plenum Press.

Nagai, H., and Toyokuni, S. 2012. Differences and similarities between carbon nanotubes and asbestos fibers during mesothelial carcinogenesis: shedding light on fiber entry mechanism. *Cancer Sci.* 103(8): 1378-90.

Napolitano, A., Pellegrini, L., Dey, A., Larson, D., Tanji, M., Flores, E. G., Kendrick, B., Lapid, D., Powers, A., Kanodia, S., Pastorino, S., Pass, H. I., Dixit, V., Yang, H., and Carbone, M. 2016. Minimal asbestos exposure in germline BAP1 heterozygous mice is associated with deregulated inflammatory response and increased risk of mesothelioma. *Oncogene* 35: 1996-2002.

Nasu, M., Emi, M., Pastorino, S., Tanji, M., Powers, A., Luk, H., Baumann, F., Zhang, Y. A., Gazdar, A., Kanodia, S., Tiirikainen, M., Flores, E., Gaudino, G., Becich, M. J., Pass, H. I., Yang, H., and Carbone, M. 2015. High Incidence of Somatic BAP1 alterations in sporadic malignant mesothelioma. *J. Thorac. Oncol*. 10: 565-76.

Nemery, B. 1990. Metal toxicity and the respiratory tract. *Eur. Respir. J.* 3(2): 202-219.

NIOSH 1994. *Method 7400: Asbestos and other fibers by PCM*. In: NIOSH Manual of Analytical Methods, Fourth Edition. National Institute for Occupational Safety and Health, Cincinnati, OH, DHHS (NIOSH), Publication No. 2003-154.

NIOSH 2011. *Asbestos Fibers and Other Elongate Mineral Particles: State of the Science and Roadmap for Research*. National Institute for Occupational Safety and Health, Cincinnati, OH, DHHS (NIOSH), Publication No. 2011-159.

Oberdörster, G., Castranova, V., Asgharian, B., and Sayre, P. 2015. Inhalation Exposure to Carbon Nanotubes (CNT) and Carbon Nanofibers (CNF): Methodology and Dosimetry. *J. Toxicol. Environ. Health B* 18: 121-212.

Oberdorster, G., Oberdorster, E., and Oberdorster, J. 2005. Nanotoxicology: an emerging discipline evolving from studies of ultrafine particles. *Environ. Health Perspect*. 113: 823-839.

Olbruck, H., Seemayer, N. H., Voss, B., and Wilhelm, M. 1998. Supernatants from quartz dust treated human macrophages stimulate cell proliferation of different human lung cells as well as collagensynthesis of human diploid lung fibroblasts in vitro. *Toxicol. Lett*. 96(7): 85-95.

Ortega-Guerrero, M. A., and Carrasco-Nùñez, G. 2014. Environmental occurrence, origin, physical and geochemical properties, and carcinogenic potential of erionite near San Miguel de Allande, Mexico. *Environ. Geochem. Health* 36: 517-529.

Ortega-Guerrero, M. A., Carrasco-Núñez, G., Barragán-Campos, H., and Ortega, M. R. 2015. High incidence of lung cancer and malignant mesothelioma linked to erionite fibre exposure in a rural community in Central Mexico. *Occup. Environ. Med*. 72: 216-218.

Ottaviani, M. F., and Venturi, F. 1996. Physico-chemical study on the adsorption properties of asbestos. An EPR study on the adsorption of organic radicals. *J. Phys. Chem*. 100: 265-269.

Ottaviani, M. F., Galarneau, A., Desplantier-Giscard, D., Di Renzo, F., and Fajula, F. 2001a. EPR Investigations on the Formation of Micelle-Templated Silica. *Micropor. Mesopor. Mat*. 44: 1-8.

Ottaviani, M. F., Lei, X., Liu, Z., and Turro, N. J. 2001b. Supramolecular structure and dynamics of organic molecules adsorbed on the external surface of MFI zeolites. A direct and indirect computational EPR analysis. *J. Phys. Chem. B.* 105: 7954-7962.

Ottaviani, M. F., Leonardis, I., Cappiello, A., Cangiotti, M., Mazzeo, R., Trufelli, H., and Palma, P. 2010. Structural modifications and adsorption capability of C18-silica/binary solvent interphases studied by EPR and RP-HPLC. *J. Coll. Interface Sci*. 352: 512-519.

Ottaviani, M. F., Mollo, L., and Fubini, B. 1997. Use of Nitroxides as Topological Monitors of the Interaction of Silica-Based Particles with Components of the Biological Environment. *J. Colloid Interface Sci.* 191(1): 154-165.

Ottaviani, M. F., Venturi, F., Pokhrel, M. R., Schmutz, T., and Bossmann, S. H. 2001c. Physico-Chemical Studies on the Adsorption Properties of Asbestos 2. An EPR and Fluorescence Study on the Adsorption of Pyrene. *J. Colloid Interface Sci*. 238(2): 371-380.

Ovrevik, J., Lag, M., Schwarze, P., and Refsnes, M. 2004. p38 and Src-ERK1/2 pathways regulate crystalline silica-induced chemokine release in pulmonary epithelial cells. *Toxicol. Sci*. 80 480-490.

Ovrevik, J., Refsnes, M., Namork, E., Becher, R., Sandnes, D., Schwarze, P., and Lag, M. 2006. Mechanisms of silica-induced IL-8 release from A549 cells: Initial kinase-activation does not require EGFR activation or particle uptake. *Toxicology* 227(1-2): 105-116.

Pacella, A., Ballirano, P., and Cametti, G. 2016. Quantitative chemical analysis of erionite fibres using a micro-analytical SEM-EDX method. *Eur. J. Mineral*. 28: 257-264.

Paoletti, L., Batisti, D., Bruno, C., Di Paola, M., Gianfagna, A., Mastrantonio, M., Nesti, M., and Comba, P. 2000. Unusually high incidence of malignant pleural mesothelioma in a town of eastern Sicily: an epidemiological and environmental study. *Arch. Environ. Health* 55(6): 392-398.

Passaglia, E. 1970. The crystal chemistry of chabazites. *Am. Mineral*. 55: 1278-1301.

Passaglia, E., and Galli, E. 1974. Levyne and erionite from Sardinia, Italy. *Contrib. Mineral. Petr*. 43: 253-259.

Passaglia, E., and Sheppard, R. A. 2001. The crystal chemistry of zeolites. In *Natural Zeolites: Occurrence, Properties, Application, Reviews in Mineralogy and Geochemistry*, ed. D. L. Bish and D. W.

Ming, 45: pp. 69-116. Chantilly, Virginia: Mineralogical Society of America and Geochemical Society.

Passaglia, E., and Tagliavini, A. 1995. Erionite from Faedo, Colli Euganei, Italy. *Neues Jb. Miner. Monat.* 185-191.

Passaglia, E., Artioli, G., and Gualtieri, A. 1998. Crystal chemistry of the zeolites erionite and offretite. *Am. Mineral*. 83: 577-589.

Passaglia, E., Tagliavini, A., and Gutoni, R. 1996. Offretite and other zeolites from Fittà (Verona, Italy). *Neues Jb. Miner. Monat.* 418-428.

Pollastri, S., D'Acapito, F., Trapananti, A., Colantoni, I., Andreozzi, G. B., and Gualtieri, A. F. 2015. The chemical environment of iron in mineral fibres. A combined X-ray absorption and Mössbauer spectroscopic study. *J. Hazard. Mater*. 298: 282-293.

Pollastri, S., Gualtieri, A. F., Gualtieri, M. L., Hanuskova, M., Cavallo, A., and Gaudino, G. 2014. The Zeta potential of mineral fibres. *J. Hazard. Mater*. 276: 469-479.

Pongiluppi, D., Passaglia, E., and Galli, E. 1974. Su alcune zeoliti della Sardegna. *Società Italiana di Mineralogia e Petrologia* 30: 77-100.

Pott, F., Ziem, U., Reiffer, F. J., Huth, F., Ernst, H., and Mohr, U. 1987. Carcinogenicity studies on fibres, metal compounds, and some other dusts in rats. *Exp. Pathol*. 32: 129-152.

Qi, F., Okimoto, G., Jube, S., Napolitano, A., Pass, H. I., Laczko, R., Demay, R. M., Khan, G., Tiirikainen, M., Rinaudo, C., Croce, A., Yang, H., Gaudino, G., and Carbone, M. 2013. Continuous exposure to chrysotile asbestos can cause transformation of human mesothelial cells via HMGB1 and TNF-α signaling. *Am. J. Pathol*. 183: 1654-1666.

Reed, S. J. B. 1993. Electron Microprobe Analysis. Cambridge, UK: 2nd ed., Cambridge University Press.

Rinaldi, R. 1976. Crystal chemistry and structural epitaxy of offretite-erionite from Sasbach, Kaiserstuhl. *Neues Jb. Miner. Monat.* 145-156.

Roggli, V. L., Vollmer, R. T., Butnor, K. J., and Sporn, T. A. 2002. Tremolite and mesothelioma. *Ann. Occup. Hyg.* 46: 447-453.

Ross, M., Kuntze, R. A., and Clifton, R. A. 1984. A definition for asbestos. *ASTM Special Technical Publication* 834: 139-147.

Ruthstein, S., Frydman, V., and Goldfarb, D. 2004. Study of the Initial Formation Stages of the Mesoporous Material SBA-15 Using Spin-Labeled Block Co-polymer Templates. J. *Phys. Chem.* B 108: 9016-9022.

Ruthstein, S., Schmidt, J., Kesselman, E., Talmon, Y., and Goldfarb, D. 2006. Resolving Intermediate Solution Structures during the Formation of Mesoporous SBA-15. *J. Am. Chem. Soc*. 128: 3366-3374.

Sabine, T.M., Hunter, B.A., Sabine, W.R., and Ball, C.J. 1998. Analytical expressions for the transmission factor and peak shift in absorbing cylindrical specimens. *Journal of Applied Crystallography* 31: 47-51.

Sacerdoti, M. 1996. New refinements of the crystal structure of levyne using twinned crystals. *Neues Jahrbuch fur Mineralogie-Monatshefte*:114-124.

Saini-Eidukat, B., and Triplet, J. W. 2014. Erionite and offretite from the Killdeer Mountains, Dunn County, North Dakota, USA. *Am. Mineral*. 99: 8-15.

Samet, J. M., Bristow, L. R., Checkoway, H., Demers, P., Eisen, E. A., Guthrie, G. D., Henderson, R. F., Hogan, J. W., Kane, A. B., Khuri, F. R., Ness, R. B., and Thun, M. J. 2006. *Asbestos-Selected Cancers.* Committee on Asbestos: Selected Health Effects, Board on Population Health and Public Health Practices: Institute of Medicine of the National Academies. Washington, DC: National Academies Press.

Santaren, J., and Alvarez, A. 1994. Assessment of the health effects of

mineral dusts. The sepiolite case. *Ind. Miner. Mag.* 101-107.

Scapoli, L., Ramos-Nino, M. E., Martinelli, M., and Mossman, B. T. 2004. Src-dependent ERK5 and Src/EGFR-dependent ERK1/2 activation is required for cell proliferation by asbestos. *Oncogene* 23: 805-813.

Schins, R. P., Duffin, R., Hohr, D., Knaapen, A. M., Shi, T., Weishaupt, C., Stone, V., Donaldson, K., Borm, P. J. 2002. Surface modification of quartz inhibits toxicity, particle uptake, and oxidative DNA damage in human lung epithelial cells. *Chem. Res. Toxicol*. 15: 1166-1173.

Sheppard, R. A., and Gude, A. J. 1969. Chemical composition and physical properties of the related zeolites offretite and erionite. *American Mineral*ogist 54(5-6): 875-886.

Stanton, M. F., Layard, M., Tegeris, A., Miller, E., May, M. and Morgan, E., and Smith, A. 1981. Relation of particles dimension to carcinogenicity in amphibole asbestoses and other fibrous minerals. *J. Natl. Cancer Inst*. 67: 965-975.

Staples, L. W., and Gard, J. A. 1959 The fibrous zeolite erionite: its occurrence, unit cell, and structure. *Mineral. Mag*. 322: 261-281.

Stephenson, D. J., Fairchild, C. I., Buchan, R. M., and Dakins, M. E. 1999. A fiber characterization of the natural zeolite, mordenite: A potential inhalation health hazard. *Aerosol Sci. Tech*. 30(5): 467-476.

Straif, K., Benbramin-Tallaa, L., Baan, R., Grosse, Y., Secretan, B., El Ghissassi, F., Bouvard, V., Guha, N., Freeman, C., Galichet, L., and Cogliano, V. 2009. Special report: Policy. A review of human carcinogens. Part C: Metals, arsenic, dusts, and fibres. *Lancet* 10: 453-454.

Suzuki, Y. Yuen, S. R., and Ashley, R. 2005. Short, thin asbestos fibers contribute to the development of human malignant mesothelioma: Pathological evidence. *Int J Hyg Environ. Health*. 208: 439-444.

Suzuki, Y., and Yuen, S. R., 2002. Asbestos fibers contributing to the induction of human malignant mesothelioma. *Ann. N. Y. Acad. Sci.* 982: 160-176.

Sweatman, T. R., and Long, J. V. P. 1969. Quantitative electron-probe microanalysis of rock-forming minerals. *J. Petrol*. 10: 332-379.

Temel, A., and Gündogdu, M. N. 1996. Zeolite occurrences and the erionite-mesothelioma relationship in Cappadocia, Central Anatolia, Turkey, *Miner. Deposita* 31: 539-547.

Tschernich, R. W. 1992. Zeolites of the world, Geoscience Press Inc., Phoenix, Arizona.

USBM. 1996. *Dictionary of Mining, Mineral, and Related Terms.* U. S. Bureau of Mines. Second edition.

Van Gosen, B. S., Blitz, T. A., Plumlee, G. S., Meeker, G. P., and Pierson, M. P. 2013. Geologic occurrences of erionite in the United States: an emerging national public health concern for respiratory disease. *Environ. Geochem. Health* 35: 419-430.

Vignaroli, G., Ballirano, P., Belardi, G., Rossetti, F. 2014. Asbestos fibre identification vs. evaluation of asbestos hazard in ophiolitic rock mélanges, a case study from the Ligurian Alps (Italy). *Environmental Earth Sciences* 72: 3679-3698.

Wagner, J. C., Skidmore, J. W., Hill, R. J., and Griffiths, D. M. 1985. Erionite exposure and mesotheliomas in rats. *Br. J. Cancer* 51: 727-730.

WHO. 1986. *Asbestos and Other Natural Mineral Fibers*. Environmental Health Criteria, 53: pp. 69-107. Geneva, World Health Organization.

Wise W.S. and Tschernich R.W. 1976. The chemical compositions and origin of the zeolites offretite, erionite and levyne. *American Mineral*ogist 61: 853–863.

Wiseman, H., and Halliwell, B. 1996. Damage to DNA by reactive oxygen and nitrogen species: Role in inflammatory disease and progression to cancer. *Biochem. J.* 313: 17-29.

Wylie, A.G. and Candela, P.A. 2015. Methodologies for Determining the Sources, Characteristics, Distribution, and Abundance of Asbestiform and Nonasbestiform Amphibole and Serpentine in Ambient Air and Water. *J. Toxicol. Environ. Health B* 18: 1-42.

Young, R.A. 1993. Introduction to the Rietveld method: In Young RA (ed) The Rietveld method. Oxford:1-38.

Zanella, C. L., Posada, J., Tritton, T. R., and Mossman, B. T. 1996. Asbestos causes stimulation of the extracellular signal-regulated kinase 1 mitogen-activated protein kinase cascade after phosphorylation of the epidermal growth factor receptor. *Cancer Res*. 56: 5334-5338.

Zanella, C. L., Timblin, C. R., Cummins, A., Jung, M., Goldberg, J., Raabe, R., Tritton, T. R., and Mossman, B. T. 1999. Asbestos-induced phosphorylation of epidermal growth factor receptor is linked to c-fos and apoptosis. *Am. J. Physiol.-Lung Cell. Mol. Physiol*. 277: 684-693.

Zebedeo, C. N., Davis, C., Peña, C., Ng, K. W., and Pfau, J. C. 2014. Erionite induces production of autoantibodies and IL-17 in C57BL/6 mice. *Toxicol. Appl. Pharmacol*. 275: 257-264.

ACKNOWLEDGMENTS

Firstly, many thanks are due to my tutor Prof. Michele Mattioli, who believed in this project and in me. His encouragement, wise counsel and patience, but also his guidance and support have been invaluable to me.

I would like to thank, in no particular order, Prof. Emma Salvioli Mariani, Prof. Danilo Bersani, Dr. Jasmine Rita Petriglieri (University of Parma), Prof. Paolo Ballirano and Dr. Alessandro Pacella (University of Roma "La Sapienza"), Dr. Meral Dogan and Prof. Ahmet Umran Dogan (University of Iowa), Prof. Rodorico Giorgi (University of Florence), Dr. Raul Carampin (University of Padova), and Dr. Laura Valentini, Prof. Alberto Renzulli, Dr. Pierluca Arcangeli, Prof. Maria Francesca Ottaviani, Dr. Michela Cangiotti, Dr. Giuseppe Avella, Prof. Elisabetta Falcieri, Dr. Michela Battistelli and Dr. Sara Salucci (University of Urbino). All of them have contributed to the collection and analysis of the data of this PhD project.

Many thanks are due to "Associazione Geologica Mineralogica Veronese" (AGMV), in particular to Amleto Longhi, Dino Agnoli, Franco Bressan and Franco Filippi, and to Matteo Boscardin, Vittorio Mattioli, Dr. Marco Cenni, and Prof. Ahmet Umran Dogan who kindly provided most of the studied samples.

Moreover, thanks are due to Società Italiana di Mineralogia e Petrologia (SIMP) for the student grants, and to European Mineralogical Union (EMU), in particular to Prof. Alessandro Gualtieri, Prof. Roberta Oberti, Prof. Jurai Majzlan and Dr. Kevin Murphy, for the received award.

I would also like to thank the reading committee, Prof. Paolo Ballirano and Prof. Mario Tribaudino for their critical review of my PhD thesis and accepting it.

Therefore, thanks to my friends and colleagues Dr. Fabrizio Frontalini and Dr. Matteo Moretti for their ideas and suggestions on my PhD project and this thesis.

On the personal level, special thanks to my parents Fausto and Andreina, my sister Veronica and my girlfriend, Elena, because they always encouraged me, supported and helped me over the years.

SUPPLEMENTARY MATERIALS

Supplementary material Chapter 3

Table S1. List of erionite occurrences in the world and associated references.

Antarctica (Vezzalini et al., 1994; Galli et al., 1996);
Australia (England and Ostwald, 1979; Birch, 1987, 1988; Passaglia et al., 1998).
Austria (Zirkl, 1963; Waltinger and Zirkl, 1974);
Bulgaria (Ivanova et al., 2001; Kirov et al., 2011);
Canada (Wise and Tschernich, 1976; Tschernich and Wise, 1982);
Canary Islands (Strasser and Kirchner, 2006);
Crimea (Suprychev and Prokhorov, 1986);
Czech Republic (Rychly et al., 1982);
Faròer Islands, Denmark (Hey, 1959);
Finland (Lehtinen, 1976);
France (Pongiluppi, 1976; Gualtieri et al., 1998);
Georgia (Batiashvili and Gvakhariya, 1968);
Germany (Rinaldi et al., 1975; Rinaldi, 1976; Betz and Hentschel, 1978; Hentschel, 1986);
Iceland (Metropolis, 1986; Saemundsson and Gunnlaugsson, 2002);
Italy (Passaglia and Galli, 1974; Pongiluppi et al., 1974; Giovagnoli and Boscardin, 1979; Passaglia and Tagliavini, 1995; Cenni, 2009; Mattioli et al., 2016; Giordani et al., 2016);
Japan (Harada et al., 1967; Kawahara et al., 1967; Shimazu and Kawakami, 1967; Shimazu and Yoshida, 1969; Muchi et al., 1972; Shimazu and Mizota, 1972; Schlenker et al., 1977; Matsubara et al., 1978; Yamamoto et al., 1980);
Kenya (Surdam and Eugester, 1976);
Korea (Noh and Kim, 1986);
Mexico (De Pablo-Galán and Chávez-García, 1996; Garcia-Sosa and Rios-Solache, 1997; Ilgren et al., 2008; Kliment et al., 2009; Ortega-Guerrero and Carrasco-Nùñez, 2014; Ortega-Guerrero et al., 2015);
New Zeland (Sameshima, 1978; Aldridge and Pope, 1981);
Northern Ireland (Passaglia et al., 1998);
Russia (Belitskii and Bukin, 1968; Alberti et al., 1997);
Scotland (Machperson and Livingstone, 1982; Passaglia et al., 1998);
Tanzania (Hay, 1964, 1966; Surdam and Sheppard, 1978);
Turkey (Baris et al., 1978, 1979; Artvinli e Baris, 1979; Mumpton, 1979; Emri et al., 2002; Dogan, 2003; Dogan et al., 2006; Carbone et al., 2007);
USA (Sheppard, 1996; Van Gosen et al., 2013);
USA, Arizona (Kamb and Oke, 1960; Wise and Tschernich, 1976; Thomssen, 1983; Anthony et al., 1995);
USA, California (Sheppard and Gude, 1965, 1969);
USA, Colorado (Larsen and Crossey, 2000);
USA, Idaho (Reed, 1937; Sheppard, 1991);
USA, Montana (Goodman and Pierson, 2010);
USA, Nevada (Deffeyes, 1959; Papke, 1972; Barrows, 1980; Gude and Sheppard, 1981);
USA, New Mexico (Gude and Sheppard, 1988);
USA, North Dakota (Goodman and Pierson, 2010; Lowers et al., 2010; Saini-Eidukat and Triplet, 2014);

USA, Oregon (Eakle, 1898; Staples, 1957; Staples and Gard, 1959; Kamb and Oke, 1960; Wise and Tschernich, 1976, 1978; Howard, 1978; Sheppard et al., 1983; Ballirano et al., 2009);
USA, South Dakota (Sheppard, 1996; Goodman and Pierson, 2010);
USA, Utah (Sheppard, 1996);
USA, Washington (Kamb and Oke, 1960; Raymond and Tillson, 1968; Wise and Tschernich, 1976; Ames, 1980);
USA, West Virginia (Haynes, 2012);
USA, Wyoming (Deffeyes, 1959; Honda and Muffler, 1970; Bargar and Beeson, 1981; Bargar et al., 1981; Bargar and Keith, 1995);
Vietnam (Dogan et al., 2011).

Cited references

Alberti, A., Martucci, A., Galli, E., and Vezzalini, G. 1997. A re-examination of the crystal structure of erionite. *Zeolites* 19: 349-352.

Aldridge, L. P., and Pope C. G. 1981. Infrared and adsorption studies of a New Zealand erionite. *N. Z. J. Sci*. 24: 263-271.

Ames, L. L. 1980. Hanford basalt flow mineralogy. Battelle Memorial Institute report for Rockwell Hanford Operations, p. 447.

Anthony, J. W., Williams S. A., Bideaux R. A., and Grant R. W. 1995. Mineralogy of Arizona, 3rd.ed. The University of Arizona Press/Tucson, p. 216.

Artvinli, M., and Baris, Y. I. 1979. Malignant mesothelioma in a small village in the Anatolian region of Turkey: An epidemiologic study. *J. Natl. Cancer Inst.* 63: 17-22.

Ballirano, P., Andreozzi, G.B., Dogan, M., and Dogan, A.U. 2009. Crystal structure and iron topochemistry of erionite-K from Rome, Oregon, U.S.A. *Am. Mineral*. 94: 1262-1270.

Bargar K. E., Beeson M. H., and Keith, T. E. C. 1981. Zeolites in Yellowstone National Park. *Miner. Record*. 12: 29-38.

Bargar, K. E., and Beeson, M. H. 1981. Hydrothermal alteration in research drill hole Y-2, Lower Geyser Basin, Yellowstone National Park Wyoming. *Am. Mineral*. 66(5-6): 473-490.

Bargar, K. E., and Keith, T. E. C. 1995. Calcium zeolites in rhyolitic drill cores from Yellowstone National Park, Wyoming. In D.W. Ming, F.A. Mumpton, F.A. (Eds.), Natural zeolites, 1993, Occurrence, properties, use. Brockport, New York: International Committee on Natural Zeolites.

Baris, Y. I., Artvinli, M., and Sahin, A. A. 1979. Environmental mesothelioma in Turkey. *Ann. N. Y. Acad. Sci* 330: 423-432.

Baris, Y. I., Sahin, A. A., Ozesmi, M., Kerse, I., Ozen, E., Kolacan, B., Altinörs, M., and Göktepeli, A. 1978. An outbreak of pleural mesothelioma and chronic fibrosing pleurisy in the village of Karain/Urgüp in Anatolia. *Thorax* 33: 181-192.

Barrows, K. J. 1980. Zeolitization of Miocene volcanoclastic rocks, southern Desatoya Mts., Nevada. *Geol. Soc. Am. Bull*. 91: 199-210.

Batiashvili, T. V., and Gvakharia, G. V. 1968. Erionite found for the first time in Georgia. *Doklady Earth Sci. Russian Acad. Sci*. 179: 122-124.

Belitskiy I. A., and Bukin, G. V. 1968. First find of erionite in the USSR. *Doklady Earth Sci. Russian Acad. Sci.* 178: 103-106.

Betz, V., and Hentschel, G. 1978. Offretit und Erionit von Gedern (Vogelsberg). *Geol. Jahrb. Hessen* 106: 419-421.

Birch, W. D. 1987. Zeolites from Jindivick, Victoria. *Aust. Mineral*. 2: 15-19.

Birch, W. D. 1988. Zeolites from Phillip Island and Flinders, Victoria. *Min. Rec*. 19: 451-460.

Carbone, M., Emri, S., Dogan, A. U., Steele, I., Tuncer, M., Pass, H. I., and Baris, Y. I. 2007. A mesothelioma epidemic in Cappadocia: Scientific developments and unexpected social outcomes. *Nat. Rev. Cancer.* 7: 147-154.

Cenni, M. 2009. Le mineralizzazioni secondarie nelle rocce basaltiche: esempi dai Monti Lessini (Italia). *PhD thesis*, University of Urbino, Italy, 193 pp.

De Pablo-Galán, L., and Chávez-García, M. L. 1996. Diagenesis of oligocene vitric tuffs to zeolites, Mexican volcanic belt. *Clays Clay Miner*. 44(3): 324-338.

Deffeyes, K. S. 1959. Erionite from Cenozoic tuffaceous sediments, Central Nevada. *Am. Mineral*. 44: 501-509.

Dogan, A. U., Baris, Y. I., Dogan, M., Emri, S., Steele, I., Elmishad, A. G., Carbone, M. 2006. Genetic predisposition to fiber carcinogenesis causes a mesothelioma epidemic in Turkey. *Cancer Res*. 66: 5063-5068.

Dogan, A. U. 2003. Zeolite Mineralogy and Cappadocian Erionite. *Indoor Built Environ.* 12: 337-342

Eakle, A. S. 1898. Erionite, a new zeolite. *Am. J. Sci.* 6: 66-68.

Emri, S., Demir, A., Dogan, M., Akay, H., Bozkurt, B., Carbone, M., and Baris, I. 2002. Lung diseases due to environmental exposures to erionite and asbestos in Turkey. *Toxicol. Lett.* 127: 251-257.

England, B. M., and Ostwald, J. 1979. Levyne-offretite intergrowths from Tertiary basalts in the Merriwa district, Hunter Valley, New South Wales, Australia. *Aust. Mineral*. 25: 117-119.

Galli, E., Quartieri, S., Vezzalini, G., and Alberti, A. 1996. Gottardiite, a new high-silica zeolite from Antarctica: the natural counterpart of synthetic NU-87. *Eur. J. Mineral*. 8: 687-693.

Garcia-Sosa, I., and Rios-Solache, M. 1997. Sorption of cobalt and cadmium by Mexican erionite. *J Radioanal. Nucl. Chem*. 218(1): 77-80.

Giordani, M., Mattioli, M., Dogan, M., and Dogan, A. U. 2016. Potential carcinogenic erionite from Lessini Mounts, NE Italy: morphological, mineralogical and chemical characterization. *J. Toxicol. Environ. Health A*. 79(18): 808-824.

Giovagnoli, L. and Boscardin, M. 1979. Ritrovamento di levyna ed erionite a Montecchio Maggiore (Vicenza). *Riv. Min. It*. 1(2): 44-45.

Goodman, B. S., and Pierson, M. P. 2010. Erionite, a naturally occurring fibrous mineral hazard in the tri-state area of North Dakota, South Dakota, and Montana. *Geol. Soc. Am. Abstracts with Programs* 42(3): 5.

Gualtieri, A., Artioli, G., Passaglia, E., Bigi, S., Viani, A., and Hanson, J. C. 1998. Crystal structure-crystal chemistry relationships in the zeolites erionite and offretite. *Am. Mineral.* 83: 590-606.

Gude, A. J., and Sheppard, R. A. 1981. Woolly erionite from the Reese River zeolite deposit, Lander County, Nevada, and its relationship to other erionites. *Clays Clay Miner.* 29: 378-384.

Gude, A. J., 3rd, Sheppard, R. A. 1988. A zeolitic tuff in a lacustrine facies of the Gila Conglomerate near Buckhorn, Grant County, New Mexico. *U.S. Geol. Surv. Bull*. 1763: 22.

Harada, K., Iwamoto, S., and Kihara, K. 1967. Erionite, phillipsite and gonnardite in the amygdales of altered basalt from Maze, Niigata Prefecture, Japan. *Am. Mineral*. 52: 1785-1794.

Hay, R. L. 1966. Zeolites and zeolitic reactions in sedimentary rocks. *Geol. Soc. Spec. Pap*. 85: 1-130.

Hay, R. L. 1964. Phillipsite of saline lakes and soils. *Am. Mineral*. 49: 1366-1387

Haynes, P. E. 2012. Zeolites and associated minerals from Sugar Grove, Pendelton County, West Virginia. New Mexico Mineral Symposium, Abstracts p. 19-20.

Hentschel, G. 1986. Paulingit und andere Seltene Zeolithe in einem gefritteten Sandsteineinschluss im Basalt von Ortenberg (Vogelsberg). *Geol. Jahrb. Hessen* 114: 249-256.

Hey, M. H. 1959. A new occurrence of erionite. *Mineral. Mag*. 32: 343.

Honda, S., and Muffler, L. J. P. 1970. Hydrothermal alteration in core from research drill hole Y-1, Upper Geyser Basin, Yellowstone National Park, Wyoming. *Am. Mineral*. 55: 1714-1737.

Howard, D. G. 1978. Zeolites from Aneroid Lake, Wallowa County, Oregon. *Ore. Bin*. 40: 117.

Ilgren, E. B., Brena, M. O., Larragoitia, J. C., Navarrete, G. L., Brena, A. F., Krauss, E., and Feher, G. 2008. A reconnaissance study of a potential emerging Mexican mesothelioma epidemic due to fibrous zeolite exposure. Indoor Built. Environ. 17: 496-515.

Ivanova, R., Yanev, Y., Iliev, Tz., Koleva, E., Popova, T., and Popov, N. 2001. Mineralogy, chemistry and ion- exchange properties of the zeolitized tuffs from the Sheinovets caldera, Eastern Rhodopes (South Bulgaria). In: Study in Surface Science Catalysis (Galarneau, A., Di Renzo, F., Fajula, F., Verdine, J. Eds.). Elsevier, Amsterdam. 135: 95-103.

Kamb, W. B., and Oke, W. C. 1960. Paulingite, a new zeolite, in association with erionite and filiform pyrite. Am. Mineral. 45: 79-91.

Kawahara, A., Takano, Y., Takabatake, M., and Uratani, Y. 1967. The composition and the crystal structure of erionite from Maze, Niigata prefecture, Japan. Scientific Papers of the College of General Education, University of Tokyo. 17(2): 237-248.

Kirov, G., Samajova, E., Nedialkov, R., and Stanimirova, T. S. 2011. Alteration processes and products of acid pyroclastic rocks in Bulgaria and Slovakia. *Clay Miner*. 46: 279-294.

Kliment, C. R., Clemens, K., and Oury, T. D. 2009. North american erionite-associated mesothelioma with pleural plaques and pulmonary fibrosis: A case report. *Int. J. Clin. Exp. Pathol.* 2: 407-410.

Larsen, D., Crossey, L. J. 2000. Sedimentary petrology and authigenic mineral distributions in the Oligocene Creede Formation, Colorado, United States. *Geol. Soc. Spec. Pap*. 346: 179-208.

Lehtinen, M. 1976. Lake Lappajärvi, a meteorite impact site in western Finland. *Geol. Survey Finland Bull.* 282: 1-92.

Lowers, H. A., Adams, D. T., Meeker, G. P., and Nutt, C. J. 2010. Chemical and morphological comparison of erionite from Oregon, North Dakota, and Turkey. *U.S. Geol. Surv.* 1286: 13. Open-File Report.

Macpherson, H. G., and Livingstone, A. 1982. Glossary of Scottish mineral species 1981. Scot. J. Geol. 18: 1-48.

Matsubara, S., Tiba, T., and Kato, A. 1978. Erionite in welded tuff from Ashio, Tochigi Prefecture, *Japan. Bull. Nat. Sci. Mus. Ser. C* 4: 1-6.

Mattioli, M., Cenni, M., and Passaglia, E. 2016a. Secondary mineral assemblages as indicators of multi stage alteration processes in basaltic lava flows: Evidence from the Lessini Mountains, Veneto Volcanic Province, Northern Italy. *Per. Mineral*. 85: 1-24.

Metropolis, W. 1986. Harvard's mineralogical tour of Iceland. *Rocks Miner*. 61: 63-68.

Muchi, M., Yamamoto, H., and Tejima, M. 1972. Erionite from Naru-Shima, Nagasaki Prefecture. *Geol. Soc. Jap*. meeting, preprint.

Mumpton, F. A. 1979. A reconnaissance study of the association of zeolites with mesothelioma occurrences in central Turkey. *U.S. Geol. Surv.* 55: 79-954. Open-File Report.

Noh, J. H, and Kim, S. J. 1986. Zeolites from tertiary tuffaceous rocks in Yeongil area, Korea. *Stud. Surf. Sci. Catal*. 28: 59-66.

Ortega-Guerrero, M A., Carrasco-Núñez, G., Barragán-Campos, H., and Ortega, M. R. 2015. High incidence of lung cancer and malignant mesothelioma linked to erionite fibre exposure in a rural community in Central Mexico. *Occup. Environ. Med.* 72: 216-218.

Ortega-Guerrero, M. A., and Carrasco-Nùñez, G. 2014. Environmental occurrence, origin, physical and geochemical properties, and carcinogenic potential of erionite near San Miguel de Allande, Mexico. *Environ. Geochem. Health* 36: 517-529.

Papke, K. G. 1972. Erionite and other associated zeolites in Nevada. *Nev. Bur. Min. Geol. Bull*. 79: 32.

Passaglia, E., Artioli, G., and Gualtieri, A. 1998. Crystal chemistry of the zeolites erionite and offretite. *Am. Mineral*. 83: 577-589.

Passaglia, E., and Galli, E. 1974. Levyne and erionite from Sardinia, Italy. *Contrib. Mineral. Petr*. 43: 253-259.

Passaglia, E., and Tagliavini, A. 1995. Erionite from Faedo, Colli Euganei, Italy. *Neues Jb. Miner. Monat.* 185-191.

Pongiluppi, D. 1976. Offretite, garronite and other zeolites from ‘‘Central Massif’’, France. *Bull. Soc. Fr. Mineral. Cristallog*. 99: 322-327.

Pongiluppi, D., Passaglia, E., and Galli, E. 1974. Su alcune zeoliti della Sardegna. *Soc. It. Min. Petr*. 30: 77-100.

Raymond, J. R. and Tillson, D. D. 1968. Evaluation of thick basalt sequence in south central Washington. Geophysical and hydrological exploration of the Rattlesnake Hills deep stratigraphic test well. Water and Land Resources Environmental and Radiological Sciences, Pacific Northwest Laborator, p. 120.

Reed, J. C. 1937. Amygdales in Columbia River lavas near Freedom, Idaho. National Research Council Transactions for the American Geophysical Union, 18th Annual Meeting, 239-243.

Rinaldi, R., Smith, J. V., and Jung, G. 1975. Chemistry and paragenesis of faujasite, phillipsite and offretite from Sasbach, Kaiserstuhl, Germany. *Neues Jb. Mineral. Monatsh* 10: 433-443.

Rinaldi, R. 1976. Crystal chemistry and structural epitaxy of offretite-erionite from Sasbach, Kaiserstuhl. *Neues Jb. Miner. Monat.* 1976: 145-156.

Rychly, R., Danek, M., Siegl, J. 1982. Structural epitaxy of offretite-erionite from Prackovice nad Labem, Bohemia. *Chem Erde* 41: 263-268.

Saemundsson, K., and Gunnlaugsson, E. 2002. Icelandic rocks and minerals, Mál og menning, Reykjavik, p. 233.

Saini-Eidukat, B., and Triplet, J. W. 2014. Erionite and offretite from the Killdeer Mountains, Dunn County, North Dakota, USA. *Am. Mineral*. 99: 8-15.

Sameshima, T. 1978. Zeolites in tuff beds of the Miocene Waitamata group, Auckland province, New Zealand. In: Sand, L. B., Mumpton, F. A., editors. Natural zeolites. Oxford: Pergamon. p 309-318.

Schlenker, J. L., Pluth, J. J., and Smith, J. V. 1977. Dehydrated natural erionite with stacking faults of the offretite type. *Acta Cryst. B* 33: 3265-3268.

Sheppard, R. A., and Gude, A. J. 1965. Zeolitic authigenesis of tuffs in the Ricardo Formation, Kern County, Southern California, *U.S. Geol. Surv. Professional Paper*, p. 525.

Sheppard, R. A. and Gude, A. J. 1969. Diagenesis of tuffs in the Barstow formation, Mud Hills, San Bernandino County, California. *U.S. Geol. Surv. Professional Paper*, p. 534.

Sheppard, R. A., and Gude, A. J., Mumpton, F. A. 1983. Zeo Trip. International Committee on Natural Zeolites. Brockport.

Sheppard, R. A. 1991. Zeolitic diagenesis of tuffs in the Miocene Chalk Hills Formation, western Snake River Plain, Idaho. *U.S. Geol. Surv. Bull.* 1963: p. 27.

Sheppard, R. A. 1996. Occurrences of erionite in sedimentary rocks of the western United States. *U.S. Geol. Surv*. 18: p. 24. Open-File Report

Shimazu, M., and Yoshida, S. 1969. Occurrence of erionite from Iwayaguchi District, Osada area, Niigata prefecture. *J. Geol. Soc. Japan* 75(7): 389-390.

Shimazu, M., and Kawakami, T. 1967. Erionite from Mazè, Niigata prefecture. *J. Japan Assoc. Mineral. Petrol. Econ. Geol*. 57: 68-71.

Shimazu, M., and Mizota, T. 1972. Levyne and erionite from Chojabaru, Iki Island, Nagasaki Prefecture, Japan. *J. Japan Assoc. Mineral. Petrol. Econ. Geol.* 67: 418-424.

Staples, L. W. 1957. X-ray study of erionite, a fibrous zeolite. *Geol. Soc. Am. Bull*. 68: 1847.

Staples, L. W., and Gard, J. A. 1959 The fibrous zeolite erionite: its occurrence, unit cell, and structure. *Mineral. Mag*. 322: 261-281.

Strasser, A., and Kirchner, E. 2006. Minerale aus einem Alkali-Basalt-Differentiat vom Risco Famara, Lanzarote, Kanarische Inseln. *Aufschluss* 57: 335-338.

Suprychev, V. A., and Prokhorov, I. G. 1986. Erionit iz keratofirovykh vulkanitov Karadagskogo zapovednika v Krymu (Erionite from keratophyre volkanites of the Karadag Reserve in the Crimea). *Mineralogicheskiy Sbornik* 40(1): 85-88.

Surdam, R. C., and Eugster, H. P. 1976. Mineral reactions in the sedimentary deposits of the Lake Magadi region, Kenya. *Geol. Soc. Am. Bull*. 87: 1739-1752.

Surdam, R. C., and Sheppard, R. A. 1978. Zeolites in saline, alkaline lake deposits. In: Sand L.B., Mumpton F.A., editors. Natural zeolites: occurrence, properties, use. Oxford: Pergamon. 145-199.

Thomssen, R. W. 1983. The minerals of Malpais Hill, Pinal County, Arizona. *Mineral. Record* 14: 109-113.

Tschernich, R. W., and Wise, W. S. 1982. Paulingite: variations in composition. *Am Mineral*. 67: 799-803.

Van Gosen, B. S., Blitz, T. A., Plumlee, G. S., Meeker, G. P., and Pierson, M. P. 2013. Geologic occurrences of erionite in the United States: an emerging national public health concern for respiratory disease. *Environ. Geochem. Health.* 35: 419-430.

Vezzalini, G., Quartieri, S., Rossi, A., and Alberti, A. 1994. Occurrence of zeolites from Northern Victoria Land (Antarctica). *Terra Antarctica* 1: 96-99.

Waltinger, H., and Zirkl, E. J. 1974. Raster elektronen mikroskopische aufnahmen von Erionit aus Kollnitz, Lavanttal, Karnten. Der Carinthia 164: 124-135.

Wise W.S. and Tschernich R.W. 1976. The chemical compositions and origin of the zeolites offretite, erionite and levyne. *Am. Mineral*. 61: 853-863.

Wise, W. S., and Tschernich, R. W. 1978. Dachiardite bearing zeolite assemblages in the Pacific Northwest. In L. B. Sand, F. A. Mumpton. Editors. Natural zeolites: Occurrence, properties, use. Oxford: Pergamon. 105-111.

Yamamoto, H., Mucci, M., and Teshima, M. 1980. Erionite from Narushima, Nagasaki Prefecture, Japan. Science Reports of the Department of Geology, Kyushu University 13: 201-207.

Zirkl, E. J. 1963. Neues über den basalt von kollnitz im Lavanttal, Kärnten. *Tschermaks Mineral. Petrol. Mitt*. 8: 96-139.

Table S2. Fractional coordinates, isotropic displacement parametres, site multiplicity and occupancy, and site scattering (*s.s.*) of samples BV201. Si, Al site partition from Jones' (1968) determinative curves. The scattering power of Ca has been used to model the Ca1, Ca2 and Ca3 extra-framework sites.

Site	*x*	y	z	B_{iso}(Å^2)	Site occ.	s.s.(e$^-$)	Proposed site partition	s.s.(e$^-$) from site partition
			Framework					
T1	0.2337(3)	-0.0003(4)	0.10433(15)	0.76(4)	1		$Si_{17.22}Al_{6.76}$	
T2	0.0981(3)	0.4276(4)	1/4	0.76(4)	1		$Si_{8.50}Al_{3.50}$	
O1	0.3495(4)	0.0273(5)	0.6604(5)	1.33(11)	1			
O2	0.0981(3)	2*x*	0.1269(6)	1.33(11)	1			
O3	0.1285(4)	2*x*	0.6366(6)	2.82(20)	1			
O4	0.2686(6)	0	0	1.33(11)	1			
O5	0.2341(5)	2*x*	1/4	2.82(20)	1			
O6	0.4535(6)	2*x*	1/4	2.82(20)	1			
			EF cations					
Ca1	1/3	2/3	0.944(2)	10.8(3)	0.56(3)*	45(2)	$Mg_{0.26}Na_{0.39}Ca_{1.16}$	31.4
Ca2	1/3	2/3	0.1225(13)	10.8(3)	0.414(8)	33.1(7)	$Ca_{1.65}$	33.0
Ca3	1/3	2/3	0.622(8)	10.8(3)	0.17(3)	14(2)	$Ca_{0.70}$	14.0
K1	0	0	1/4	2.42(20)	1	38	$K_{2.00}$	38.0
K2	1/2	0	0	2.42(20)	0.089(9)	10.2(11)	$K_{0.21}$	4.0
					$\Sigma_{cat.}$	140(7)		120.4
			Water molecules					
OW7	0.24(2)	2*x*	3/4	5.37(16)	0.05(7)	2(3)		
OW8	0.2447(6)	2*x*	-0.0067(14)	10.8(3)	0.747(10)	71.7(10)		
OW9	0.4541(12)	2*x*	0.904(2)	10.8(3)	0.666(20)	63.9(19)		
OW10	0.4196(17)	2*x*	0.680(3)	10.8(3)	0.71(3)	68(3)		
OW11	0.2447(15)	2*x*	0.688(3)	10.8(3)	0.432(19)	41.5(18)		
OW12	0.4407(12)	2*x*	0.019(2)	10.8(3)	0.581(20)	55.8(19)		
					Σ_{water}	303(13)		

Supplementary material Chapter 5

Supplementary Data 1 (SD1)

Details of investigated materials

A total of four samples, selected from different localities, have been investigated in this study. Two samples represent erionite: the sample GF1 is from Reese River deposits (Nevada, USA), where erionite occurs in a lacustrine environment as joint fillings in brownish-gray mudstone stratigraphically just beneath a thick gray vitric tuff, and the sample MD08-114 (MD8 for simplicity) is from Karain (Cappadocia, Turkey), where a volcanic-sedimentary succession together with lacustrine sediments and andesitic lava flows extensively crop out and zeolites are found in several members of this succession. The sample BV12 is representative of offretite from Lessini Mounts (northern Italy) where zeolites are widespread within lava flows, tuffs, and volcanoclastic deposits of the Veneto volcanic province. The fourth sample (SC1) is another prismatic zeolite called scolecite from Poone (Deccan Trap, India) with a chemical composition of $Ca(Al_2Si_3O_{10})$ $3H_2O$; this zeolite is considered a non-carcinogenic, non-fibrous mineral and has been used for comparison.

Details of experimental methods

SEM-EDS & EPMA

Morphological observations were achieved with a Quanta FEI 200 ESEM equipped with an energy dispersive spectrometer (EDS) for semi-quantitative chemical analyses. The micro-chemical characterization was performed using a JEOL 6400 SEM equipped with an EDX Genesis EDS system. Operating conditions were 15 kV accelerating voltage, 11 mm working distance, 0° tilt angle and 1 μm beam diameter. An first set of data was acquired with 100 s counting time. To test the reliability of SEM-EDS results, two duplicate of each samples were prepared for electron probe micro analysis (EPMA) by embedding a fraction of fibers in epoxy resin. Compositions were determined using a Cameca SX50 EPMA equipped with wavelength-dispersive spectrometry (WDS), with the following conditions: 10 s counting time, beam diameter 20 μm, accelerating voltage 15 kV, beam current 20 nA. The comparison with EMPA highlighted a significant reduction of the alkali metals (particularly Na) in the first set of SEM-EDS chemical data. As widely suggested in literature, in order to minimize the alkali metal migration, we acquired another set of chemical data using reduced counting times (up to 10 s) and, when possible, using a raster scan-mode to reduce the temperature increase. With these optimized experimental conditions, no significant differences between the EMPA and SEM-EDS data sets were observed, indicating the reliability of the collected data.

Chemical data were collected from 10 to 20 individual point analyses for each sample, depending on the number of crystals available. In elongated crystals or crystal aggregates, at least 3-4 point analyses were performed along the fiber to check for chemical homogeneity. The point analyses of each sample were highly consistent, showing a variation of major elements within 2-3% of the estimated instrumental errors and indicating a high degree of chemical homogeneity within each sample. Silicates, oxides, and pure elements were used as standards; analytical errors are 1-2% rel. and 3-5% rel. for major and minor elements, respectively. The final crystal chemical formula of erionite was calculated on the basis of 36 ($Si+Al+Fe^{3+}$) apfu based on 72 oxygen atoms, while in offretite ($Si+Al+Fe^{3+}$) should be equal to 18 atoms based on 36 oxygen atoms. Here, for a better comparison, all data are calculated on the basis of 72 oxygen atoms. The reliability of the chemical analysis used to determine the erionite and offretite species was evaluated by using a charge balance

error formula (E%) and the Mg-content test. Chemical analyses for zeolites are considered to be reliable if the balance error (E%) is equal to or less than ±10%.

XRPD

After preliminary screening, a sufficient amount of pure crystals was selected from each sample under a binocular microscope on the basis of the absence of any recognizable impurity phase. They were subsequently disaggregated and carefully pulverized in an agate mortar, and the powder was loaded in a 0.7 mm side-opened aluminum holder. XRPD data were collected using a Philips X'Change PW1830 powder diffractometer. Analytical conditions were 35 kV accelerating voltage and 30 mA beam current, with CuKα radiation (λ = 1.54056 Å). The data were collected in Bragg-Brentano geometry from 2 to 65° 2Θ, with a step size of 0.01° 2Θ and 2.5 s counting time per step. Semi-quantitative XRPD analyses were performed on all samples. The following software packages were used for the measurements and subsequent analysis: X'Pert Quantify 3.0 for data collection and instrument control, and X'Pert HighScore 3.0 for semi-quantitative phase analysis.

Surface area - BET

Representative crystals from each sample were carefully screened for phase purity and then prepared for subsequent analyses. To evaluate the specific surface area, the pore volume and the porosity of the various zeolite samples, Brunauer-Emmett-Teller (BET) method based on nitrogen-adsorption measurements was used. Pore size distribution was calculated using Barrett-Joyner-Halenda (BJH) method applied to the nitrogen desorption curve. Nitrogen adsorption isotherms at 77 K were recorded by means of a COULTER SA 3100 surface analyzer. Samples were outgassed under 0.01 atm vacuum at 135°C for 6 hours. After completing the outgas process, when the room temperature was achieved, samples were moved to the test chamber for the measurement.

EPR

Selected zeolite crystals (after purity screening) were taken in oven (under vacuum) at 135 °C for 6 hours to dry them before preparing the samples for EPR analysis. The samples were prepared by equilibrating overnight 200 mg of the various zeolites with 0.5 ml of 1 mM water (Millipore) solution of CAT1 or CAT8. Then, the supernatant solutions were taken away to be analyzed by electron paramagnetic resonance (EPR) using 2 mm tubes in controlled and reproducible conditions to allow reliable evaluations of the spectral intensities. The stock solutions of CAT1 and CAT8 were also analyzed by EPR in the same experimental conditions as the supernatant solutions to evaluate the intensity variations. After filtration, the solid fibers were gently dried onto a filter paper until the solids recovered the apparently dry powder conditions. Each zeolite solid sample was inserted in a 2 mm tube and tested by EPR.
EPR spectra were recorded by means of an EMX-Bruker spectrometer operating at X band (9.5 GHz) and interfaced with a PC (software from Bruker for handling and analysis of the EPR spectra). The temperature was controlled with a Bruker ST3000 variable-temperature assembly cooled with liquid nitrogen. The EPR spectra were recorded for the different samples at 298 K, but temperature scans were performed to verify the adsorption conditions.
In all cases, we controlled the reproducibility of the results by repeating the EPR analysis at least three times in the same experimental conditions for each sample.

Simulation of the EPR spectra

Simulation of the EPR line shape was performed by using Budil and Freed program, and the main parameters extracted from computation were: (a) the A_{ii} components of the hyperfine coupling

tensor A for the coupling between the electron spin (S=1/2) and the nitrogen nuclear spin (I=1; n. of lines= 2I+1=3). For simplicity, we took constant the A_{xx} and A_{yy} values which were first calculated by simulating the most resolved spectrum among those obtained in the present study in slow motion conditions as A_{xx}=3 G, and A_{yy}=9.5 G. Therefore, we only changed A_{zz} which provides a measure of the environmental polarity of the nitroxide group. The accuracy in the calculation of A_{zz} is ± 0.01 G for the well resolved spectra and ± 0.05 G for the broadened ones; (b) the correlation time for the rotational diffusion mobility of the probe (τ). An increase of this parameter indicates an increase of the local microviscosity, corresponding to an increase of probe-surface strength of interaction. The accuracy in this parameter is ± 0.001 ns for the well resolved spectra and ± 0.1 ns for the broadened ones; (c) the line width which increases due to spin-spin interactions, mainly due to probes interacting with close surface sites, or more generally, to paramagnetic species close to each other. The accuracy of this parameter is ± 0.01 G for the well resolved spectra and ± 0.1 G for the broadened ones.

In several cases, the spectra are constituted by different components superimposing each other. These components arise from probes distributed in different environments, mostly different interacting sites. The components were extracted by subtracting different experimental spectra from each other. Then, each component was computed to obtain the structural and dynamical parameters. Finally, the subtraction procedure allowed us to quantify (in relative percentages) to fractions of probes distributed in the different environments. The accuracy of the relative percentages is ± 1 %.

Supplementary Data 2 (SD2)

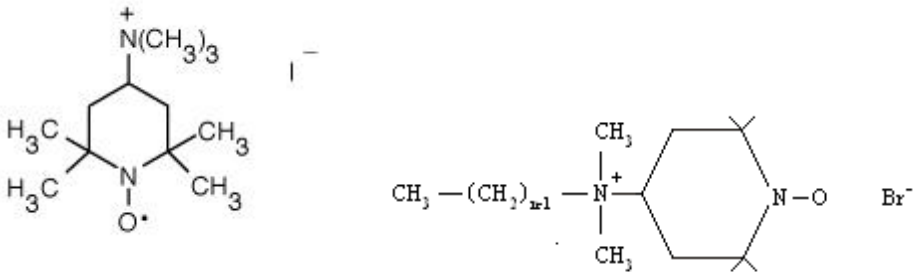

Figure S1. Formulas of CAT1 and CATn probes.

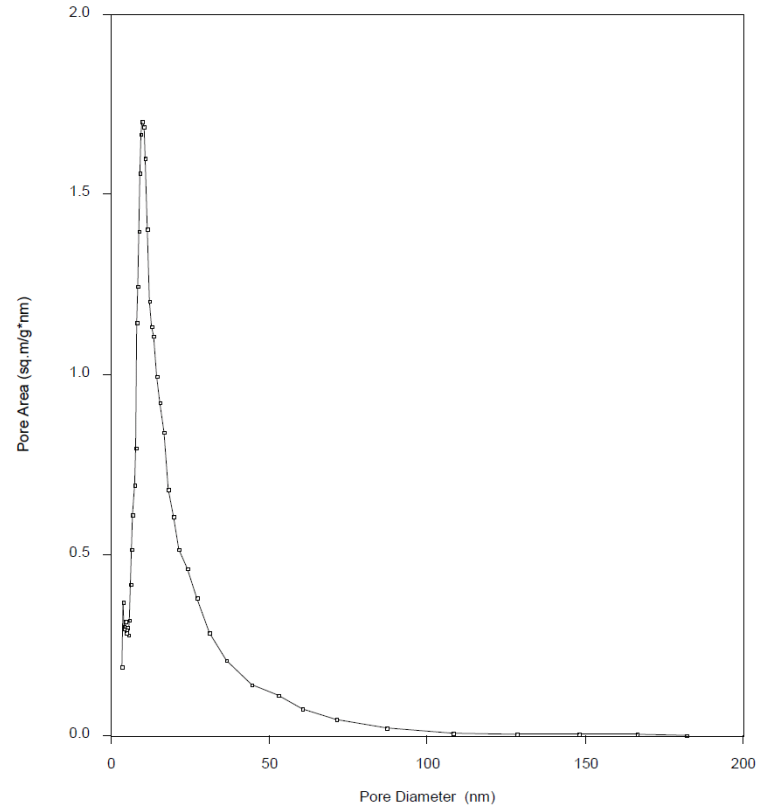

(a)

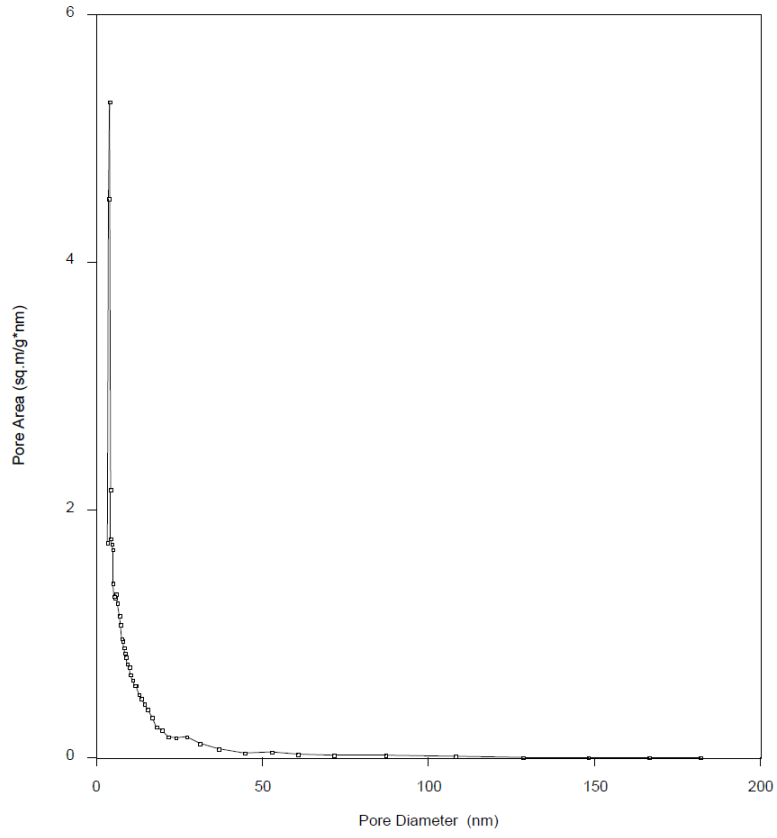

(b)

Figure S2(1). Variation of the pore diameter as a function of the pore area for GF1 (a), MD8 (b), BV12 (c), and SC1 (d).

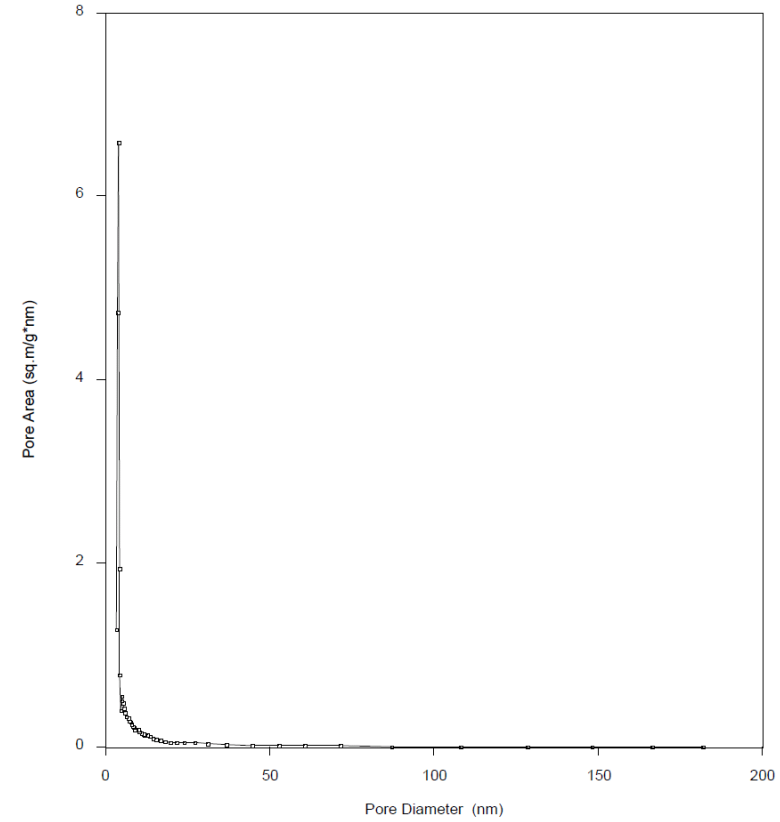

(c)

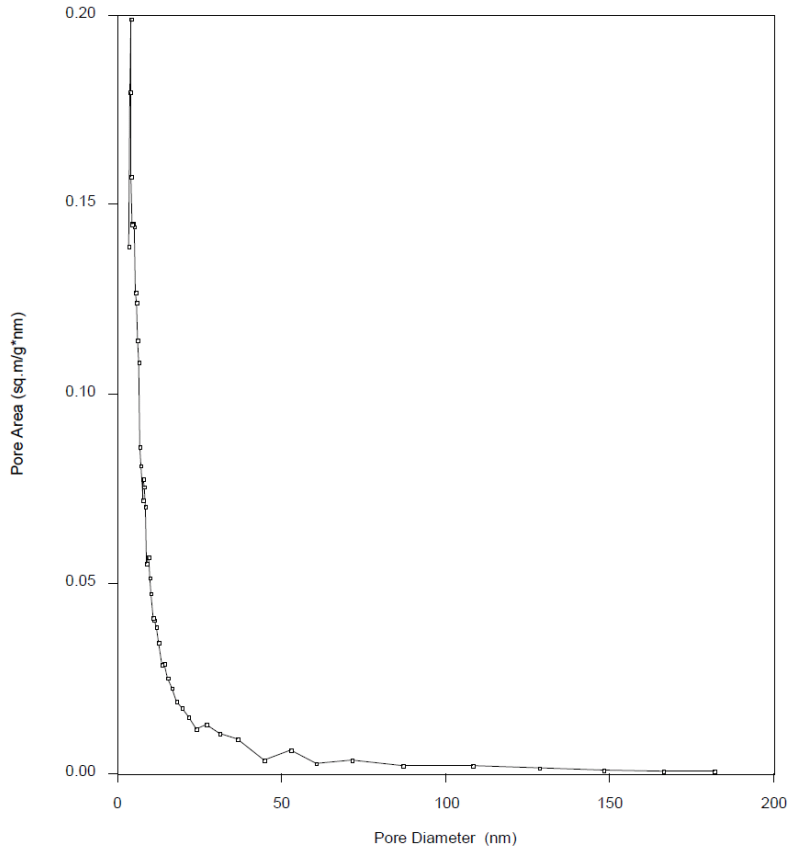

(d)

Figure S2(2). Variation of the pore diameter as a function of the pore area for GF1 (a), MD8 (b), BV12 (c), and SC1 (d).

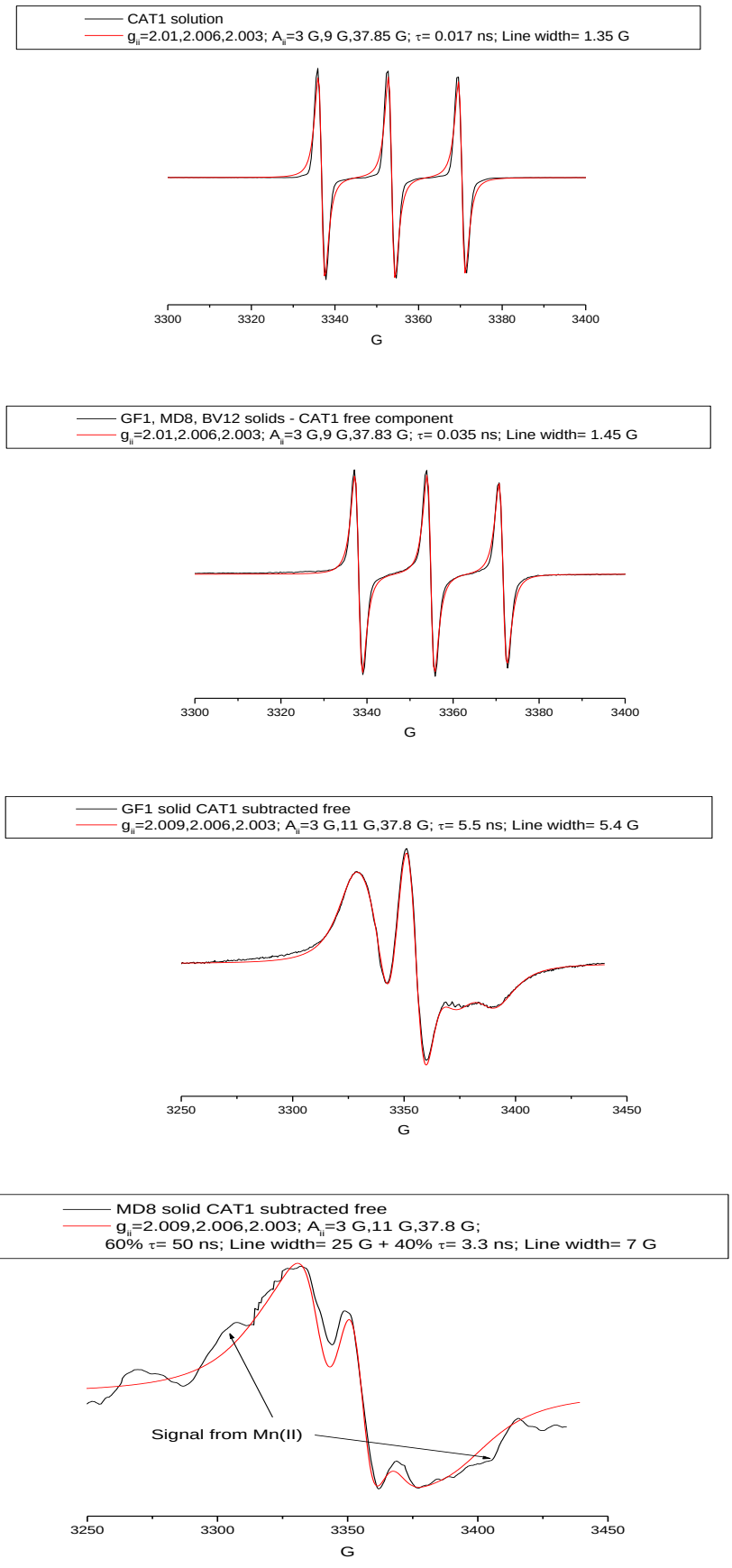

Figure S3(1). Experimental and computed spectra and components for CAT1 and CAT8 in solution and adsorbed onto the solid zeolites.

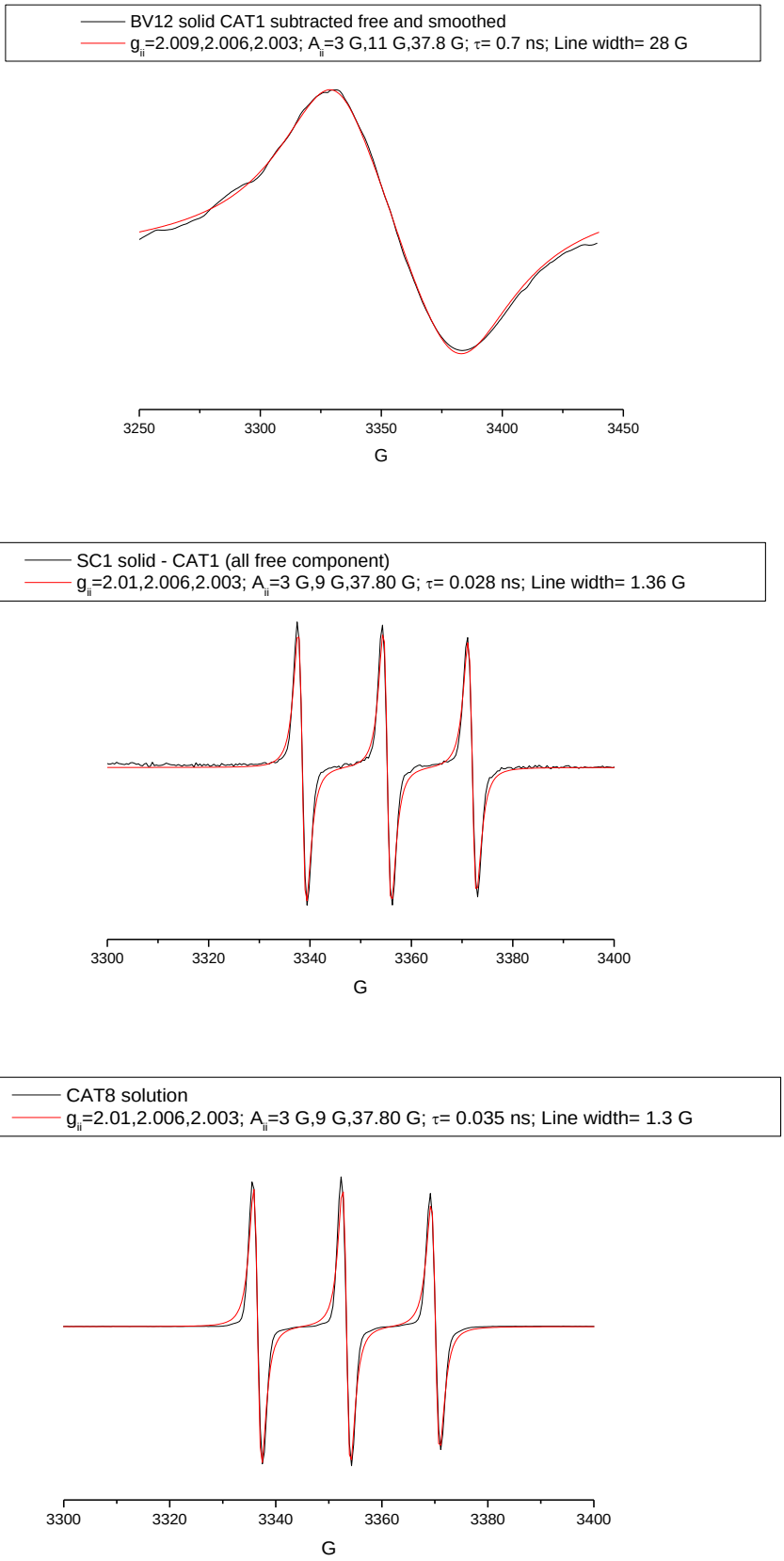

Figure S3(2). Experimental and computed spectra and components for CAT1 and CAT8 in solution and adsorbed onto the solid zeolites.

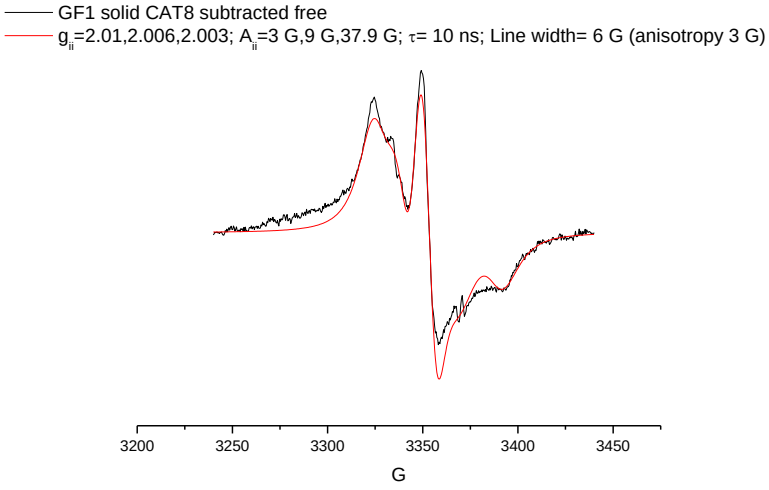

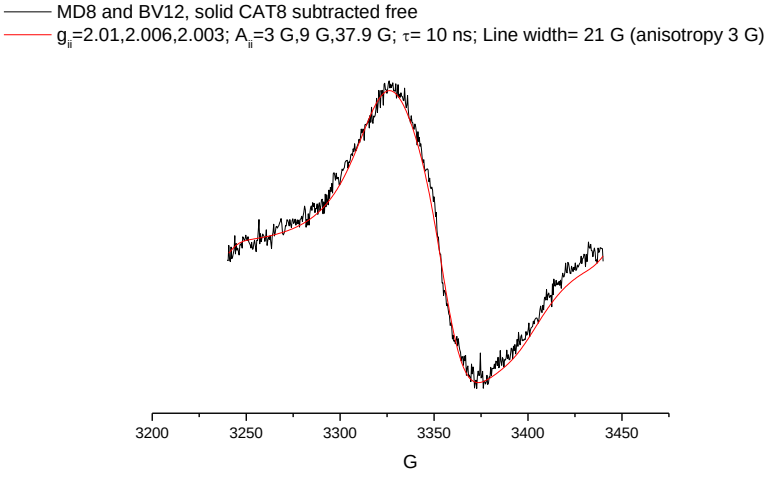

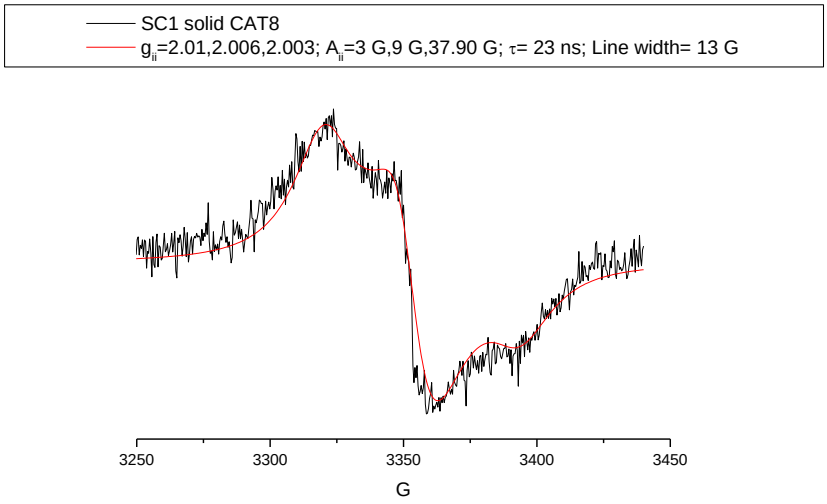

Figure S3(3). Experimental and computed spectra and components for CAT1 and CAT8 in solution and adsorbed onto the solid zeolites.

Supplementary material Chapter 6

Details of investigated materials

The GF1 sample is erionite from Nevada, USA and has been chosen as representative sample of extremely fibrous, asbestiform-type habit. It consists of hair-like fibers with a diameter ranging from 0.5 to 3 μm and an extremely variable length, up to 200-300 μm. The fibers are tensile, elastic and flexible, and each fiber is composed of very thin fibrils of 10-15 nm. The MD8 sample is erionite from Karain, Turkey and is made up of acicular to fibrous crystals with diameter of 2-5 μm and length up to 30 μm, usually associated in parallel growing forming bundles up to 100 μm in length and variable diameters, with a pronounced tendency to separate individual fibrils of 0.5 μm in diameter. The sample BV12 is offretite from Lessini Mountains, Italy, consisting of acicular to fibrous crystals < 1 μm in diameter and 10 to 20 μm in length, frequently grouped in roughly prismatic forms of 40 to 60 μm in length. These prismatic forms have a tendency to separate very small fibers and fibrils, less than 0.5 μm in diameter, with a rigid behavior. The sample SC1 is scolecite from Poone, India and it is made up by prismatic, elongated crystals with diameter ranging from 0.5 mm to 30 μm, and variable lengths, often associated in radiating aggregates; in these crystals, the predisposition to generate thin fibers is very low to absent. This latter is considered a non-carcinogenic fibrous mineral and has been used for comparison.

Experimental details

Preparation of liposome and micelle solutions: Liposome solutions were obtained by drying a chloroform solution of lecithin or DMPC (0.1 M), respectively, also containing the spin probes (0.5 mM), under a nitrogen stream for 30 min so that a thin film is formed at the bottom of a large glass tube and then hydrating the film with a buffer (5 mM K-HEPES at pH 7.2) solution and vortexing the dispersion for 15 s. The liposome preparation was performed at 298 K. For the preparation of the CTAB solutions containing the spin probes, aliquots of the chloroform solutions of the spin probes, necessary to get a final concentration of 0.5 mM in the CTAB solutions, were left evaporating in tubes. Then, the CTAB solution (0.1 M) was added and left equilibrating overnight.

Main parameters extracted from spectral analysis: The main parameters extracted from the spectral analysis were.: (a) the A_{ii} components of the hyperfine coupling tensor **A** for the coupling between the electron spin (S=1/2) and the nitrogen nuclear spin (I=1; n. of lines= 2I+1=3). The average $<A_N>=(A_{xx}+A_{yy}+A_{zz})/3$ provides a measure of the environmental polarity of the nitroxide group. These parameters were first obtained from low temperature (150 K) spectra. Then, the computation in some cases needed to change them in order to obtain the best fitting between the experimental and computed line shapes. The accuracy in this parameter is ± 0.01 G for well resolved EPR signals, while it decreases to ± 0.1 G for broadened-lines signals; (b) the correlation time for the rotational diffusion mobility of the probe (τ). Both the Brownian and the Jump rotational diffusion models were used, which have different relationships between τ and the diffusion constant D, that is, $\tau=1/6D$ and $\tau=1/D$, respectively. An increase of τ indicates an increase of the local microviscosity, corresponding to an increase of probe-surface strength of interaction. The accuracy in this parameter is ± 0.005 ns for well resolved EPR signals, while it decreases to ± 0.1 ns for broadened-lines signals; (c) the order parameter, S, which is needed when the surfactant-probe is inserted in a micro-ordered structure (like a palisade). Complete order gives S=1, while no order corresponds to S=0. In several cases the spectra were constituted by two or more components due to different locations or interactions of the probe with the environmental molecules. The subtraction between the spectra in different experimental conditions allowed extraction of the spectral components constituting the overall EPR spectra. The different components were computed separately. In case, one component was computed and subtracted from the overall spectrum to extract the second component. The subtraction procedure also allowed us to calculate, by double integration of each component, the relative percentages of the different components, with an accuracy of 2 %.

(A)

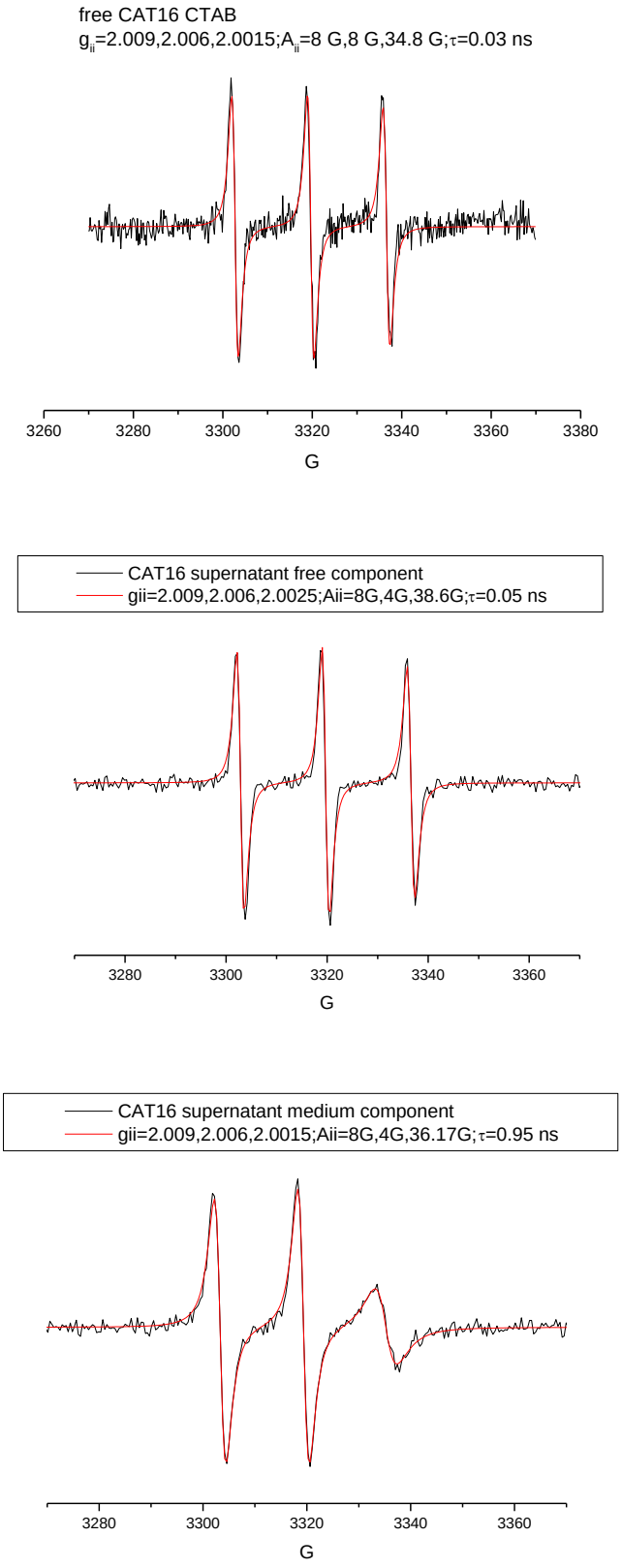

Figure S1(1): experimental and computed spectra and components of the various zeolites with CTAB: CAT16 **(A)**; 5DSA **(B)**

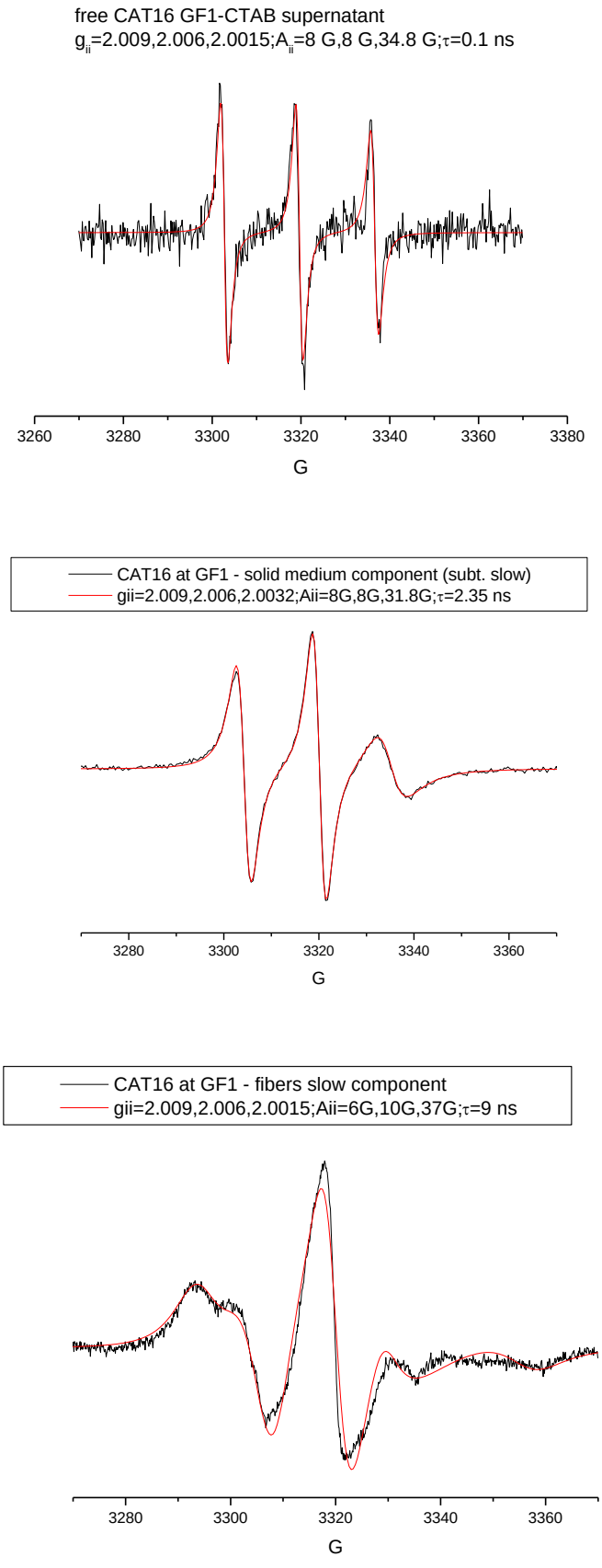

Figure S1(2): experimental and computed spectra and components of the various zeolites with CTAB: CAT16 **(A)**; 5DSA **(B)**

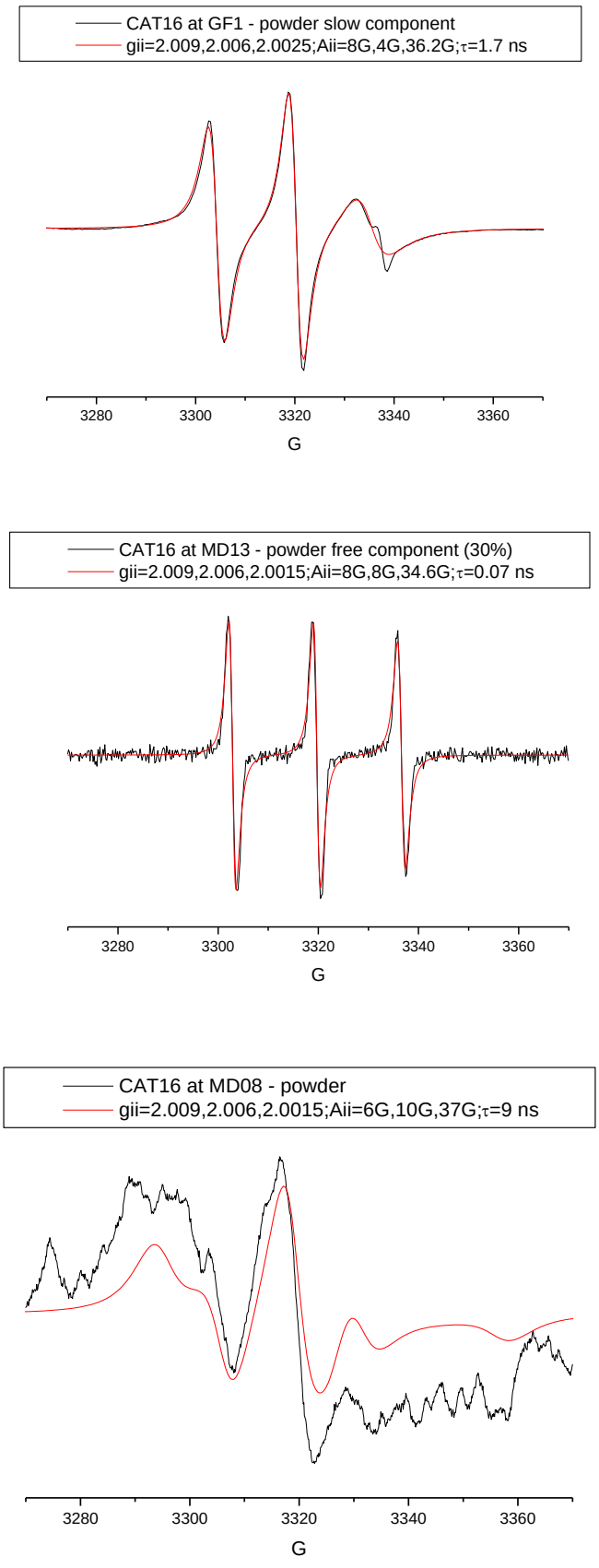

Figure S1(3): experimental and computed spectra and components of the various zeolites with CTAB: CAT16 **(A)**; 5DSA **(B)**

(B)

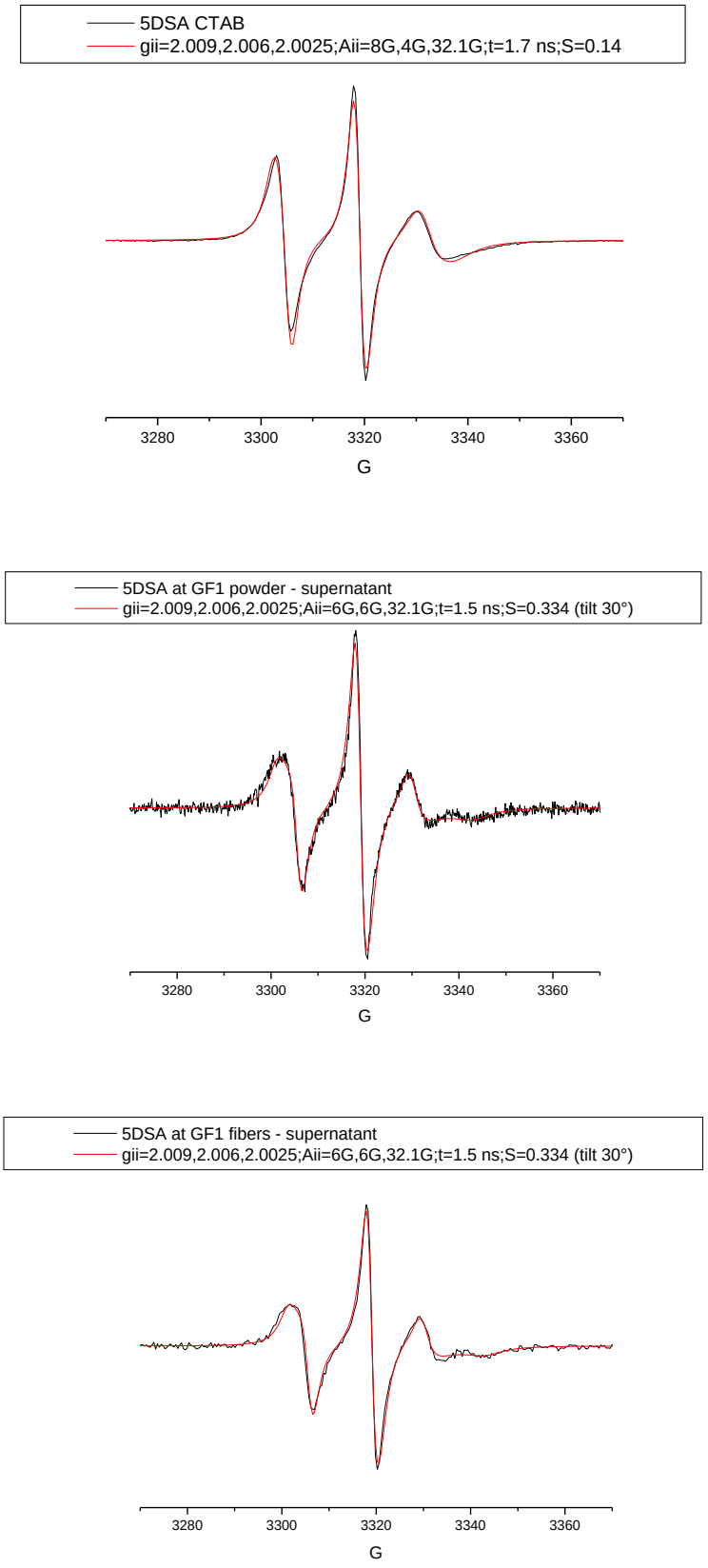

Figure S1(4): experimental and computed spectra and components of the various zeolites with CTAB: CAT16 **(A)**; 5DSA

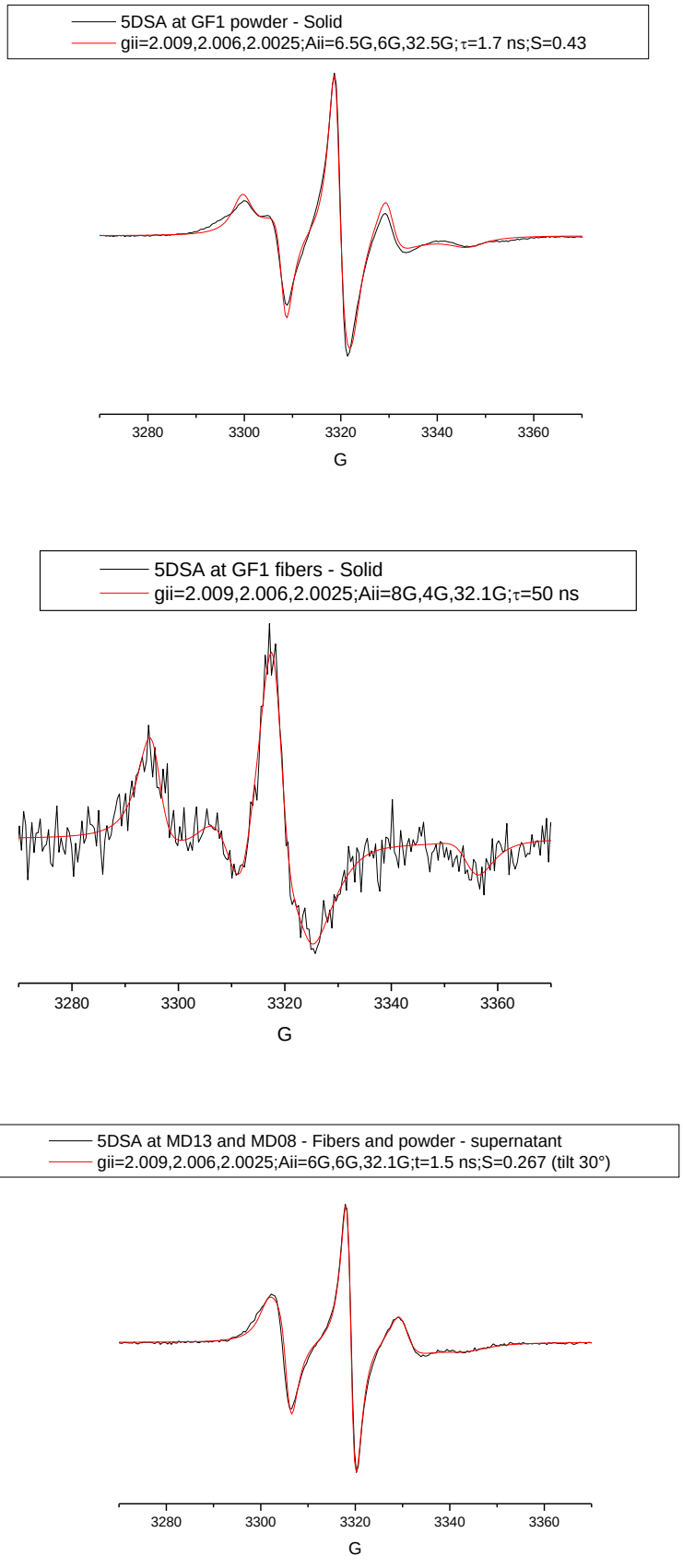

Figure S1(5): experimental and computed spectra and components of the various zeolites with CTAB: CAT16 **(A)**; 5DSA

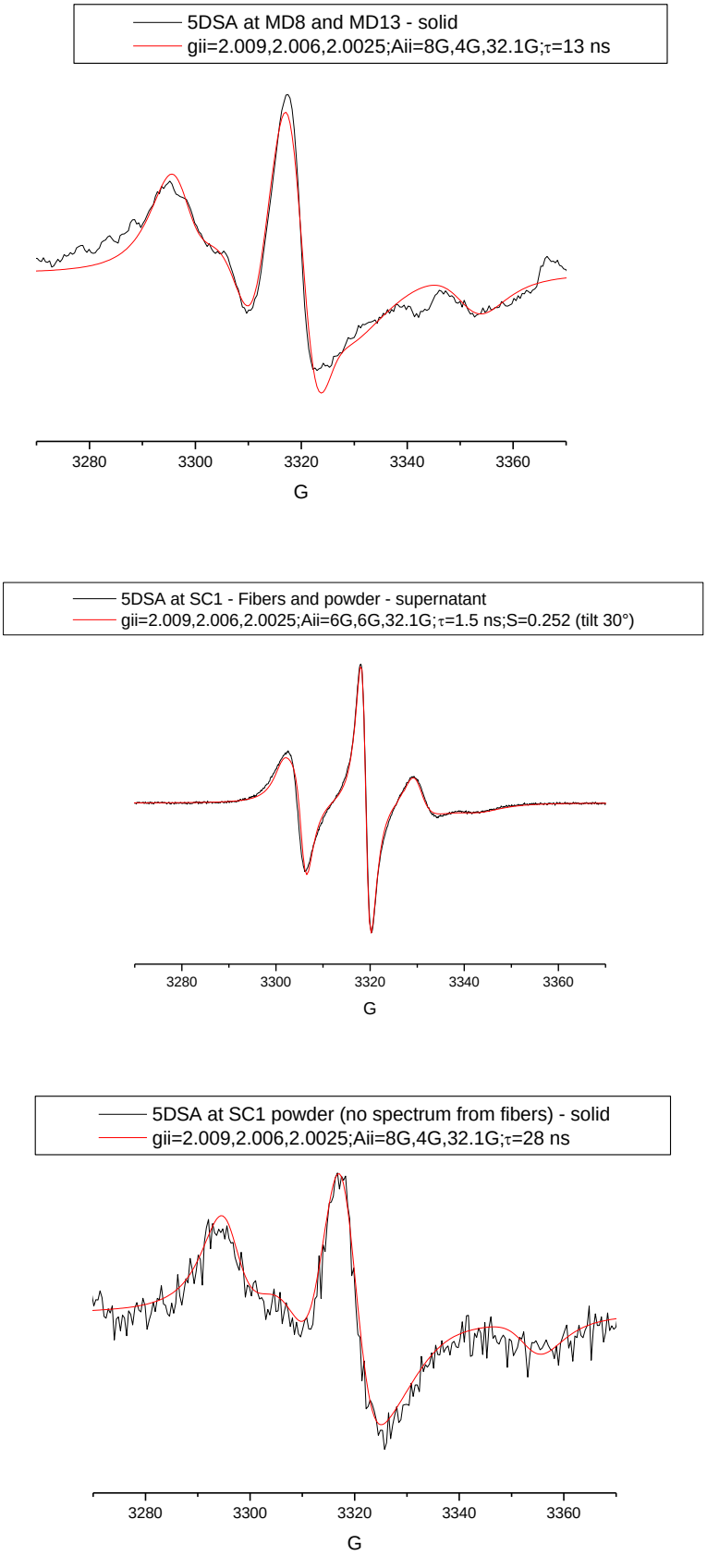

Figure S1(6): experimental and computed spectra and components of the various zeolites with CTAB: CAT16 **(A)**; 5DSA **(B)**